Astrophysics of Galaxies
Padova 2024

Scaling Relations for Galaxies and SMBHs

Stellar Structures, their Kinematics and Stellar Populations

Dimitri Gadotti
Centre for Extragalactic Astronomy
Durham University

Scaling Relations in Galaxies

Galaxies span a wide range in mass and size (as well as other important physical parameters). The way these two parameters relate to each other across the different scales – and the way they relate with other fundamental physical parameters – can give us clues about how galaxies form and evolve.

In addition, many of these relations can be used to estimate distances to individual galaxies. These are the relations that depend on the distance of the galaxies, such as the Faber-Jackson, $D_n - \sigma$, and Tully-Fisher relations.

Scaling Relations in Galaxies

- Luminosity
  - Absolute magnitude
  - Effective intensity or surface brightness
  - Mean effective intensity or surface brightness
- Mass
  - Stellar mass
  - Dynamical mass
- Size
  - Effective radius (or half-light radius)
  - Isophotal radius/diameter
  - Scale-length
- Kinematics
  - Rotational velocity
  - Velocity dispersion (central)
- Colour
- Age
- Metallicity

Scaling Relations in Galaxies

1. The Virial Theorem → what does it mean to be virialized?
2. The Faber-Jackson Relation (FJ)
3. The $D_n - \sigma$ Relation
4. The Kormendy Relation

   (2, 3, 4 → FP projections)
5. The Fundamental Plane (FP)
6. The Colour-Magnitude Relation
7. The Tully-Fisher Relation → FJ for disc galaxies
8. The Mass-Size Relation → FP projection
9. The Mg_2-σ Relation
10. The Mass-Metallicity Relation
11. SMBHs and their Scaling Relations

The Virial Theorem

The Virial Theorem

Let's consider the general motion of particles such as electrons, molecules or stars… calling X, Y and Z the components of the forces applied to the particles, we have from Newton's law (for each particle or star; see Chandrasekhar 1939):

$$m\frac{d^2x}{dt^2} = X;\; m\frac{d^2y}{dt^2} = Y;\; m\frac{d^2z}{dt^2} = Z$$

We can also write:

$$\frac{1}{2}\frac{d^2}{dt^2}(mx^2) = m\frac{d}{dt}\left(x\frac{dx}{dt}\right) = mx\frac{d^2x}{dt^2} + m\left(\frac{dx}{dt}\right)^2 = m\left(\frac{dx}{dt}\right)^2 + xX$$

And similarly:

$$\frac{1}{2}\frac{d^2}{dt^2}(my^2) = m\left(\frac{dy}{dt}\right)^2 + yY,$$

$$\frac{1}{2}\frac{d^2}{dt^2}(mz^2) = m\left(\frac{dz}{dt}\right)^2 + zZ.$$

The Virial Theorem

If we sum all force components then we have:

$$\frac{1}{2}\frac{d^2}{dt^2}(mr^2) = \underbrace{m\left[\left(\frac{dx}{dt}\right)^2 + \left(\frac{dy}{dt}\right)^2 + \left(\frac{dz}{dt}\right)^2\right]}_{\text{twice the kinetic energy}} + (xX + yY + zZ)$$

And summing over all particles/stars:

$$\frac{1}{2}\frac{d^2I}{dt^2} = 2T + \sum(xX + yY + zZ)$$

where $I = \sum(mr^2)$ is the total moment of inertia about the origin of the stellar system, and T is the total kinetic energy of the stellar system. Now, $\sum(xX + yY + zZ)$ is called the virial of Clausius.

The Virial Theorem

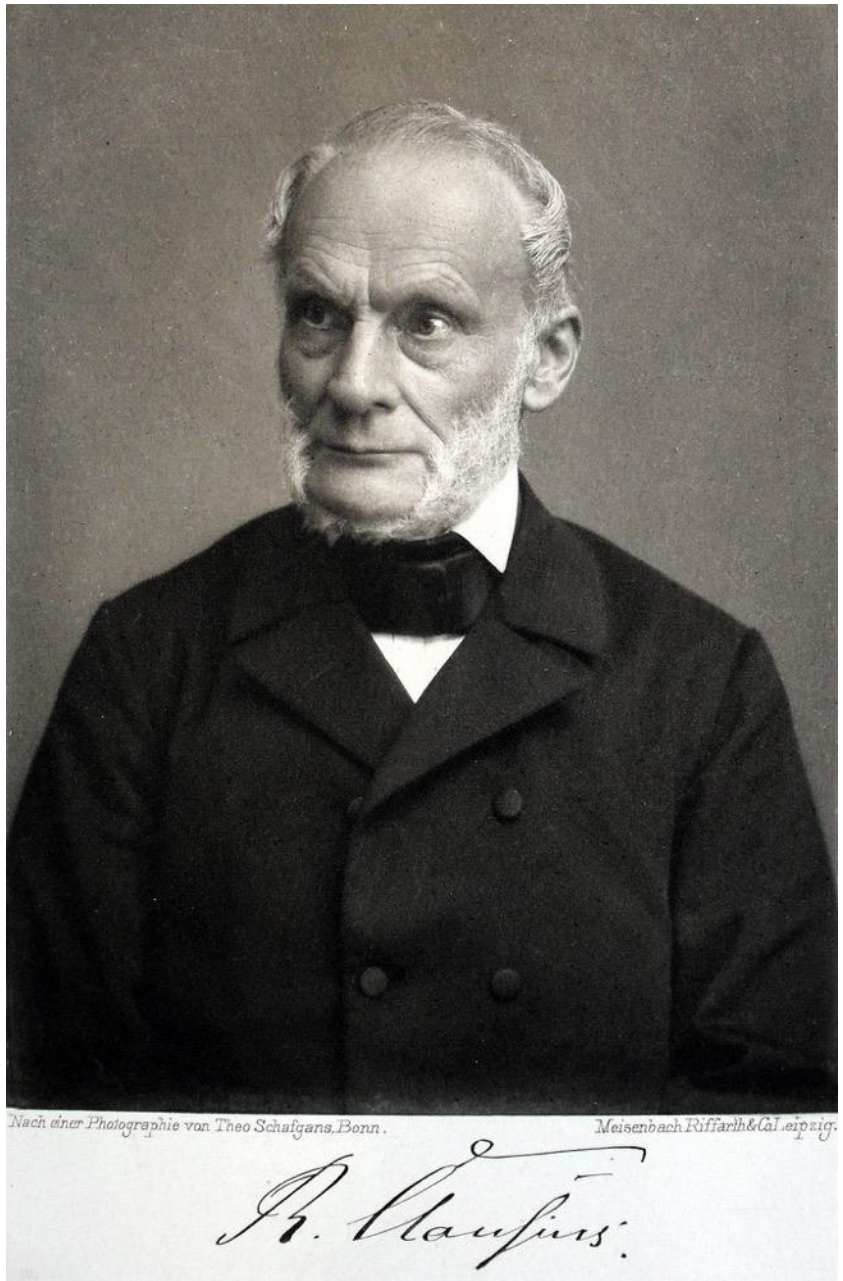

Rudolf Clausius (1822-1888): one of the founding fathers of Thermodynamics

The Virial Theorem

Now consider two stars with masses m_1 and m_2, such that the gravitational force exerted on the first star by the second has components A, B and C. Then the force exerted by the first star on the second has components -A, -B and -C.

The contribution of this pair of forces to the virial is:

$$A(x_1 - x_2) + B(y_1 - y_2) + C(z_1 - z_2)$$

And summing over all pairs of stars, the virial becomes:

$$\sum\sum[A(x_1 - x_2) + B(y_1 - y_2) + C(z_1 - z_2)]$$

Now the components of the gravitational force exerted by the first star on the second are the components of:

$$\frac{Gm_1m_2}{r_{12}^2}$$

The Virial Theorem

So the components of the virial for each star are:

$$-\frac{Gm_1m_2}{r_{12}^2} \times (x_1 - x_2), \text{ along the } X\text{-axis},$$
$$-\frac{Gm_1m_2}{r_{12}^2} \times (y_1 - y_2), \text{ along the } Y\text{-axis},$$
$$-\frac{Gm_1m_2}{r_{12}^2} \times (z_1 - z_2), \text{ along the } Z\text{-axis}.$$

Negative because the force is attractive from one star to the other. And summing over all stars the total virial becomes:

$$-\sum\sum \frac{Gm_1m_2}{r_{12}}$$

That's the gravitational potential energy of the system (Ω)!

The Virial Theorem

Hence, we have:

$$\frac{1}{2}\frac{d^2 I}{dt^2} = 2T + \Omega$$

If the system is in a steady state (virialized!), I is constant and then finally:

$$2T + \Omega = 0$$

Henri Poincaré (1854-1912)

Luckily for us only the second derivative of the moment of inertia needs to be zero!

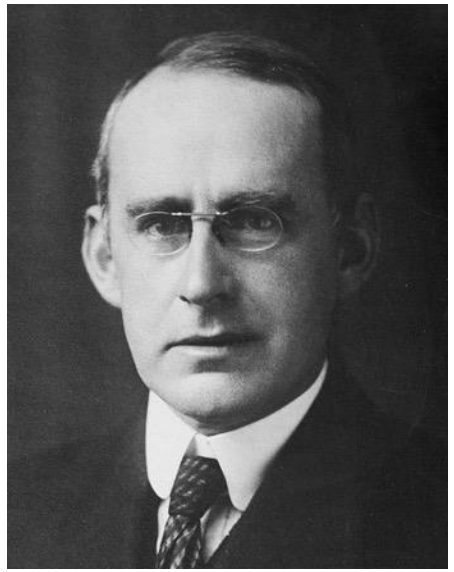

Arthur Eddington (1882-1944)

The Virial Theorem

From the virial theorem to the Tully-Fisher and Faber-Jackson relations

We have that $2T + \Omega = 0$, and thus, for a stellar system:

$$\frac{GMM}{\langle R \rangle} = M\langle v^2 \rangle \Rightarrow \frac{GM}{\langle R \rangle} = \langle v^2 \rangle$$

How do we use this to find a relation between galaxy luminosity L and stellar velocity? Let's assume a constant mass-to-light ratio M/L, such that:

$$\frac{GL}{\langle R \rangle} \propto \langle v^2 \rangle \Rightarrow \langle R \rangle \propto \frac{GL}{\langle v^2 \rangle}$$

Let us now bring the concept of mean surface brightness:

$$L \propto \pi \langle I \rangle R^2$$

The Virial Theorem

From the virial theorem to the Tully-Fisher and Faber-Jackson relations

Replacing R from the previous equation we have:

$$L \propto \pi \langle I \rangle R^2 \Rightarrow L \propto \pi \langle I \rangle \left(\frac{GL}{\langle v^2 \rangle} \right)^2$$

And moving $\langle I \rangle$ to the proportionality constant:

$$L \propto \langle v^4 \rangle$$

For a disc galaxy, dynamically supported by rotation, v will be the peak rotational velocity, and so we have the Tully-Fisher relation. For an elliptical galaxy, dynamically supported by the stellar velocity dispersion, v will be the central velocity dispersion, and so we have the Faber-Jackson relation.

The Virial Theorem

Incidentally, two orbiting bodies, like the Sun and Jupiter should also obey the virial theorem, and we can obtain from Newtonian mechanics the same relation derived from the virial theorem, namely:

$$\frac{GM}{\langle R \rangle} = \langle v^2 \rangle \Longrightarrow \langle v \rangle = \sqrt{\frac{GM}{\langle R \rangle}}$$

Simply equating the gravitational force from the Sun on Jupiter to Jupiter's radial acceleration times its mass, we have:

$$\frac{GM_{\text{Sun}}M_{\text{Jupiter}}}{R^2} = \frac{M_{\text{Jupiter}}v^2}{R} \Longrightarrow v = \sqrt{\frac{GM_{\text{Sun}}}{R}}$$

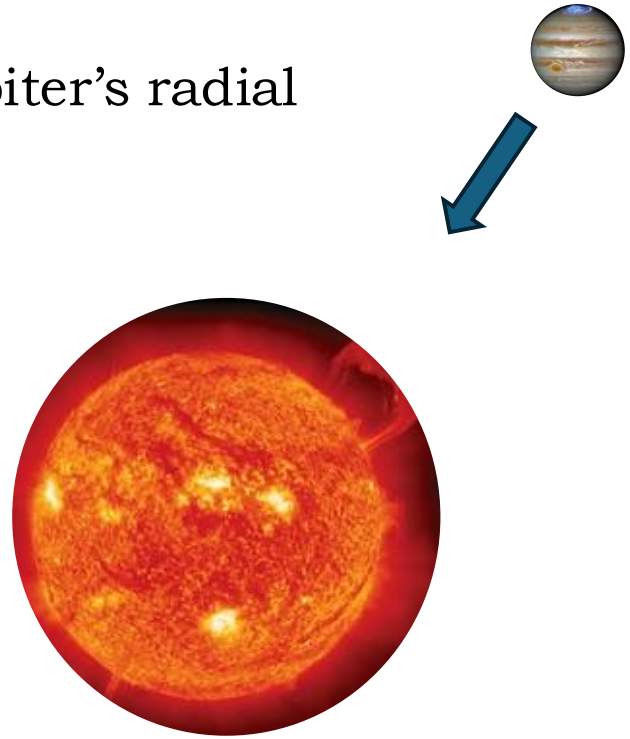

And, of course, it better be the case!

The Faber Jackson Relation

Luminosity (or mass) vs. velocity dispersion

The Faber-Jackson Relation

$$L = \sigma^{\beta}$$

- More luminous/massive elliptical galaxies are expected to have higher central stellar velocity dispersions

- Virial theorem indicates $\beta = 4$ (since a considerable fraction of the kinetic energy is in random motion)

- Faber & Jackson (1976)

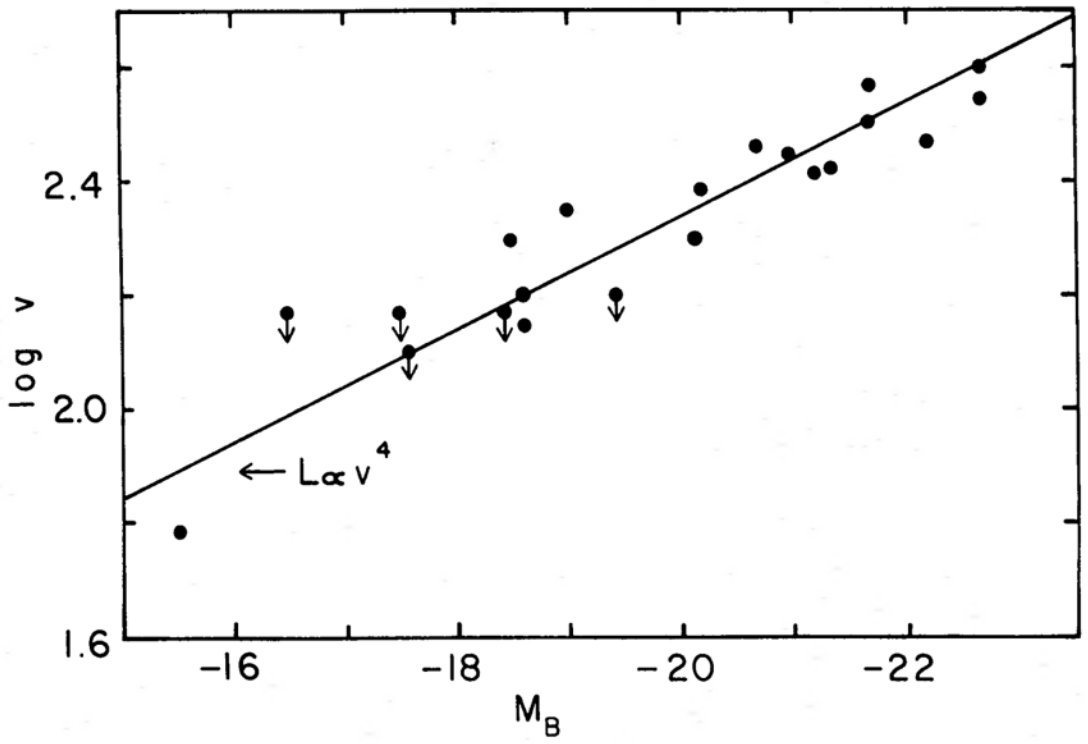

FIG. 16.—Line-of-sight velocity dispersions versus absolute magnitude from Table 1. The point with smallest velocity corresponds to M32, for which the velocity dispersion (60 km s^{-1}) was taken from Richstone and Sargent (1972).

The Faber-Jackson Relation

$$L = \sigma^{\beta}$$

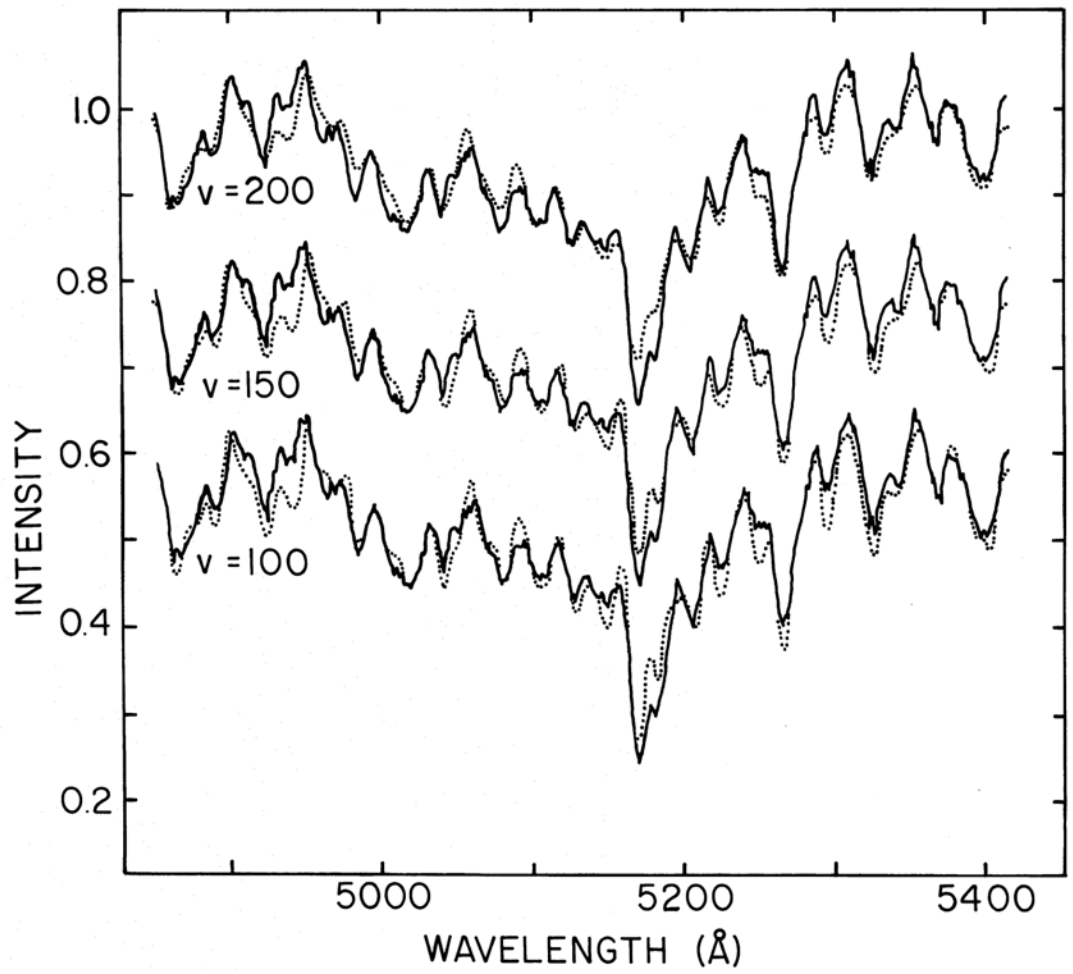

FIG. 13.—The nucleus of M31 compared with broadened spectra of standard star HR 2600 (K2 III) (*dotted line*). Adopted mean visual velocity is 180 km s^{-1}. (Sum of two observations.)

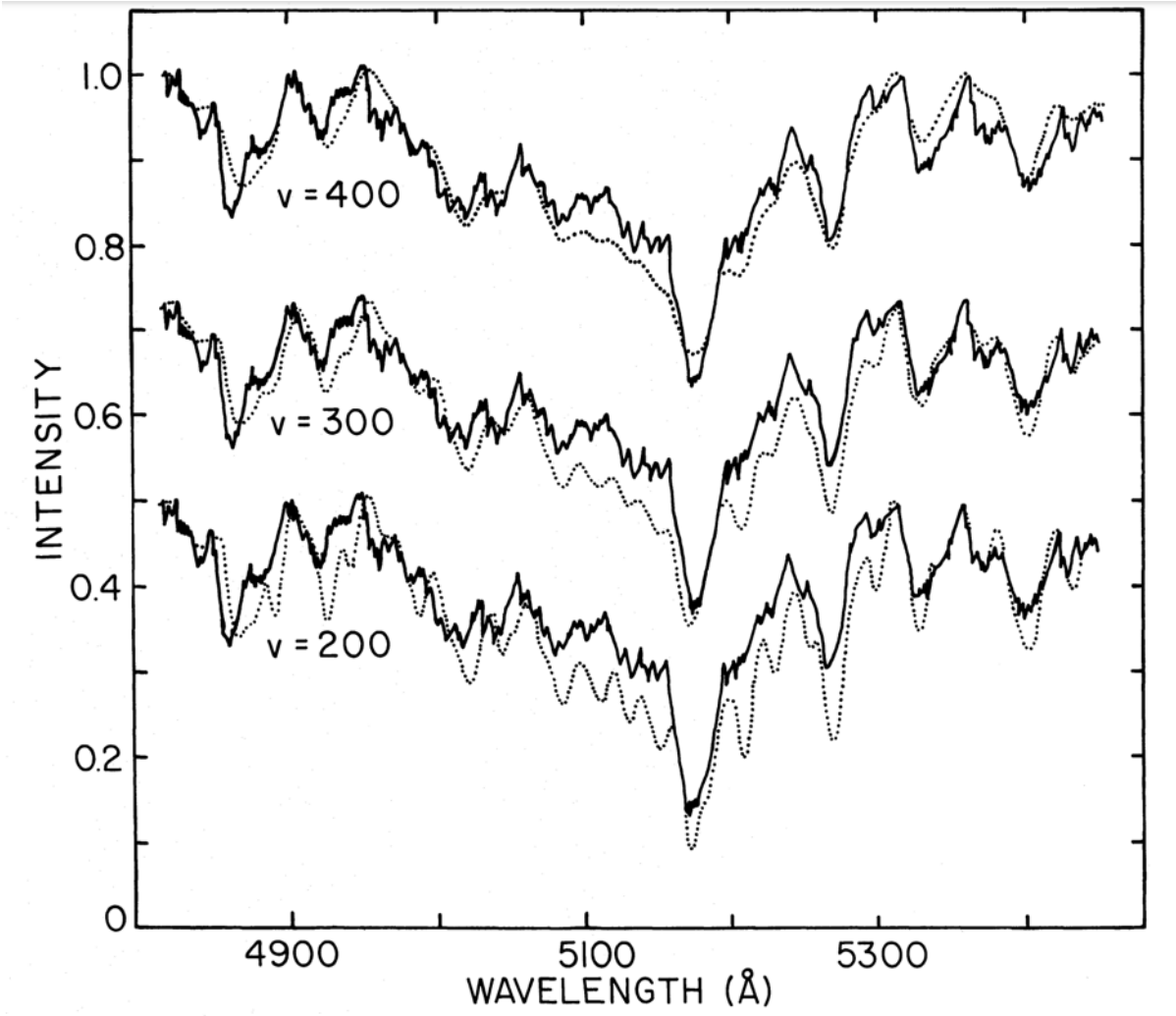

FIG. 3.—NGC 4472 compared with standard star HR 1805 (K3 III), broadened by various line-of-sight velocities (*dotted line*)

Faber & Jackson (1976)

The Faber-Jackson Relation

$$L = \sigma^{\beta}$$

- More recent studies find different values for β or that it might not be constant

- Gallazzi+2006 also investigate the relation when luminosity is replaced by stellar mass

- Galaxies with higher mass and older stellar populations seem to result in a steeper slope
  - This suggests variations in the formation processes of elliptical galaxies of different mass (more on this later)

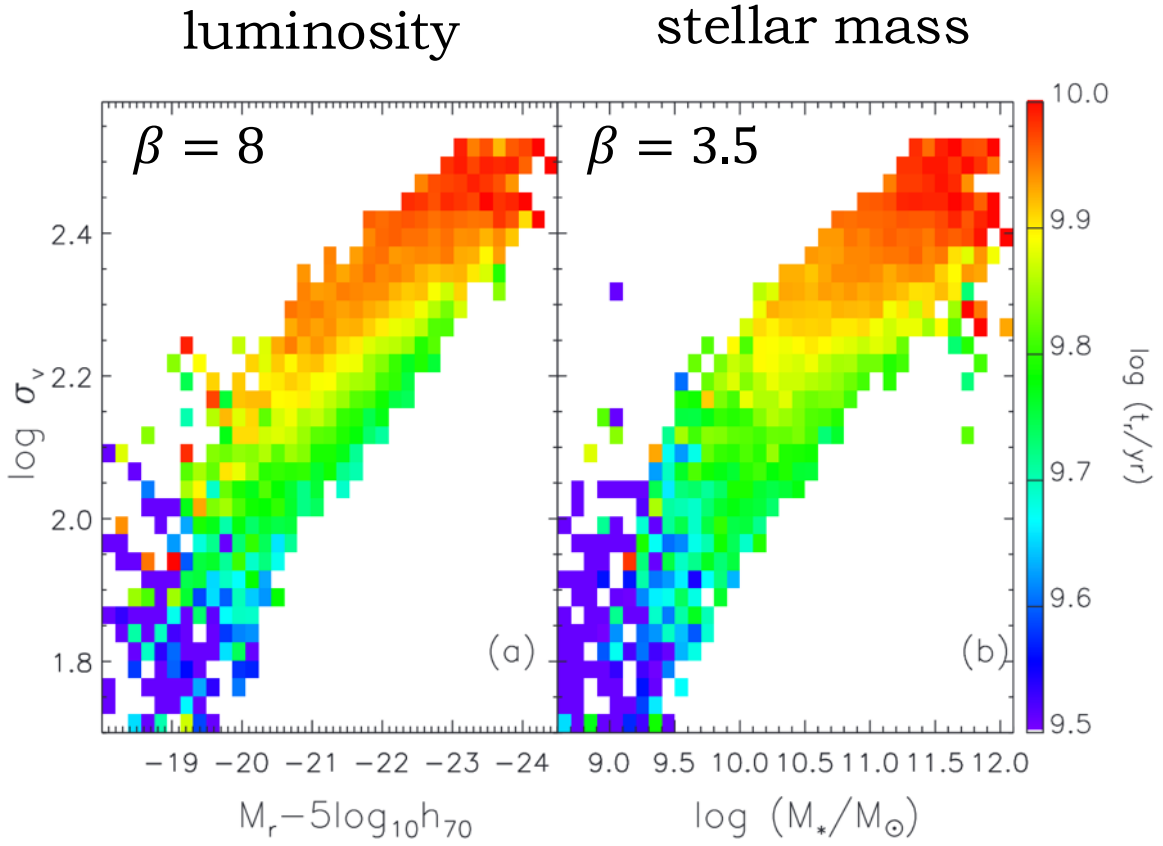

Figure 15. Relation between velocity dispersion and r-band absolute magnitude (panel a), colour coded to reflect the average light-weighted age of the galaxies falling into each $\log \sigma_V - M_r$ bin. For M_r brighter than −20, lines of constant age are approximately parallel to the relation. Panel (b) shows the result of substituting absolute magnitude with stellar mass.

Core and Power-Law Ellipticals

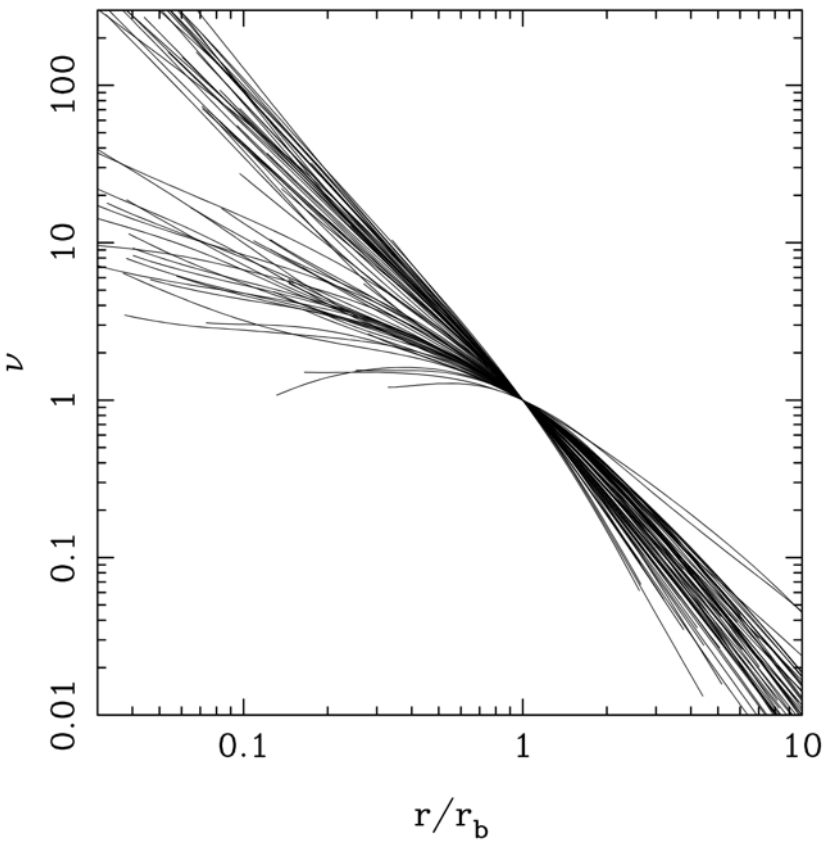

FIG. 6.—Luminosity density profiles for the subset of galaxies for which WFPC2 brightness profiles are available (as opposed to galaxies for which we have only the Nuker law parameters). The Laine et al. (2003) BCG sample is also excluded. The radial scale is normalized by Nuker law break radius, but the real measured brightness profiles were used rather than the Nuker law fits. The slopes of the profiles for $r < r_b$ are strongly bimodal. The bottom panel excludes galaxies in Lauer et al. (2005) with dust strength greater than 1.0.

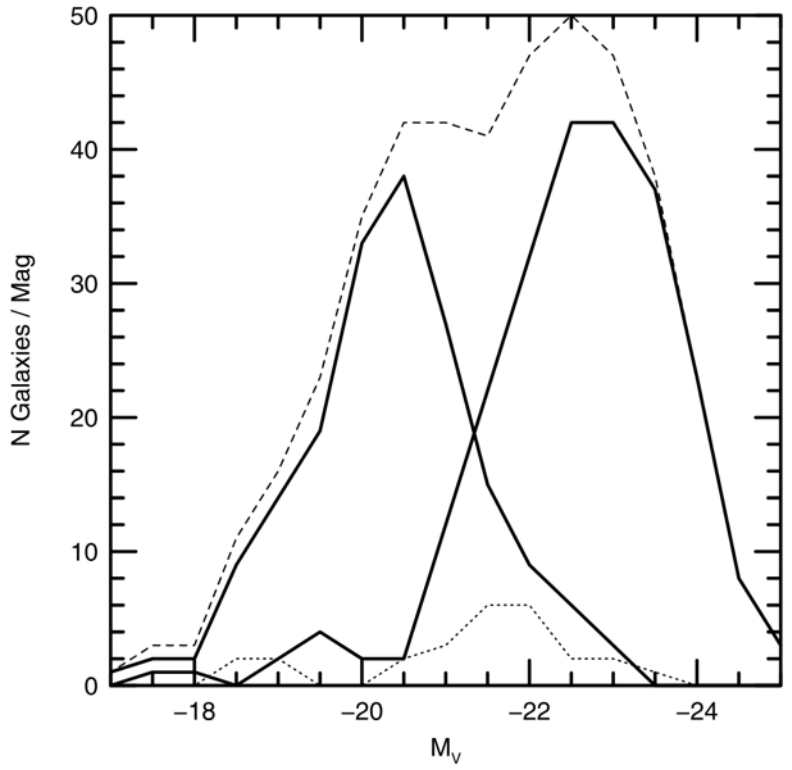

FIG. 1.—Histograms showing the frequency of core galaxies (*solid line peaking at higher luminosities*), power-law galaxies (*solid line peaking at lower luminosities*), and intermediate galaxies (*dotted line*) as a function of luminosity in our sample of 219 galaxies. The dashed line shows the total distribution of galaxies with luminosity. Note that the low-luminosity end of the power-law galaxy distribution and the high-luminosity end of the core galaxy distribution are likely to reflect biases with luminosity in the construction of the sample, but there are no obvious biases that affect the luminosity range $-22.5 \leq M_V \leq -20.5$ over which the frequency of power-law galaxies decreases as that of the core galaxies increases. [*See the electronic edition of the Journal for a color version of this figure.*]

- There seems to be a dichotomy between massive and less massive elliptical galaxies, in which the former have cores in their luminosity radial profiles. The cores are created (we think) by the ejection of stars by a supermassive black hole binary
- See Lauer+2007b
- Much more about this later, including contrasting results

The Faber-Jackson Relation

$$L = \sigma^{\beta}$$

- Lauer+2007a find that β varies from ~ 2 for power-law elliptical galaxies to ~ 7 for brightest cluster galaxies (BCGs); see also Bernardi+2006

- Consistently with Gallazzi+2006, more more massive ellipticals result in a higher β

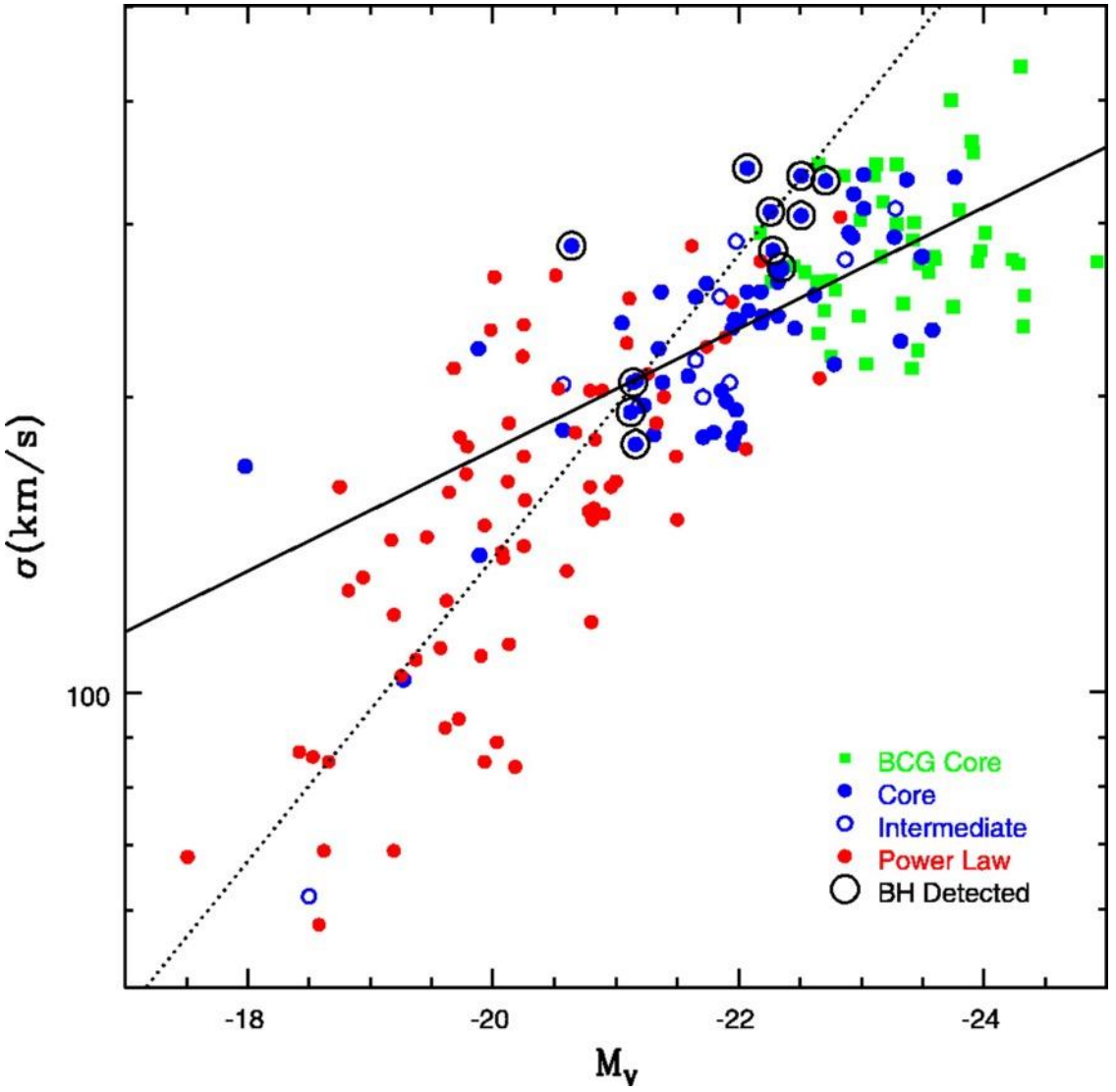

FIG. 3.—Relationship between central velocity dispersion, σ, and L for the sample. A fit to just the core galaxies and BCGs (*solid line*; eq. [7]) gives $L \sim \sigma^7$, a much steep relationship than the standard $L \sim \sigma^4$ Faber-Jackson relationship, and $L \sim \sigma^2$ for the power-law galaxies alone (*dotted line*; eq. [8]). It is this change in slope that leads to conflicting predictions for $M_\bullet$ from the $M_\bullet$-L and $M_\bullet$-σ relations for the most luminous galaxies. Core galaxies with directly measured BH masses are circled. [*See the electronic edition of the Journal for a color version of this figure.*]

The Faber-Jackson Relation

$$L = \sigma^{\beta}$$

- Simulations with more radial, dissipation-less mergers (small pericentre passages) to build more massive ellipticals lead to higher values of β (Boylan-Kolchin+2006)

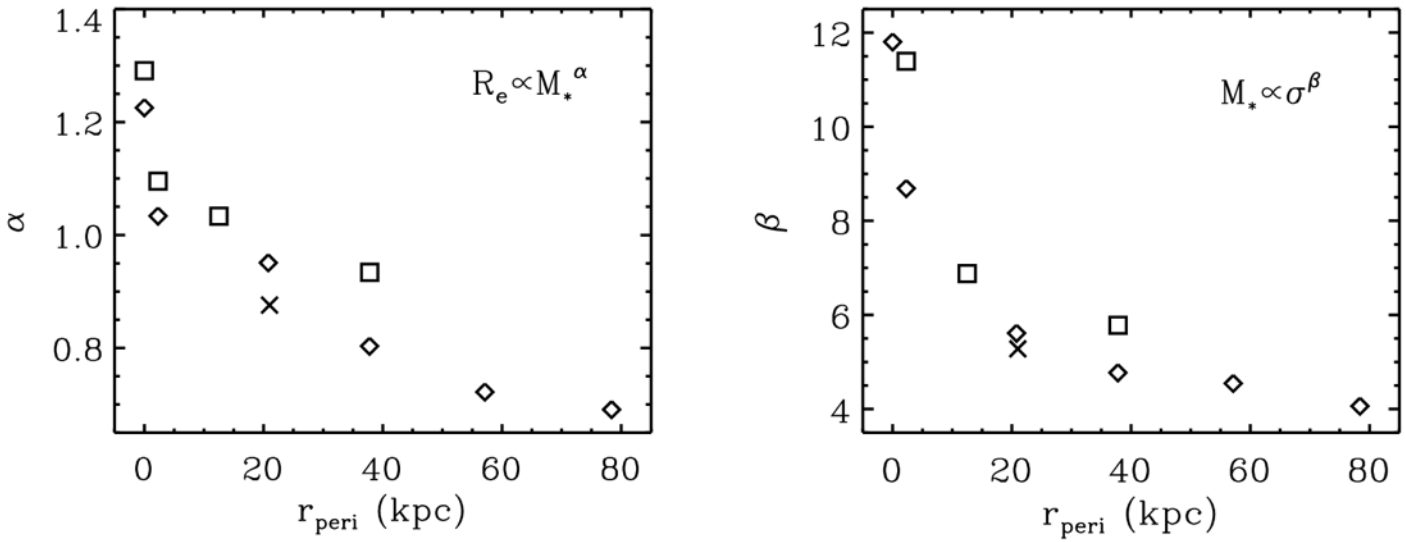

Figure 3. Logarithmic slopes of the mass–size relation ($R_e \propto M_*^{\alpha}$; left) and Faber–Jackson ($M_* \propto \sigma_e^{\beta}$; right) relations as a function of orbital pericentric distance for each of the equal-mass merger simulations listed in Table 1. The two orbital energies are shown as diamonds (bound) and squares (parabolic), while the remerger run is marked with an X symbol. At a given r_{peri}, the bound orbits produce remnants with a slightly lower α and β than parabolic orbits. The parabolic head-on orbit has $\beta \approx 28$, so it is not plotted here. For orbits with significant orbital angular momentum (large r_{peri}), our merger simulations reproduce the observed values of $\alpha \sim 0.6$ and $\beta \sim 4$ but we predict a sharp increase in α and β for more radial mergers. The results for the remerger run agree well with those for the first generation mergers, indicating that the spherical and isotropic galaxy models used in the first generation mergers do not strongly bias our results.

The Faber-Jackson Relation

$$L = \sigma^{\beta}$$

- Desroches+2007: *The variations in the FP projections we find at the luminous end are consistent with less and less dissipation during the formation of elliptical galaxies with increasing luminosity. Less dissipation would result in increasingly larger, less dense, lower surface brightness and lower σ galaxies, relative to fiducial power-law scalings for the elliptical galaxy population.*

The $D_n - \sigma$ Relation

Isophotal diameter vs. velocity dispersion

The $D_n - \sigma$ Relation

$$\log D_n = a \log \sigma + c$$

- D_n is an isophotal diameter (size – in arcsec), originally set to the B-band 20.75 mag arcsec^{-2} isophote (Dressler+1987a,b)

$$\langle I \rangle_n = \frac{2\pi \int_0^{D_n/2} I(R)\, R\, \mathrm{d}R}{\frac{1}{4}\pi D_n^2}$$

Mo+2010, Eq. (13.68)

integrated intensity over annuli

area within isophote

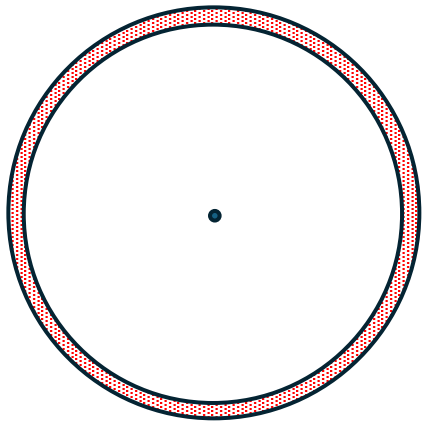

The $D_n - \sigma$ Relation

$$\log D_n = a \log \sigma + c$$

- Scatter in the determined distance a factor two better than Faber-Jackson relation
- Distance to Coma cluster estimated as 10 times larger than distance to Virgo cluster

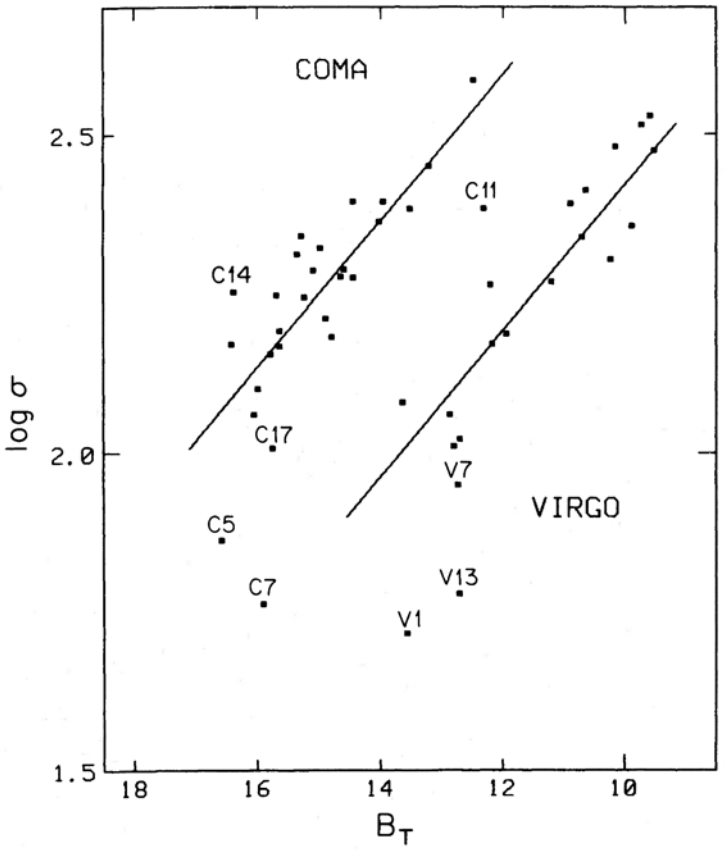

FIG. 1a

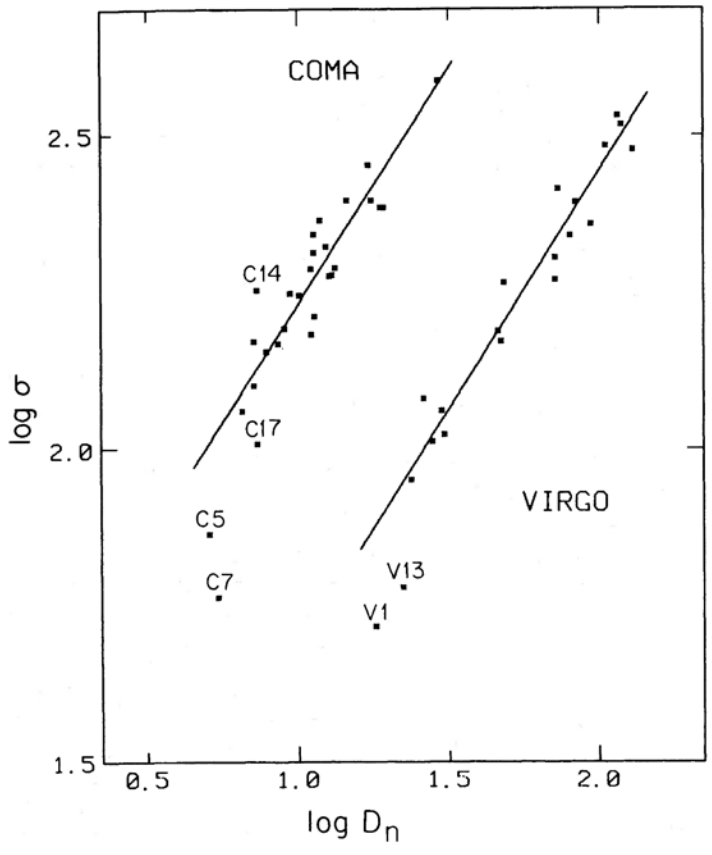

FIG. 1b

Today's estimates:
Virgo: 16.5 Mpc
Coma: 99 Mpc

FIG. 1.—(*a*) B_T, the total blue magnitude, vs. log σ, the central velocity dispersion, for ellipticals in the Coma and Virgo clusters. These are the variables of the Faber-Jackson relationship. The lines $\log \sigma = -0.114 B_T + C$, where $C = 3.561$ for Virgo and $C = 3.960$ for Coma, are best median fits, as described in the text. The rms scatters in B_T from these lines are 0.57 mag for Virgo and 0.69 mag for Coma. (*b*) log D_n, the diameter within which the integrated blue surface brightness is 20.75 B mag arcsec^{-2}, vs. log σ for the same galaxies. The horizontal scales correspond to a factor of 10 in distance in both figures. The lines $\log \sigma = 0.750 \log D_n + C$, where $C = 0.934$ for Virgo and $C = 1.475$ for Coma, are best median fits. The rms scatter in log D_n is 0.059 for Virgo and 0.072 for Coma, a factor of 2 smaller scatter than with the Faber-Jackson relationship.

The Kormendy Relation

Effective radius vs. mean effective surface brightness

The Kormendy Relation

$$\langle \mu_e \rangle = \alpha + \beta \log r_e$$

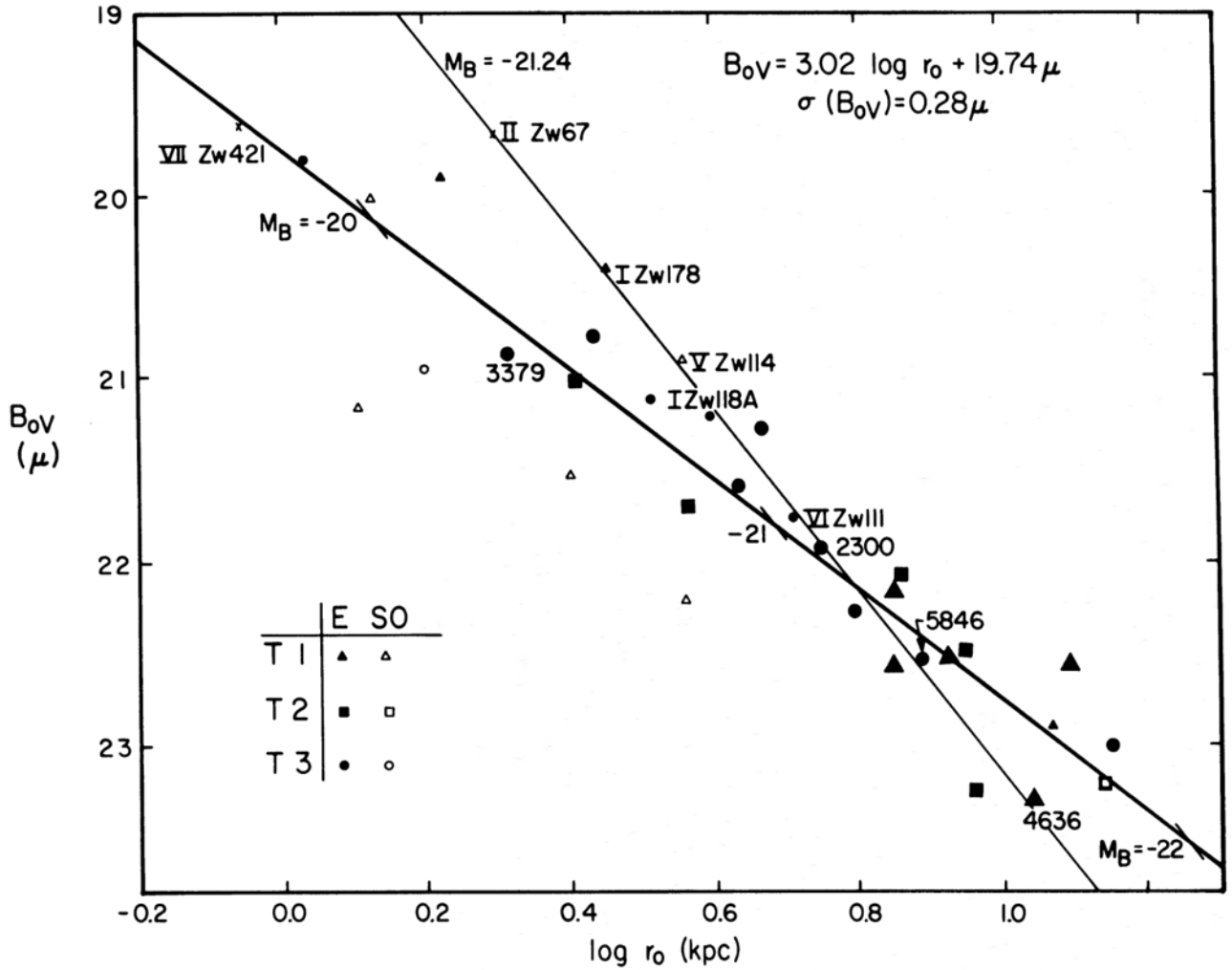

FIG. 2.—B_{0V} versus log r_0 for de Vaucouleurs law fits to compact (*small symbols*) and normal (*large symbols*) galaxies. The heavy line is the least-squares relation for normal galaxies, given at upper right. Average absolute magnitude ticks are defined by eq. (5). Also shown is a typical line of constant M_B, defined by the labeled galaxies.

Kormendy (1977):

- Larger r_e leads to fainter μ_e
- Relation runs at an angle with lines of constant absolute magnitude M

The Kormendy Relation

$$\langle \mu_e \rangle = \alpha + \beta \log r_e$$

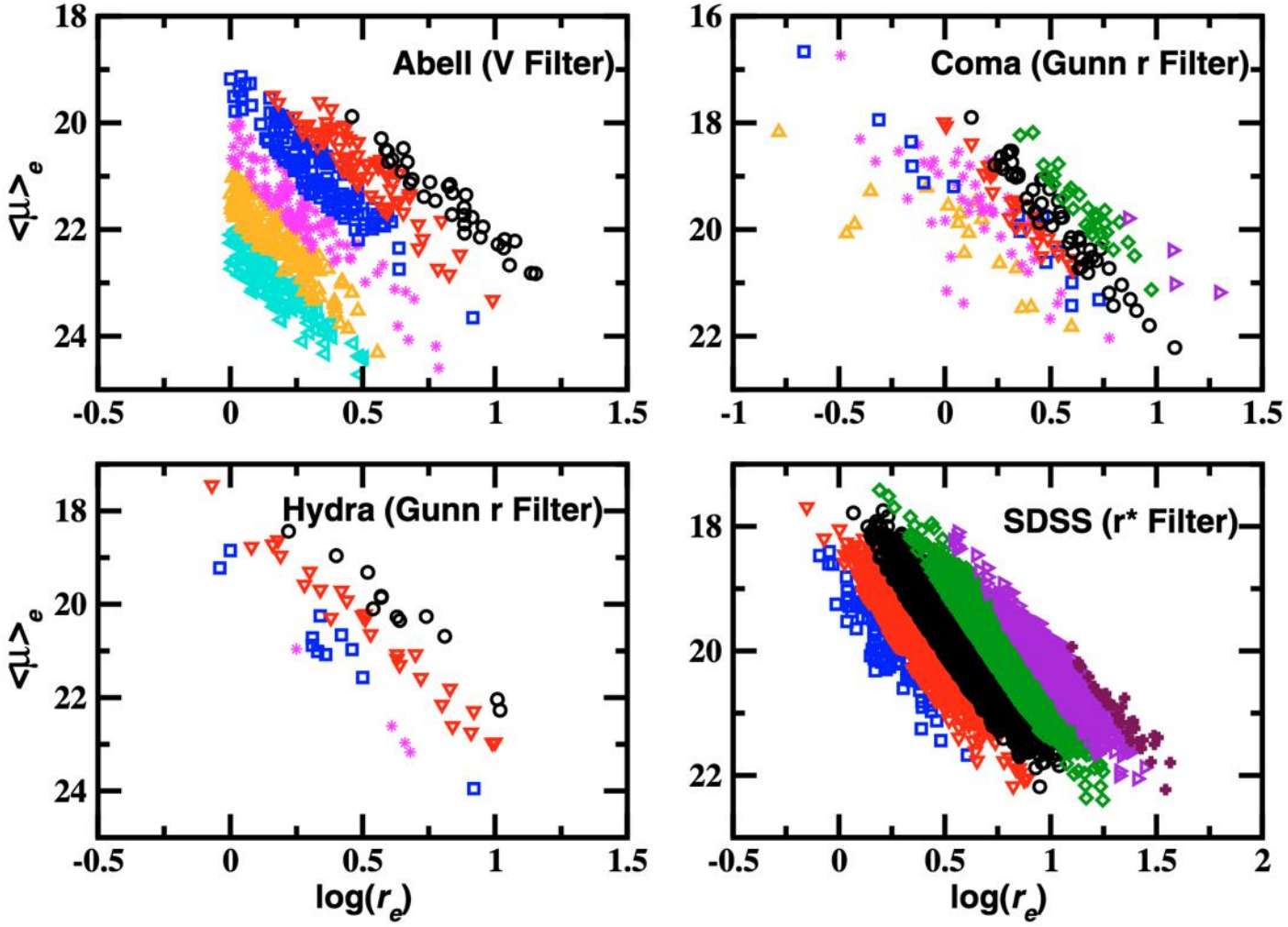

Nigoche-Netro+2008

Fig. 3. Distribution of the Abell, Coma, Hydra and SDSS (r^* filter) galaxies on the $\log(r_e) - \langle\mu\rangle_e$ plane. Each symbol represents a 1 mag interval. The circles represent the $(-21, -22]$ mag interval.

The Kormendy Relation

$$\langle \mu_e \rangle = \alpha + \beta \log r_e$$

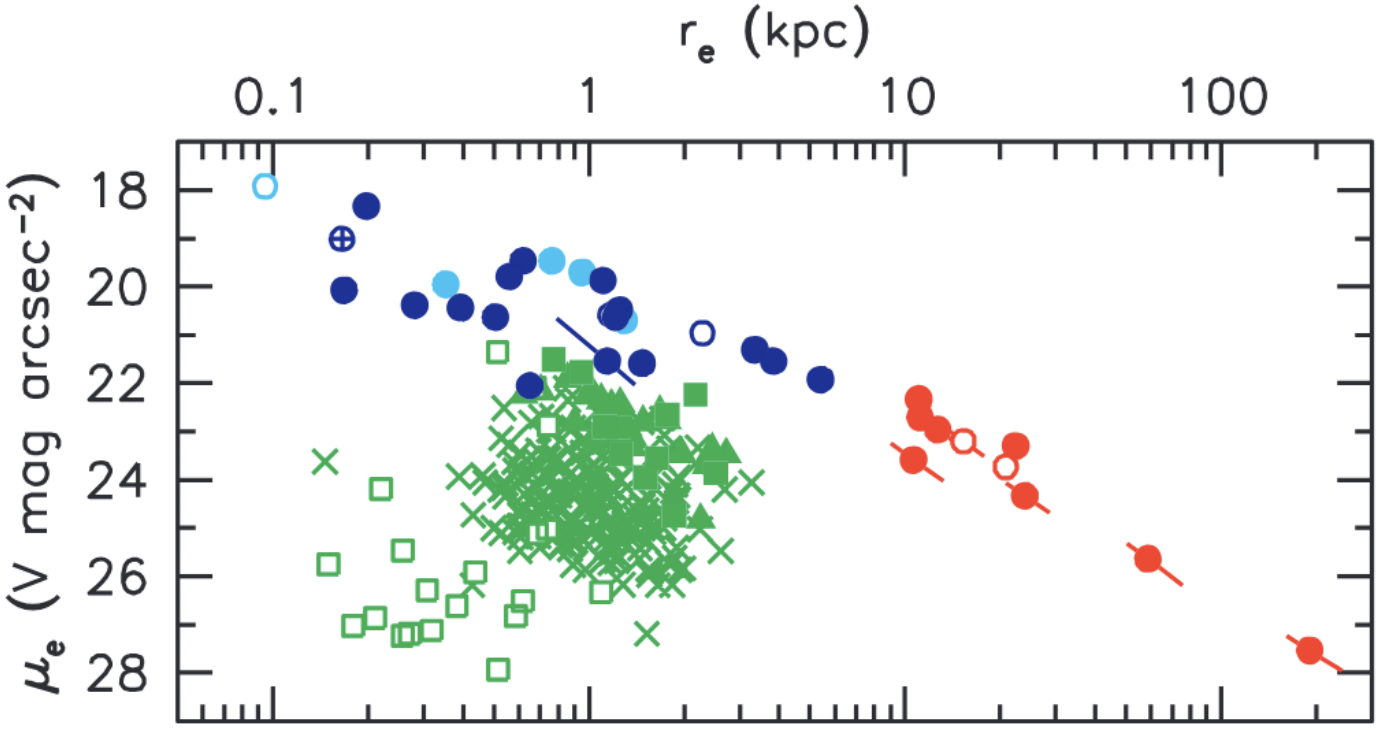

Core ellipticals
Power-law ellipticals
Bulges of S0s
Spheroidals

Kormendy+2009

Elliptical galaxies and the massive bulges in some S0s follow a tight Kormendy relation, but spheroidal galaxies do not.

This points out that the formation processes of spheroidal galaxies is different.

Spheroidal Galaxies

Kormendy+2009

Spheroidal galaxies were initially thought to be dwarf ellipticals, but they follow different relations. The current picture is that spheroidals were faint disc galaxies that were stripped of gas by environmental effects and/or supernova feedback.

So there seems to be 3 types of quiescent galaxies with different formation processes:

1. Core ellipticals: mergers with binary SMBHs scouring
2. Power-law ellipticals: mergers
3. Spheroidals: disc galaxies transformed by environment and feedback

More later!

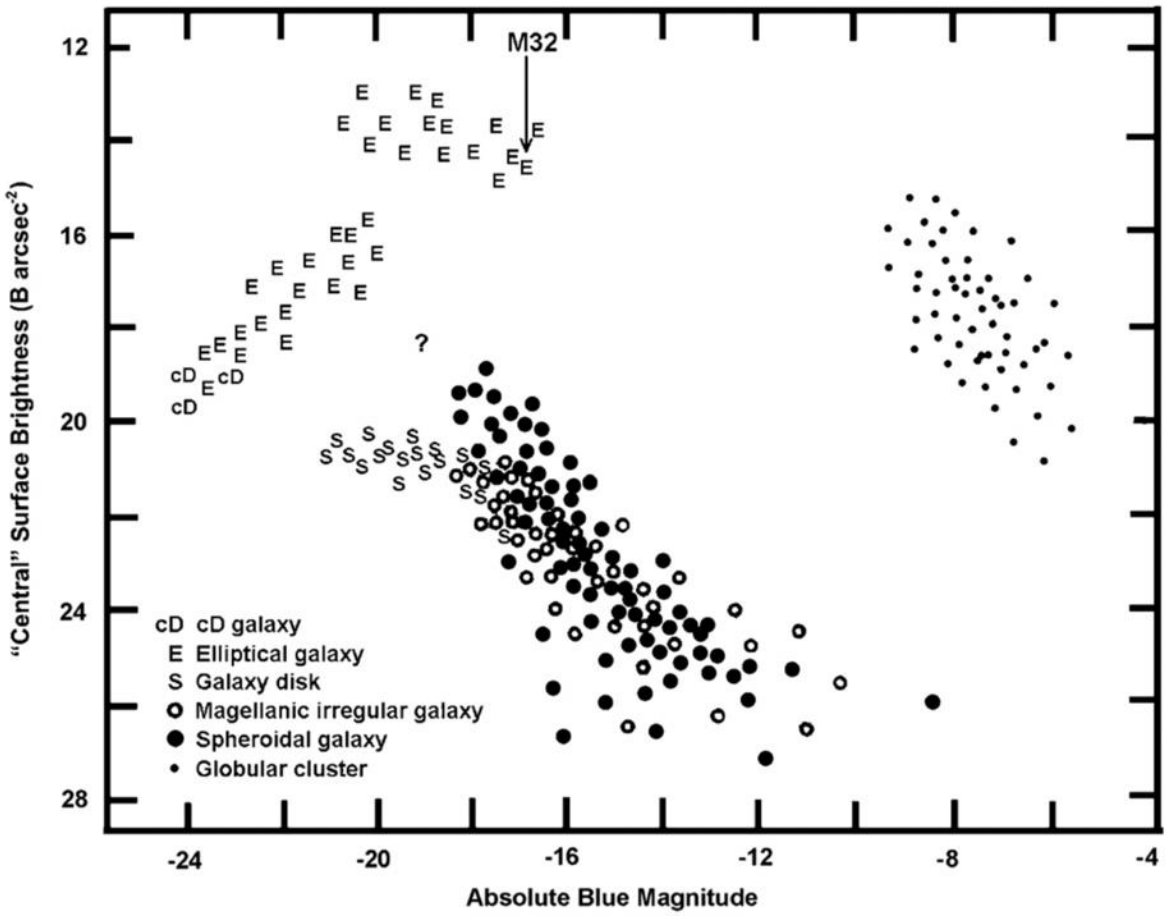

Figure 1. Schematic illustration of the dichotomies discussed in this paper. The figure sketches the correlation between the total absolute magnitude and central surface brightness (for spheroidal and irregular galaxies, galaxy disks, and globular clusters), or the highest surface brightness resolved by the *Hubble Space Telescope* (for elliptical and cD galaxies). Surface brightnesses apply to the main bodies of the galaxies; that is, nuclear star clusters and AGNs are omitted. This figure is adapted from Binggeli (1994) but with the dichotomy between "core" and "power-law" ellipticals—i.e., the discontinuity in E points at $M_B \sim -20.5$—added from Faber et al. (1997). M 32 is one of the lowest-luminosity true ellipticals; the arrow points from the maximum surface brightness observed at a distance of 0.8 Mpc to the lower limit that would be observed if the galaxy were moved to the Virgo cluster. M 32 resembles the faintest ellipticals in Virgo. The distribution of Sph and S+Im galaxies is disjoint from that of ellipticals. Sph and S+Im galaxies have similar global parameters at low luminosities, but the most luminous spheroidals "peel off" of the distribution of late-type galaxies toward higher surface brightness. Spheroidals with $M_B \lesssim -18$ are rare, so the degree to which the Sph sequence approaches the E sequence is poorly known (see the question mark). Note: Binggeli (1994) and some other authors call spheroidal galaxies "dwarf ellipticals" (dEs). We do not do this, because correlations like those in this figure and in Figures 34–38 and 41, as well as the considerations discussed in Sections 2.1 and 8, persuade us that they are not small ellipticals but rather are physically related to late-type galaxies.

The Kormendy Relation

$$\langle \mu_e \rangle = \alpha + \beta \log r_e$$

Gadotti (2009)

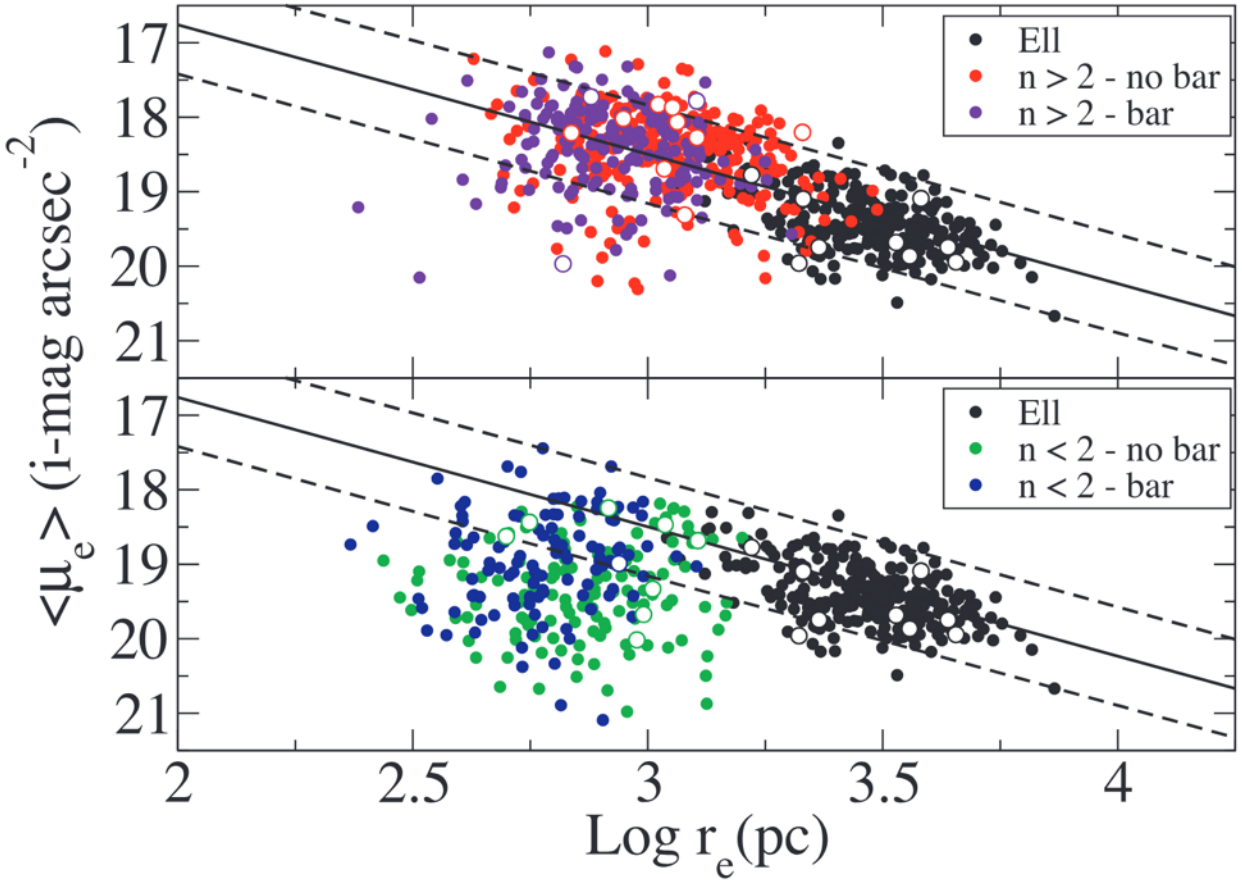

The bulges of disc galaxies can also be divided into the ones which follow the Kormendy relation and the ones which do not. Again, this indicates different formation processes.

Much more about this later.

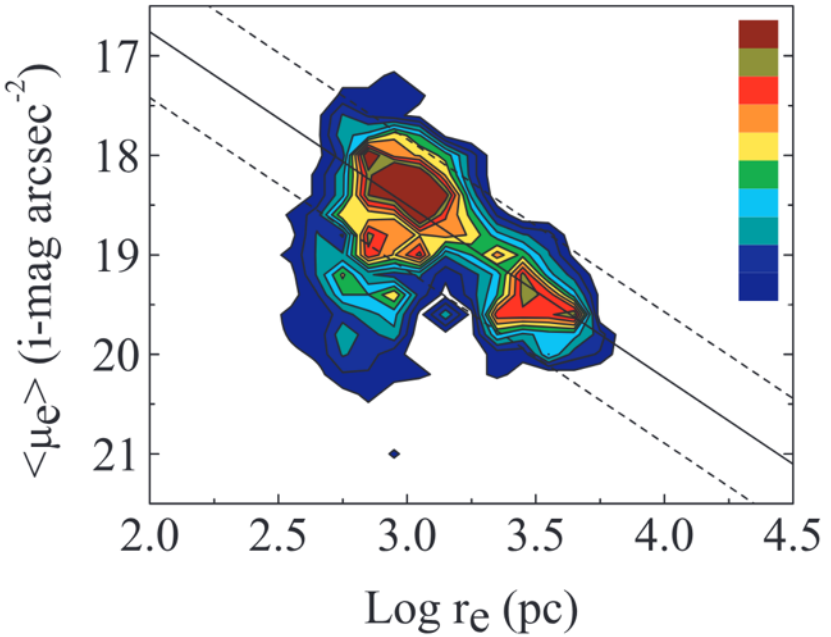

The Different Bulge Families

THE CLASSICAL BULGE

- More or less spheroidal
- Mostly old stars (not much dust or star-forming regions)
- Kinematically hot, i.e., dynamically supported by stellar velocity dispersion σ (but it does rotate!)

- Presumably built in violent events, inducing fast bursts of star formation if gas is available: mergers or clump coalescence

The Different Bulge Families

THE NUCLEAR DISC

- May contain sub-structures such as nuclear bars, spiral arms, rings…
- May show signs of dust obscuration, young stellar populations or ongoing star formation
- Kinematically colder, i.e., dynamically supported by rotation of its stars V_{rot}

- Built mostly via bar-driven gas inflow

Nuclear discs have been called ‘pseudobulges’, ‘disc-like bulges’, ‘discy bulges’ and ‘disc-like pseudobulges’ – but they are discs.

The Fundamental Plane

Effective radius vs. effective intensity vs. velocity dispersion

The Fundamental Plane

$$\log r_e = a \log \sigma + b \log \langle I_e \rangle + c$$

- The previous relations show that elliptical galaxies with larger central velocity dispersion, σ, are both brighter (the Faber-Jackson relation) and larger (the D_n-σ relation). In addition, the Kormendy relation shows that larger ellipticals have fainter surface brightness. This suggests the existence of a 3D relation (or a plane in 3D space) formed by parameters associated to the size, luminosity and velocity dispersion of elliptical galaxies. This is the Fundamental Plane (Djorgovski & Davis 1987, Dressler+1987a).

- The Faber-Jackson relation, the Dn-σ relation and the Kormendy relation are projections of the Fundamental Plane.

The Fundamental Plane

$$\log r_e = a \log \sigma + b \log \langle I_e \rangle + c$$

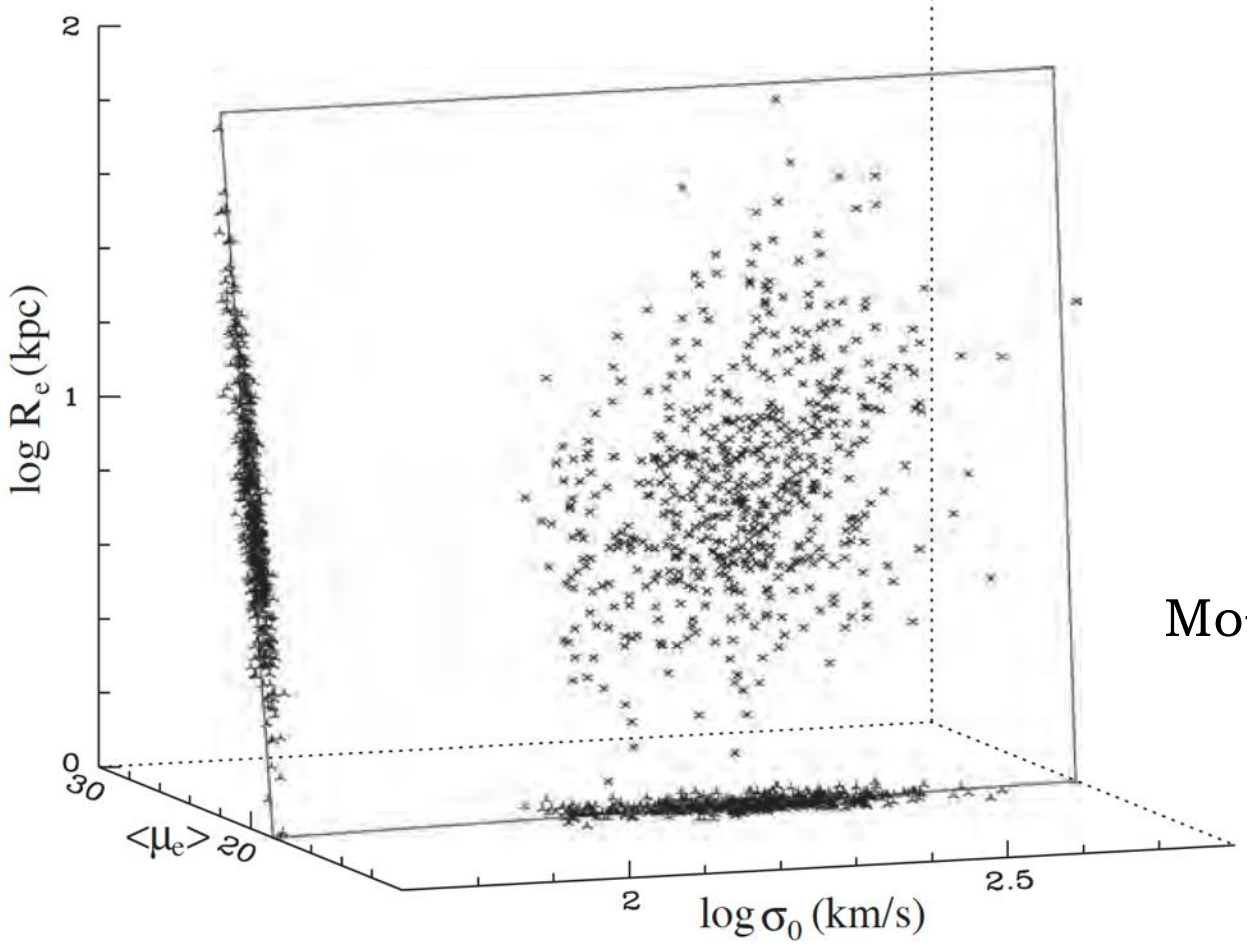

Mo+2010: Fig. 2.18

Fig. 2.18. The fundamental plane of elliptical galaxies in the $\log R_e$-$\log \sigma_0$-$\langle \mu \rangle_e$ space (σ_0 is the central velocity dispersion, and $\langle \mu \rangle_e$ is the mean surface brightness within R_e expressed in magnitudes per square arcsecond). [Plot kindly provided by R. Saglia, based on data published in Saglia et al. (1997) and Wegner et al. (1999)]

The Fundamental Plane

$$\log r_e = a \log \sigma + b \log \langle I_e \rangle + c$$

- From the Virial Theorem:

Absolute value of the mean potential energy per unit mass ← $\frac{GM}{\langle R \rangle} = \langle v^2 \rangle$ → twice the mean kinetic energy per unit mass

We can also write $R_e = k_r \langle R \rangle$ and $\sigma_0 = k_v \sqrt{\langle v^2 \rangle}$, where k_r and k_v describe, respectively, the density profile and orbital structure of the galaxy. Given that:

$$L = 2\pi \langle I_e \rangle R_e^2$$

We can write the top equation as:

$$\frac{G\left(\frac{M}{L}\right)L}{\langle R \rangle} = \langle v^2 \rangle = \frac{\sigma_0^2}{k_v^2}$$

Mo+2010: Sect. 13.4

The Fundamental Plane

$$\log r_e = a \log \sigma + b \log \langle I_e \rangle + c$$

$$\frac{G\left(\frac{M}{L}\right) L}{\langle R \rangle} = \langle v^2 \rangle = \frac{\sigma_0^2}{k_v^2}$$

$$\frac{G\left(\frac{M}{L}\right) 2\pi \langle I_e \rangle R_e^2}{\frac{R_e}{k_r}} = \frac{\sigma_0^2}{k_v^2}$$

$$R_e = \mathcal{C}_r \sigma_0^2 \langle I_e \rangle^{-1} \left(\frac{M}{L}\right)^{-1}$$

where $\mathcal{C}_r = \frac{1}{2\pi G k_r k_v^2}$.

Mo+2010: Sect. 13.4

The Fundamental Plane

$$\log r_e = a \log \sigma + b \log\langle I_e \rangle + c$$

If elliptical galaxies are homologous, i.e., have self-similar density and orbital distributions, then $\mathcal{C}_r$ is the same for all ellipticals. If, in addition, all ellipticals have the same $\left(\frac{M}{L}\right)$, then the FP can be written as:

$$\log r_e = 2 \log \sigma_0 - \log\langle I_e \rangle.$$

I.e., $a = 2$, $b = -1$ and $c = 0$. If the observed values are different, then it means that $\left(\frac{M}{L}\right)$ and/or $\mathcal{C}_r$ have power-law dependence on $\langle I_e \rangle$, σ_0 and/or r_e. Deviations from the virial predictions are called the 'tilt' of the fundamental plane.

Mo+2010: Sect. 13.4

The Fundamental Plane

$$\log r_e = a \log \sigma + b \log\langle I_e \rangle + c$$

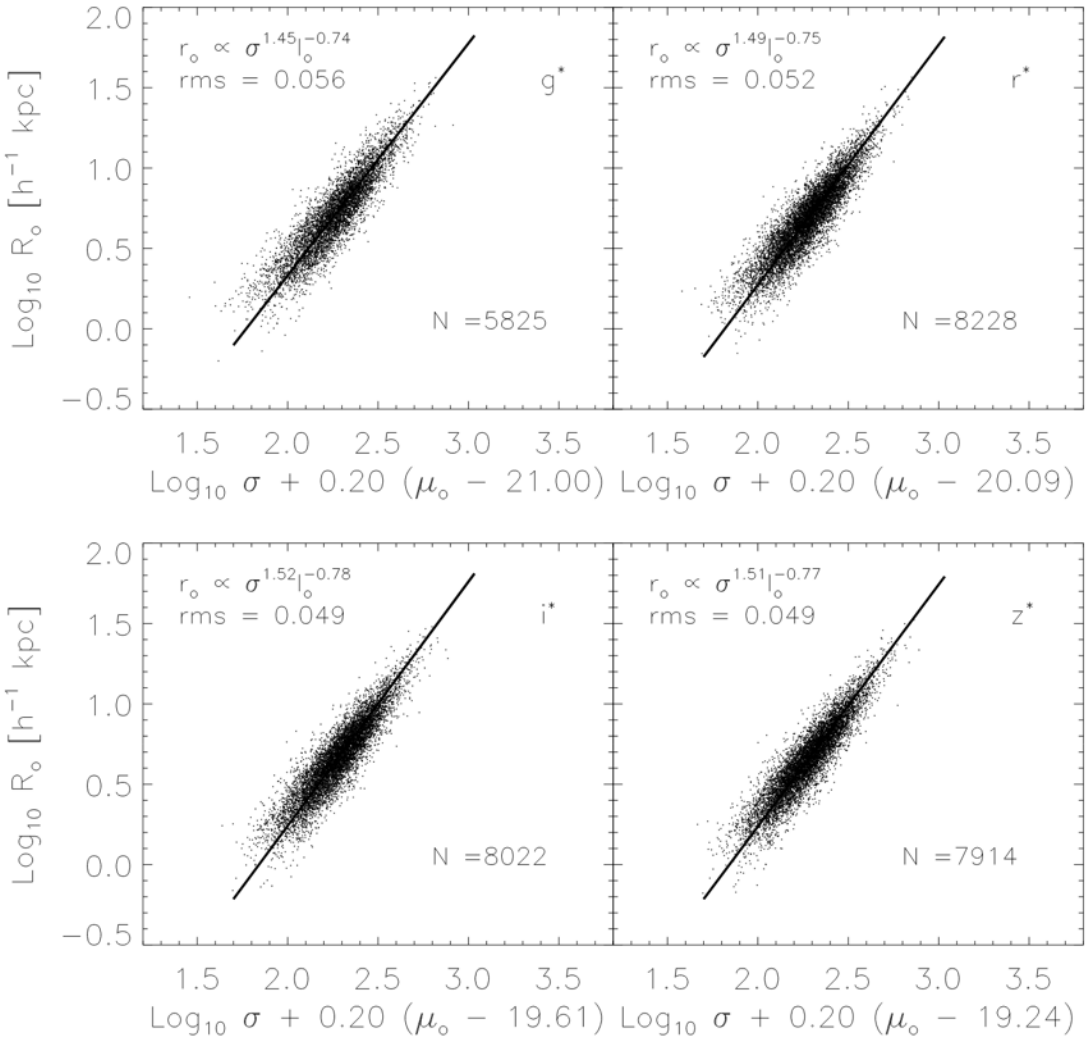

FIG. 1.—FP in the four SDSS bands. Coefficients shown are those that minimize the scatter orthogonal to the plane, as determined by the maximum likelihood method. Surface brightnesses have been corrected for evolution.

The FP using nearly 9000 SDSS galaxies in four different bands (Bernardi+2003).

In the r* band, the observed FP relation is:

$$\log r_e = 1.5 \log \sigma_0 - 0.75 \log\langle I_e \rangle.$$

So the FP is indeed 'tilted', i.e.:

$a = 1.49 \pm 0.05$ instead of 2, and $b = -0.75 \pm 0.01$ instead of -1.

In the K band [where (M/L) effects are minimised], Pahre+1998 find $a = 1.53$ and $b = -0.79$. So (M/L) effects seem small.

The Fundamental Plane

$$\log r_e = a \log \sigma + b \log\langle I_e \rangle + c$$

This is not surprising. Ellipticals may not be homologous, i.e., may not have the same density and orbital distributions. We have seen (and will see more later) that the density profile of elliptical galaxies can be varied. This also certainly affects the orbital distribution.

$\left(\frac{M}{L}\right)$ is probably also not the same in every elliptical. Different galaxies may have a different distribution of stellar populations (see, e.g., the colour-magnitude relation). In addition, the contribution of dark matter may also vary. How these different factors play a role in the tilt of the FP is still a matter of debate and investigation.

Nonetheless, the tightness of the FP is a strong constraint to models of galaxy formation and evolution.

The Fundamental Plane

$$\log r_e = a \log \sigma + b \log \langle I_e \rangle + c$$

Even with the 'tilt', the existence of a tight fundamental plane – instead of galaxies being randomly distributed in the r_e- σ- $\langle I_e \rangle$ space – indicates that elliptical galaxies:

1. Are virialized systems
2. Are to some extent homologous: i.e., have (close to) self-similar density and orbital distributions
3. Contain stellar populations which must fulfill tight age and metallicity constraints (since variation in M/L is limited)

And what does the 'tilt' teach us?

The Fundamental Plane

$$\log r_e = a \log \sigma + b \log \langle I_e \rangle + c$$

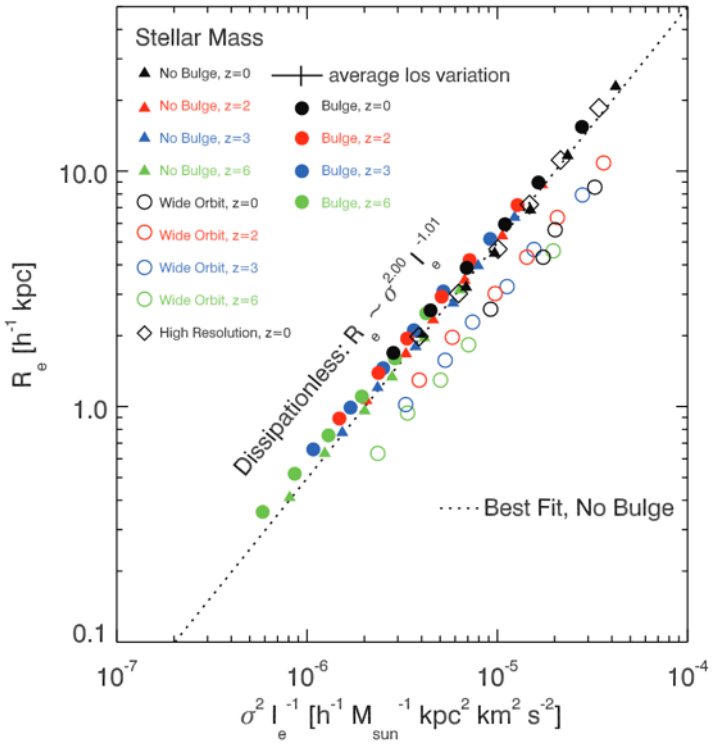

FIG. 1.—FP relation produced by the merging of dissipationless disk galaxy models appropriate for redshifts $z = 0$ (*black*), $z = 2$ (*red*), $z = 3$ (*blue*), and $z = 6$ (*green*) on nearly radial, parabolic orbits. All models include dark matter halos. The dissipationless merging of pure disk models (*filled triangles*) and disk models with bulges (*filled circles*) produce similar FP relations nearly parallel to the plane defined by the virial relation. Increasing the angular momentum of the orbit by lengthening the pericentric passage distance of the orbit produces an offset in the FP by increasing the effective radius of the remnants (*open circles*), but the systems still obtain an FP scaling similar to the virial plane. Select higher resolution runs closely follow the FP delineated by their lower resolution counterparts (*open diamonds*). For comparison, the best least-squares fit to the FP of pure disk merger remnants is plotted (*dotted line*). Also shown is the mean deviation induced by line-of-sight variations in projected quantities for a given remnant (*detached error bars*).

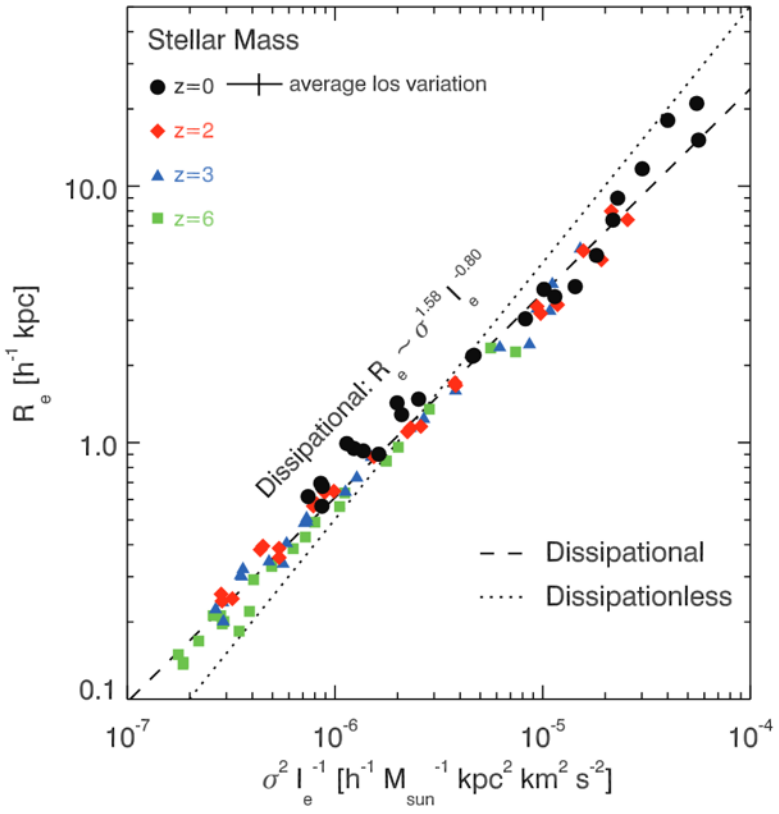

FIG. 3.—FP relation produced by the merging of gas-rich disk galaxies with dark matter halos, star formation and supernova feedback. Shown are remnants produced by mergers appropriate for redshifts $z = 0$ (*black circles*), $z = 2$ (*red diamonds*), $z = 3$ (*blue triangles*), and $z = 6$ (*green squares*) with nearly radial, parabolic orbits. The dissipational merging of pure disk models produces an FP nearly parallel to the observed infrared FP (Pahre et al. 1998b) and is almost independent of the redshift scalings of the progenitor systems. For comparison, the best least-squares fit to the FP delineated by the remnants is plotted (*solid line*). Also shown is the mean deviation induced by line-of-sight variations in projected quantities for a given remnant (*detached error bars*).

Robertson+2006 find that dissipation-less mergers produce an FP that matches the Virial prediction:

$a = 2.00$ and $b = -1.01$.

By adding gas to the mergers, they find a tilted FP relation close to the observed values:

$a = 1.58$ and $b = -0.80$.

Dissipation and star formation in less massive systems thus plays a fundamental role in galaxy formation and evolution.

The Fundamental Plane

$$\log r_e = a \log \sigma + b \log \langle I_e \rangle + c$$

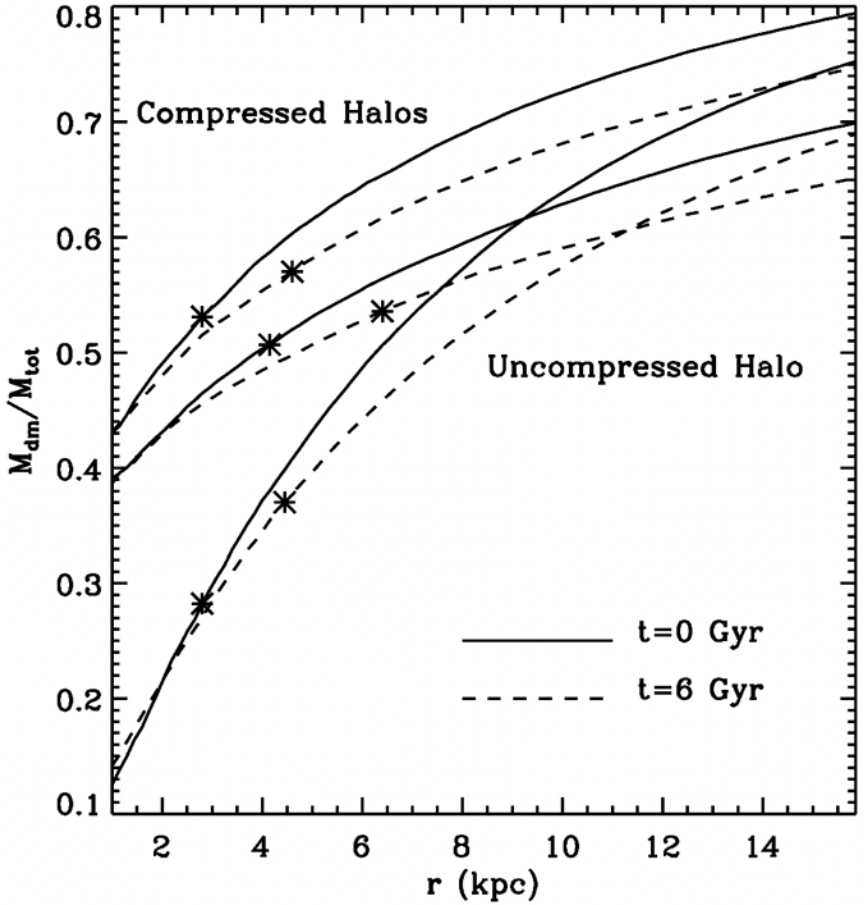

Figure 5. Ratio of dark matter mass to total mass interior to radius r as a function of r for initial condition (solid curve) and remnant system (dashed curve) for simulation M20 (compressed halo; upper curves), M10 (compressed halo; middle curves) and M20u (uncompressed halo; lower curves). The symbols mark the effective radius R_e for the given simulation. In each case, the fraction of dark matter interior to R_e increases after the merger.

Boylan-Kolchin+2005: the amount of dark matter within the effective radius increases after mergers that produce the most massive ellipticals, as long as the mergers occur from radial orbits.

This increases $\left(\frac{M}{L}\right)$ if there is no additional star formation, contributing to the 'tilt'.

The Fundamental Plane

$$\log r_e = a \log \sigma + b \log \langle I_e \rangle + c$$

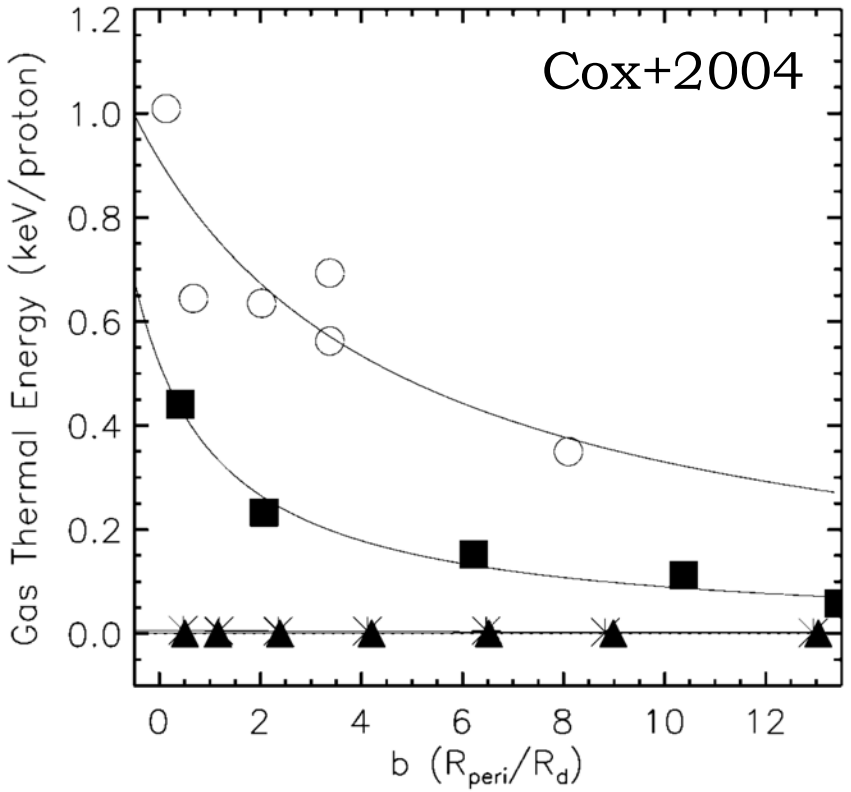

FIG. 2.—Remnant gas energy in units of keV per proton as measured 500 Myr after the merger between two disk galaxies plotted as a function of the orbital pericentric distance R_{peri} divided by the original disk scale length R_d. Open circles are the progenitor disk galaxy 5 × MW, the largest progenitor disk galaxy; filled squares are MW disks; the asterisks are Dwarf1; and the filled triangles are Dwarf2. Solid lines are fits to the data using eq. (4) and described in the text.

But the observed FP requires that gas does not dissipate and form stars in massive galaxies. This suggests that gas is heated via shocks that are more powerful for more massive systems – because the central gas density is larger in deeper potential wells – and for more radial orbits (due to the stronger impact).

The heated gas is observed as X-ray haloes in massive ellipticals.

X-Ray Haloes

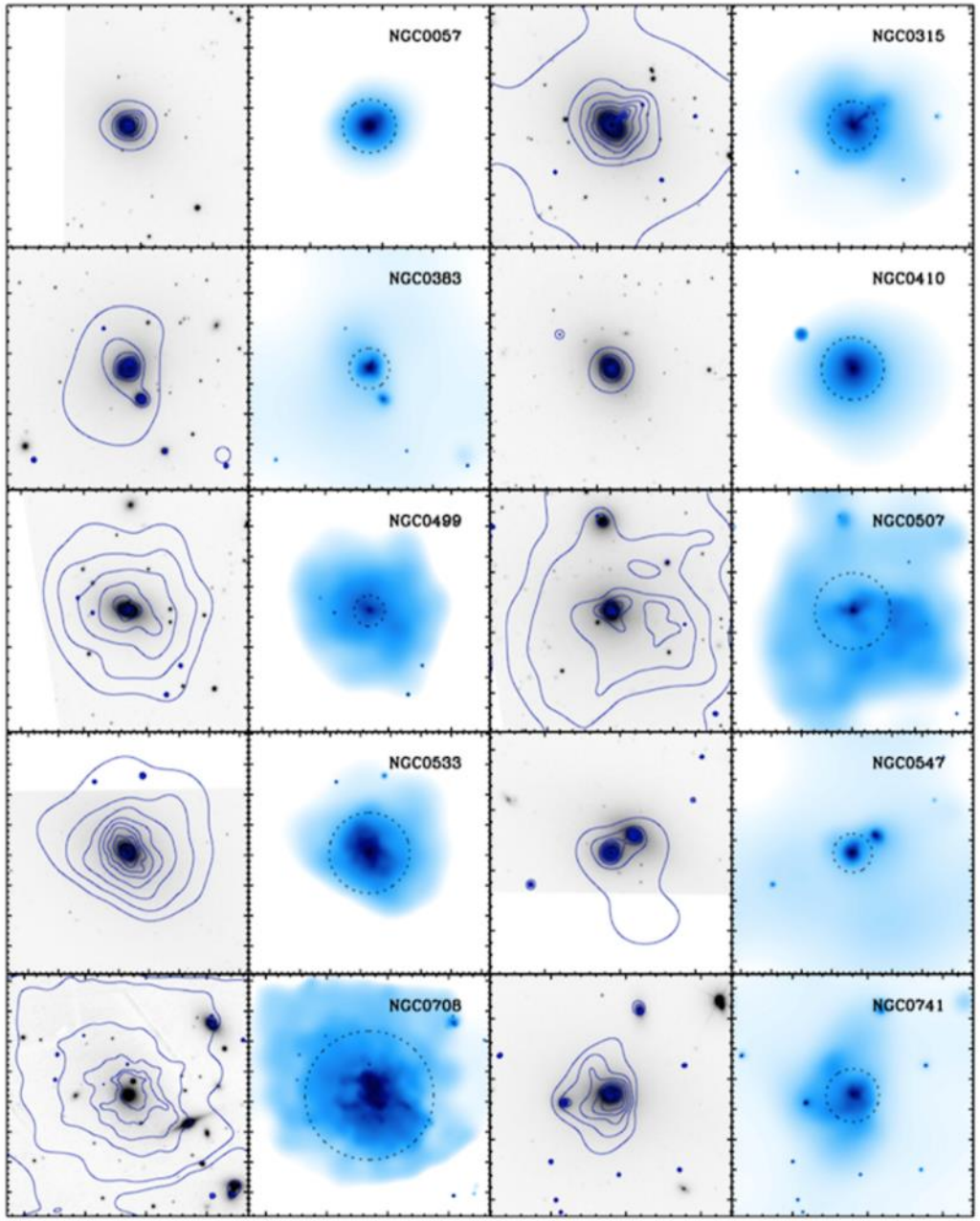

Goulding+2016

FIG. 2.— 4×4 arc-minute cutouts of the MASSIVE galaxies with publicly available archival *Chandra* X-ray observations performed with the ACIS instrument. Left column shows the optical *i*-band SDSS DR12 Atlas image, logarithmic X-ray contours are overlaid in solid blue. *g*-band PANSTARRS images are shown for NGC 708, 1600, 2340, 6482, 7052, 7265 and 7618 as they do not fall within the SDSS survey footprint. The logarithm of the adaptively-smoothed, vignetting and exposure-corrected *Chandra* ACIS-S (NGC 1129: ACIS-I) images are shown to the right of the optical images. Dashed circles represent one effective radius derived from optical and near-infrared imaging.

What have we learned?

So what have we learned so far from the Fundamental Plane?

1. Elliptical galaxies (and maybe the most massive – classical – bulges) are consistent with being formed from mergers and being virialized

2. Gas dissipation and star formation are required in the least massive systems and need to be prevented for the most massive systems

3. Radial orbits are required for the most massive systems

The κ Space

Bender+1992 have proposed a quasi-orthogonal combination of R_e, σ_0 and $\langle I_e \rangle$ that is particularly useful:

$$\kappa_1 \equiv \left(\log \sigma_0^2 + \log R_e\right) / \sqrt{2},$$

$$\kappa_2 \equiv \left(\log \sigma_0^2 + 2\log \langle I \rangle_e - \log R_e\right) / \sqrt{6},$$

$$\kappa_3 \equiv \left(\log \sigma_0^2 - \log \langle I \rangle_e - \log R_e\right) / \sqrt{3},$$

κ_1 is proportional to log mass ($\log \sigma_0^2 R_e$), κ_3 is a measure of (M/L) – because it is proportional to $\log\left[\frac{\sigma_0^2 R_e}{\langle I_e \rangle R_e^2}\right]$, and κ_2 is proportional to $\log\left[\left(\frac{M}{L}\right)\langle I_e \rangle^3\right]$ to ensure quasi-orthogonality.

The κ_1-κ_2 projection is very close to a face-on projection of the FP, while the κ_1-κ_3 projection is nearly an edge-on projection of the FP.

The κ Space

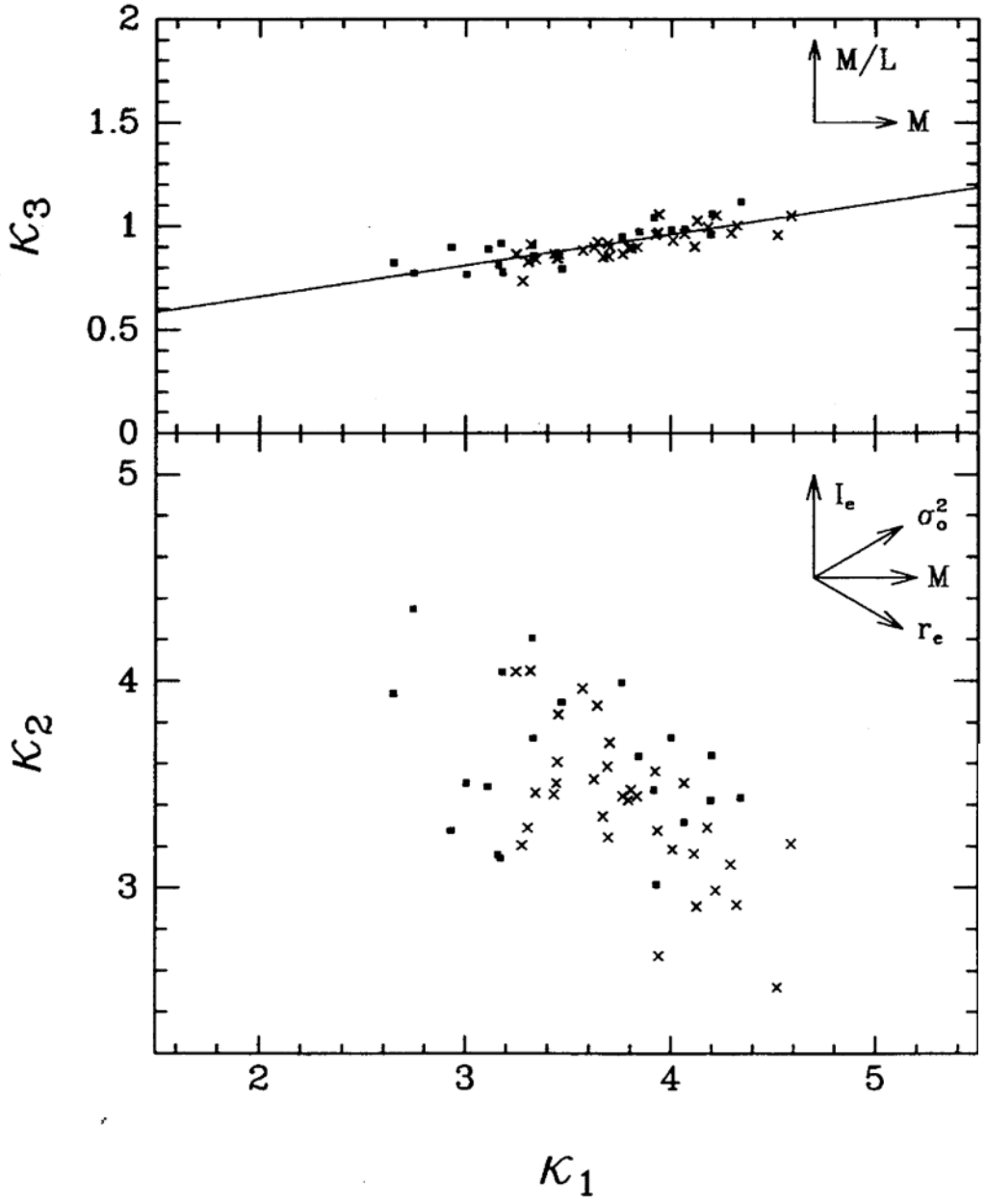

Elliptical galaxies in the Virgo and Coma cluster in the κ space (Bender+1992).

FIG. 1.—The distribution of elliptical galaxies in the Virgo Cluster and the Coma Cluster in the 3-space of the basic global parameters: central velocity dispersion (σ_o^2), surface brightness [$\log I_e = -0.4(SB_e - 27)$], and effective radius r_e. The coordinate system (κ_1, κ_2, κ_3) has been chosen to emphasize the fundamental plane while retaining physically meaningful variables: $\kappa_1 \propto \log M$, $\kappa_2 \propto \log (M/L)I_e^3$ and $\kappa_3 \propto \log M/L$. (*a*) *Upper panel:* the edge-on view of the plane occupied by Virgo (*closed boxes*) and Coma (*crosses*) ellipticals. The fundamental plane defined by the Virgo galaxies ($\kappa_3 = 0.15\ \kappa_1 + 0.36$) is shown by the straight line. (*b*) *Lower panel:* nearly face-on view of the plane.

The κ Space

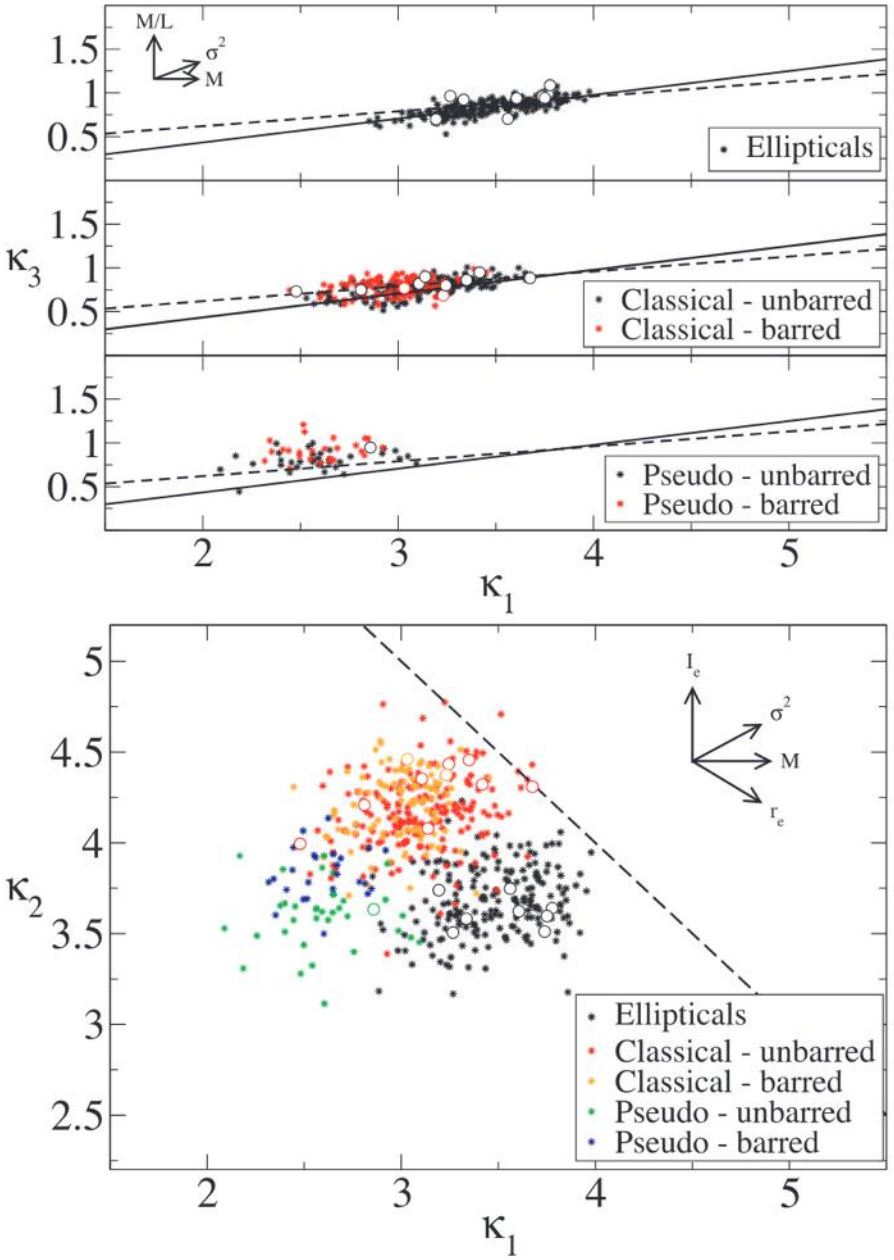

Elliptical galaxies and different bulge families in the κ space (Gadotti 2009). Massive bulges lie relatively close to the FP relation of ellipticals, but less massive bulges are systematically off the plane, indicating different formation processes.

More about this later.

dissipation

merger

Figure 16. Elliptical galaxies, classical bulges and pseudo-bulges in the κ-space formulation of the fundamental plane (FP). The top three panels show the edge-on view of the FP, κ_3 plotted against κ_1, while the bottom panel shows its nearly face-on view, κ_2 plotted against κ_1. Barred and unbarred galaxies are also indicated. In the top panels, the solid line is a fit to our ellipticals, while the dashed line is the fit obtained by Bernardi et al. (2003b) for nearly 9000 early-type galaxies. The dashed line in the bottom panel shows the limit of the zone of avoidance. The arrows indicate how some important physical parameters vary across the FP. Bigger, white-filled circles represent systems with $0.5 < b/a < 0.7$, with similar colour coding.

The κ Space

The locus occupied by the less massive bulges is the same as pure disc systems, as seen in the H-band FP of Pierini+2002

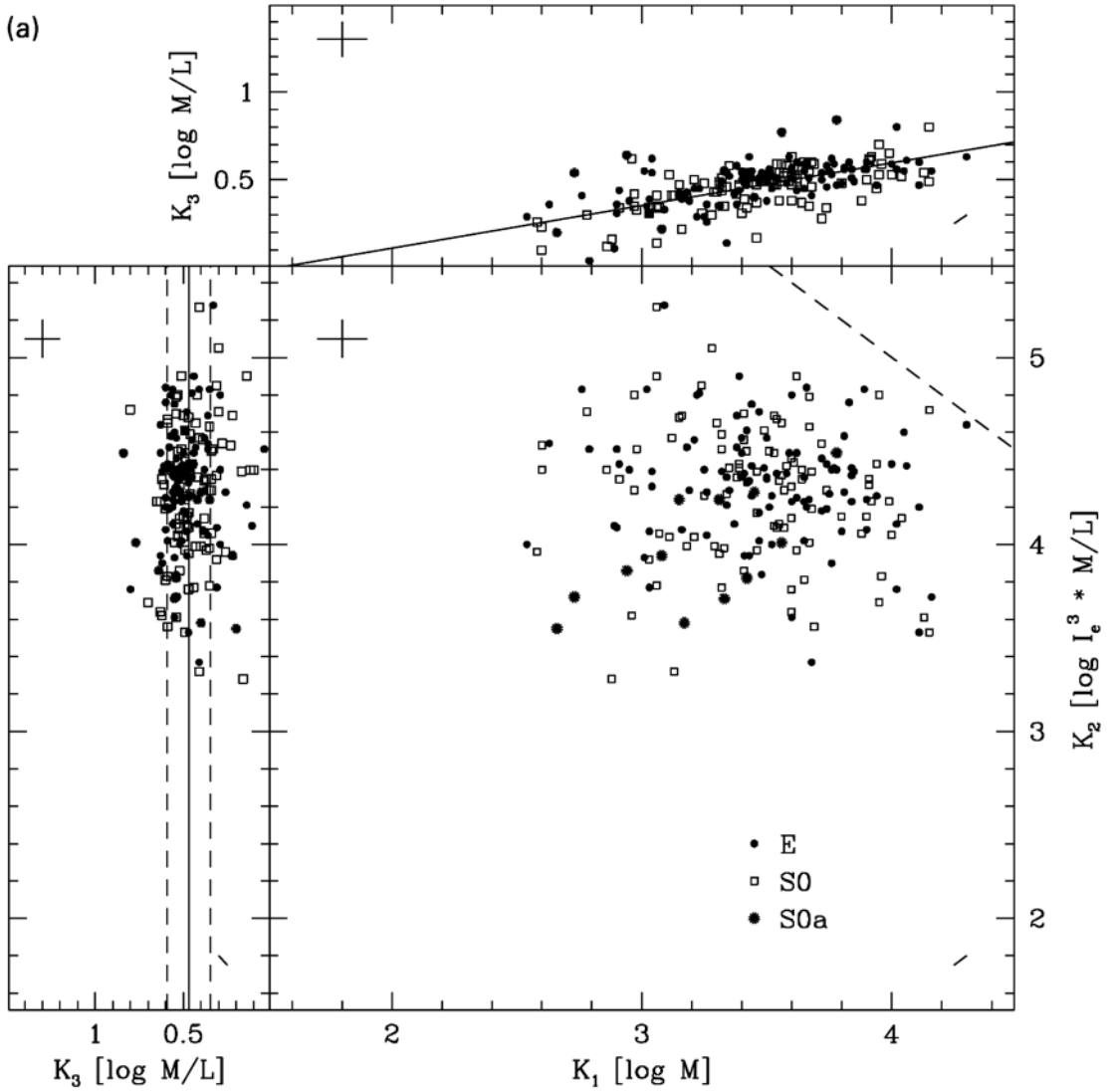

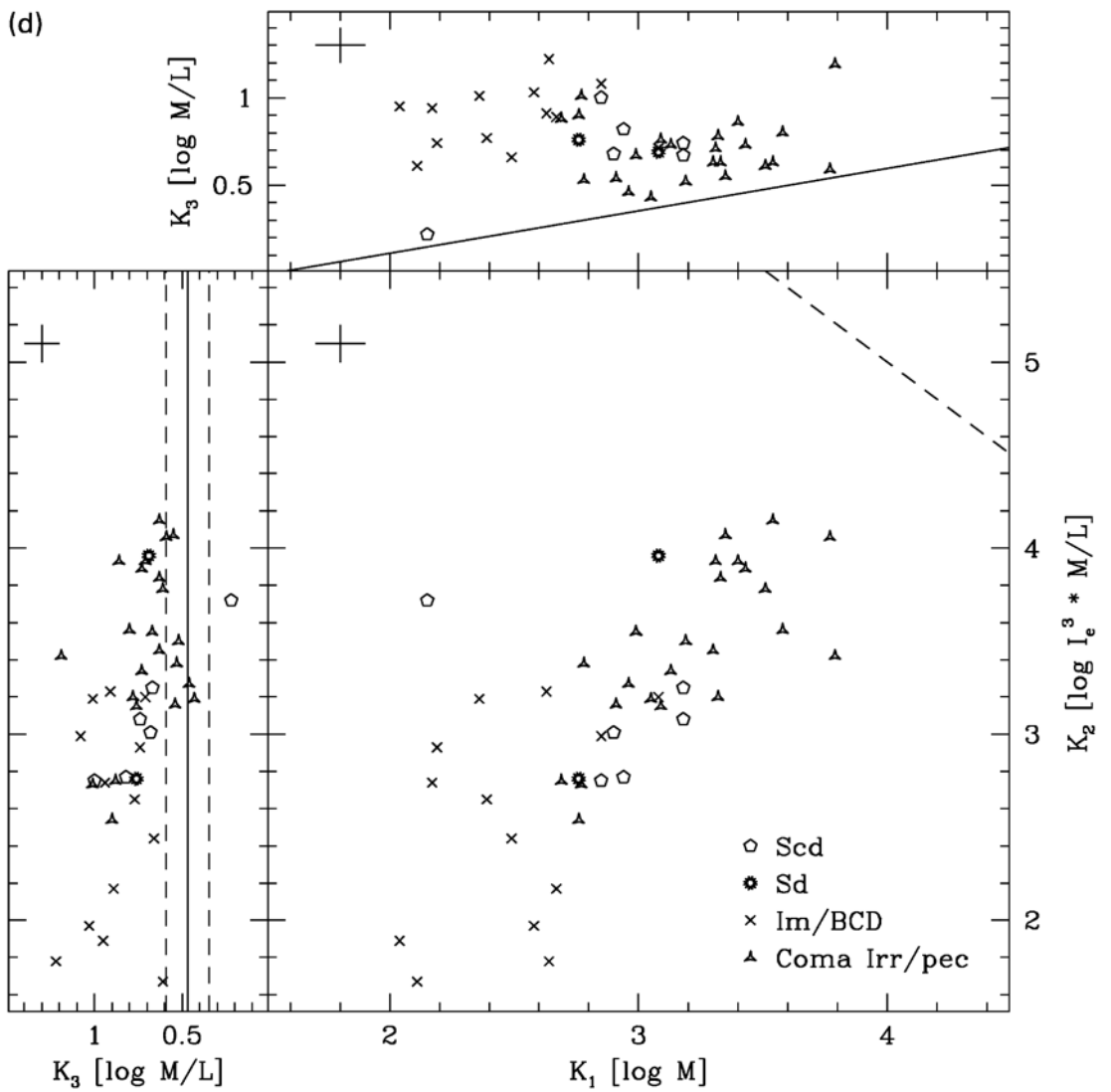

The Colour-Magnitude Relation

Colour vs. luminosity or absolute magnitude

The Colour-Magnitude Relation

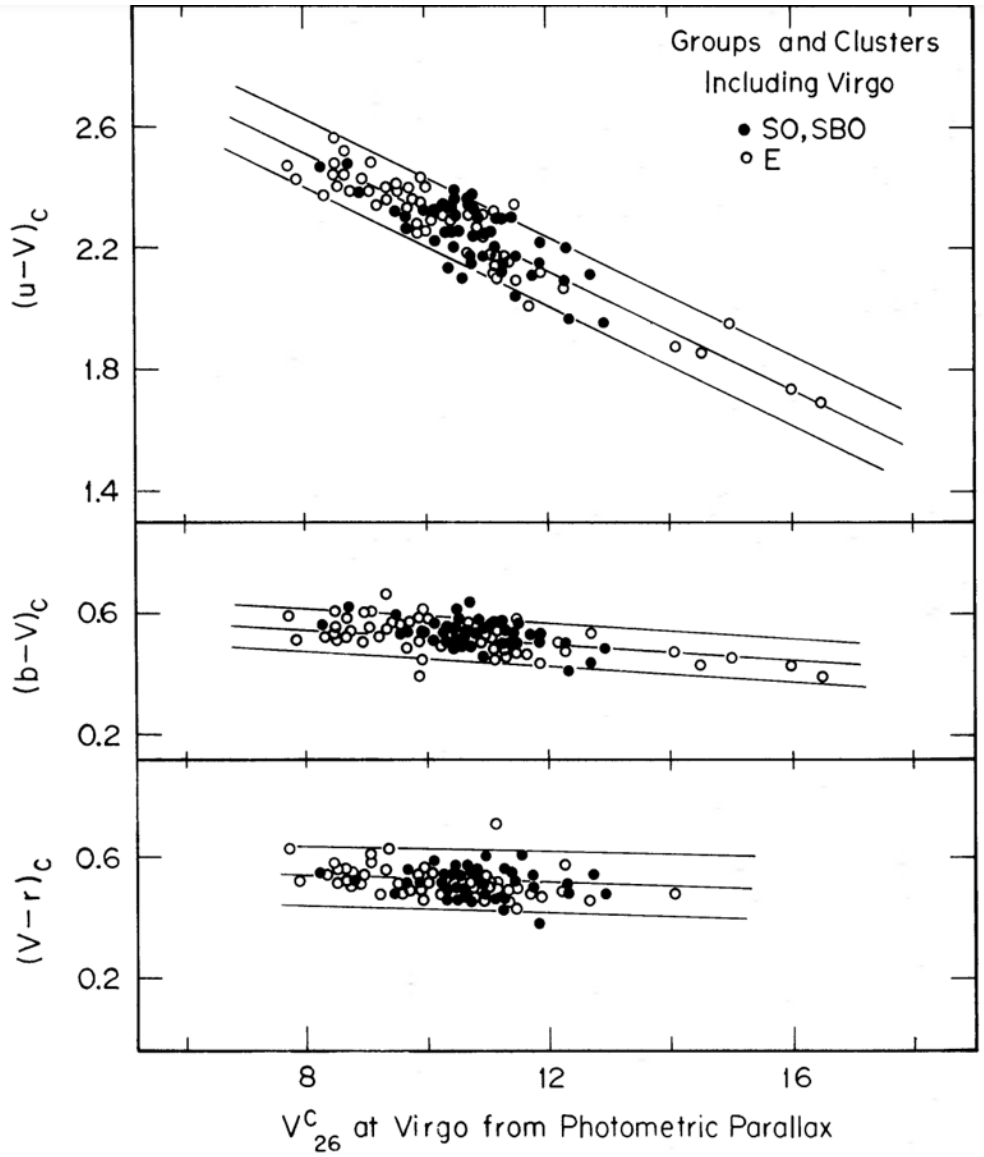

FIG. 7.—Composite C-M diagram for all galaxies in the sample, shifted to the Virgo cluster distance by magnitude differences calculated from the photometric parallaxes. Galaxies of E and S0 types are shown with different symbols. The ridge line is the Virgo cluster solution of Fig. 3. Boundary lines are at $\pm 2\,\sigma$ in the color residuals.

Visvanathan & Sandage (1977): brighter galaxies are redder

The Colour-Magnitude Relation

The colours of stars/galaxies can reflect the age of the stellar population, as more massive stars are bluer and have shorter lives. But stars that are poor in metals are also bluer, and dust absorbs more blue light, re-emitting it in the red, so all these process contribute to some extent to the observed colours of galaxies.

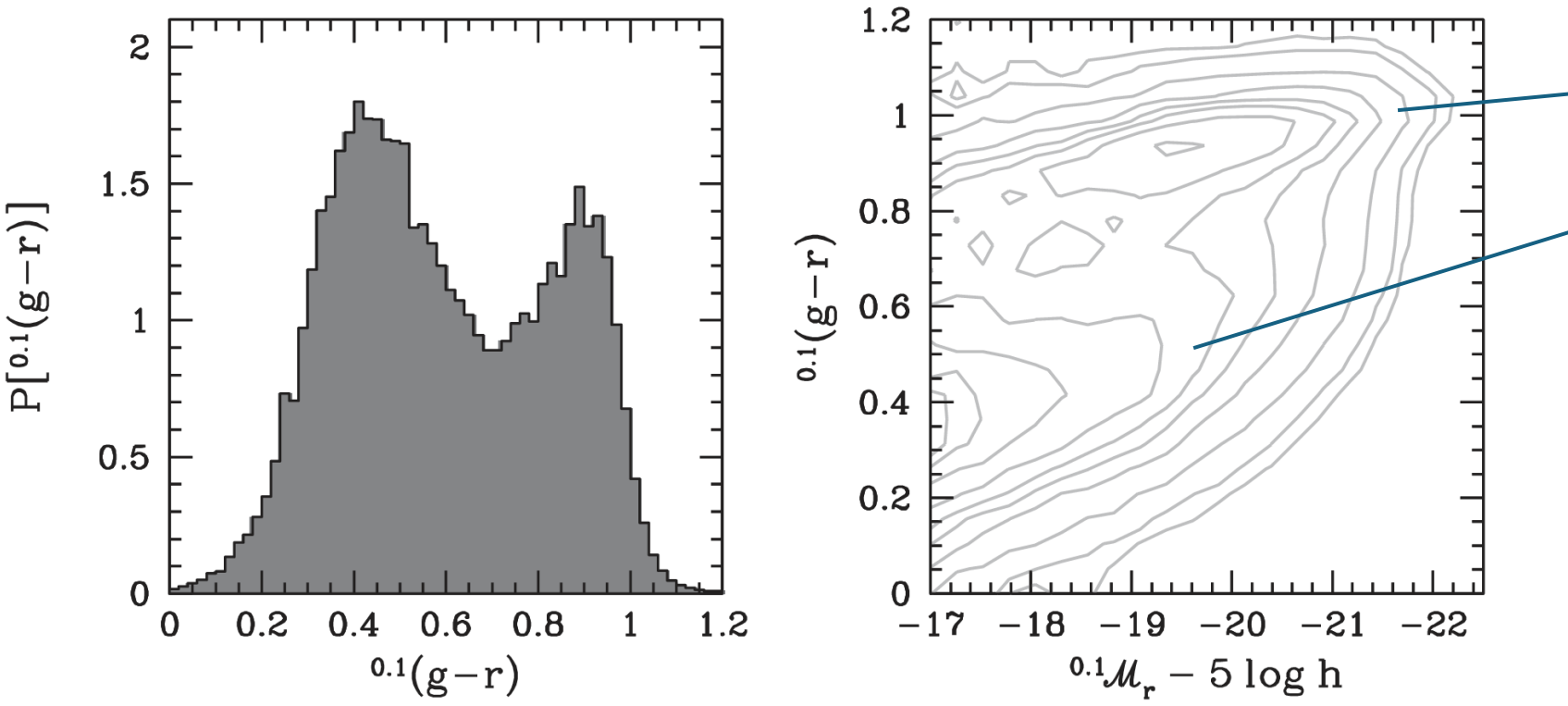

Colour bimodality is clear and reflects, on average, early-type and late-type galaxies.

Fig. 2.27. The probability density of galaxy colors (left) and the color–magnitude relation (right) of $\sim$ 365,000 galaxies in the SDSS. Each galaxy has been weighted by $1/V_{\rm max}$ to correct for Malmquist bias. Note the pronounced bimodality in the color distribution, and the presence of both a red sequence and a blue sequence in the color–magnitude relation.

Mo+2010: Fig. 2.27

The Colour-Magnitude Relation

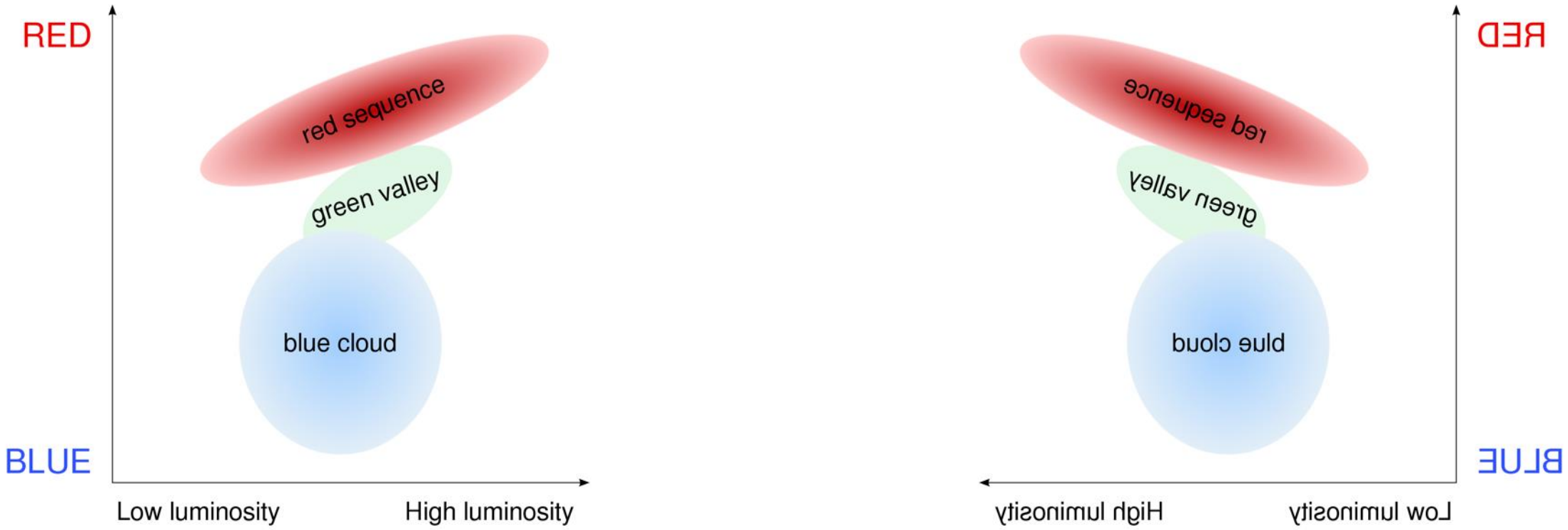

The Colour-Magnitude Relation

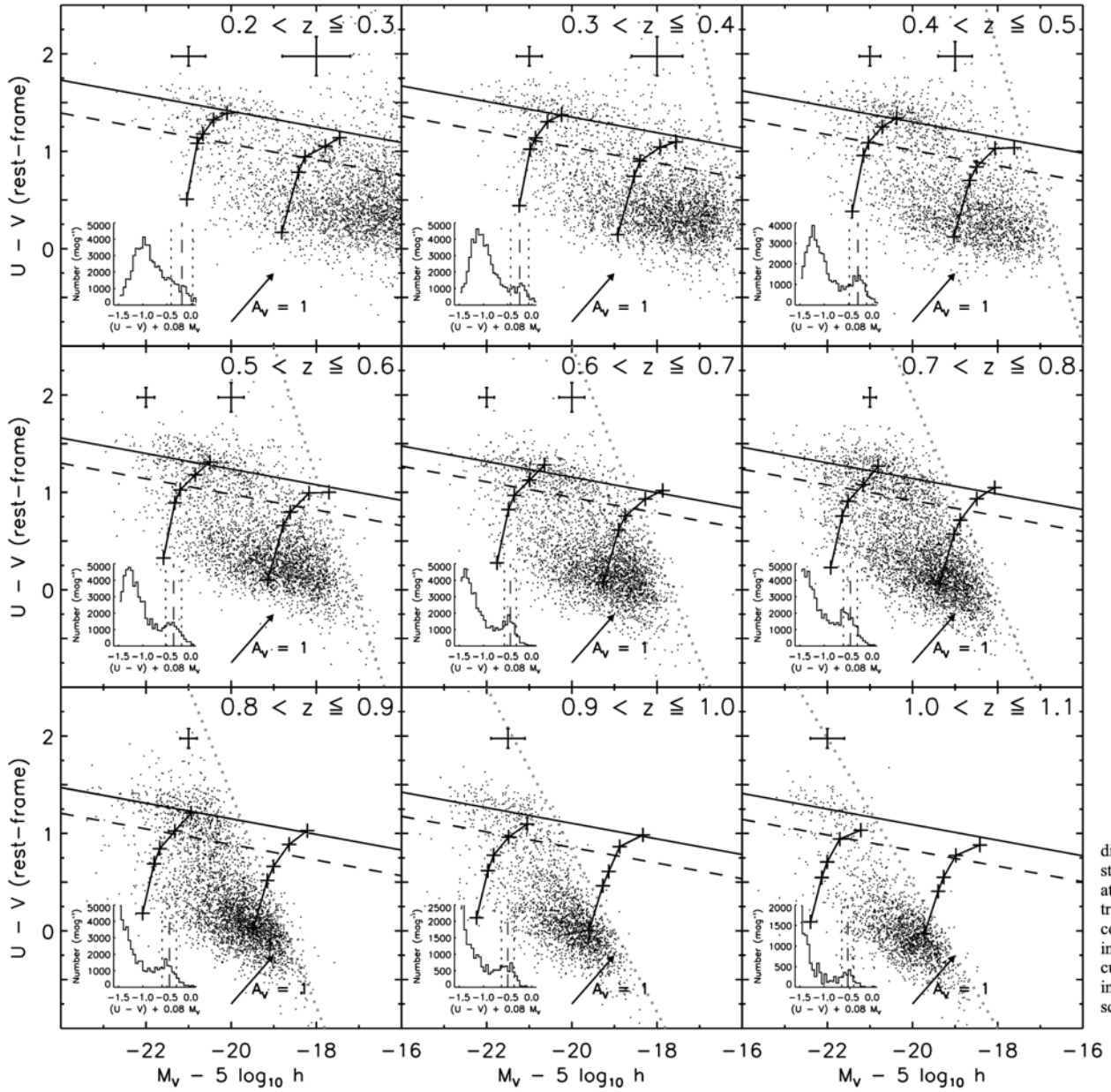

- Bell+2004 show that the colour bimodality was in place already at $z \sim 1$. The blue peak becomes redder with time and the red sequence appears even when all environments are considered.

FIG. 1.—Rest-frame $U-V$ color of ~25,000 galaxies against the absolute magnitude in V band, $M_V - 5 \log h$. We show the distribution of galaxies in nine different redshift bins. A fit to the color-magnitude relation of red-sequence galaxies with a fixed slope of −0.08 is shown by the solid line, and the Butcher-Oemler–style cut between red and blue galaxies is shown by the dashed line parallel to the early-type galaxy CMR (see § 5). The sloping cutoff in the distribution of galaxies at the faint end is due to the $m_R \lesssim 24$ mag limit of the survey. This cutoff cannot be exactly depicted because of the color dependence in completeness and the varying transformation between observed R-band magnitude and rest-frame V-band magnitude; nevertheless, the dotted gray line shows very schematically the rough completeness limit. The lines with crosses show the colors and magnitudes of model galaxies with truncated SFHs at constant stellar mass, described in more detail in § 6.4. Representative error bars are shown. For reference, we show a reddening vector from Calzetti et al. (2000), assuming $A_V = 1$ mag; a Milky Way extinction curve gives the same vector. Shown in the insets is the color distribution of the red peak at each redshift (with the slope of the CMR taken out); the dashed line indicates the position of the biweight mean that we adopt as the CMR ridgeline, and the dotted lines show the biweight σ that we adopt as the CMR red sequence's scatter.

The Colour-Magnitude Relation

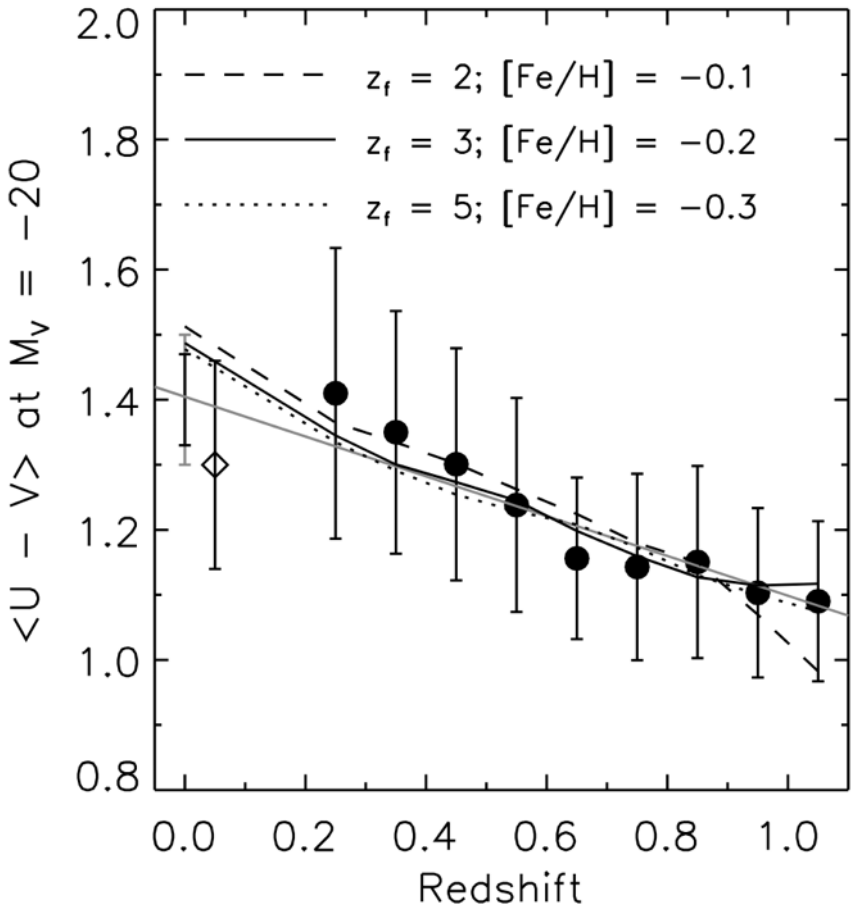

Bell+2004

- The mean colour of the red galaxy sequence evolves with redshift in a way that is consistent with the aging of an ancient stellar population (relation is driven by metallicity).

- When the change in stellar mass-to-light ratio implied by the redshift evolution in red galaxy colours is accounted for, the data indicate an increase in stellar mass on the red sequence by a factor of two since $z \sim 1$.

FIG. 2.—Color evolution of the red sequence, represented by the intercept of the CMR fits at $M_V - 5 \log h = -20$ (*circles*) as a function of redshift. The error bars show the biweight scatter in each redshift bin. These highly conservative errors are much larger than the formal errors and likely overestimate the systematic errors from calibration, template/galaxy SED mismatches, and small redshift focusing issues, which we expect to be less than 0.1 mag in $U-V$ color. The lines show the expected color evolution of single-age stellar populations with different formation redshifts and metallicities, as given in the label. The diamond with error bars (offset from zero redshift for clarity) shows the $U-V$ CMR zero point at $z = 0$ synthesized from SDSS *ugr* data analyzed in the same way as these data (see the Appendix for details). The naked error bars show the $U-V$ CMR zero point for the A754 galaxy cluster (McIntosh et al. 2004), which is also consistent with the Nearby Field Galaxy Survey (Jansen et al. 2000) early-type galaxy CMR. The black naked error bar shows the A754 scatter around the CMR, and the expected systematic uncertainty is shown by a gray error bar. The gray line shows a fit to all the data (including the A754 and SDSS colors).

The Tully-Fisher Relation

Luminosity (or mass) vs. velocity

The Tully-Fisher Relation

$$L = A v_{\max}^{\alpha}$$

- A consequence from the Virial Theorem is that the average speed with which material orbits in a gravitating system increases with the mass of the system. In stellar systems, this means that the orbital velocities of the stars – be them in the form of random motion (σ) or regular rotation (v) – are proportional to the system's mass (be it a star cluster or a galaxy, for example).

- For elliptical galaxies, dominated by random motion, the Faber-Jackson relation ($L = \sigma^{\beta}$) is a reflection of the Virial Theorem.

- For disc galaxies, dominated by regular rotation, the analogous relation is the Tully-Fisher relation.

- A is the zero point, α is the slope. And, again, the Virial Theorem prediction is that $\alpha = 4$.

The Tully-Fisher Relation

$$L = Av_{\max}^{\alpha}$$

- But where do you measure v and how? And how does the inclination of the galaxy affect the measurements?

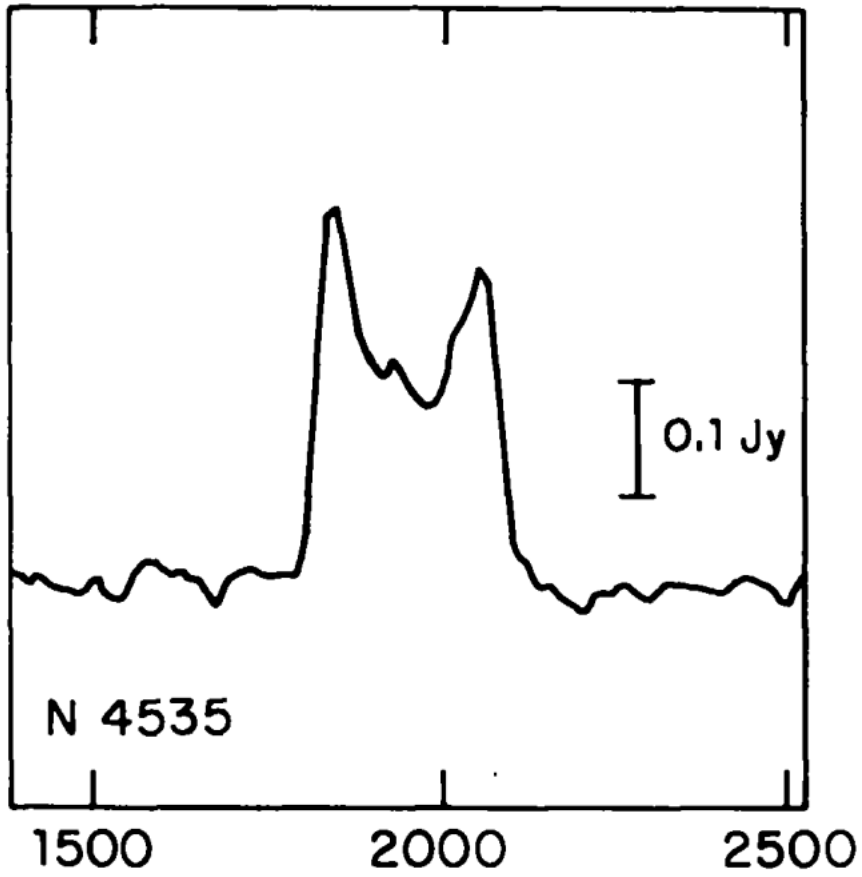

- You need to go as far from the galaxy centre as you can if you want to include all the galaxy mass/light in the relation. But stars are faint in the outer disc, and the gaseous (neutral Hydrogen) disc extends beyond the stellar disc.

- The original paper by Tully and Fisher used single dish radio telescope observations of the 21cm HI line that do not resolve the gaseous disc.

The Tully-Fisher Relation

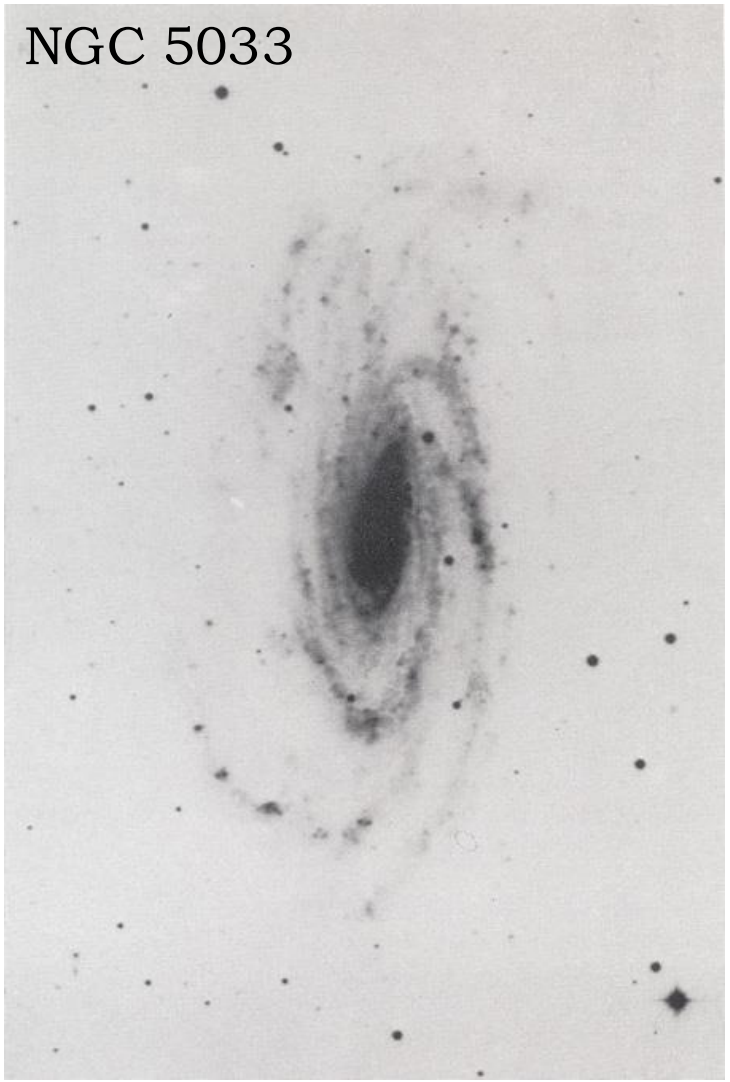

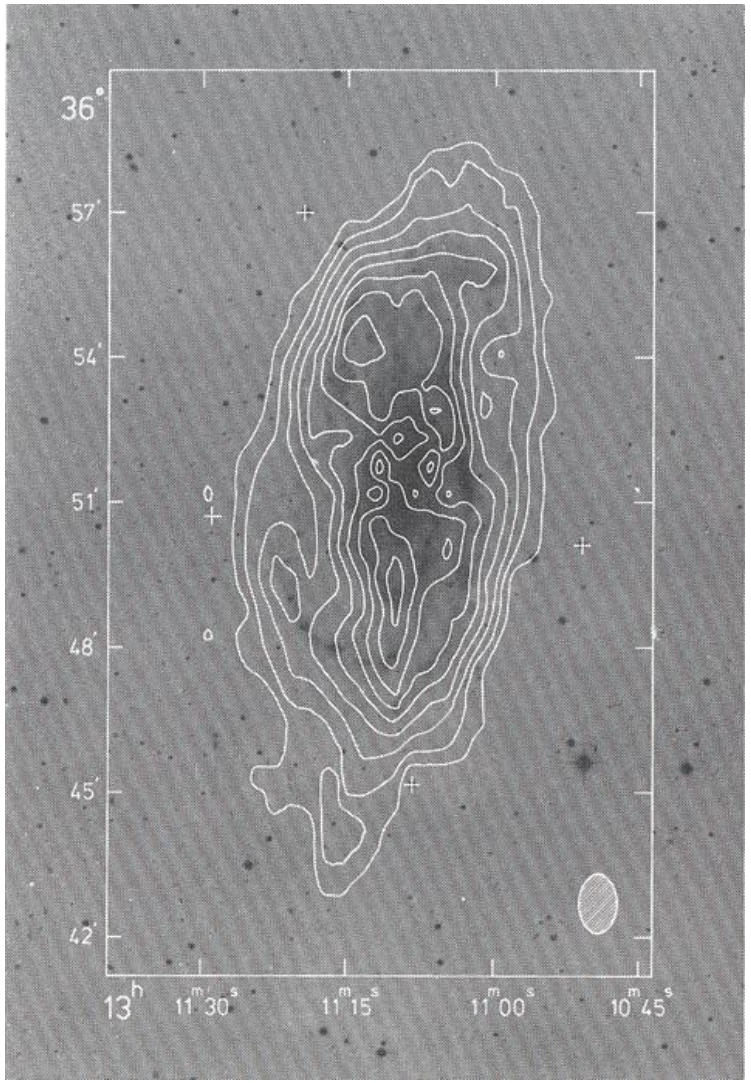

HI column density contours

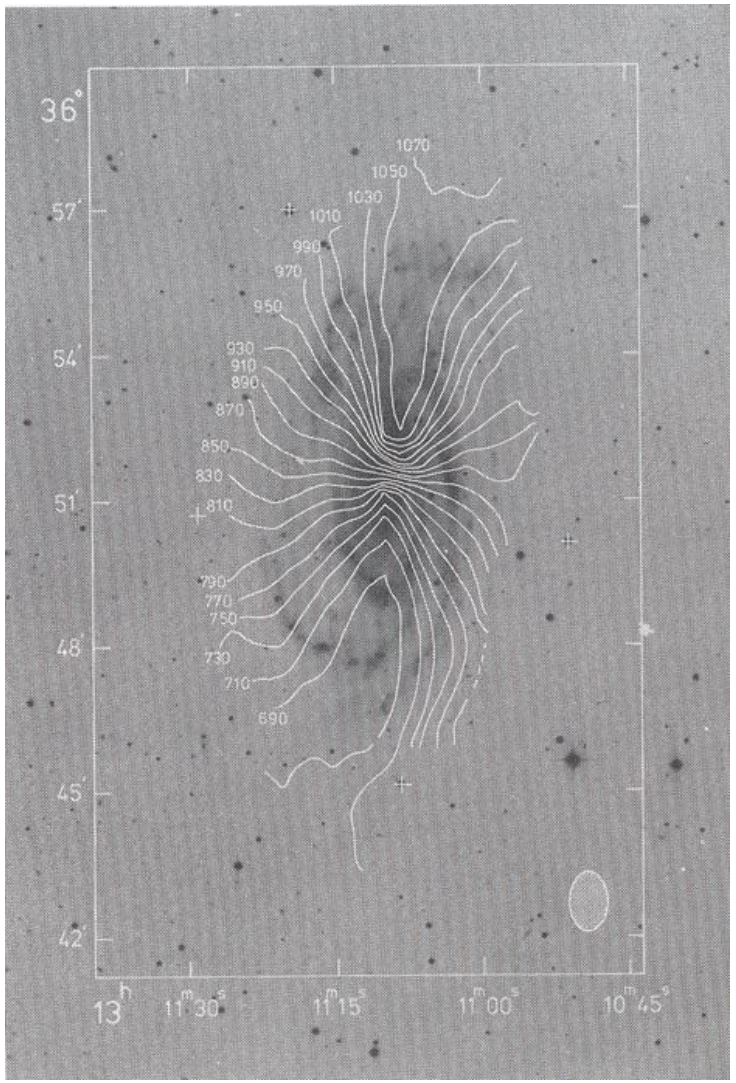

HI iso-velocity contours

Bosma (1978)

The Tully-Fisher Relation

$$L = A v_{\max}^{\alpha}$$

- The velocity thus derived needs to be corrected for inclination. The intrinsic velocity v is equal to the velocity measured along the line-of-sight $v_{\rm los}$ divided by $\sin i$, where i is the inclination of the galaxy:

$$v = v_{\rm los} / \sin i .$$

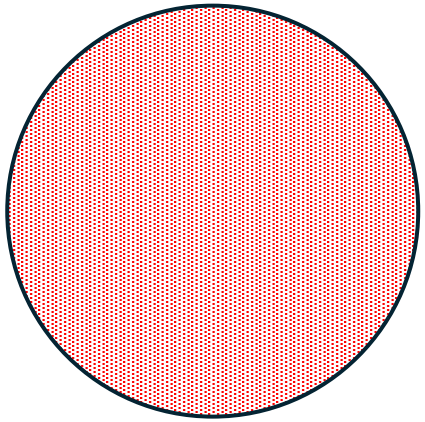

face-on: $i = 0°$

(can't measure v!)

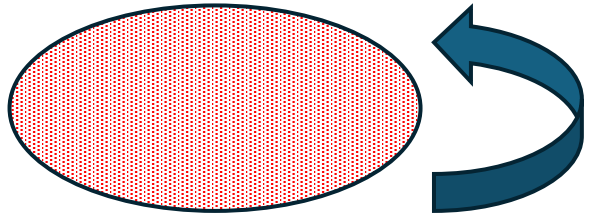

$i = 60°$

$\sin i = 0.5$

edge-on: $i = 90°$

$\sin i = 1$

The Tully-Fisher Relation

$$L = Av_{\max}^{\alpha}$$

- There are two other corrections to be made. The first is to remove from the width of the HI line any contribution from the random motion of the HI clouds (which is small for massive galaxies). This correction is calculated from the velocity dispersion of gas clouds (either observed or modelled).

- The second correction is to account for dust in the luminosity of the galaxy. This is generally done by modelling the dust layer. Observations in the infrared minimize the effects of dust.

The Tully-Fisher Relation

$$L = A v_{\max}^{\alpha}$$

- Finally, the relation needs to be calibrated with galaxies whose distances are well known, for example from the period-luminosity relation of Cepheid stars (see more on Binney & Merrifield 1998).

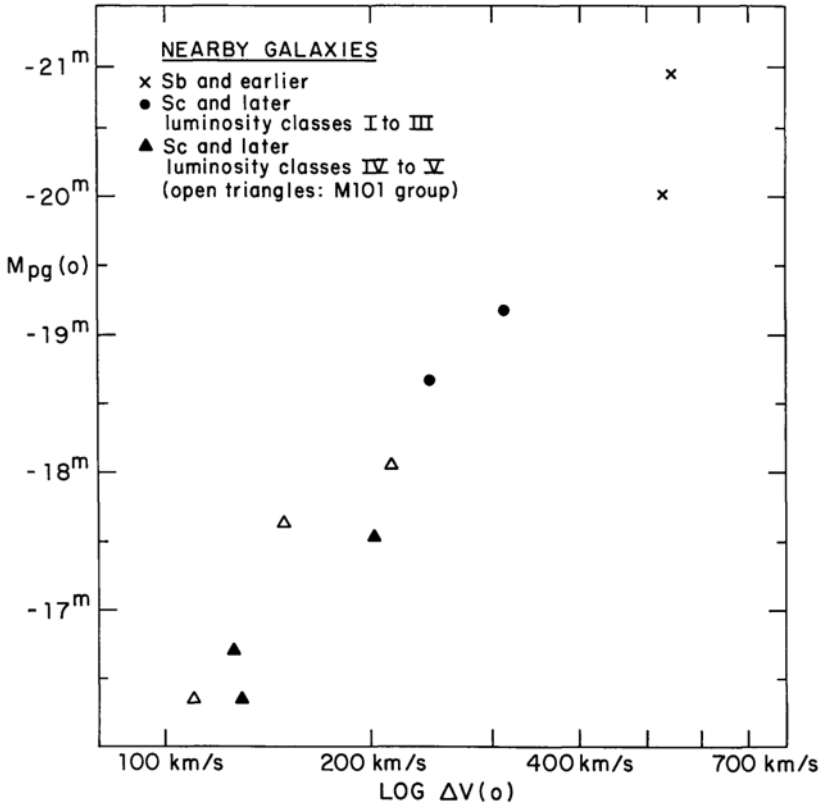

Fig. 1. Absolute magnitude – global profile width relation for nearby galaxies with previously well-determined distances. Crosses are M31 and M81, dots are M33 and NGC 2403, filled triangles are smaller systems in the M81 group and open triangles are smaller systems in the M101 group

Tully & Fisher (1977)

The Tully-Fisher Relation

$$L = A v_{\max}^{\alpha}$$

- With radio interferometers one can produce HI rotation curves (e.g., Begeman 1989); v is taken as the maximum velocity in the rotation curve $v_{\max}$.

Position-Velocity Diagram

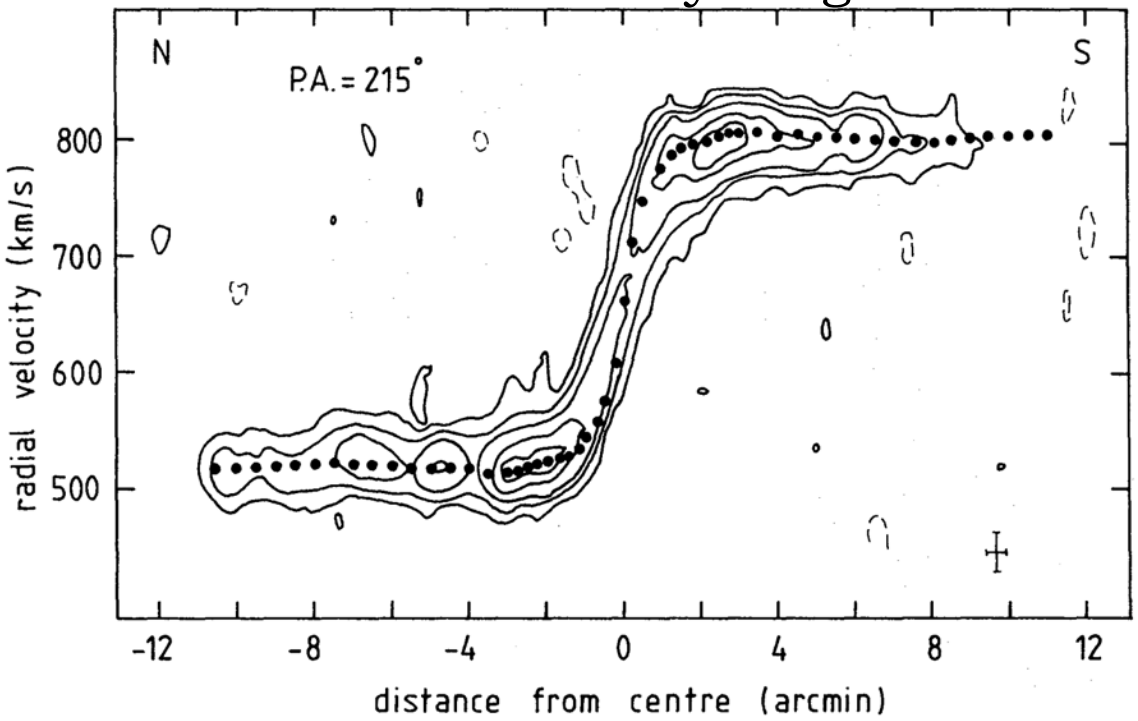

Fig. 9. The mean rotation curve for northern and southern half projected on a position-velocity map at a position angle of 215°. Contour levels are −1, 1, 3, 6, 13, 19 K. This map has not been corrected for primary beam attenuation

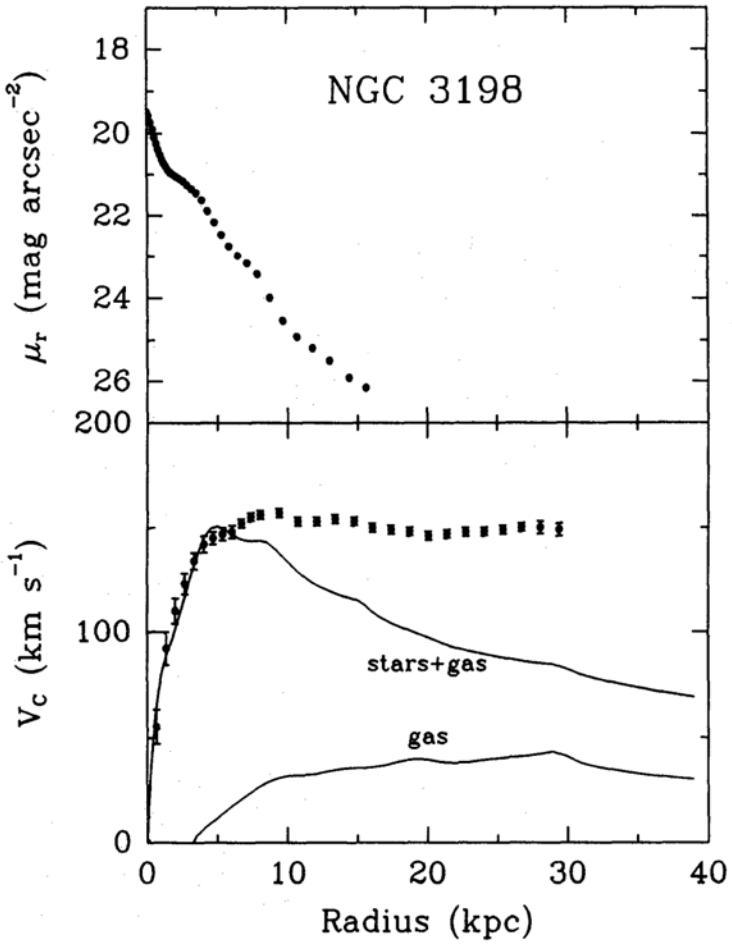

Fig. 15. Plot of observed rotation velocities (bottom) compared with rotation curve predicted from the photometric data (top, Kent, 1987) assuming a constant M/L ($3.8\,M_{\odot}/L_{B\odot}$) and z-thickness following a sech-squared law (van der Kruit and Searle, 1981) with disk thickness of 0.2 × the disk scale length. The contribution of the gas component has been included. The photometric data have not been corrected for inclination. Note the discrepancy between observed and predicted curves beyond 7 kpc

The Tully-Fisher Relation

$$L = A v_{\max}^{\alpha}$$

- With radio interferometers one can produce HI rotation curves (e.g., Begeman 1989)

$$M(r) = r v_{\mathrm{rot}}^2(r)/G$$

If v_{rot} is constant, then $M(r) \propto r$, so the enclosed galaxy mass is not converging.

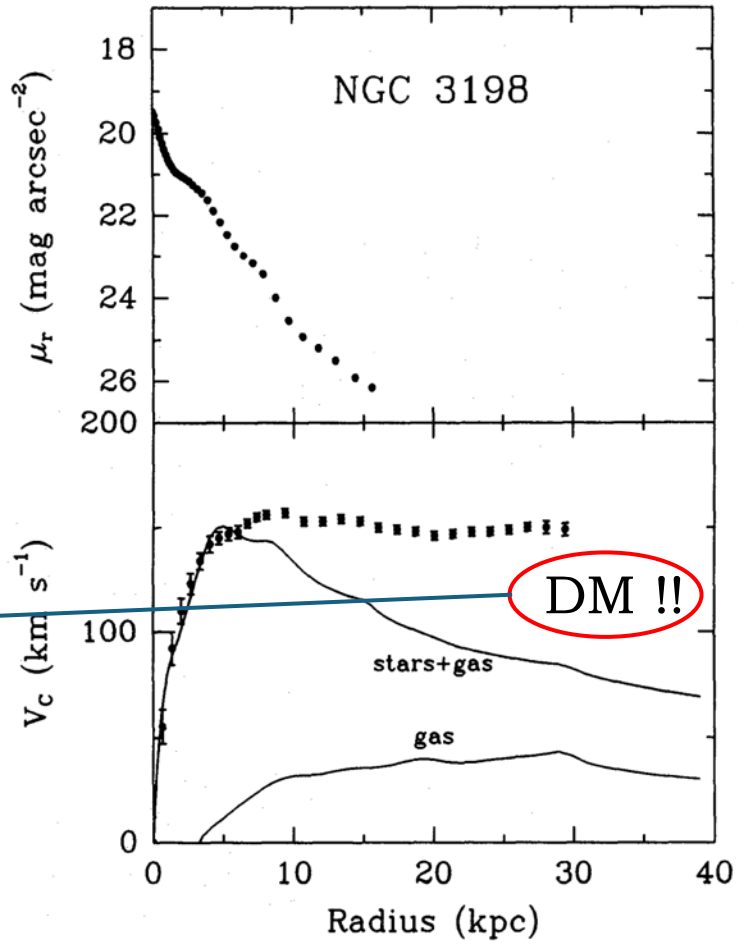

Fig. 15. Plot of observed rotation velocities (bottom) compared with rotation curve predicted from the photometric data (top, Kent, 1987) assuming a constant M/L ($3.8\,M_{\odot}/L_{B\odot}$) and z-thickness following a sech-squared law (van der Kruit and Searle, 1981) with disk thickness of 0.2 × the disk scale length. The contribution of the gas component has been included. The photometric data have not been corrected for inclination. Note the discrepancy between observed and predicted curves beyond 7 kpc

The Tully-Fisher Relation

$$L = A v_{\max}^{\alpha}$$

- So dark matter is necessary, but how much, and how is it distributed? The disc-halo degeneracy makes it difficult to answer.

maximal disc (halo less important in central regions)

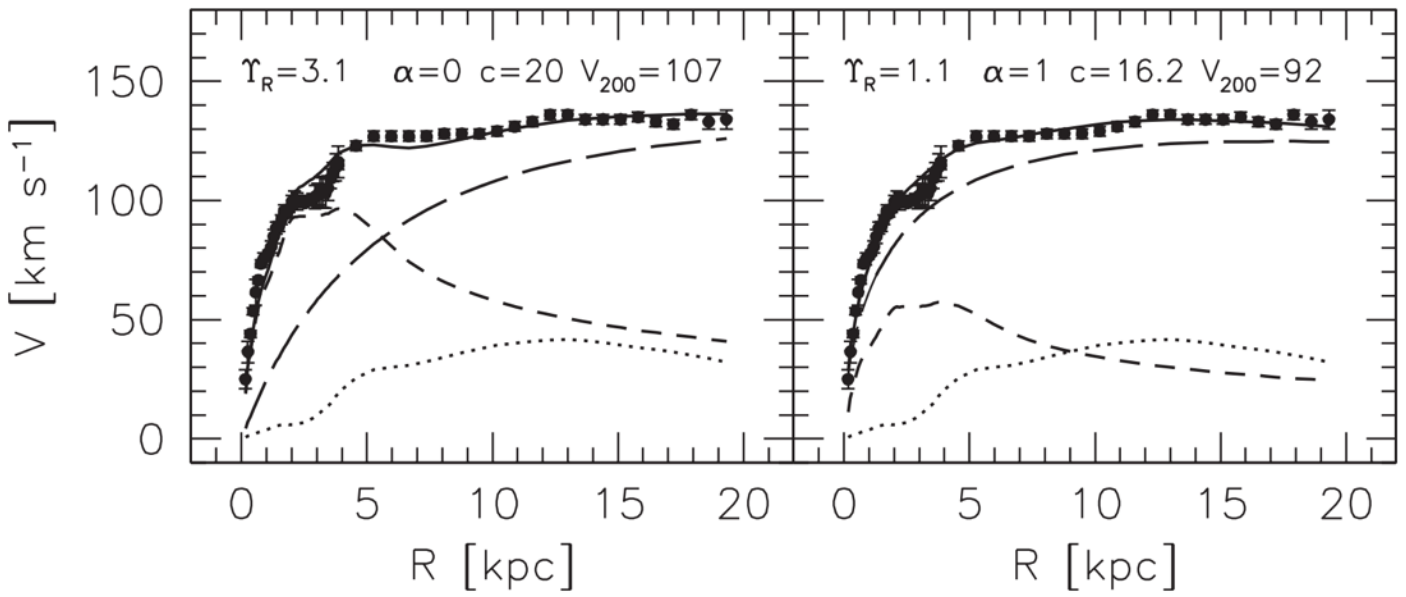

sub-maximal disc (halo more important in central regions)

Mo+2010: Fig. 11.1

Fig. 11.1. The rotation curve of NGC 2403 (solid dots with error bars) and two decompositions in contributions from the stellar disk (short-dashed lines), the gas disk (dotted lines) and the dark matter halo (long-dashed lines). In the left panel, a maximal disk with $\Upsilon_R = 3.1(M/L_R)_\odot$ is used together with a dark matter halo with a central density core, while the decomposition in the right panel uses a NFW halo and a submaximal disk with $\Upsilon_R = 1.1(M/L_R)_\odot$. Both decompositions fit the observations equally well, illustrating the disk–halo degeneracy. [After Dutton et al. (2005); courtesy of A. Dutton]

The Tully-Fisher Relation

$$L = Av_{\max}^{\alpha}$$

- α ranges from ~ 2.5 in the B band to ~ 4 in the K band reflecting the colour-magnitude relation (brighter galaxies are redder).

Mo+2010: Fig. 2.22

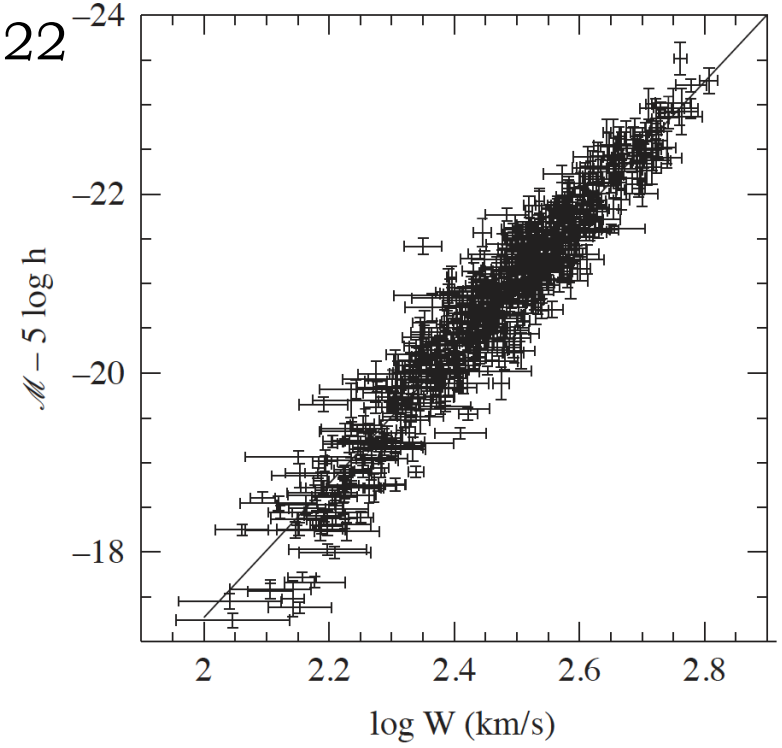

Fig. 2.22. The Tully–Fisher relation in the I-band. Here W is the linewidth of the HI 21-cm line which is roughly equal to twice the maximum rotation velocity, $V_{\max}$. [Adapted from Giovanelli et al. (1997) by permission of AAS]

Bell & de Jong (2001)

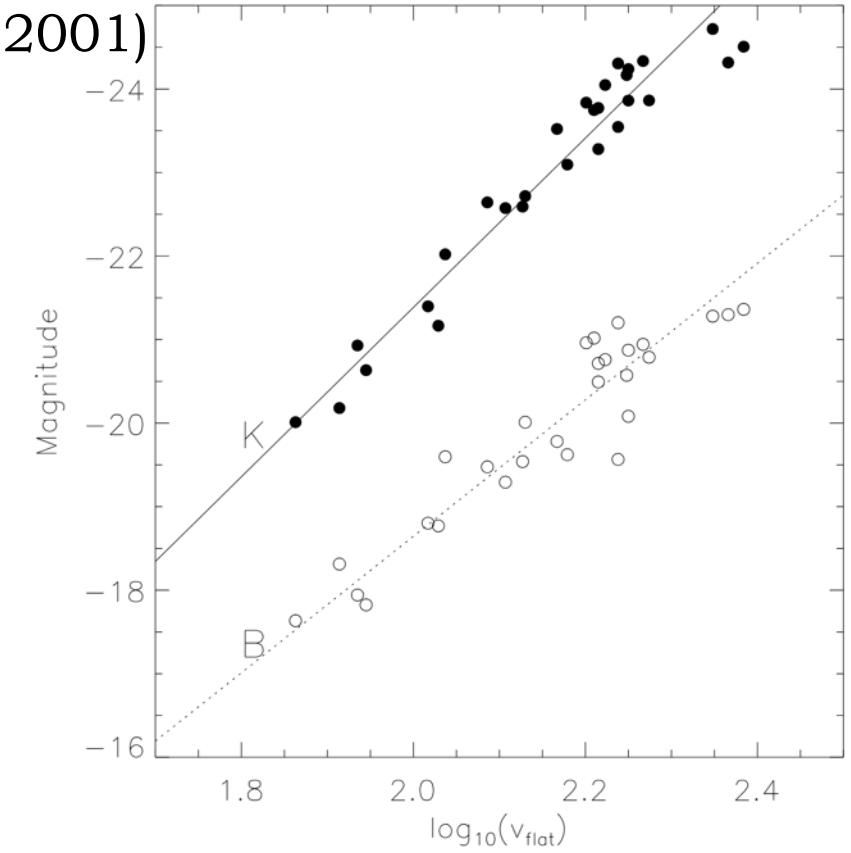

FIG. 7.—T-F relation in *B* and *K* passbands. Solid and open circles denote the data of Verheijen (1997) in *K* and *B* bands, respectively, corrected using the Tully et al. (1998) mass-dependent dust corrections. The lines denote the least-squares bisector fits (Isobe et al. 1990) to the mass-dependent dust-corrected T-F relations.

The Tully-Fisher Relation

$$L = Av_{\max}^{\alpha}$$

- Courteau+2007 find that the scatter in the TF relation does not depend on the central surface brightness of the galaxies. Why is this important?

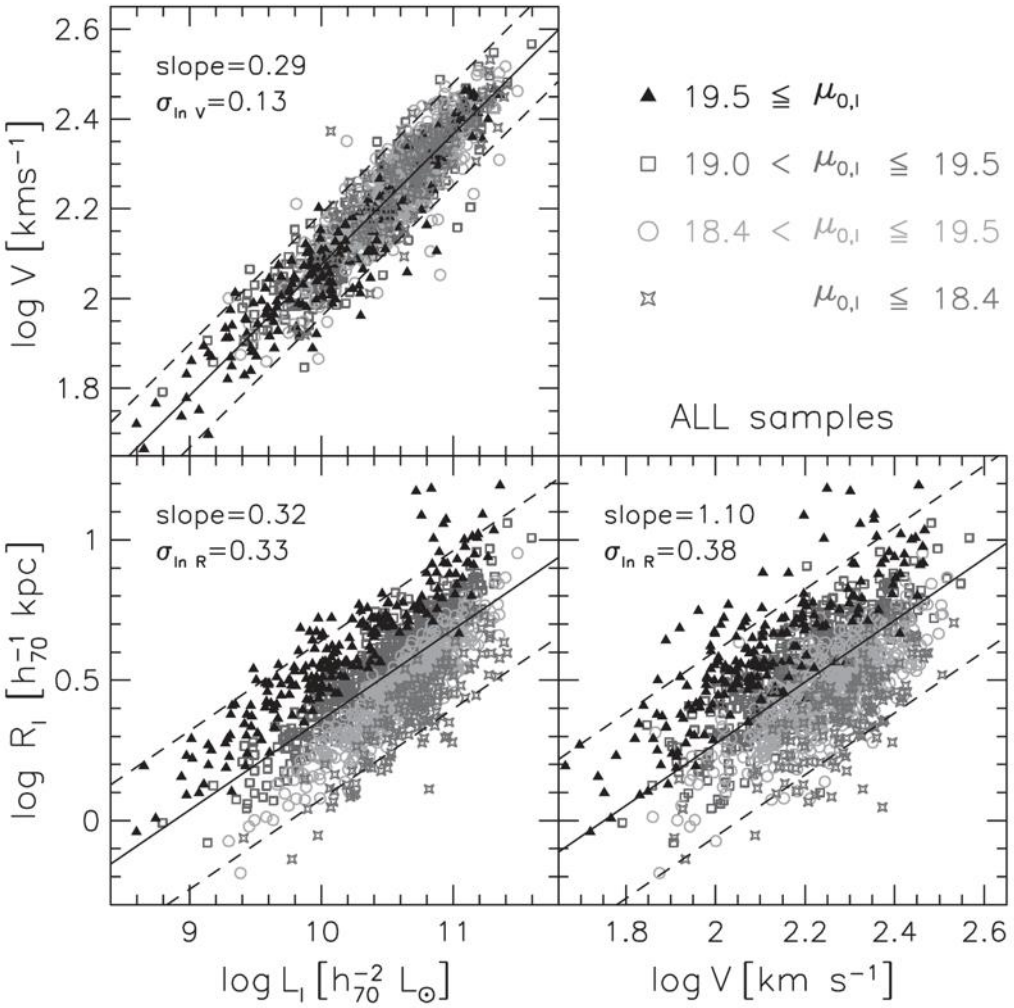

$$L_{\rm d} = 2.9 \times 10^{10} h^{-2} {\rm L}_\odot \left(\frac{V_{\rm obs}}{200\,{\rm km\,s^{-1}}} \right)^{3.44}$$

Fig. 11.2. The scaling relations between rotation velocity V, luminosity L, and scale length R. Different symbols represent different bins in central surface brightness, as indicated (all photometry is in the I band). Solid lines show the best-fit linear relations between $\log V$, $\log L$ and $\log R$. The 2σ observed scatter is indicated by the dashed lines, and the slope and scatter are listed in each panel. [Adapted from Courteau et al. (2007) by permission of AAS]

The Tully-Fisher Relation

$$L = A v_{\max}^{\alpha}$$

- For maximal, thin exponential discs (self-gravitating discs), it can be shown that the rotation velocity peaks at $R \approx 2.16\, R_d$, where R_d is the scale length of the disc (see Mo+2010, Sect. 11.1), such that the total mass of the disc is $M_d = 2\pi\Sigma_0 R_d^2$ (Σ_0 is the central surface mass density of the disc).

From the virial theorem, $v_{\max}^2 \propto \frac{M}{R} \propto \Sigma_0 R_d^2 / R_d \propto \Sigma_0 R_d$. With that, let's try to write luminosity as a function of $v_{\max}$ for this disc. Since:

$$v_{\max}^4 \propto \Sigma_0^2 R_d^2 \propto M \Sigma_0$$

we can write:

$$L \propto v_{\max}^4 \frac{1}{\Sigma_0} \frac{1}{\Upsilon}$$

where Υ is the mass/light ratio of the disc.

The Tully-Fisher Relation

$$L = A v_{\max}^{\alpha}$$

Now, the central surface brightness of the disc is $I_0 \equiv \Sigma_0/\Upsilon$. So the previous equation can be written as:

$$L \propto v_{\max}^4 \frac{1}{\Sigma_0}\frac{1}{\Upsilon} \Rightarrow L \propto v_{\max}^4 \frac{1}{I_0}\frac{1}{\Upsilon^2}$$

This implies that the scatter in the Tully-Fisher relation should depend on I_0, but this conflicts with observations. Unless there is a tight relation between Υ and I_0, such that $\Upsilon \propto I_0^{-1/2}$, the observed TF relation argues against the rotation of the disc being completely dominated by baryonic matter.

The Stellar and Baryonic Tully-Fisher Relations

$$M = Av_{\max}^{\alpha}$$

Bell & de Jong (2001)

$$M_{\star} \propto v_{\max}^{4.4\pm0.2}$$

$$M_{\text{baryon}} \propto v_{\max}^{3.5\pm0.2}$$

$$M_{\text{baryon}} = M_{\star} + M_{\text{HI}}$$

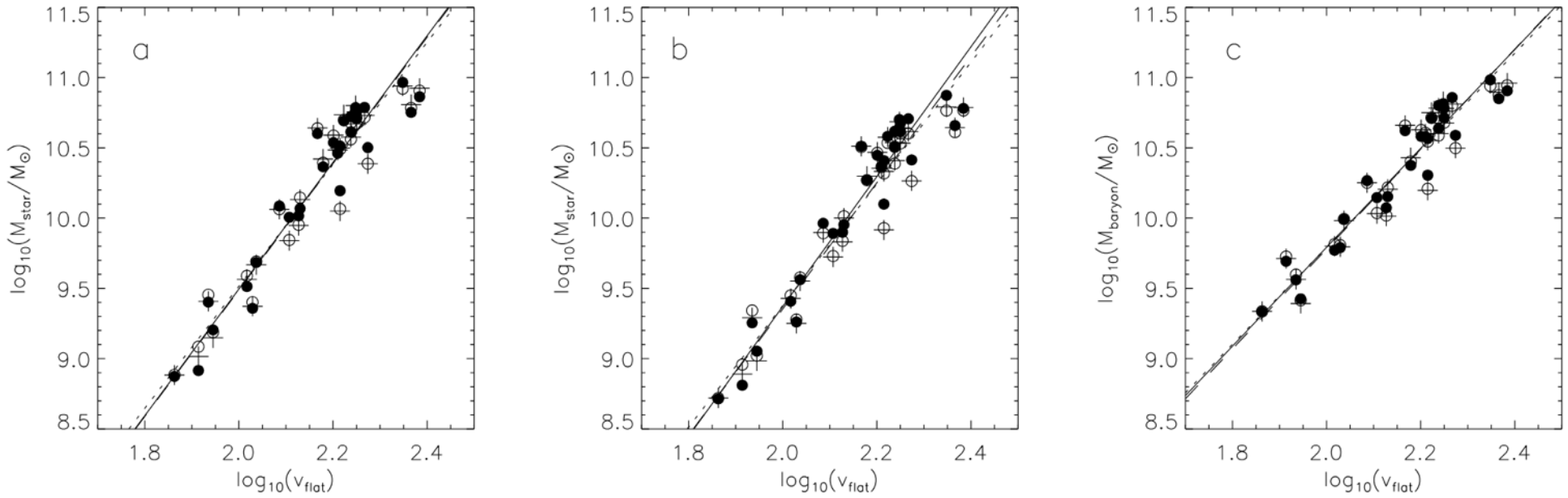

FIG. 8.—T-F relations: (*a*) stellar mass with mass-dependent extinction correction, (*b*) stellar mass with mass-independent extinction correction, and (*c*) baryonic T-F relation with mass-dependent extinction correction. Masses derived from *B* and *R* data are shown as open circles (the masses are identical as $B-R$ colors are used to construct the stellar M/L ratios), *I*-band data as crosses, and *K*-band data as solid circles. Least-squares bisector fits to each passband's T-F relations are presented for the *B* and *R* data (*dotted lines*), *I*-band data (*dashed lines*), and *K*-band data (*solid lines*).

The Mass-Size Relation

Can tell us how galaxies and stellar structures grow

The Mass-Size Relation

$$\log r_e \propto \alpha \log M$$

- van der Wel+2015: analysis of a parent sample of galaxies in the CANDELS/3D-HST fields
- At fixed stellar mass, late-type galaxies have on average larger r_e than early-type galaxies, but the latter have a steeper mass-size relation

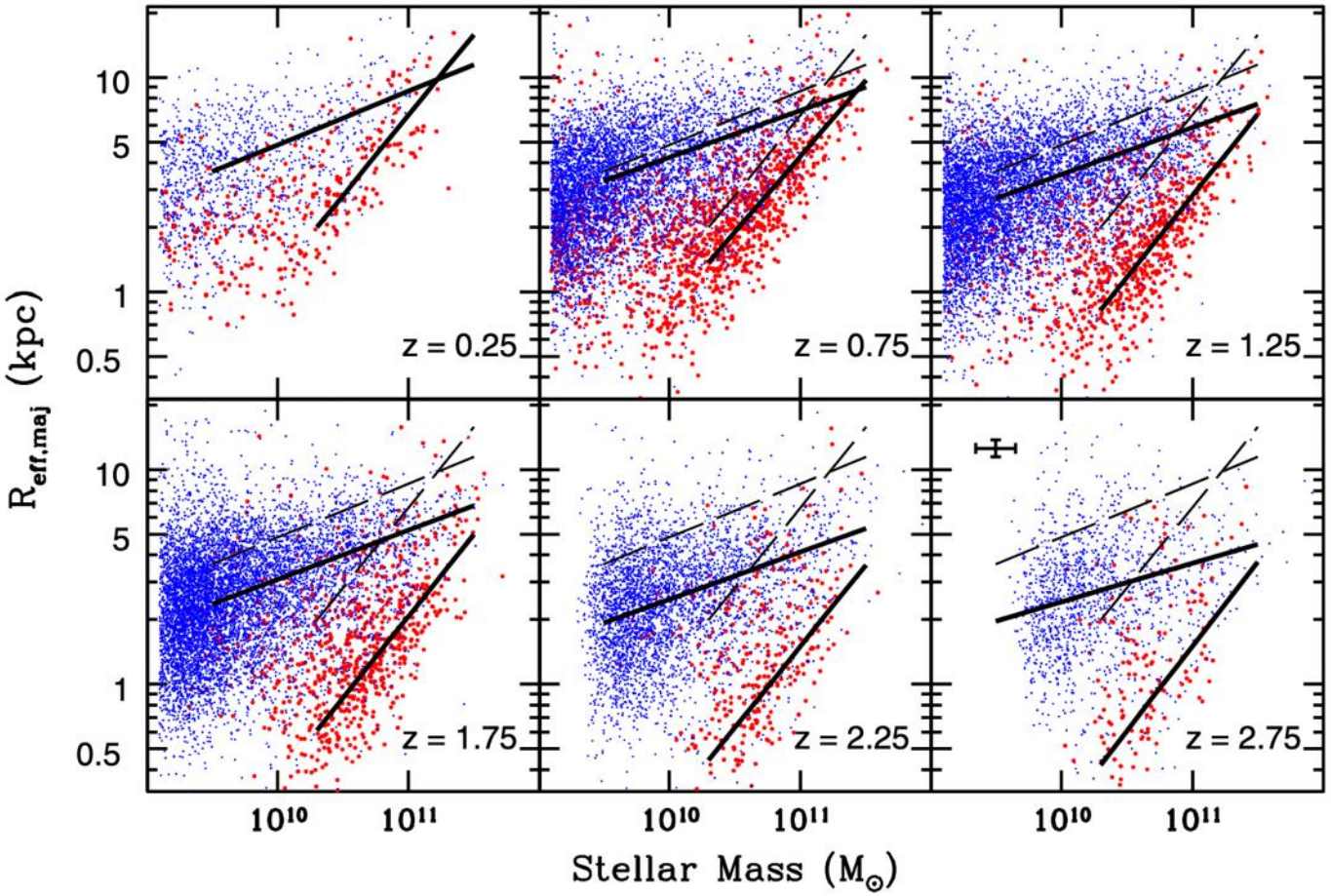

Figure 5. Size–stellar mass distribution of late- and early-type galaxies (same symbols as in Figure 2). A typical 1σ error bar for individual objects in the higher-redshift bins is shown in the bottom right panel. The lines indicate model fits to the early- and late-type galaxies as described in Section 3.1. The dashed lines, which are identical in each panel, represent the model fits to the galaxies at redshifts $0 < z < 0.5$. The solid lines represent fits to the higher-redshift samples. The mass ranges used in the fits are indicated by the extent of the lines in the horizontal direction. Strong evolution in the intercept of the size–mass relation is seen for early-type galaxies, and moderate evolution is seen for the late-type galaxies (also see Figure 6. There is no significant evidence for evolution in the slope (also see Figure 6). The parameters of the fits shown here are given in Table 1.

The Mass-Size Relation

$$\log r_e \propto \alpha \log M$$

- van der Wel+2015: in addition, the intercepts of these relations evolve from z ~ 3 to z ~ 0, but more so for early-type galaxies
- These observations are consistent with a more dramatic growth of early-type galaxies, presumably by mergers

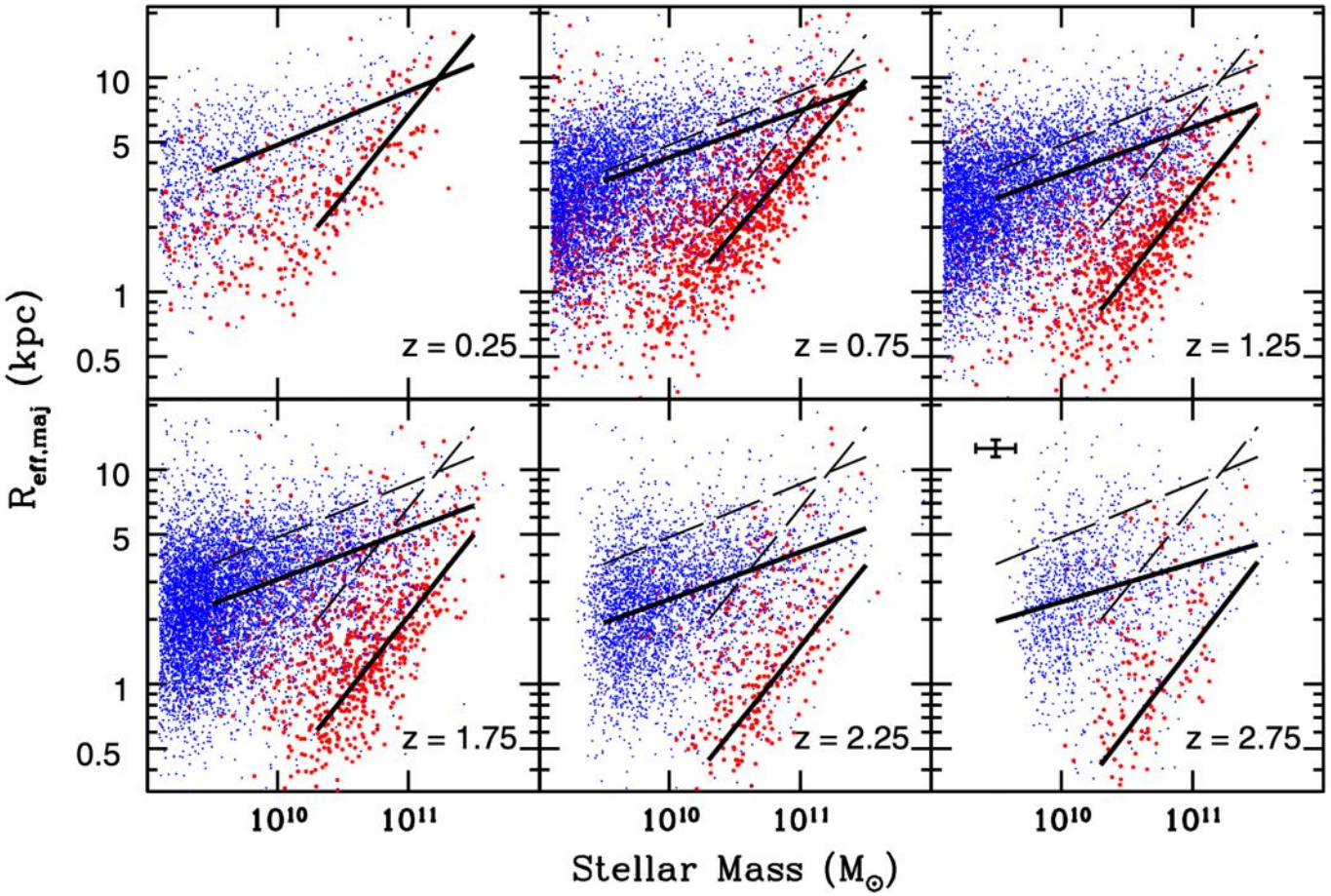

Figure 5. Size–stellar mass distribution of late- and early-type galaxies (same symbols as in Figure 2). A typical 1σ error bar for individual objects in the higher-redshift bins is shown in the bottom right panel. The lines indicate model fits to the early- and late-type galaxies as described in Section 3.1. The dashed lines, which are identical in each panel, represent the model fits to the galaxies at redshifts $0 < z < 0.5$. The solid lines represent fits to the higher-redshift samples. The mass ranges used in the fits are indicated by the extent of the lines in the horizontal direction. Strong evolution in the intercept of the size–mass relation is seen for early-type galaxies, and moderate evolution is seen for the late-type galaxies (also see Figure 6. There is no significant evidence for evolution in the slope (also see Figure 6). The parameters of the fits shown here are given in Table 1.

The Mass-Size Relation

$$\log r_e \propto \alpha \log M$$

- Mowla+2019: using r_{80} instead of r_e makes the sizes of early- and late-type galaxies more similar
- This suggests a single, broken power law, where the slope changes at a pivot mass M_p

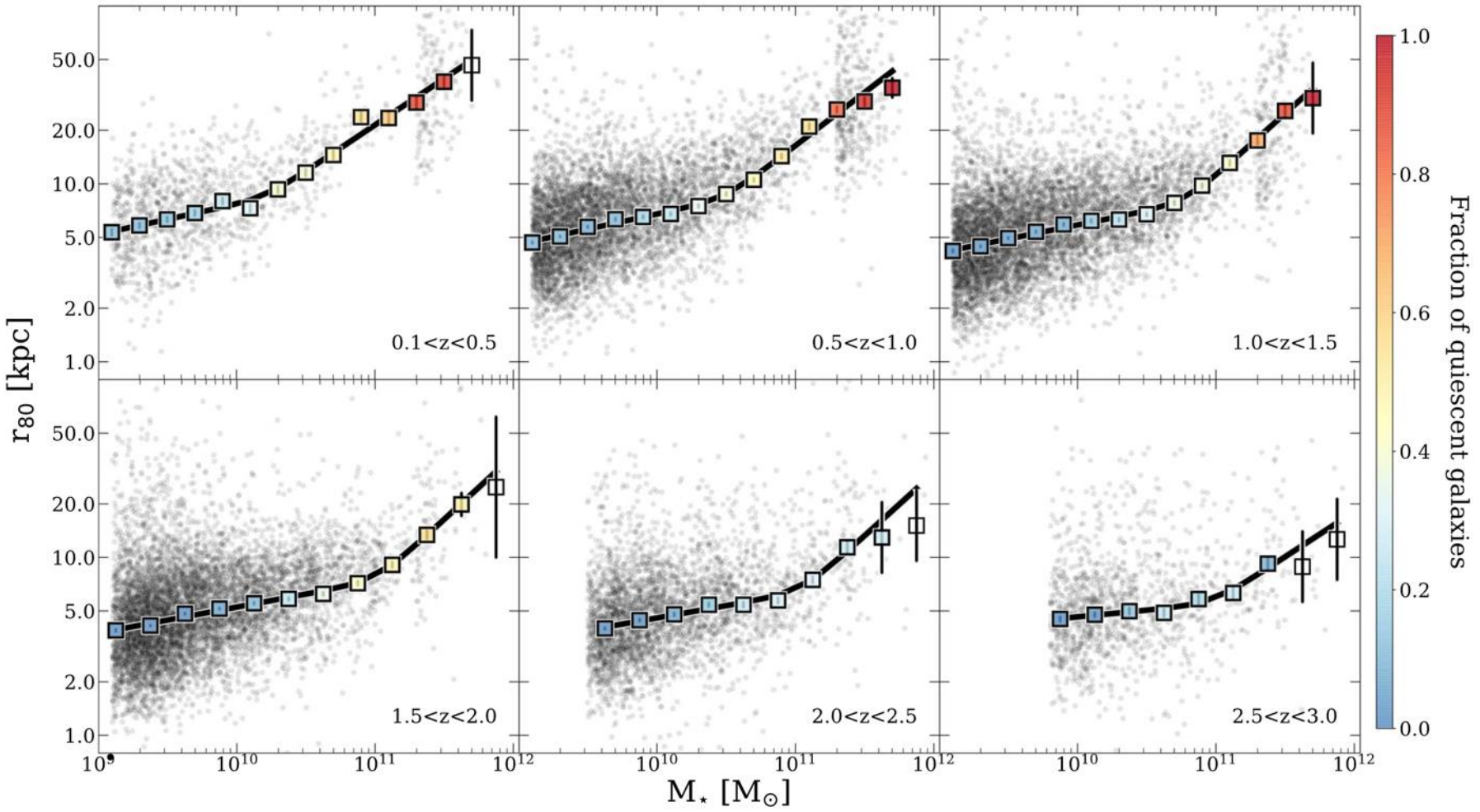

Figure 1. Size–stellar mass distribution of galaxies at $0 < z < 3$ from van der Wel et al. (2014) and Mowla et al. (2018). The squares show the median of r_{80} in bins of $\log(M_\star/M_\odot)$, color-coded by the fraction of quiescent galaxies in the bin; rest-frame $U - V$ and $V - J$ color space was used to separate galaxies into star-forming and quiescent. Unfilled squares represent bins with less than 15 galaxies. Smoothly broken power-law fits given by Equation (2) to the median size–mass relation are shown by the black lines.

The Mass-Size Relation

$$\log r_e \propto \alpha \log M$$

- Mowla+2019:

$$r_{80} \propto M_{\star}^{0.15} \ (M_{\star} < M_p)$$

$$r_{80} \propto M_{\star}^{0.6} \ (M_{\star} > M_p)$$

where:

$\log M_p \approx 10.2 M_{\odot}$ (at z=0.4)
$\log M_p \approx 10.9 M_{\odot}$ (at z=1.7-3)

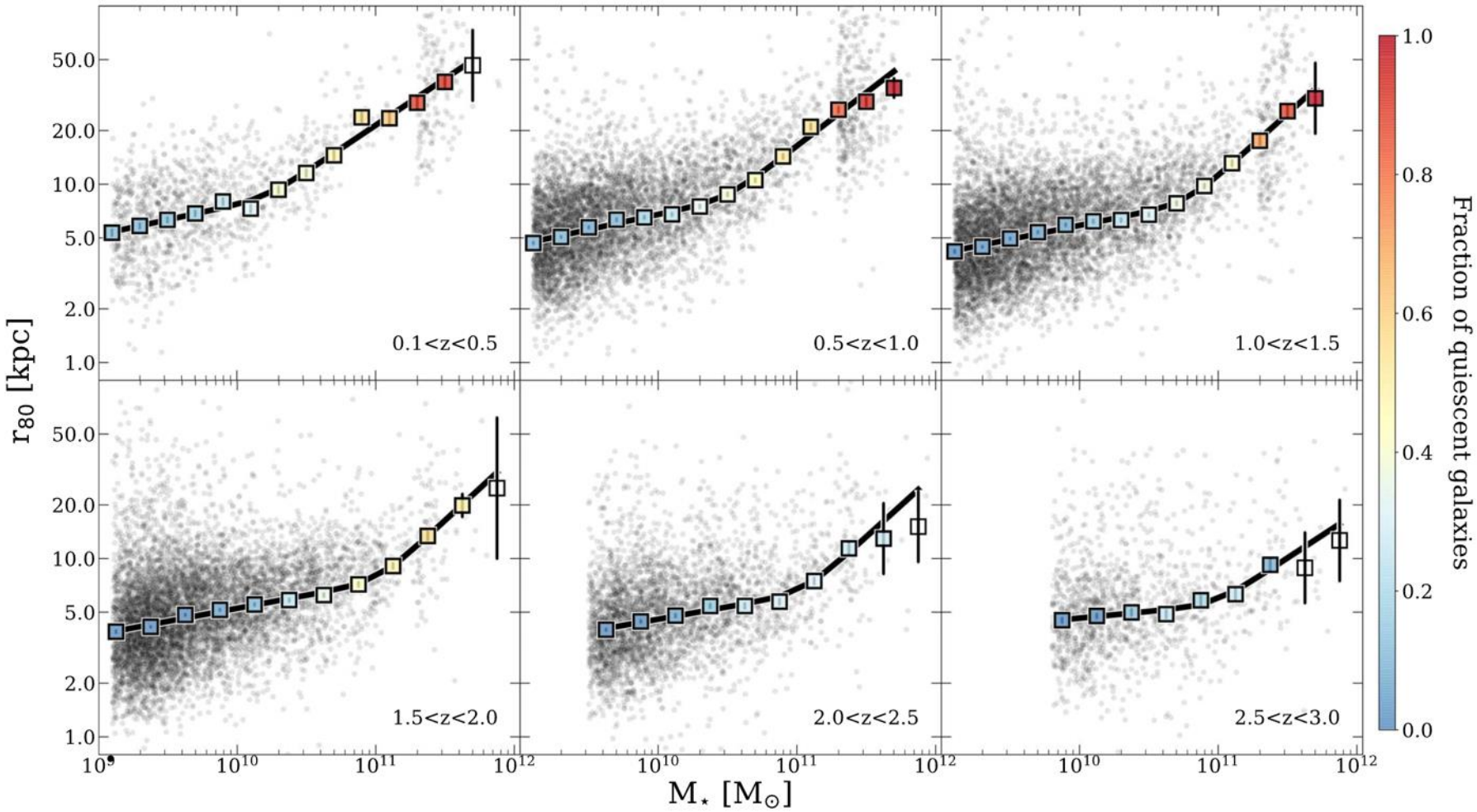

Figure 1. Size–stellar mass distribution of galaxies at $0 < z < 3$ from van der Wel et al. (2014) and Mowla et al. (2018). The squares show the median of r_{80} in bins of $\log(M_{\star}/M_{\odot})$, color-coded by the fraction of quiescent galaxies in the bin; rest-frame $U - V$ and $V - J$ color space was used to separate galaxies into star-forming and quiescent. Unfilled squares represent bins with less than 15 galaxies. Smoothly broken power-law fits given by Equation (2) to the median size–mass relation are shown by the black lines.

The Mass-Size Relation

$$\log r_e \propto \alpha \log M$$

- Mowla+2019: *the pivot mass coincides with the mass where the fraction of star-forming galaxies is 50%, suggesting that the pivot mass reflects a transition from dissipational to dissipationless galaxy growth*

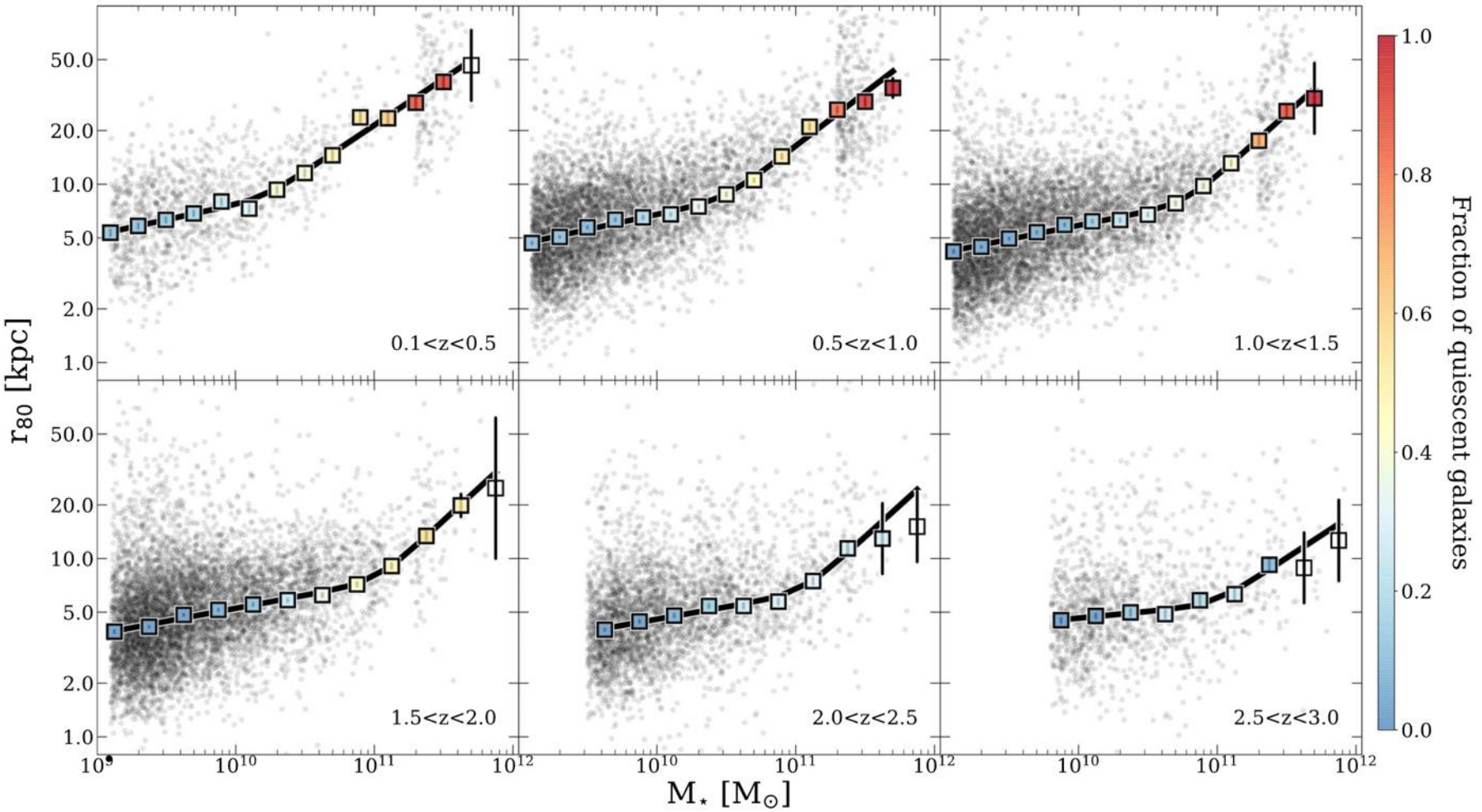

Figure 1. Size–stellar mass distribution of galaxies at $0 < z < 3$ from van der Wel et al. (2014) and Mowla et al. (2018). The squares show the median of r_{80} in bins of $\log(M_\star/M_\odot)$, color-coded by the fraction of quiescent galaxies in the bin; rest-frame $U - V$ and $V - J$ color space was used to separate galaxies into star-forming and quiescent. Unfilled squares represent bins with less than 15 galaxies. Smoothly broken power-law fits given by Equation (2) to the median size–mass relation are shown by the black lines.

The Mass-Size Relation

$$\log r_e \propto \alpha \log M$$

- Gadotti (2009): bulge/disc/bar decompositions of 1000 SDSS galaxies at z = 0.02-0.07

bars: α = 0.21
discs: α = 0.33
disc-like: α = 0.20 (±0.02)
classical: α = 0.30
ellipticals: α = 0.38

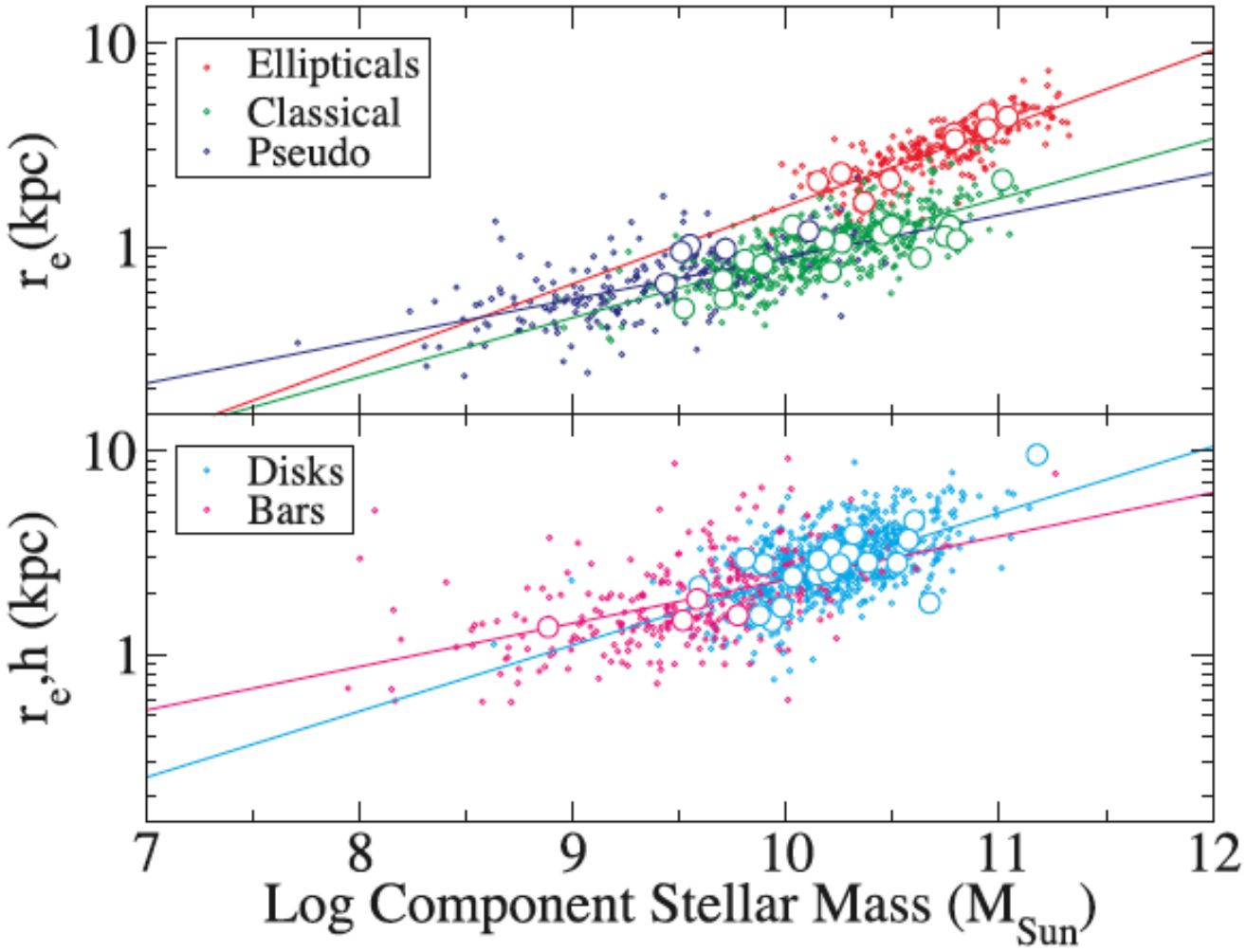

The Mass-Size Relation

$$\log r_e \propto \alpha \log M$$

- The mass-size relation of disc-like bulges is different from that of classical bulges by 5σ
- The mass-size relation of classical bulges is different from that of ellipticals by 4σ
- The only pair of components with similar mass-size relations are disc-like bulges and bars, corroborating the picture in which the former grow from the latter (much more about this later)

Gadotti (2009):

bars: $\alpha = 0.21$
discs: $\alpha = 0.33$
disc-like: $\alpha = 0.20$ (± 0.02)
classical: $\alpha = 0.30$
ellipticals: $\alpha = 0.38$

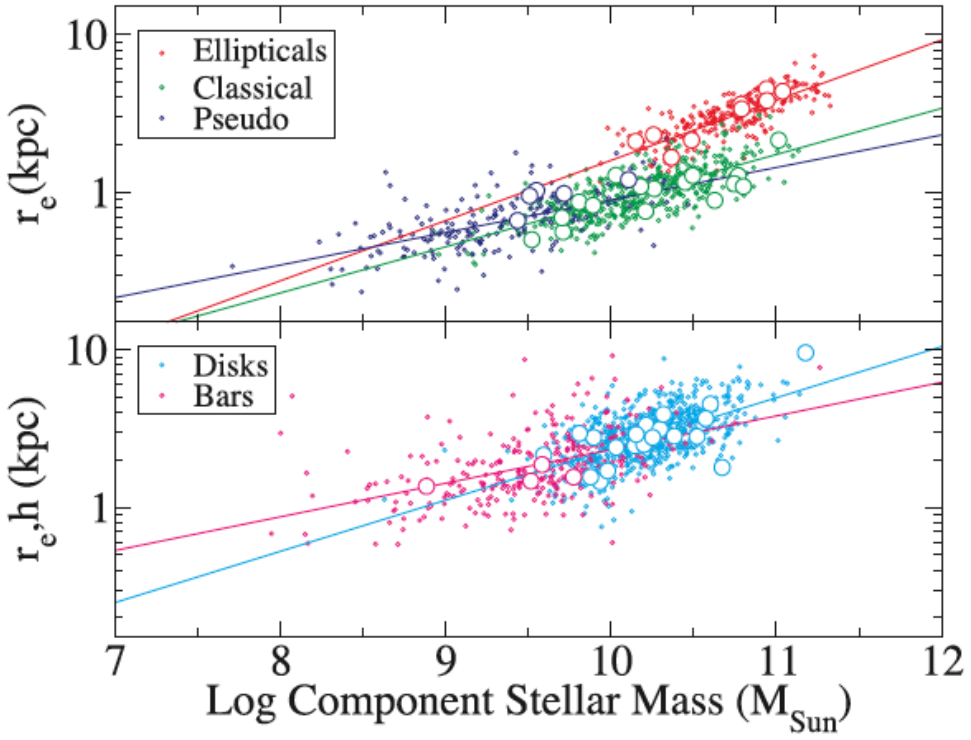

The Mass-Size Relation

$$\log r_e \propto \alpha \log M$$

- At the high-mass end, classical bulges are not just ellipticals surrounded by discs
- Unless the bulge gets compressed with the formation of the disc (Debattista+2013) but this does nor work out quantitatively (yet)

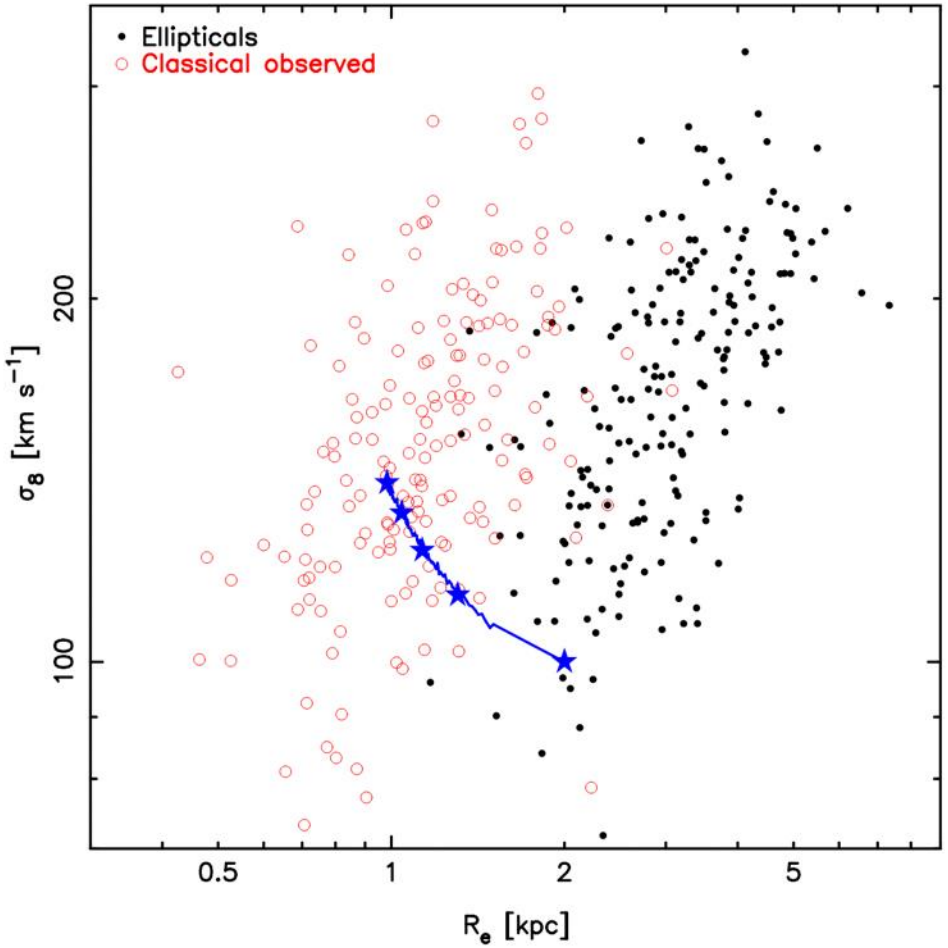

Altogether, this suggests an increasing role of dissipation from the formation of ellipticals ($\alpha = 0.38$) to classical bulges ($\alpha = 0.30$) and to disc-like bulges ($\alpha = 0.20$)

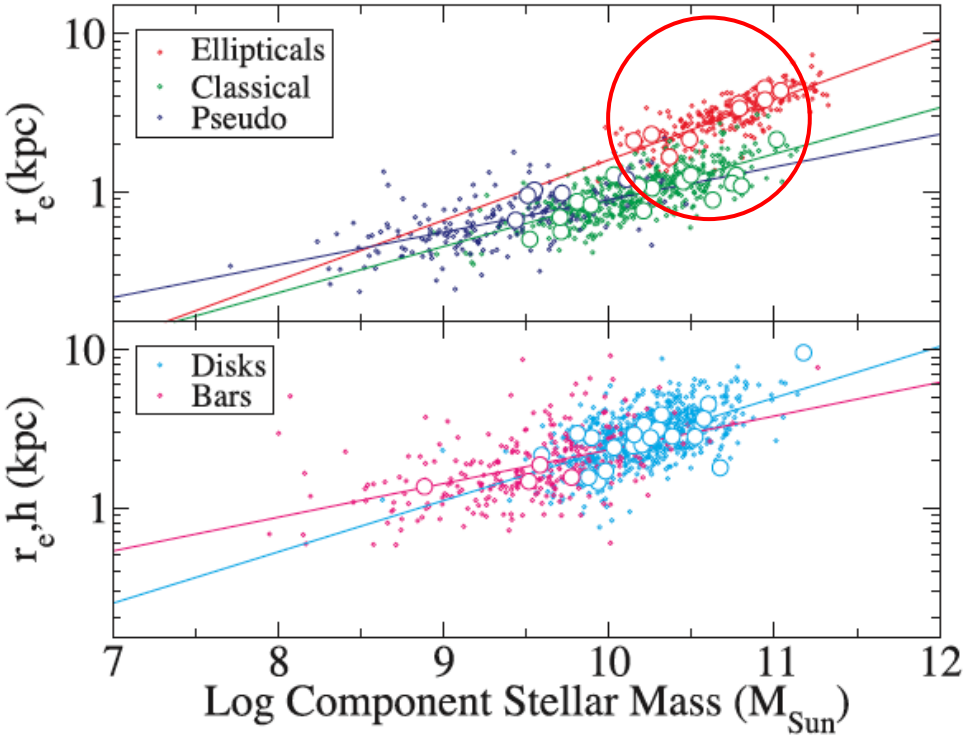

FIG. 9.— The σ_8-R_e projection of the fundamental plane for the Gadotti & Kauffmann (2009) sample. The (black) filled circles show elliptical galaxies while the (red) open circles show the observed unbarred classical bulges. The diagonal (blue) line shows the evolution of the model in the simulation with $R_d/R_{e,0} = 2$, assuming $R_{e,0} = 2$ kpc and $\sigma_{e,0} = 100\,\mathrm{km\,s^{-1}}$. The star symbols correspond to the system at D/B = 0 (bottom right), 5, 10, 15 and 20 (top left).

→ Seems to work only for very small bulges

The Mg_2-σ Relation

Metallicity vs. velocity dispersion

The Mg_2-σ Relation

- The Mg2 index is a spectral index that incorporates lines from Mg around 5175Å and it is shown to correlate well with total metallicity Z (see, e.g., Burstein+1984, Casuso+1996)

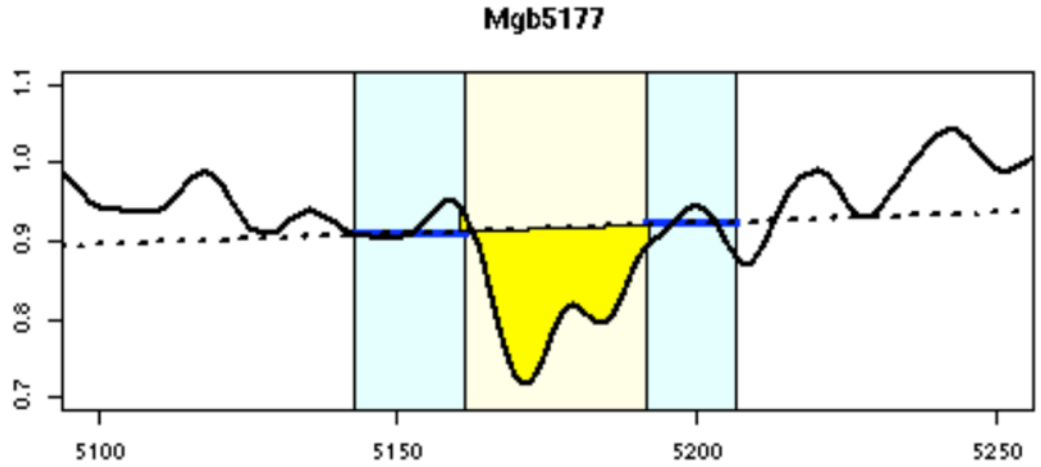

Name	Main Passband (Å)	Blue Sideband (Å)	Red Sideband (Å)
Mg1	5069.125 – 5134.125	4895.125 – 4957.625	5301.125 – 5366.125
Mg2	5154.125 – 5196.625	4895.125 – 4957.625	5301.125 – 5366.125
Mgb	5160.125 – 5192.625	5142.625 – 5161.375	5191.375 – 5206.375

The Mg_2-σ Relation

- The Mg2 index is a spectral index that incorporates lines from Mg around 5175Å and it is shown to correlate well with total metallicity Z (see, e.g., Burstein+1984, Casuso+1996)

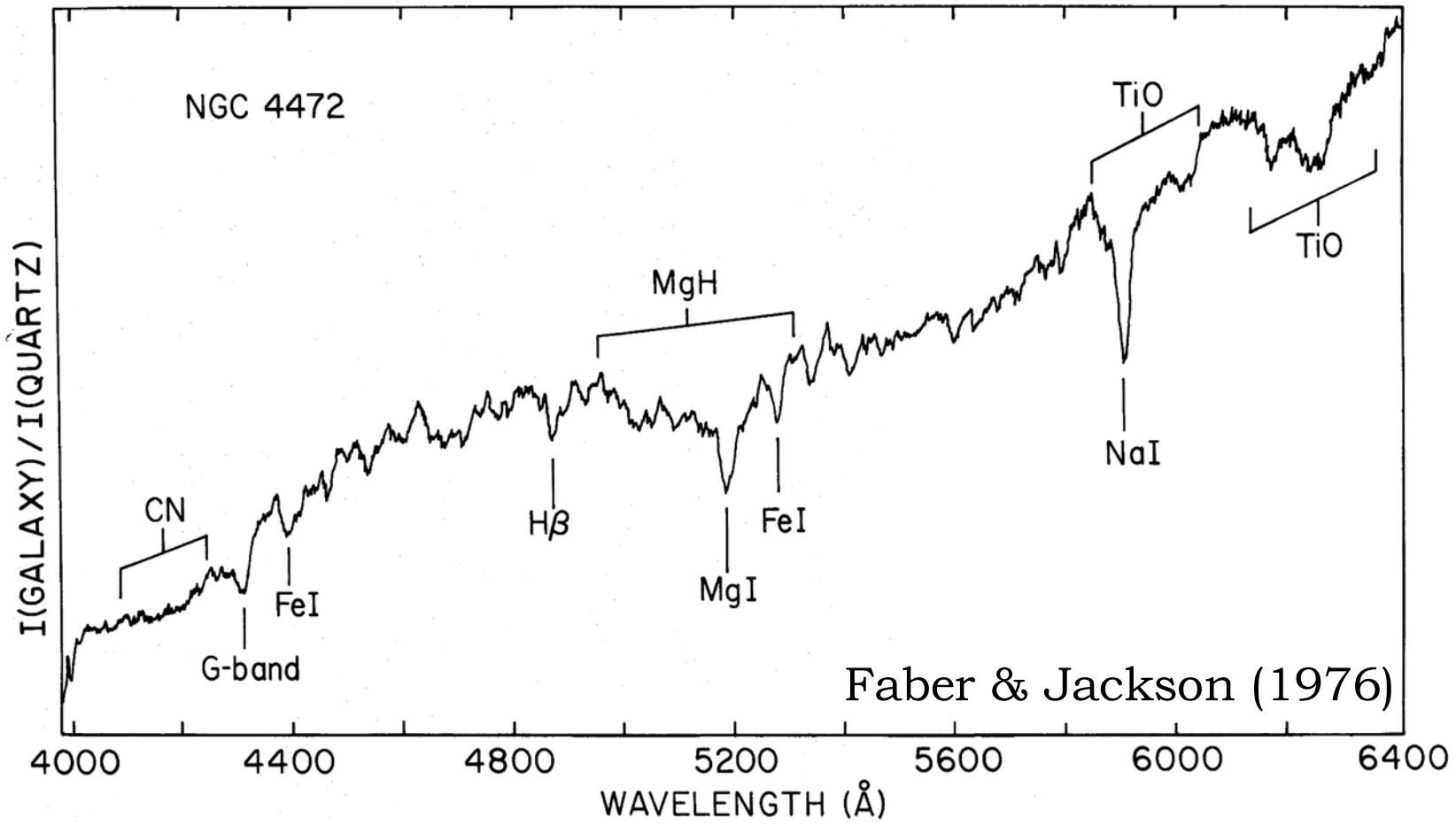

FIG. 1.—Typical scan of giant elliptical galaxy, divided by the tungsten lamp (denoted by "quartz")

The Mg_2-σ Relation

- The Mg2 index is a spectral index that incorporates lines from Mg around 5175Å and it is shown to correlate well with total metallicity Z (see, e.g., Burstein+1984, Casuso+1996)

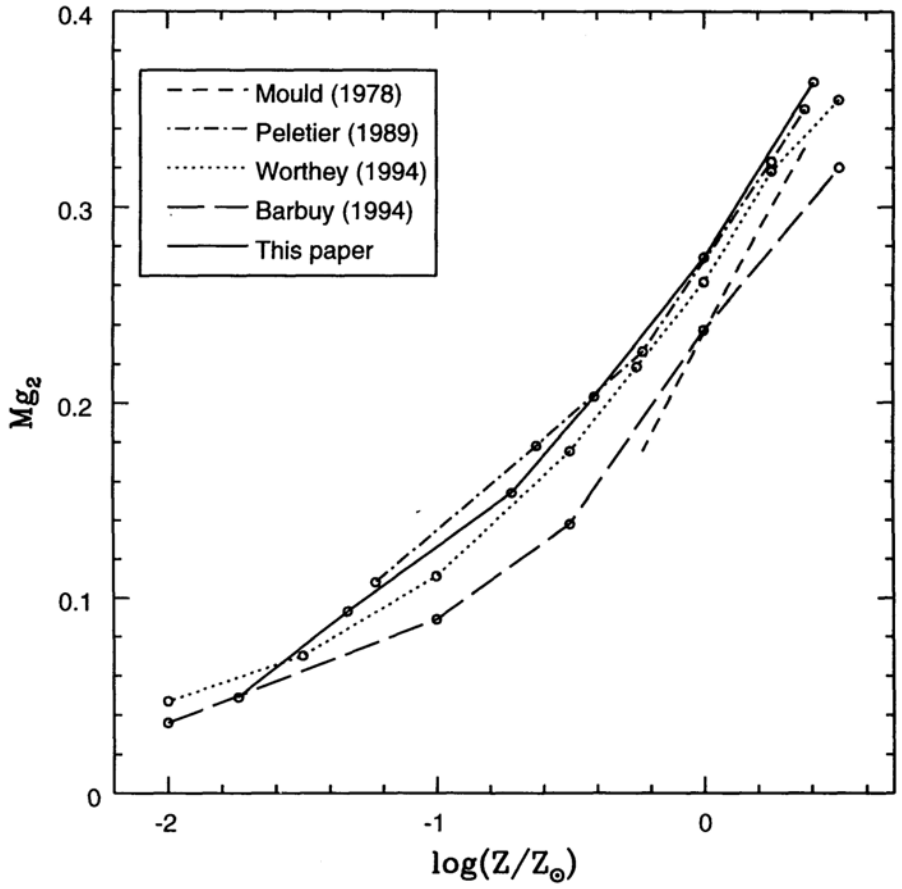

FIG. 1.—Mg_2-Z calibration for an age of 13 Gyr. Compared are Mould (1978), Peletier (1989), Worthey (1994), Barbuy (1994), and this work.

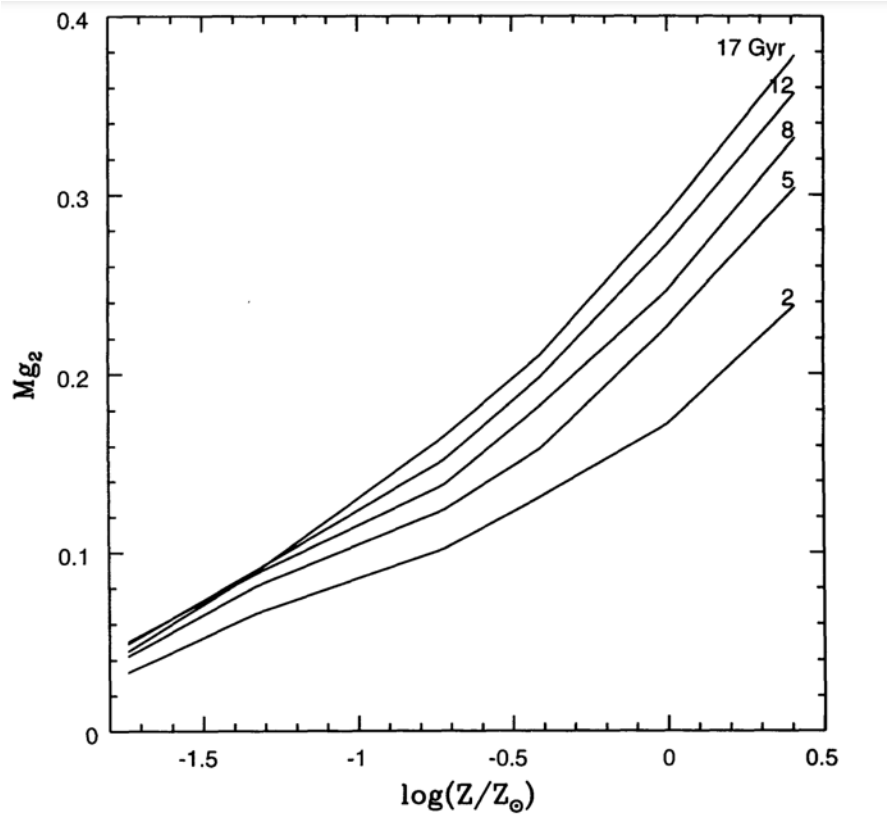

FIG. 2.—Mg_2 vs. Z for five stellar population ages: 2, 5, 8, 12, and 17 Gyr. The lines are from this work. We note that these curves are based on a single-burst hypothesis and assume the metallicity attained in the burst. [Mg/Fe] is assumed to be 0. Their use in the calibration of Mg_2 is explained in the text. Models with a distribution of stellar populations, having different ages, would always yield a higher metallicity for a given maximum age.

The Mg_2-σ Relation

- The Mg2-σ relation is a reflection of the mass-metallicity relation (remember that from the virial theorem $\frac{GM}{\langle R \rangle} = \langle v^2 \rangle$).

Dressler+1987

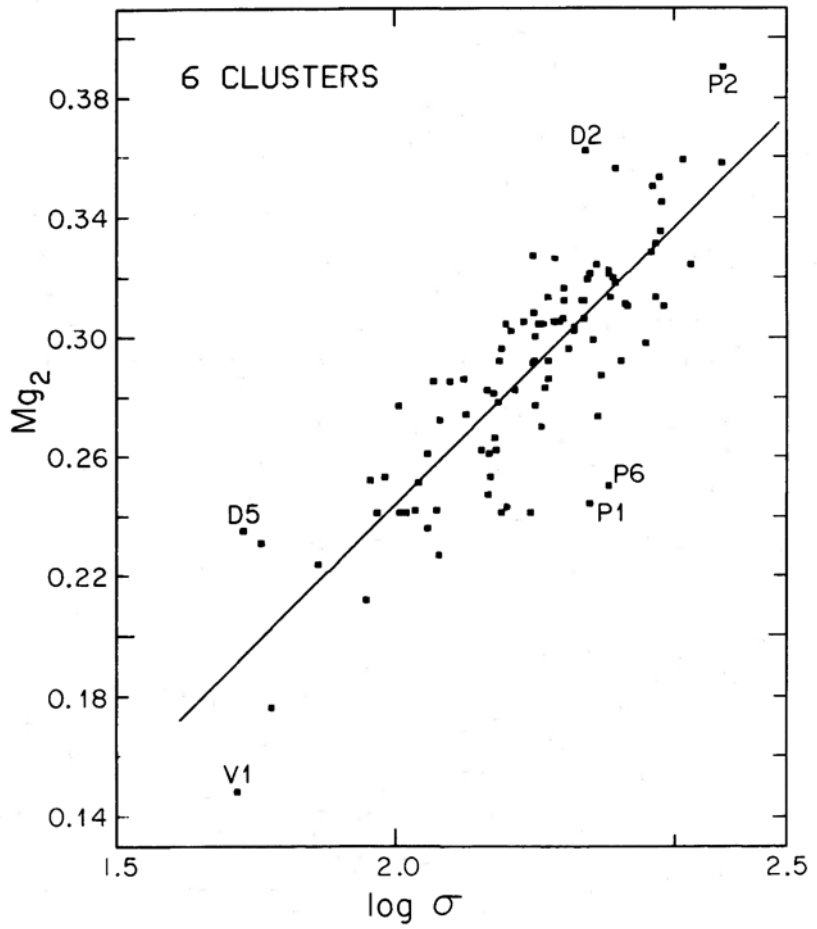

FIG. 9.—Correlation of distance-independent parameters Mg_2 and log σ. The fact that this relationship is relatively tight in spite of some of the large differences seen in Figs. 2 and 6 again demonstrates that in some cases the residuals are correlated, as also shown in the δ-δ diagram of Fig. 8. The line plotted is $Mg_2 = 0.186 \log \sigma - 0.129$, and the rms dispersion is 0.021 in Mg_2, or 0.113 in log σ. The correlation coefficient is 0.79.

The Mass-Metallicity Relation

The Mass-Metallicity Relation

- Metallicity (Mo+2010): *reflects the amount of gas that has been reprocessed by stars and exchanged with its surroundings. Gas-phase metallicities can be measured from the emission lines in a galaxy spectrum, while the metallicity of the stars can be obtained from the absorption lines which originate in the atmospheres of the stars. They can be very different.*

- Metals are retained by the potential well, but relation eventually saturates at high masses, providing a constraint to the chemical evolution of a star-forming galaxy.

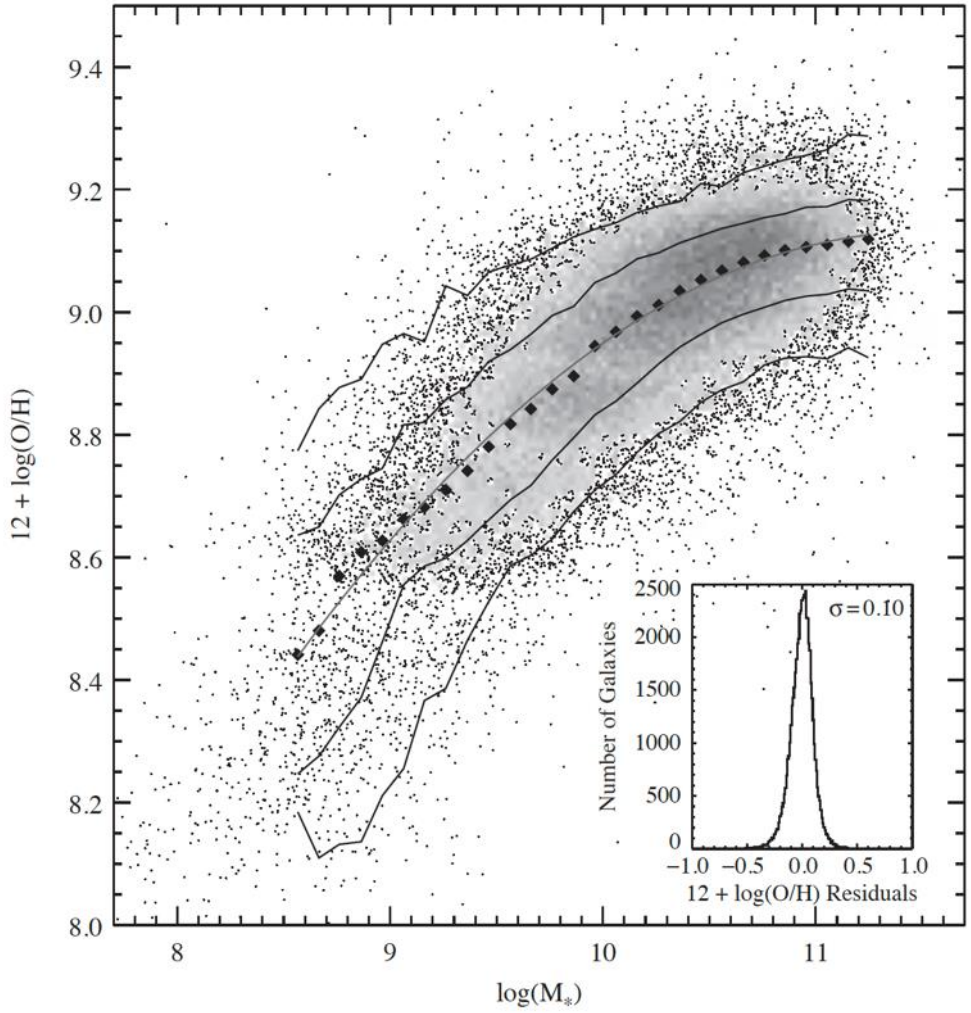

Fig. 2.28. The relation between stellar mass, in units of solar masses, and the gas-phase oxygen abundance for ~53,400 star-forming galaxies in the SDSS. For comparison, the Sun has $12 + \log[(O/H)] = 8.69$. The large black points represent the median in bins of 0.1 dex in mass. The solid lines are the contours which enclose 68% and 95% of the data. The gray line shows a polynomial fit to the data. The inset shows the residuals of the fit. [Adapted from Tremonti et al. (2004) by permission of AAS]

The Mass-Metallicity Relation

- Gallazzi+2005: *Despite the large scatter, the relation between stellar metallicity and stellar mass is similar to the correlation between gas-phase oxygen abundance and stellar mass for star-forming galaxies.*

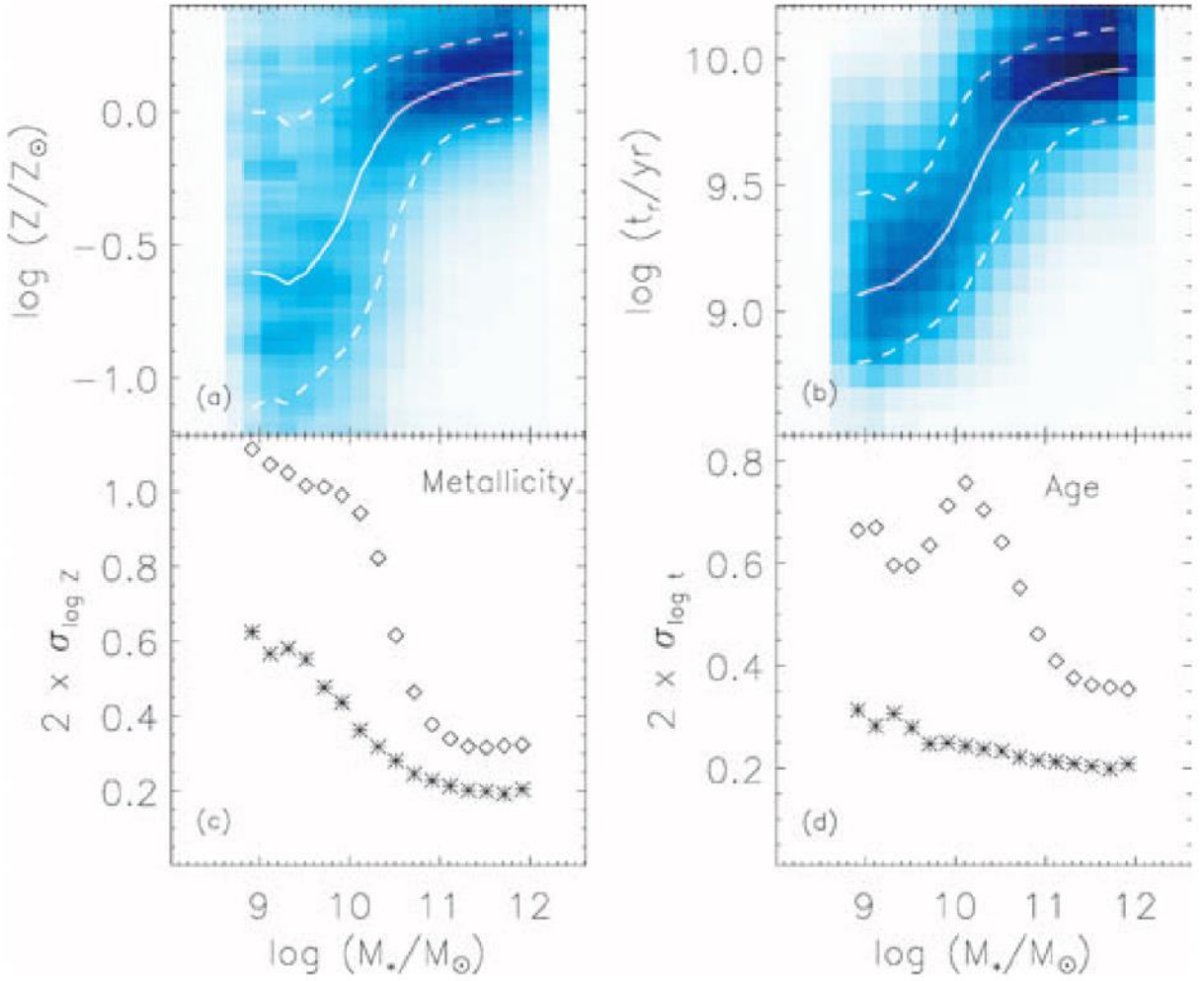

Figure 8. Panels a and b: Conditional distribution of stellar metallicity and age as a function of stellar mass for 44 254 SDSS-DR2 galaxies with median S/N per pixel greater than 20. Each distribution was obtained by co-adding the normalized 2D likelihood distributions of the desired parameter (stellar metallicity or age) and stellar mass for all the galaxies and then re-normalizing along the y-axis in bins of stellar mass (of width 0.2 dex). The solid line indicates the median of the final conditional distribution, and the dashed lines the 16th and 84th percentiles. Panels c and d: Comparison of the scatter in the metallicity and age distributions with the mean uncertainty of the metallicity and age estimates as a function of stellar mass. The diamonds show the difference in $\log(Z/Z_{\odot})$ or $\log(t_r/\mathrm{yr})$ between the 16th and 84th percentiles of the conditional distributions of panels a and b, while the stars represent the mean 68 per cent confidence range in $\log(Z/Z_{\odot})$ or $\log(t_r/\mathrm{yr})$ for the galaxies in each stellar mass bin.

The Mass-Metallicity Relation

- Gallazzi+2005: *This is confirmed by the good correlation between stellar metallicity and gas-phase oxygen abundance for galaxies with both measures. The substantial range in stellar metallicity at fixed gas-phase oxygen abundance suggests that gas ejection and/or accretion are important factors in galactic chemical evolution.*

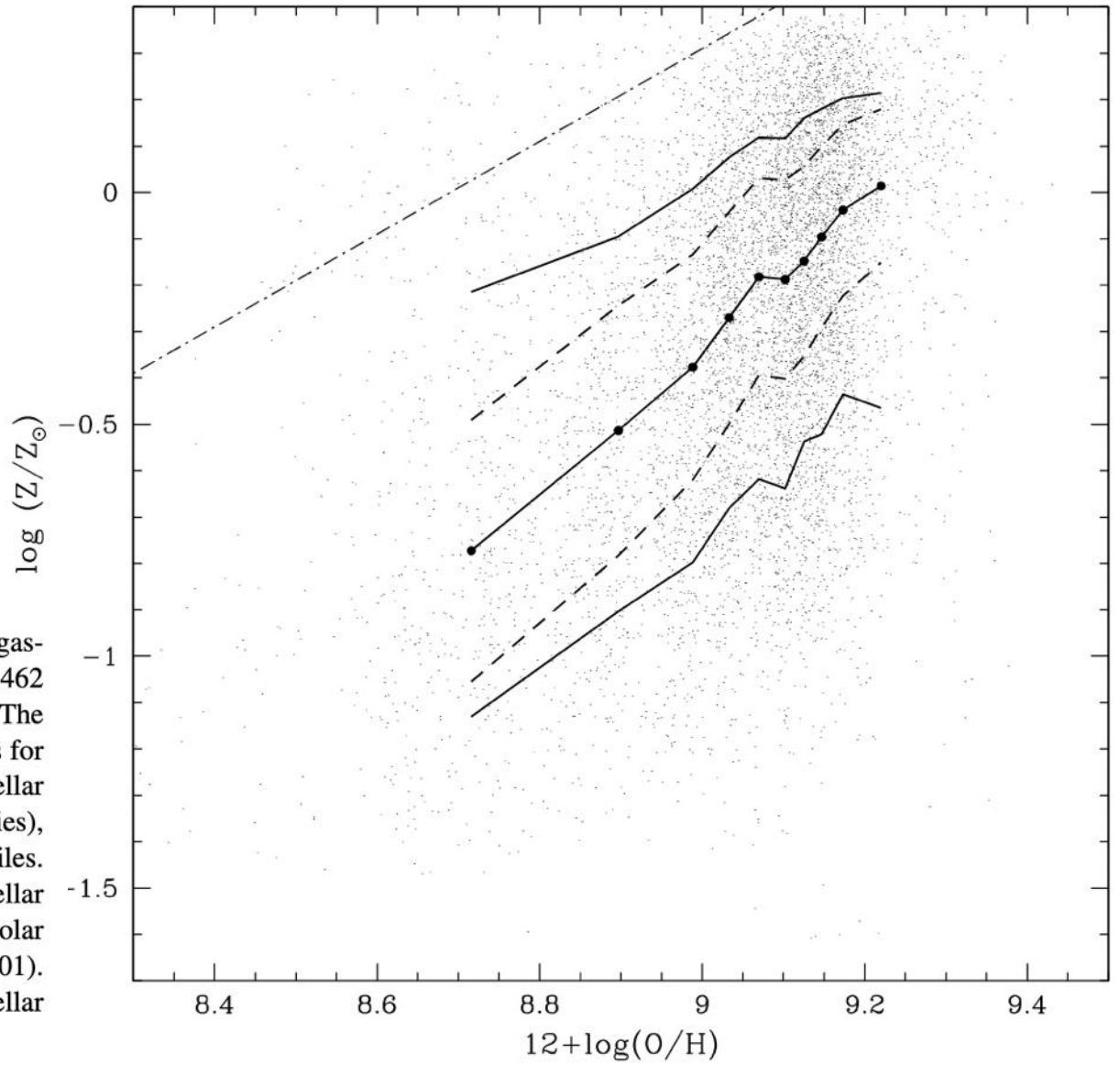

Figure 9. Stellar metallicity estimates (present work) plotted against gas-phase oxygen abundance 12 + log(O/H) (Tremonti et al. 2004) for 7462 high-S/N SDSS-DR2 galaxies for which both measures are available. The small dots show the median-likelihood estimates of the two parameters for each galaxy. The larger points (joined by a solid line) show the median stellar metallicity in bins of 12 + log(O/H) (each bin containing ∼300 galaxies), while the outer solid lines show the corresponding 16th and 84th percentiles. The dashed lines indicate the mean 68 per cent confidence range in the stellar metallicity estimates for the galaxies in each bin of 12 + log(O/H). Solar metallicity is 8.69 in these units (Allende Prieto, Lambert & Asplund 2001). The dot-dashed line represents the one-to-one relation, showing that stellar metallicity is always lower than gas-phase metallicity.

The Mass-Metallicity Relation

- Sanders+2021: no evolution of the slope of the relation from $z \sim 3.3$ to $z = 0$. But gas gets increasingly more metal rich, as expected.

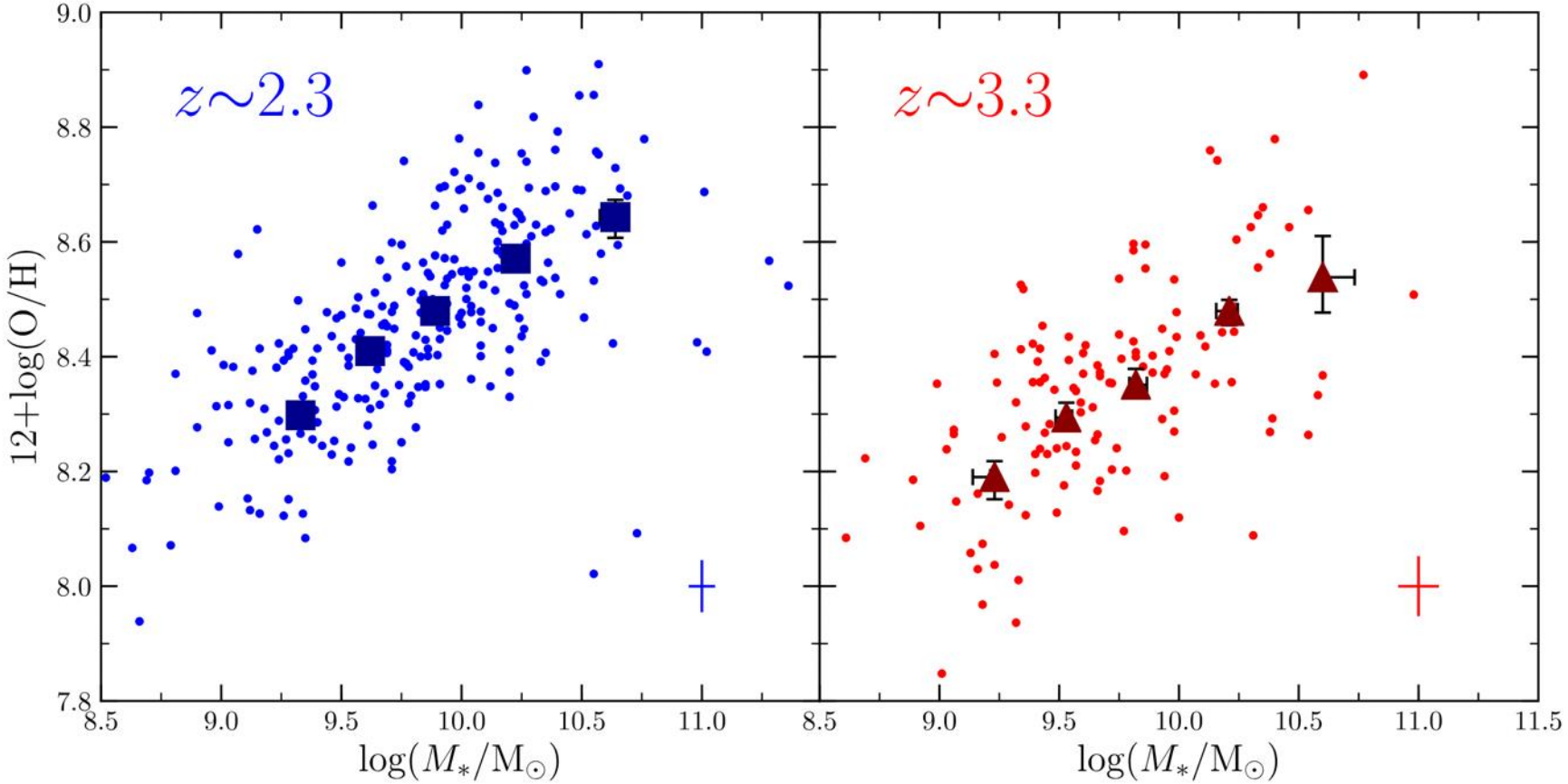

Figure 7. The MZR at $z \sim 2.3$ (left) and $z \sim 3.3$ (right) for individual galaxies (small circles) and stacked spectra in bins of M_* (large squares/triangles). The error bar in the lower-right corner of each panel displays the median uncertainty of the individual galaxies.

The Mass-Metallicity Relation

- Sanders+2021: no evolution of the slope of the relation from z ~ 3.3 to z = 0. But gas gets increasingly more metal rich, as expected.

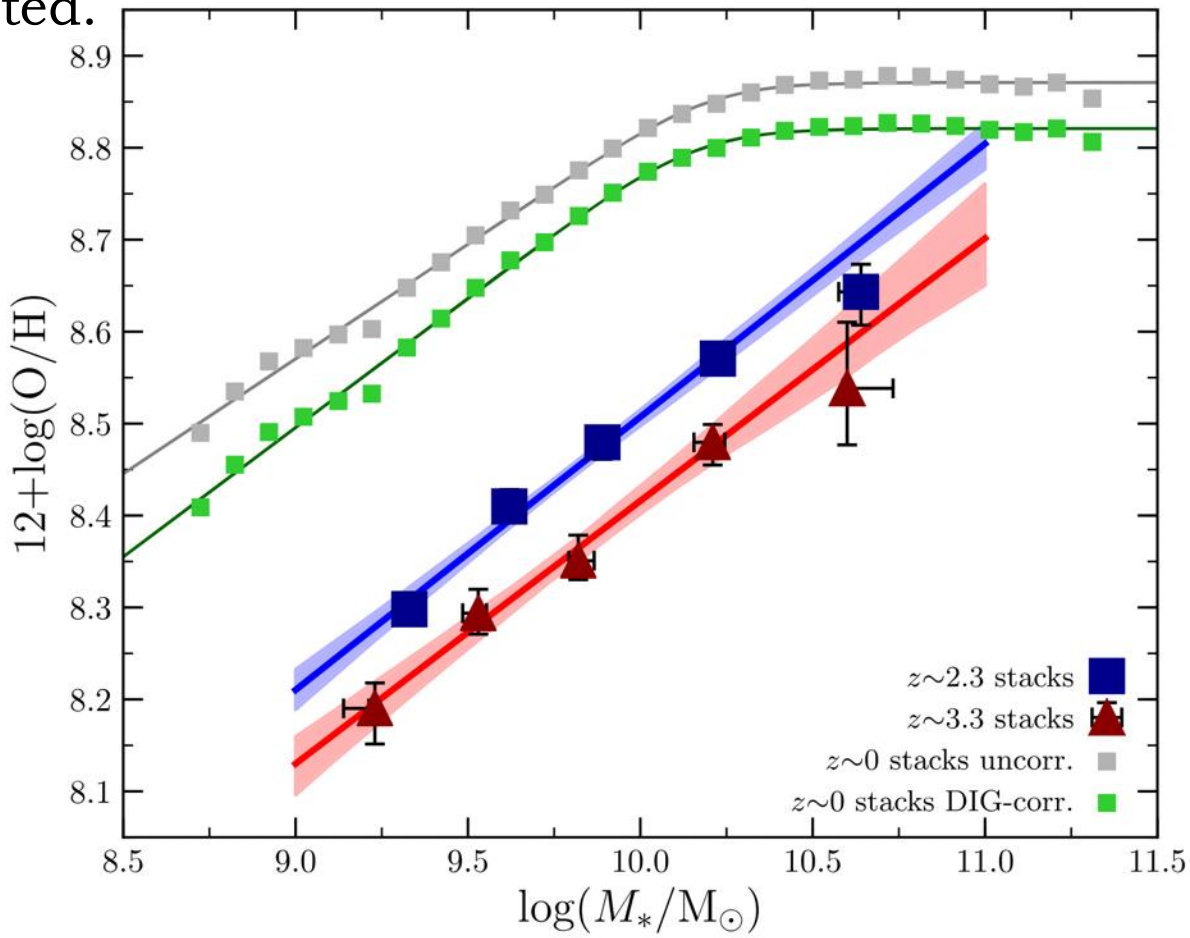

Figure 8. MZR for stacked spectra at $z \sim 0$, $z \sim 2.3$ (blue), and $z \sim 3.3$ (red). Both DIG-corrected (green) and uncorrected (gray) values are shown for the $z \sim 0$ stacks. The formal uncertainty in O/H for the $z \sim 0$ stacks is typically smaller than the size of the points. The solid lines represent the best-fit relations at each redshift, while the shaded regions display the 1σ uncertainties of the fits at $z \sim 2.3$ and $z \sim 3.3$. The $z \sim 0$ data are fit using a smoothly broken power law (Equation (8)). At $z \sim 2.3$ and $z \sim 3.3$, the stacks (excluding the highest-mass bin) are fit with a power law (Equation (7)).

SMBHs and their Scaling Relations

- Supermassive black holes are our best answer to explain AGN activity and kinematics at the centre of massive galaxies (e.g., Beifiori+2009 and references therein), including our own MW.

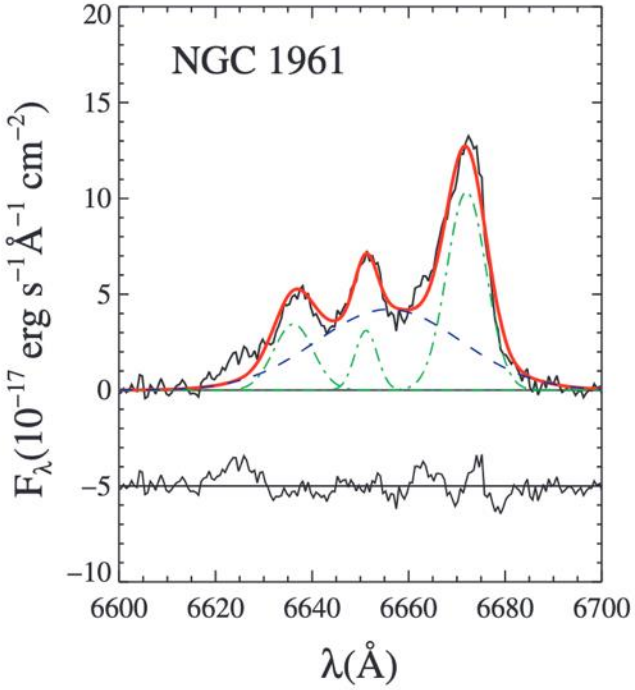

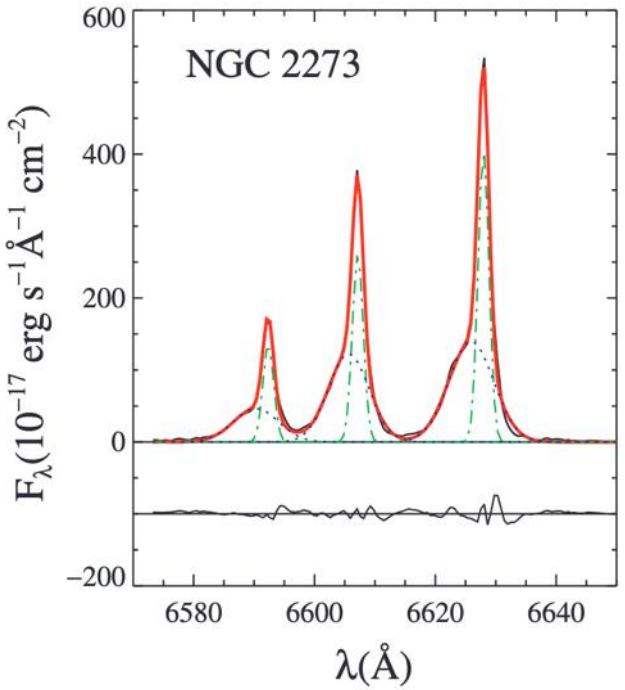

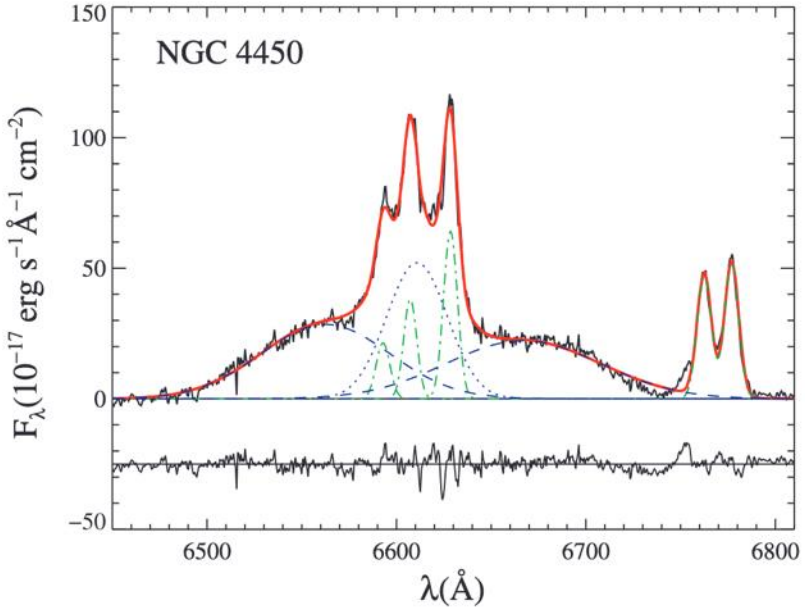

Figure 1. Few examples of continuum-subtracted central G750M spectra from our spectral atlas illustrating the various fitting strategies adopted to match Hα, [N II] λλ6548, 6583 and [S II] λλ6716, 6731 emission lines. In each panel, the red solid line show the overall line blend, whereas the green dashed-dotted lines and blue dotted or dashed lines show the adopted narrow and broad Gaussian components, respectively. Shown are also the fit residuals, offset for better visibility. For NGC 4548, the nebular emission could be matched with single Gaussian profiles. For NGC 1961, we needed to add a broad Hα component, whereas for NGC 2273 an additional broad and blue-shifted component was needed to macth the profile of all lines. For NGC 4450, we added two extremely broad Gaussian shoulders to offset from the center by several thousand kilometers per second, in addition to a more typical broad Hα component (see also Ho et al. 2000, for a match to the double-peaked profile of this LINER 1.9 nucleus).

SMBHs and their Scaling Relations

- The mass of the SMBH correlates with central velocity dispersion and the luminosity of the galaxy/bulge, suggesting that the growth of galaxies is connected to the growth of the SMBH.

Gültelkin+2009

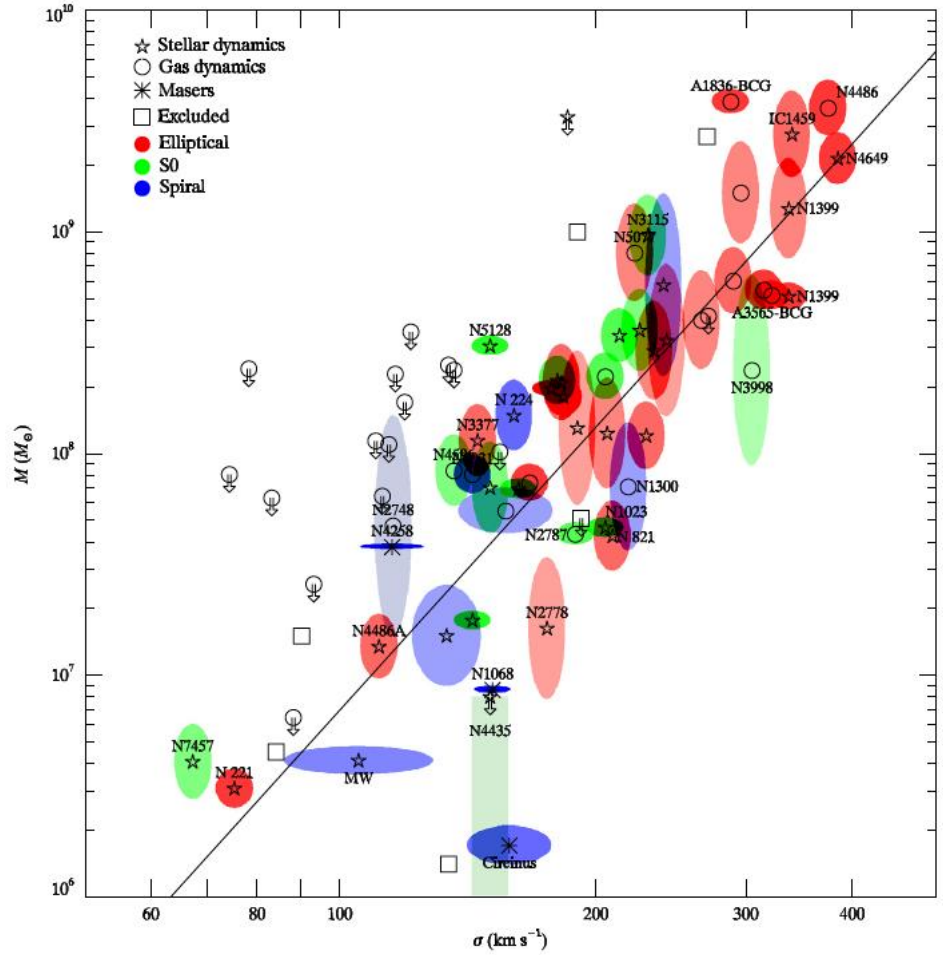

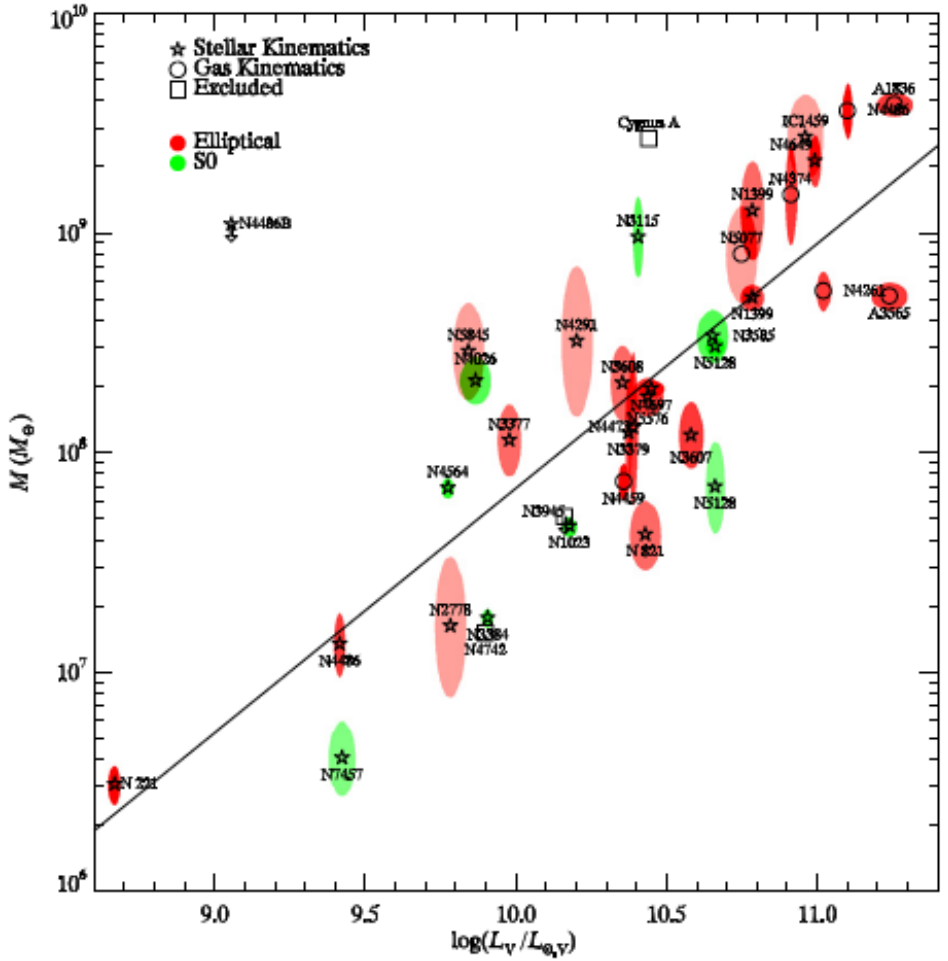

SMBHs and their Scaling Relations

- SMBHs would accrete mass until AGN feedback regulates the inflow of gas, the growth of the SMBH and the formation of stars in the bulge (or elliptical; see, e.g., Younger+2008).

- But nuclear discs – again – do not follow the same relations, pointing to a later formation process, where AGN feedback is not sufficiently strong.

Kormendy & Ho (2013)

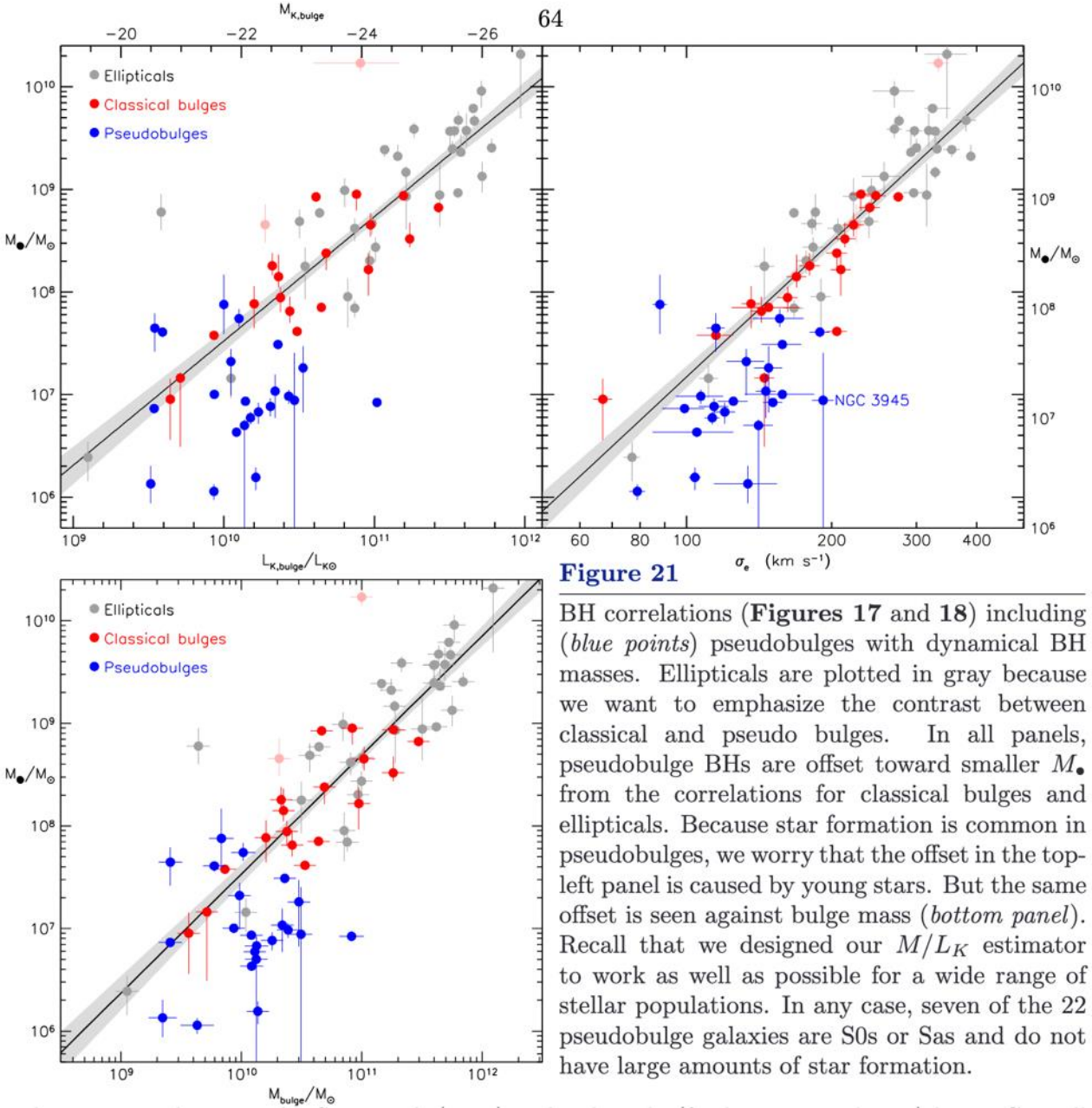

Figure 21

BH correlations (**Figures 17** and **18**) including (*blue points*) pseudobulges with dynamical BH masses. Ellipticals are plotted in gray because we want to emphasize the contrast between classical and pseudo bulges. In all panels, pseudobulge BHs are offset toward smaller $M_\bullet$ from the correlations for classical bulges and ellipticals. Because star formation is common in pseudobulges, we worry that the offset in the top-left panel is caused by young stars. But the same offset is seen against bulge mass (*bottom panel*). Recall that we designed our M/L_K estimator to work as well as possible for a wide range of stellar populations. In any case, seven of the 22 pseudobulge galaxies are S0s or Sas and do not have large amounts of star formation.

SMBHs and their Scaling Relations

- In galaxies with composite bulges (i.e., both a classical bulge and a nuclear disc), the mass of the SMBH correlates better with the classical bulge mass only (Erwin 2010; see also Kormendy+2011).

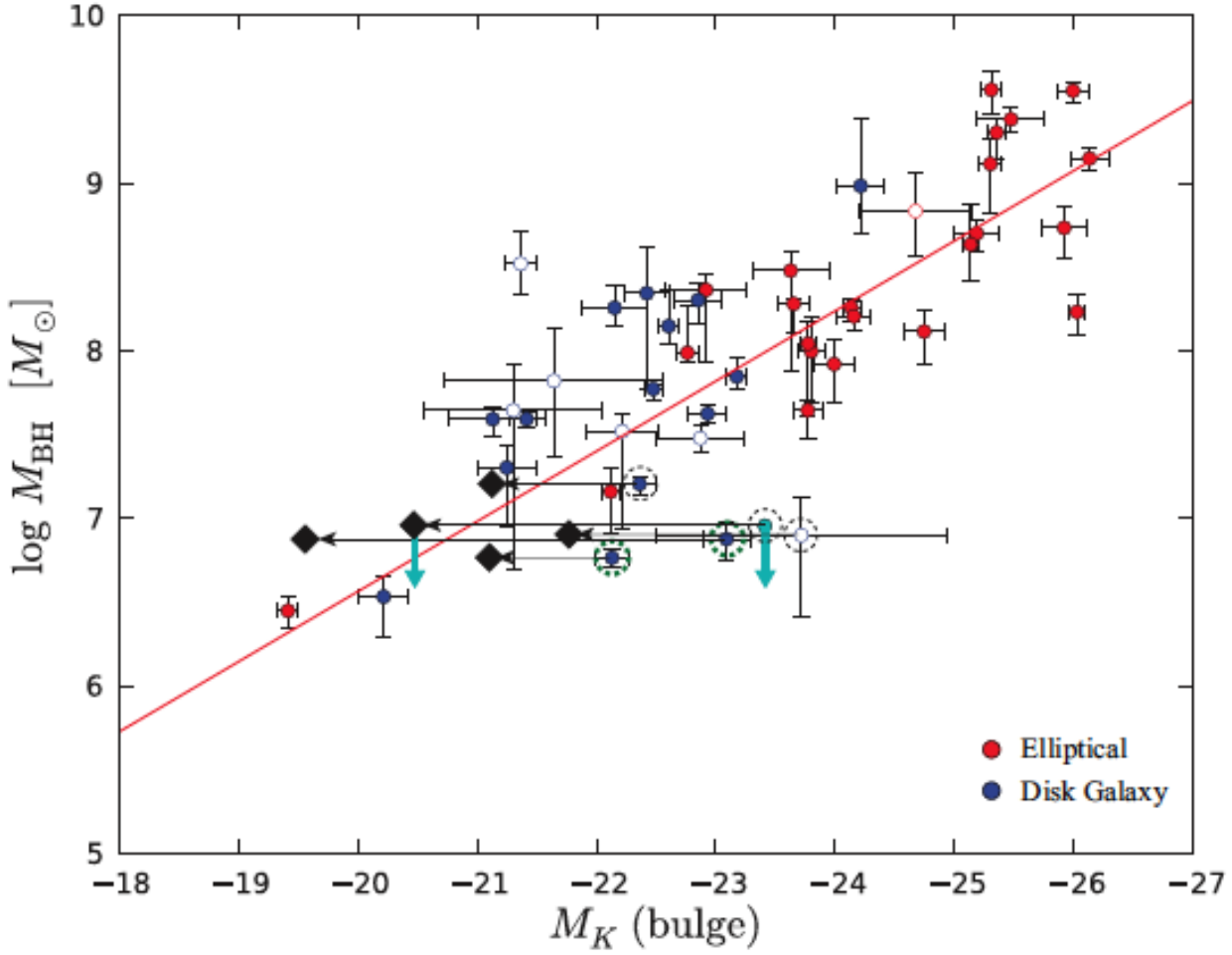

Stellar Structures in Galaxies

- Elliptical Galaxies
  - Spheroid
  - Nuclear discs: gas accretion

- Disc Galaxies
  - Disc
  - Central structures (Classical bulge, bar-built nuclear disc)
  - Bar
  - And more…

Elliptical Galaxies

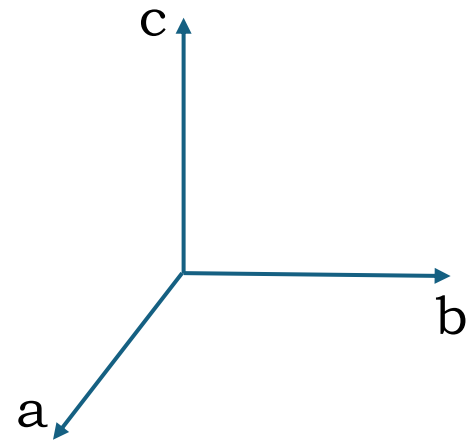

- Spheroids can be oblate, prolate or triaxial
  - Oblate: a=b>c
  - Prolate: a=b<c
  - Triaxial: a≠b≠c

- Ellipticals are often oblate, flattened by rotation, except most massive systems, which are prolate (but rotate too; Krajnović+2018)

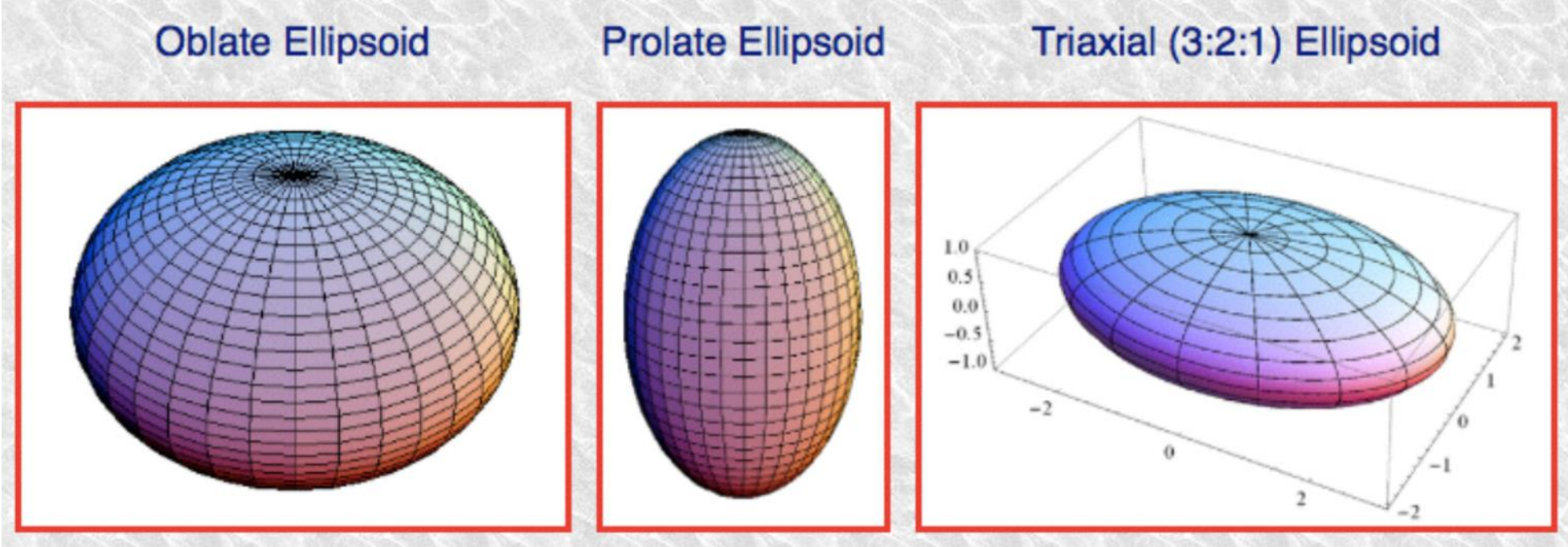

Elliptical Galaxies

- Kormendy+2009: core and power-law ellipticals

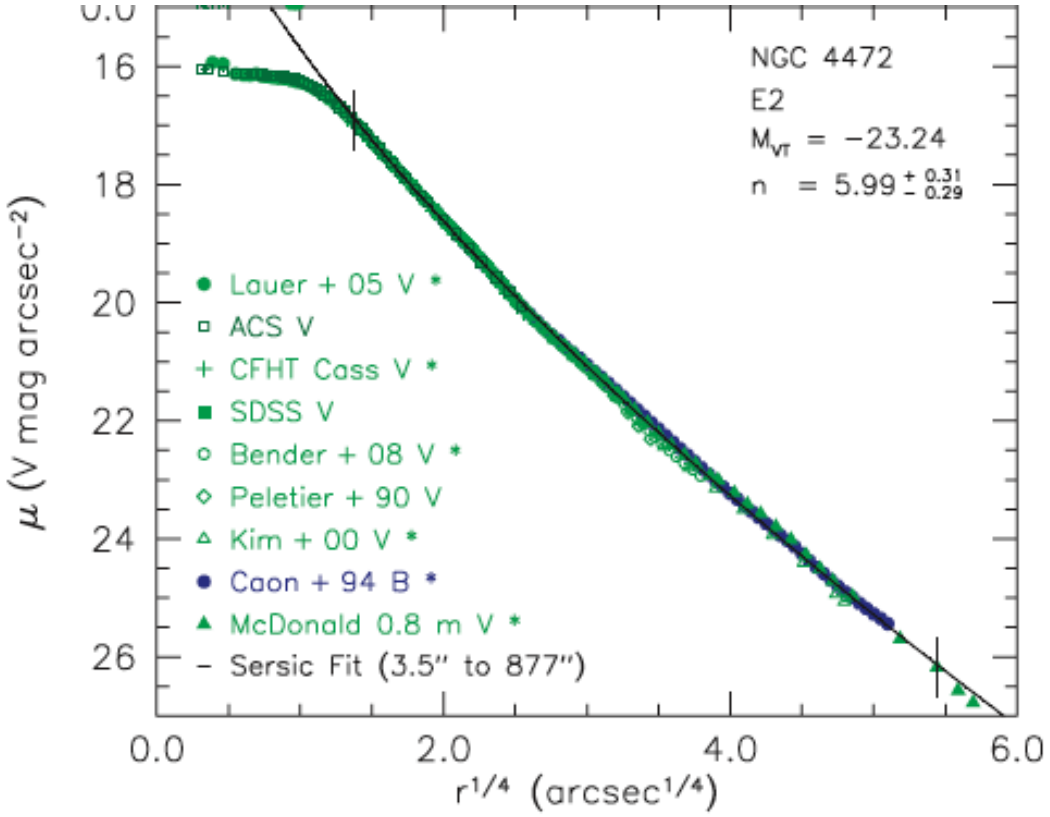

Sometimes called 'core-depleted'

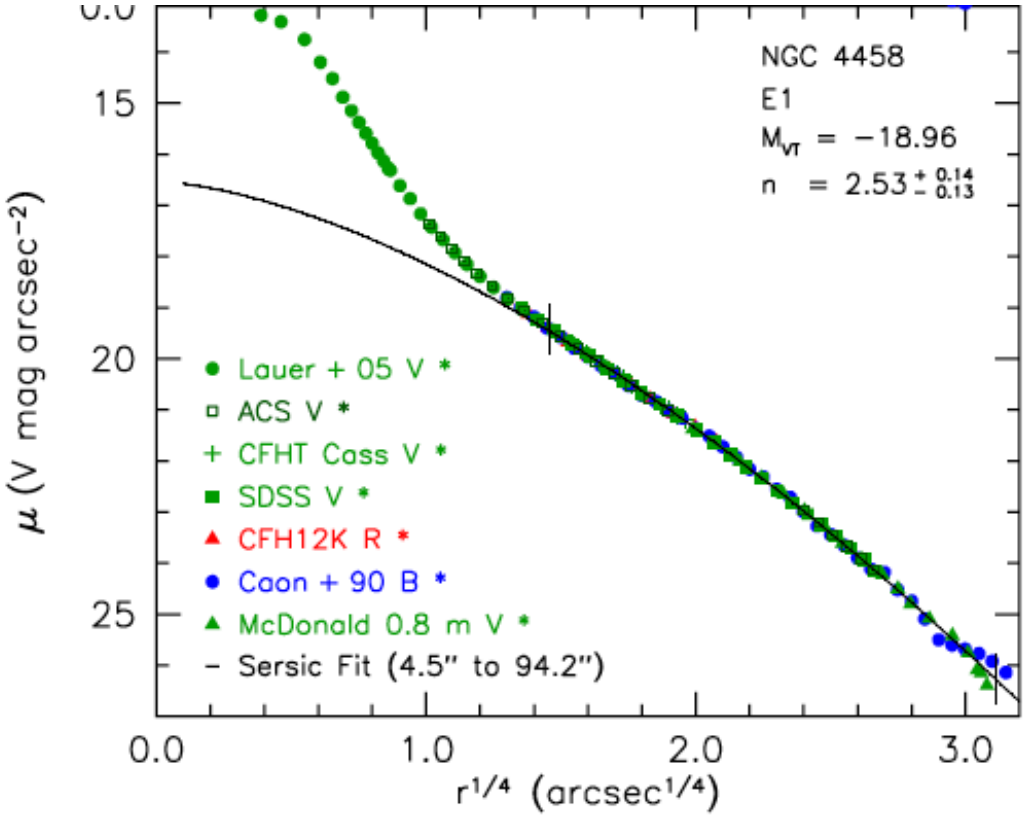

Sometimes called 'coreless' or 'extra-light'

Elliptical Galaxies

- Kormendy+2009: core-depleted vs. extra-light (coreless; power-law)

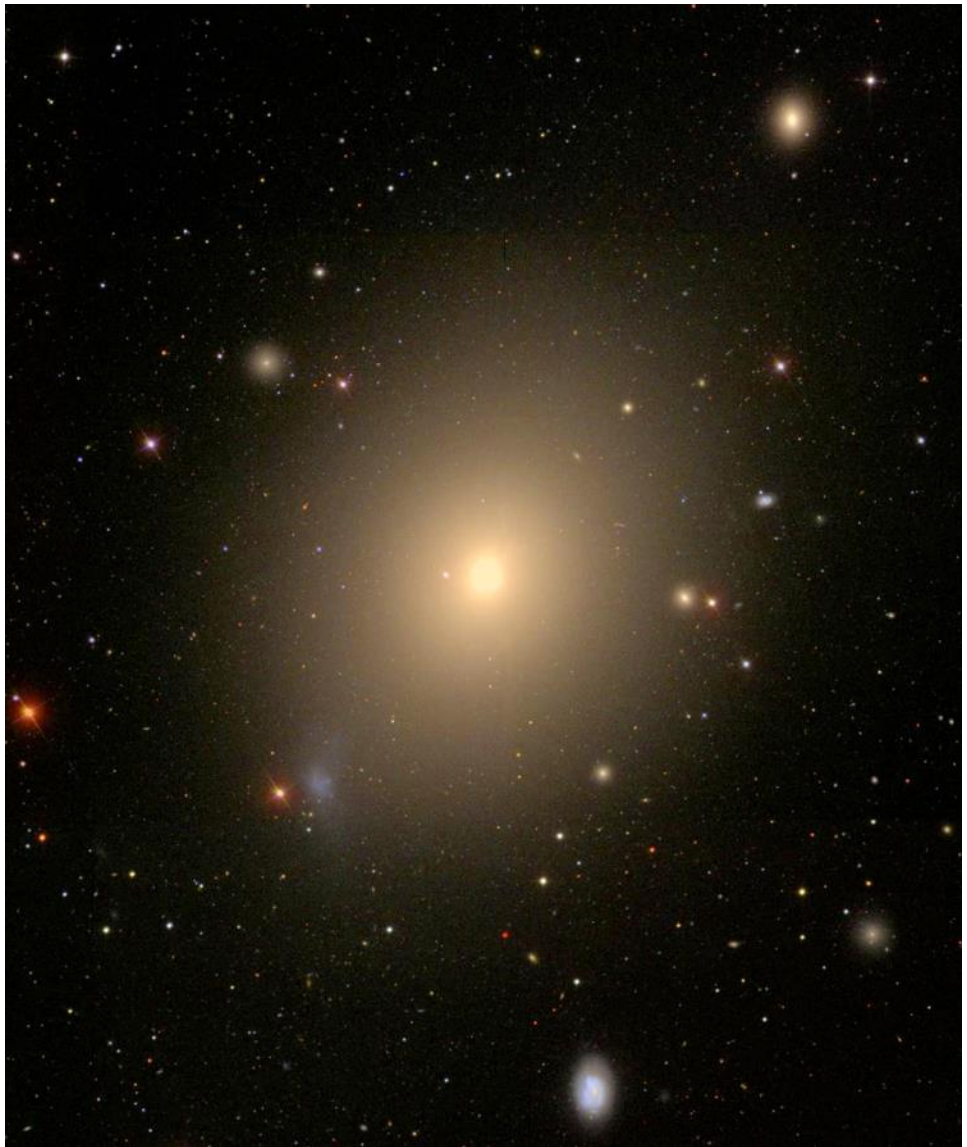

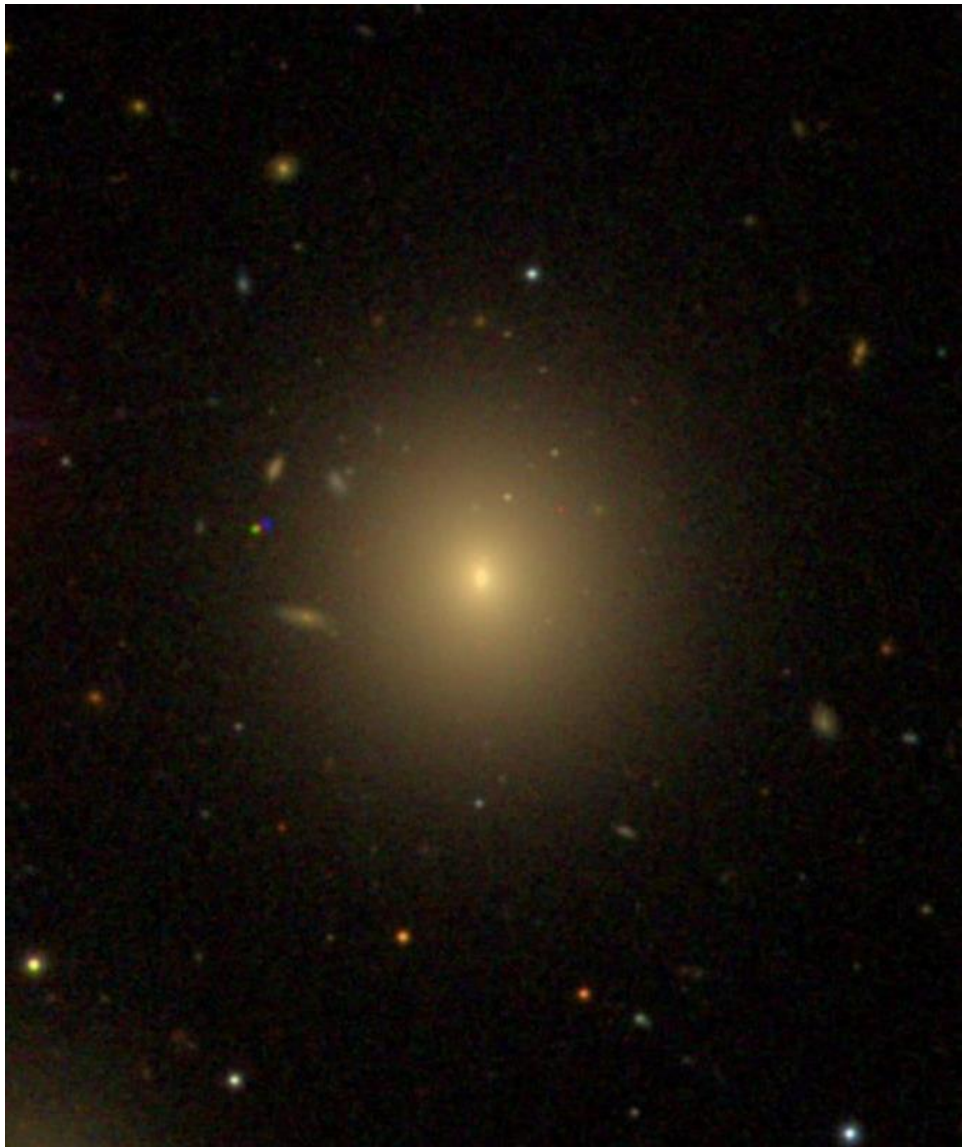

Elliptical Galaxies

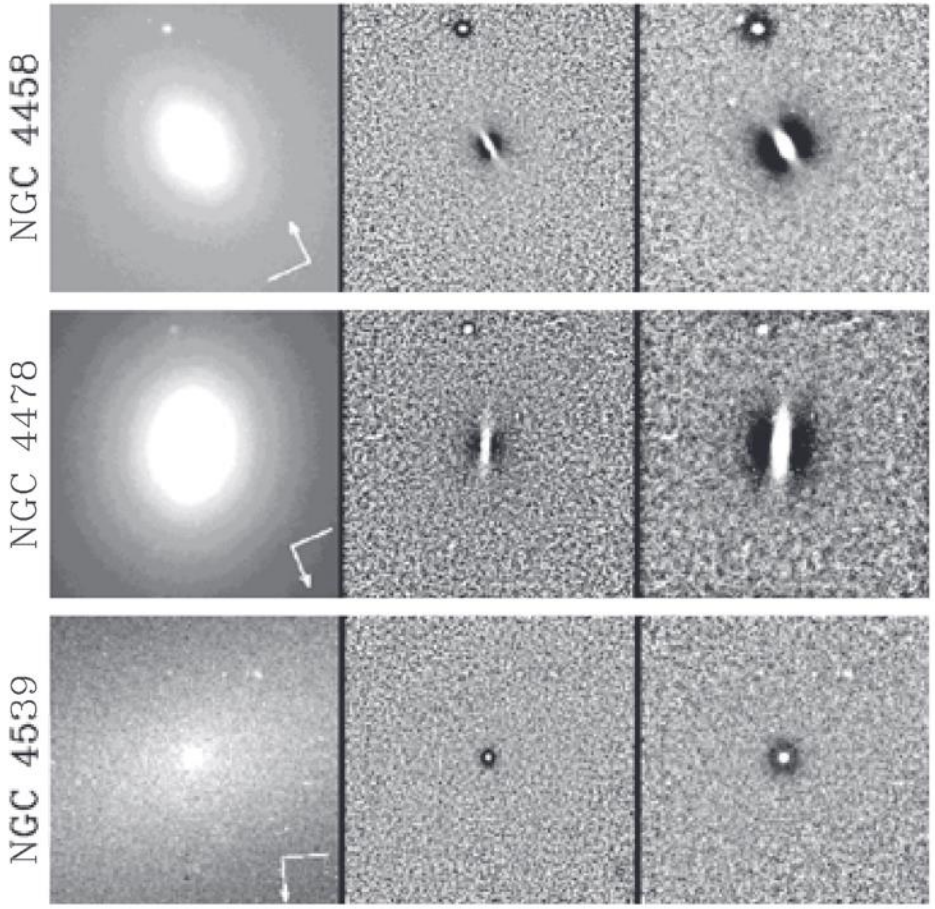

Figure 1. Left panels: WFPC2/F814W images of NGC 4458 and 4478 (for which nuclear discs were detected) and NGC 4539 (for which a nuclear disc was not detected). The size of the plotted region is 19.3×19.3 arcsec^2. The orientation is specified by the arrow indicating north and the segment indicating east in the lower-right corner of each panel. Middle and right panels: unsharp masking of the WFPC2/F814W images obtained with $\sigma =$ 2 and 6 pixels, respectively. Sizes and orientations are as in the left-hand panels.

- HST was transformational in revealing the inner structures in galaxies, due to the tenfold increase in spatial resolution.
- Unsharp masking
  1. Smooth image with a kernel
  2. Subtract from original image
- Morelli+2004: nuclear discs in elliptical galaxies (many other examples)
- Sometimes they are called Kinematically Decoupled Cores

Elliptical Galaxies

- Emsellem+2011: Atlas3D census of early-type galaxies (the power of integral field spectroscopy)

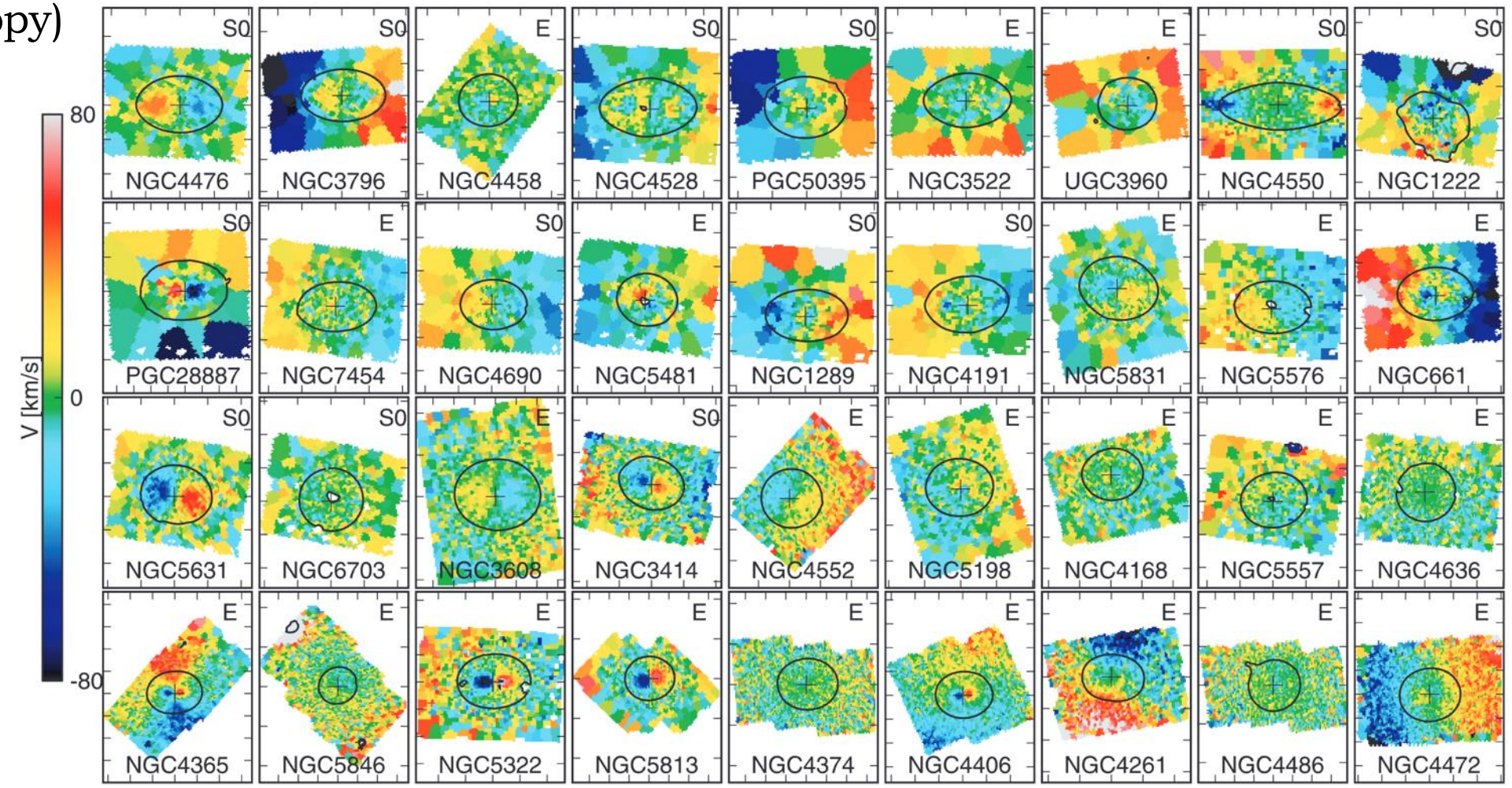

Figure A1. Stellar velocity fields for the 36 early-type SRs in the ATLAS^{3D} sample. We used the outer photometric axis to align all galaxies horizontally. Colour cuts have been adapted to each individual map. The solid black contour corresponds to a representative isophote and the centre of the galaxy is indicated by a cross. From the top to bottom (left-hand to right-hand side) the order follows the (increasing) dynamical mass values. The names of the galaxies and their Hubble types (E or S0) are also indicated. The colour cuts have been set up to ± 80 (km s^{-1}) for all maps.

Elliptical Galaxies

- Emsellem+2011: Atlas3D census of early-type galaxies

- These nuclear discs are often counter-rotating, indicating an external origin, via gas accretion

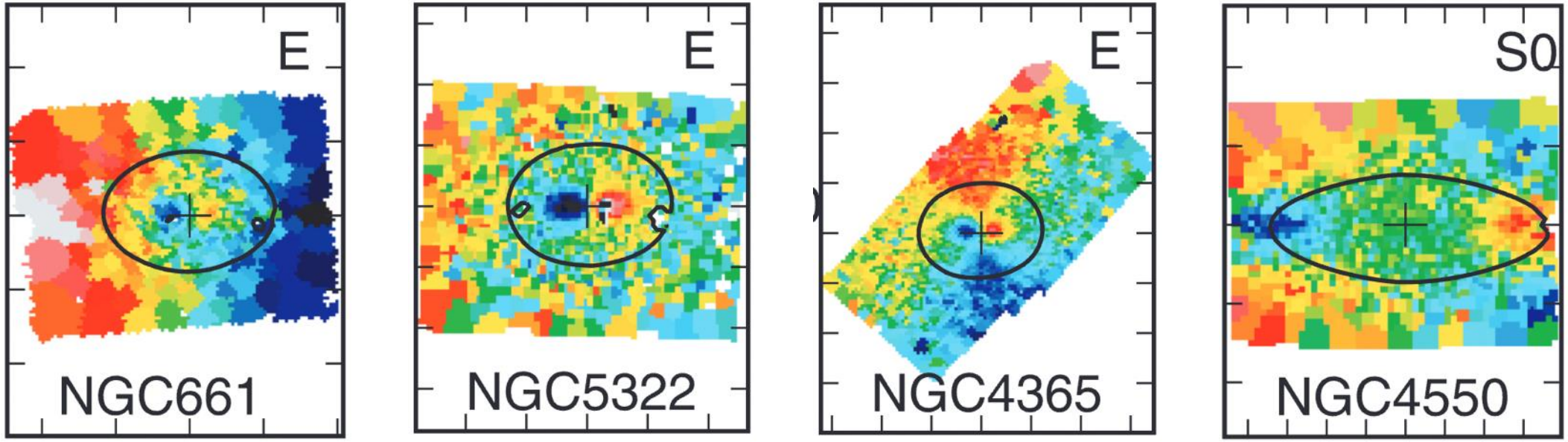

Elliptical Galaxies

- Shells and other signs of unvirialised mergers (Kormendy+2009)

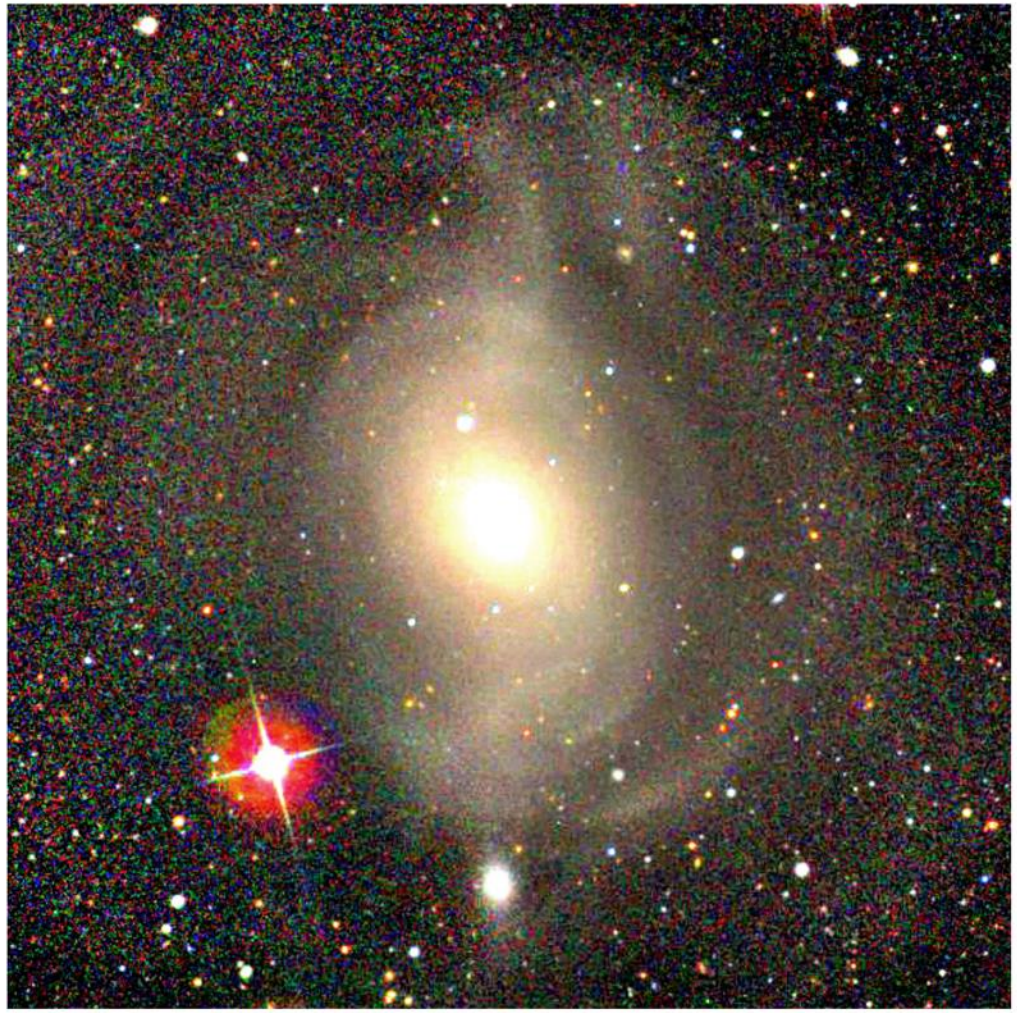

Figure 9. Contrast-enhanced gri-band color image of NGC 4382 from the SDSS online site http://www.wikisky.org. Strong fine-structure features are signs that the galaxy has not finished relaxing after a recent merger.

Elliptical Galaxies

- Different image processing leads to similar results
- Tidal debris contributes to 3-10% of the total mass only (minor merging?)
- Galaxies still follow same scaling relations as unperturbed galaxies

Kim+2011

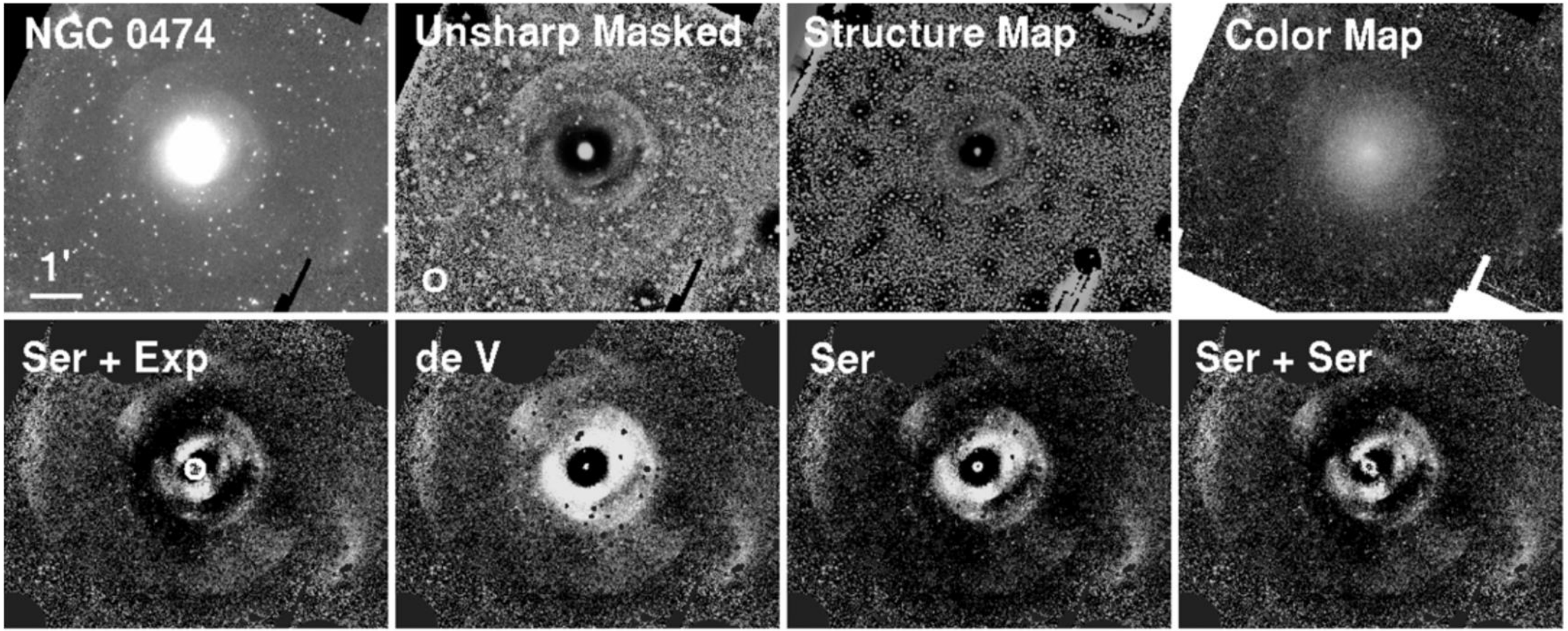

Elliptical Galaxies

Light (or mass) radial profiles can be well described by the Sérsic (1968) function:

$$I(R) = I_e \exp\left\{-\beta_n \left[\left(\frac{R}{R_e}\right)^{1/n} - 1\right]\right\}$$

or, for surface brightness (mag arcsec^{-2}):

$$\mu(R) = \mu_e + 1.086\beta_n \left[\left(\frac{R}{R_e}\right)^{1/n} - 1\right]$$

where $\beta_n = 2n - 0.324$ for n $\gtrsim 1$ following the definition of R_e.

- Gadotti (2009): $2 \lesssim n \lesssim 6$

Elliptical Galaxies

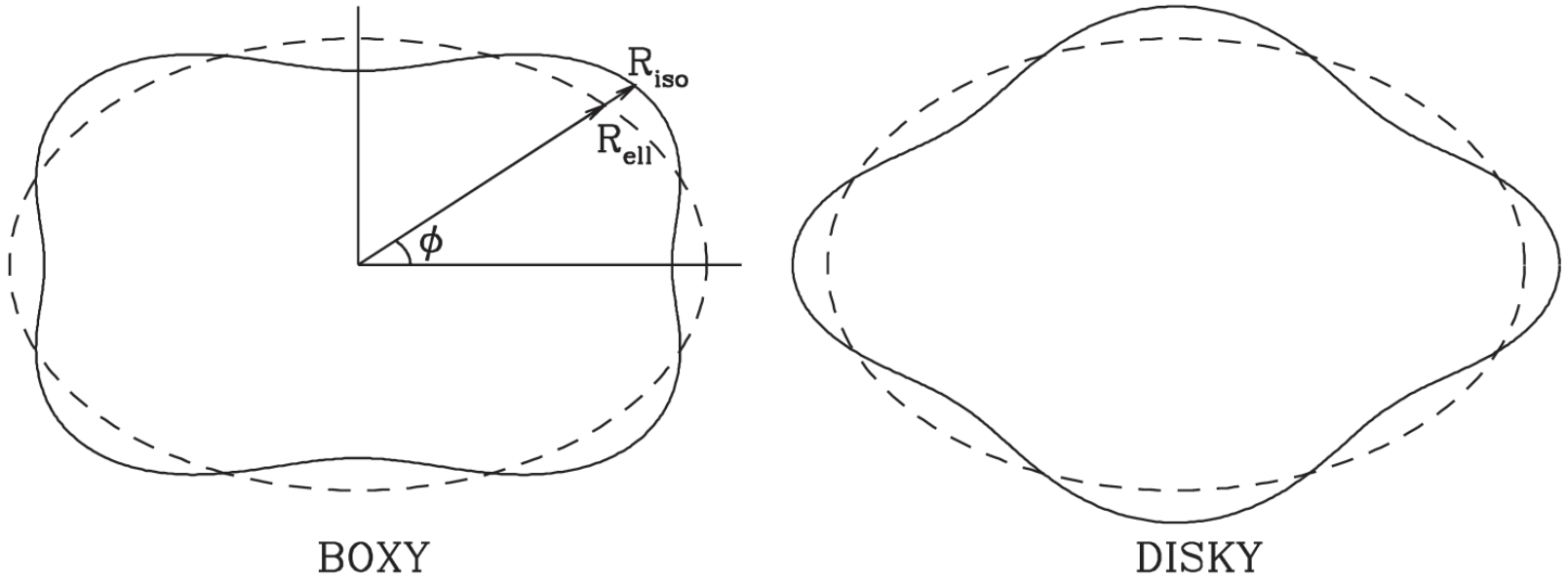

Mo+2010

Fig. 2.15. An illustration of boxy and disky isophotes (solid curves). The dashed curves are the corresponding best-fit ellipses.

Isophotal shapes: "Boxy ellipticals are usually bright, rotate slowly, and show stronger than average radio and X-ray emission, while disky ellipticals are fainter, have significant rotation and show little or no radio and X-ray emission (e.g. Bender et al., 1989; Pasquali et al., 2007). In addition, the diskiness is correlated with the nuclear properties as well; disky ellipticals typically have steep cusps, while boxy ellipticals mainly harbor central cores (e.g. Jaffe et al., 1994; Faber et al., 1997)."

Disc Galaxies

- Include spirals and lenticulars (S0s)

- Richer structure

1. disc (thin/thick)
2. classical bulge
3. bar+**box/peanut**+**barlens**
4. spiral arms
5. **nuclear disc**
6. **nuclear bar**
7. **nuclear spiral arms**
8. **lens(es)**
9. **nuclear ring**
10. inner ring
11. outer ring
12. stellar halo
13. nuclear star cluster

- In **red**: just part of the bar (historically associated to 'pseudo bulges')

- In **blue**: can be associated to nuclear discs (historically associated to 'pseudo bulges')

Thin/Thick Disc

Light (or mass) radial profiles can be well described by the Sérsic function with $n = 1$, which is an exponential function (incidentally, $n = 0.5$ corresponds to a Gaussian):

$$I(R) = I_0 \exp\left(-\frac{R}{R_d}\right)$$

with $R_d = h \simeq \frac{1}{1.67} R_e$ and $I_0 = \frac{L}{2\pi R_d^2}$. Discs often show breaks in the profiles, though (e.g., Erwin+2008:

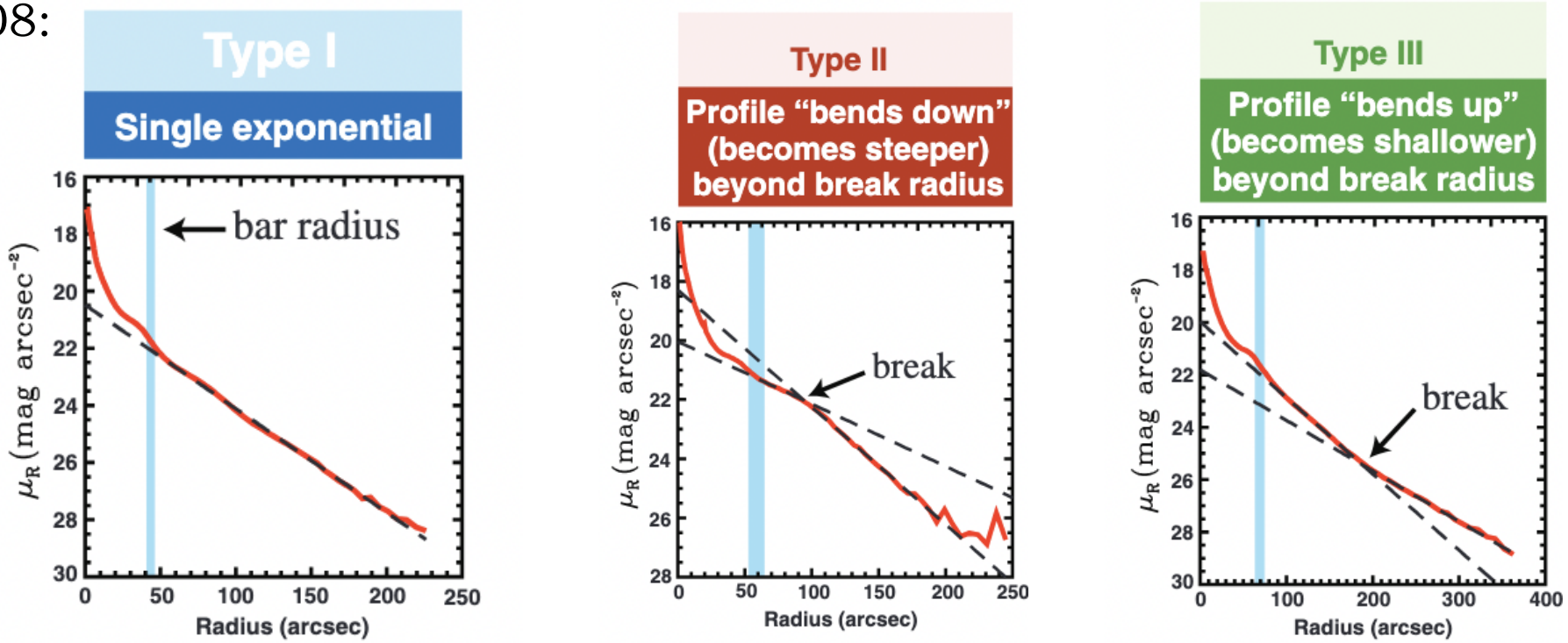

Thin/Thick Disc

Erwin+2008

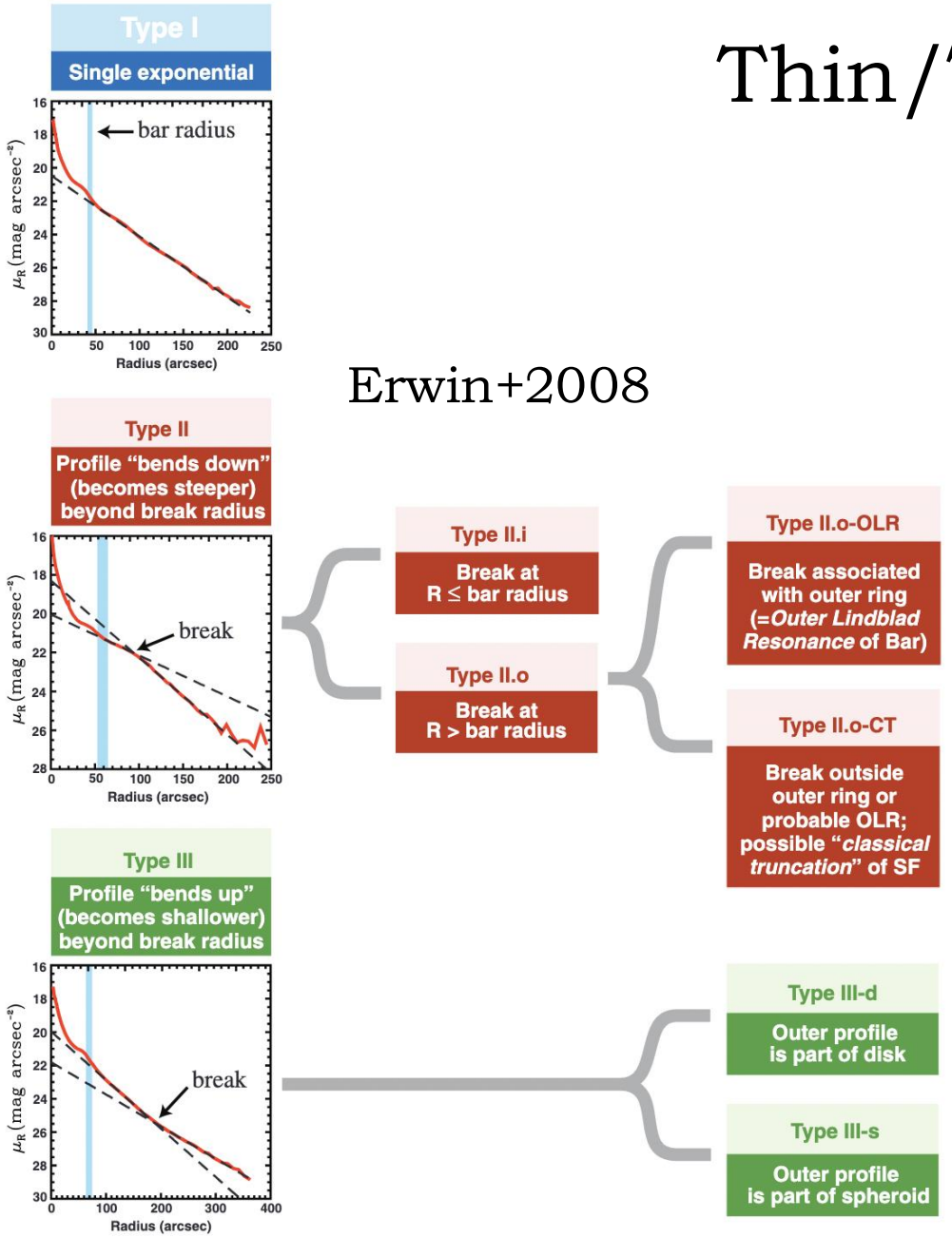

Figure 5. Overview of our scheme for classifying surface-brightness profiles. The basic level recognizes types I, II, and III, based on their overall shape (ignoring the central excess associated with the bar/bulge). Type II profiles can be further subdivided into II.i and II.o, based on where the break in the profile is located. Finally, type II.o and type III profiles can be further classified based on the probable nature of the break (type II.o-OLR versus type II.o-CT) or the disk versus spheroid nature of the outer profile (type III-d versus type III-s). See the text and subsequent figures for more details.

- Type II breaks may be associated to bars or truncation of star formation
- Type III breaks may be associated to the stellar halo
- But these associations are still very tentative

Thin/Thick Disc

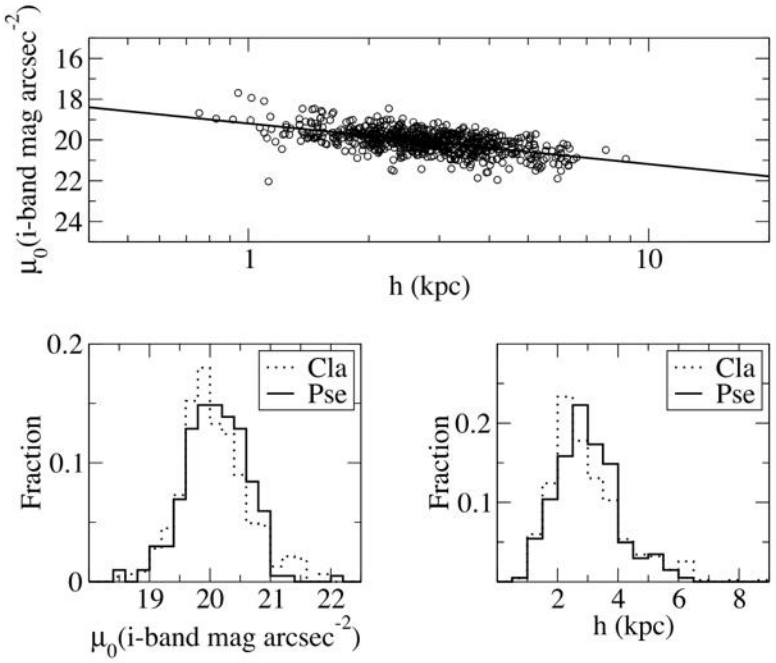

Figure 18. Scaling relation between disc scalelength and central surface brightness. The histograms at the bottom show that galaxies with pseudo-bulges have more extended discs, with fainter central surface brightness, on average, as compared with galaxies hosting classical bulges, albeit with significant overlap. A Kolmogorov–Smirnov test rejects the null hypothesis of no difference between such distributions at a 92 per cent confidence level.

The central surface brightness increases with mass but saturates at large masses.

For galaxies with $M_\star \geq 10^{10}\mathrm{M}_\odot$ (Gadotti 2009)

For a wider range of stellar masses (Yoachim & Dalcanton 2006)

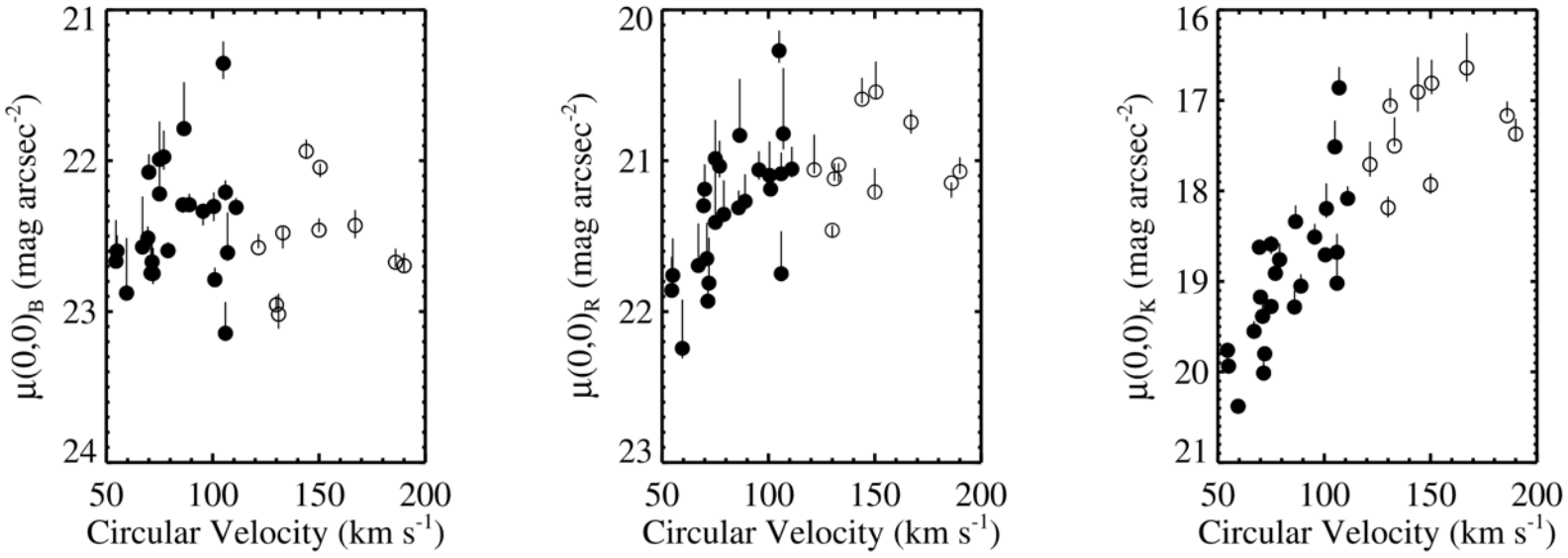

FIG. 6.—Edge-on peak surface brightnesses for the single-disk fits. Open symbols are used for galaxies with prominent dust lanes. Points have not been corrected for internal extinction.

Thin/Thick Disc

- Because the surface brightness in the vertical direction is to a first approximation independent of the distance from the centre, the disc 3D luminosity density is usually modelled as (see Mo+2010, Sect. 2.3.3):

$$\nu(R,z) = \nu_0 \exp\left(-\frac{R}{R_d}\right) f_n(z)$$

with:

$$f_n(z) = \mathrm{sech}^{2/n}\left(\frac{n|z|}{2z_d}\right)$$

(n controls the shape of the profile near $z = 0$ and z_d is the scale height). Typically, $z_d/R_d \sim 0.1$.

Thin/Thick Disc

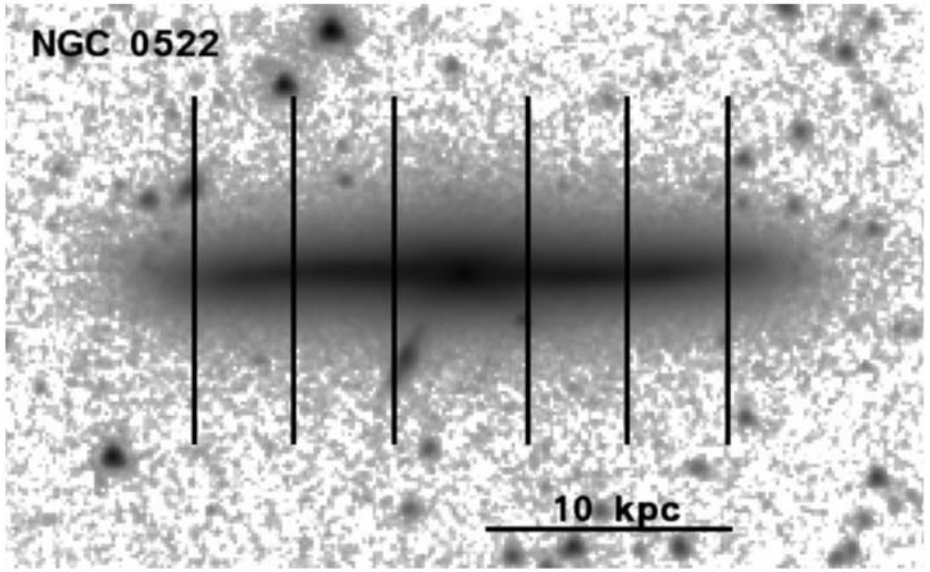

Figure 2. 3.6 μm-band S^{4}G image of NGC 0522, one of the galaxies in our sample. NGC 0522 is similar to the Milky Way both in morphological type and in size. The vertical lines indicate the limits of the bins for which luminosity profiles have been produced, from left to right, at galactocentric distances of $-0.8\,r_{25} < R < -0.5\,r_{25}$, $-0.5\,r_{25} < R < -0.2\,r_{25}$, $-0.2\,r_{25} < R < 0.2\,r_{25}$, $0.2\,r_{25} < R < 0.5\,r_{25}$, and $0.5\,r_{25} < R < 0.8\,r_{25}$. In order to avoid the influence of the bulge we have ignored the central ($-0.2\,r_{25} < R < 0.2\,r_{25}$) bin throughout the paper, in all galaxies.

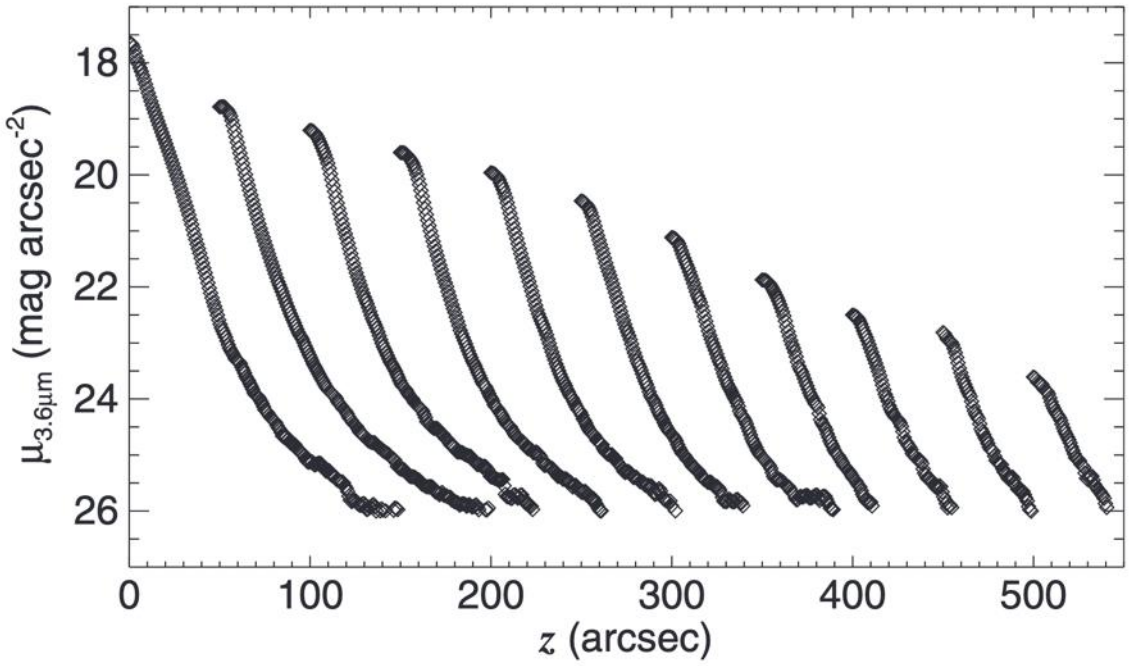

Figure 1. Reproduction of Figure 12 in van der Kruit & Searle (1981) using S^{4}G data. The plot displays luminosity profiles of NGC 4565, going from a galactocentric distance $R = 0$ outward using a radial bin width of 46″. The data of the four quadrants have been averaged in order to produce the plot.

Thick discs are often seen in edge-on disc galaxies (e.g., Comerón+2011), often kinematically hotter and with older and more metal-poor stellar populations, as compared to the thin disc.

Thin/Thick Disc

Comerón+2011

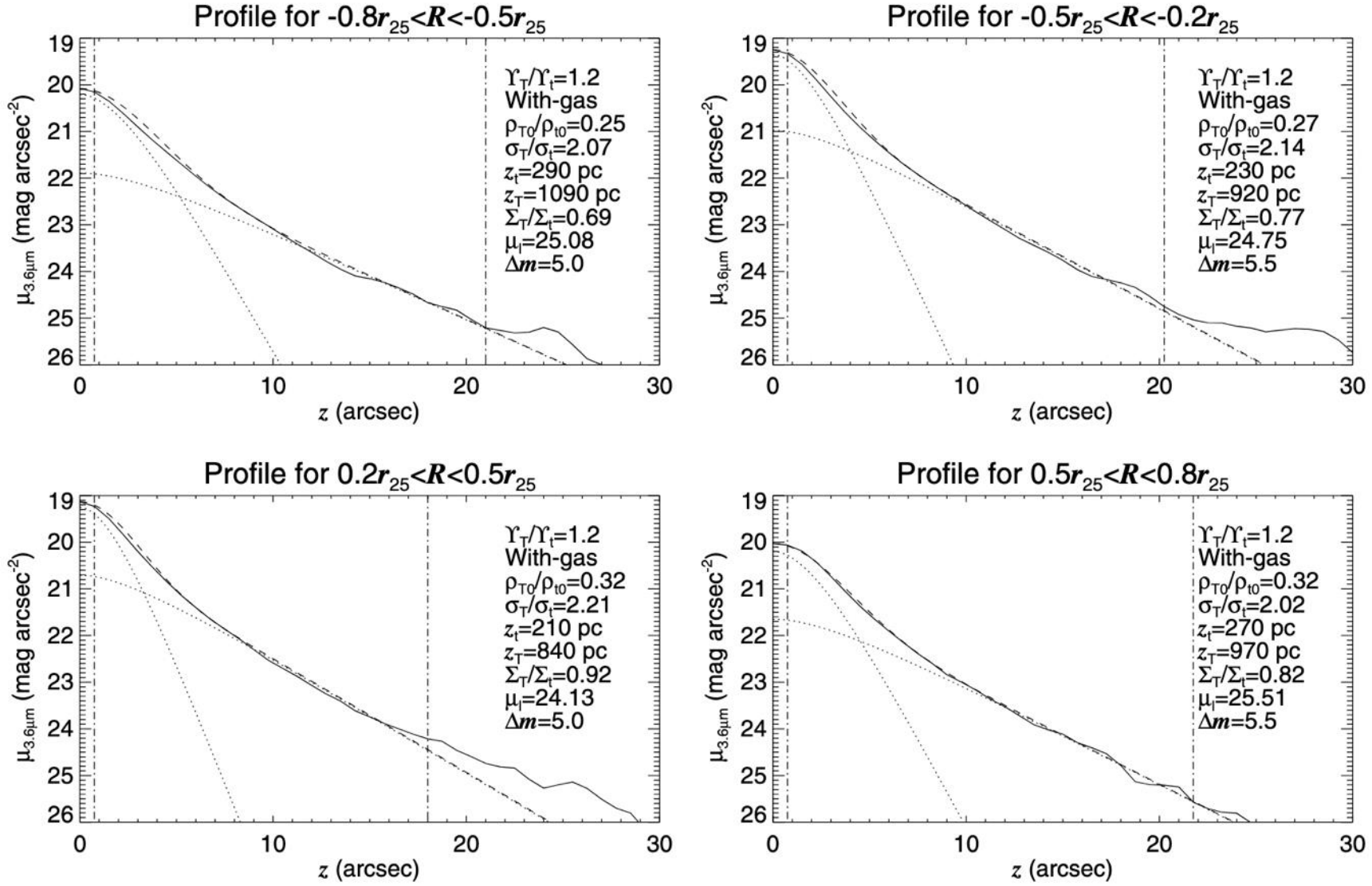

Figure 5. Fits to the surface brightness profiles of NGC 0522 for the four fitted bins for the case $\Upsilon_T/\Upsilon_t = 1.2$ and with-gas. The solid curve represents the observed luminosity profile, and the dashed curve the best fit. The dotted curves indicate the contributions of the thin and thick disks. The dash-dotted vertical lines indicate the limits of the range in vertical distance above the midplane used for the fit.

Thin/Thick Disc

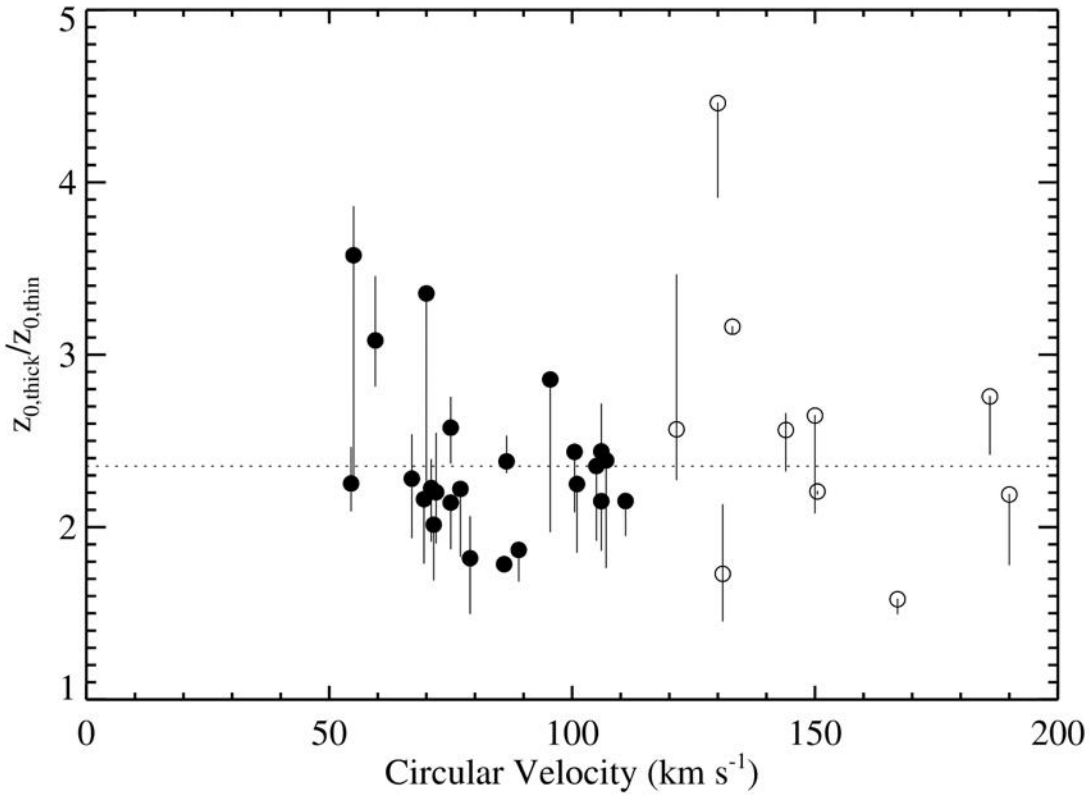

FIG. 10.—Ratios of the scale heights for the thick and thin disks. Error bars represent the full range of ratios to which different models converged. Galaxies with prominent dust lanes are plotted as open circles. The dotted line shows the median value of $z_{0,thick}/z_{0,thin} = 2.35$.

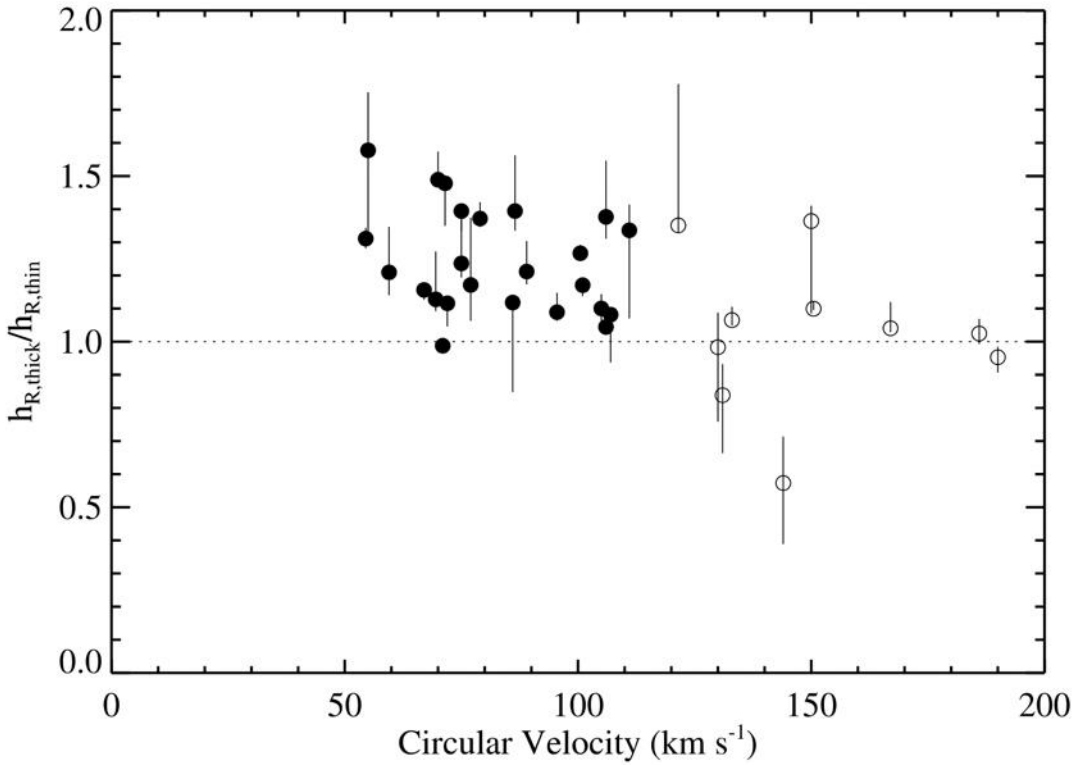

FIG. 14.—Ratios of the scale lengths for the thick and thin disks. The horizontal line indicates where the thin and thick disk components have equal scale lengths. Error bars represent the full range of ratios to which different models converged and are indicators of our systematic errors. Open symbols are used for galaxies with prominent dust lanes.

Yoachim & Dalcanton (2006): thick discs have scale heights 2-3 times larger than thin discs, and scale lengths systematically larger.

Thin/Thick Disc

- Thick disc formation scenarios:

1. Formed thick at high redshifts

2. Thicken from the thin disc

    1. Naturally due to dynamical processes
    2. Due to interactions with companion galaxies

3. All of the above?

This is a topic of active current research.

Classical Bulge

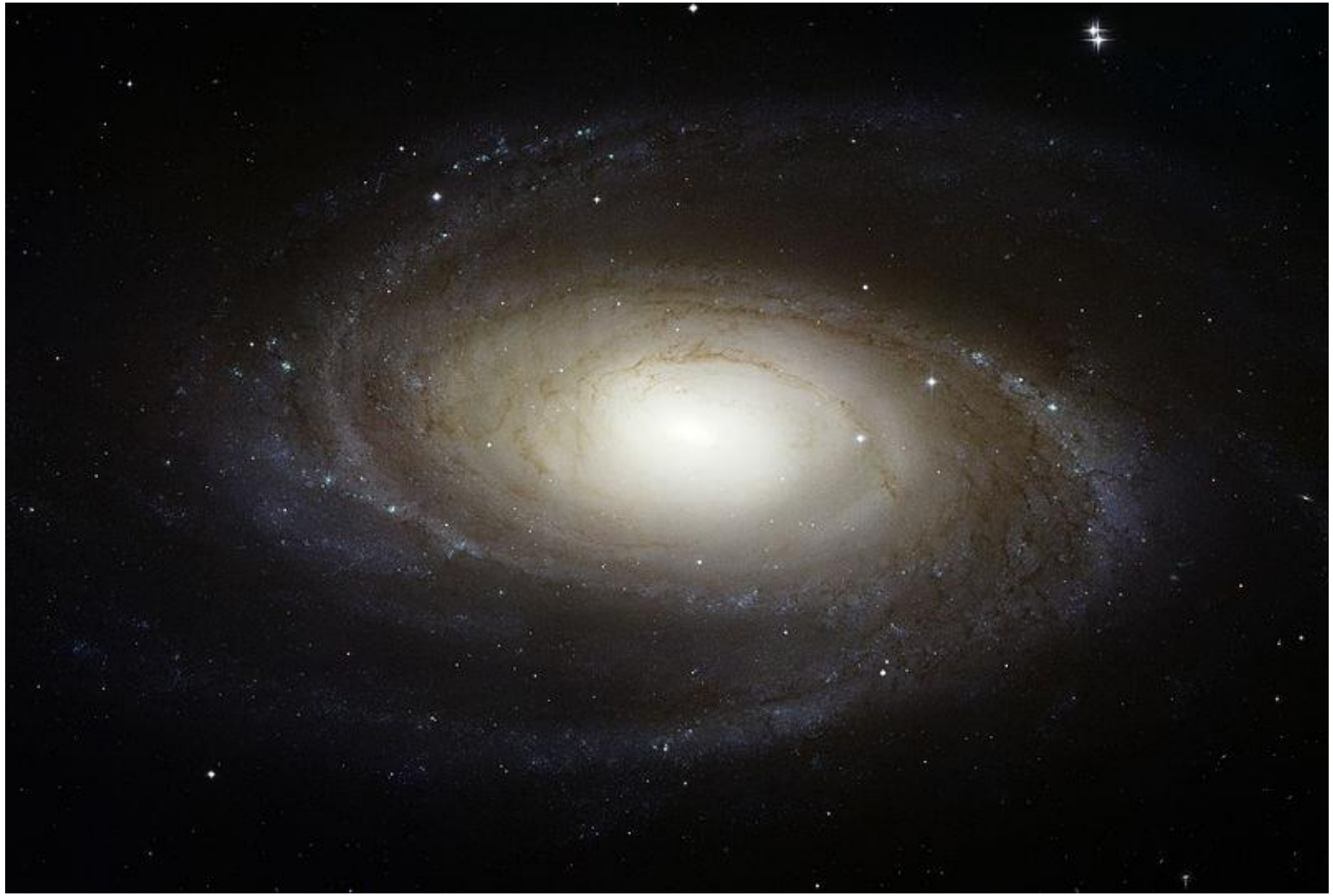

Classical Bulge

- Stick out of disc plane, i.e., not as flat as the disc (when seen at sufficient inclinations)
- More or less spheroidal (hard to see at low inclinations)
- Featureless (no spiral arms, bars, rings…)
- Mostly old stars (not much dust or star-forming regions)
- Kinematically hot, i.e., dynamically supported by stellar velocity dispersion σ (but it does rotate!)

- Presumably built in violent events, inducing fast bursts of star formation if gas is available: mergers or clump coalescence

Classical Bulge

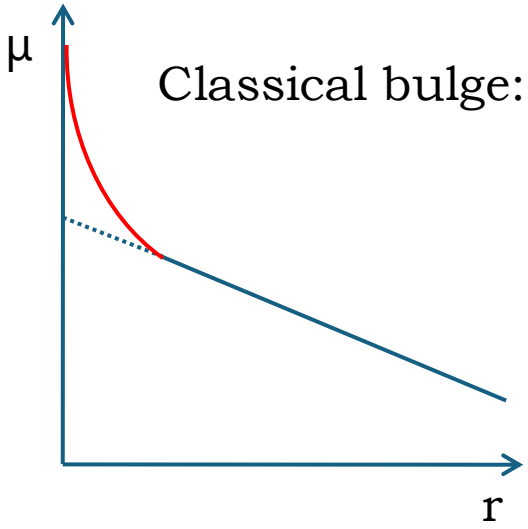

Classical bulge: high Sérsic index (n>3)

The Sérsic Function

$$\mu_b(r) = \mu_e + c_n[(r/r_e)^{1/n} - 1]$$

Bar


NGC 1300 – HST


NGC 1365 – SSRO


NGC 1433 – HST


NGC 4303 – HST

An Unbarred Galaxy

Bar

How many bars are there?

- About 2/3 of disc galaxies in the local Universe are barred (de Vaucouleurs+1991)
  - 1/3 weakly barred (SAB)
  - 1/3 strongly barred (SB)

- More modern studies report fractions from ~30% to ~70% (e.g., Eskridge+2000, Menéndez-Delmestre+2007, Gadotti 2009, Aguerri+2009, Masters+2011, Buta+2015, Erwin 2018)
  - Data quality is key (physical spatial resolution and depth)
  - Projection effects (bars not easy to see in close to edge-on galaxies)
  - Bars are more prominent in the NIR (old stellar populations)
  - Bar fraction varies with galaxy mass (so beware of sample selection effects)

Bar

Basic Properties

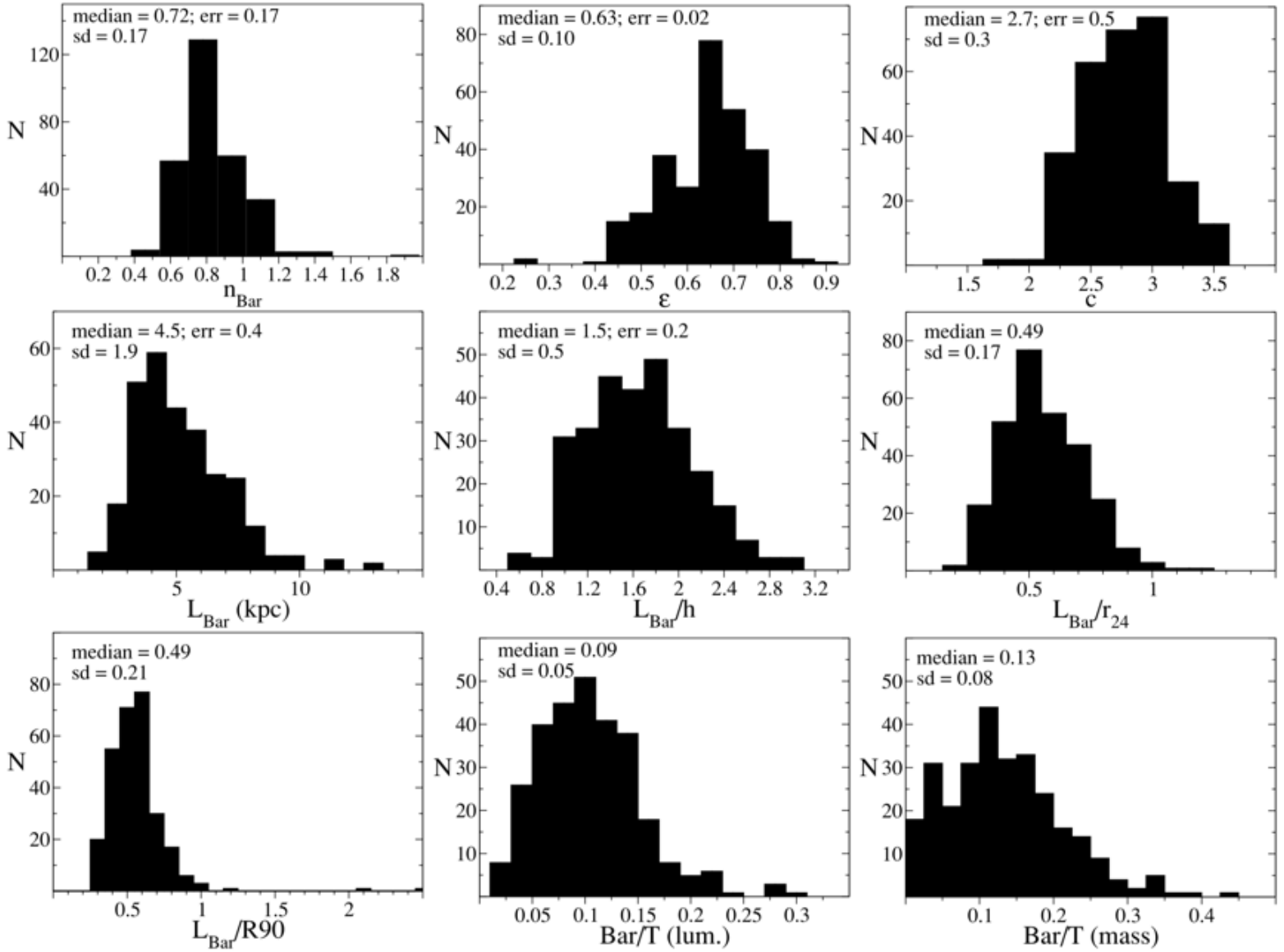

See also Erwin (2005) for bar sizes

Gadotti 2011

Bar

How do bars form?

- Bars are a global dynamical instability in the disc, which leads to a minimum energy state.

- Toomre's (1964) stability criterion: $Q \equiv \frac{\sigma_R \kappa}{3.36 G \Sigma} > 1$
  - Cold discs are unstable

- Halo can stabilise discs (Ostriker & Peebles 1973)
  - Only if halo is static

- Bars can also form in interactions (which may trigger the dynamical instability). But if the interaction is too strong, it may weaken/destroy the bar, or heat up the disc too much, preventing bar formation.

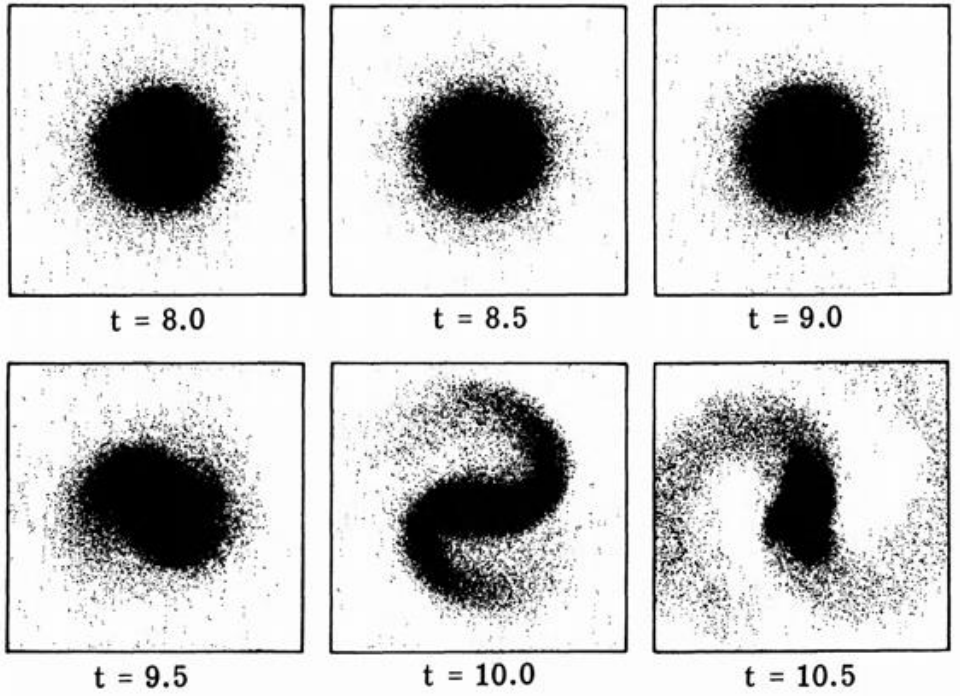

Hohl 1971

Bar

How do bars form?

- Responsive halo or central spheroid can delay bar formation but eventually lead to stronger bars (e.g., Athanassoula & Misiriotis 2002, Athanassoula 2003, Valenzuela & Klypin 2003, Martinez-Valpuesta+2006, Berentzen+2006,2007, Athanassoula+2013). This is due to the halo (or spheroid) acquiring angular momentum from the bar.
    - Halo shape and kinematics are also important
        - Triaxial halo excites bar formation earlier, but a spherical halo strengthens the bar eventually
    - Gas fraction also plays a role: bars form later in gas-rich discs

Bar

Orbits and resonances

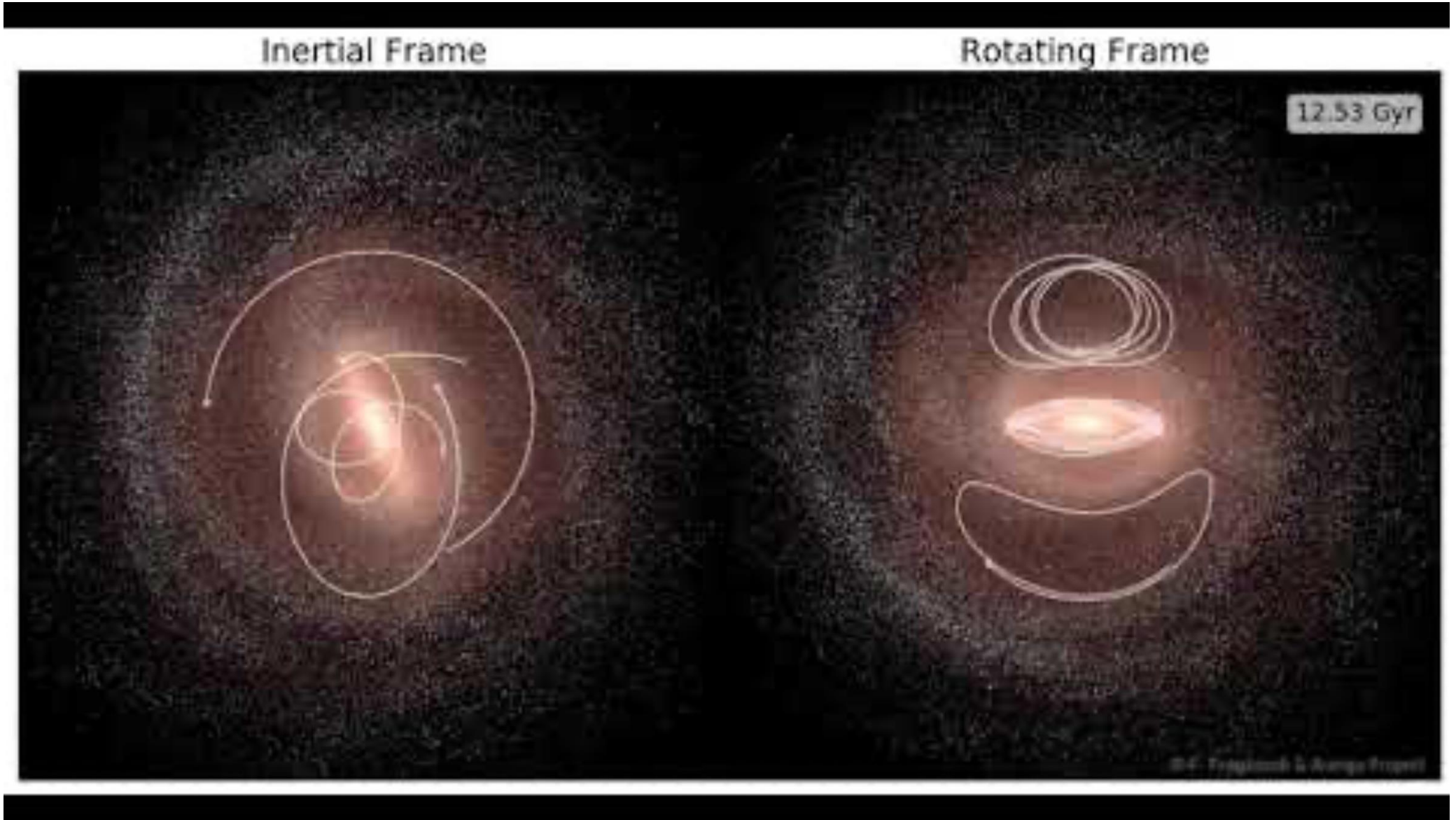

Bar

Orbits and resonances

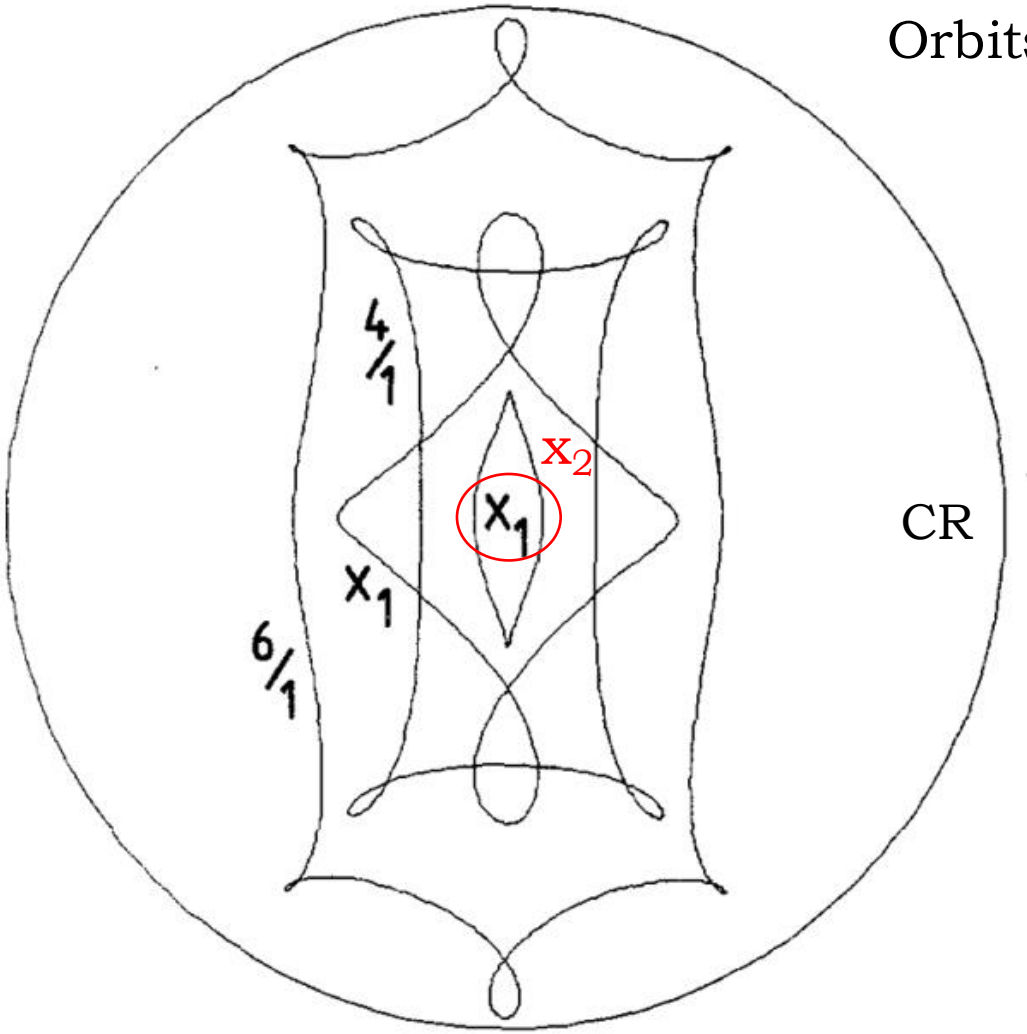

Contopoulos & Grosbøl 1989

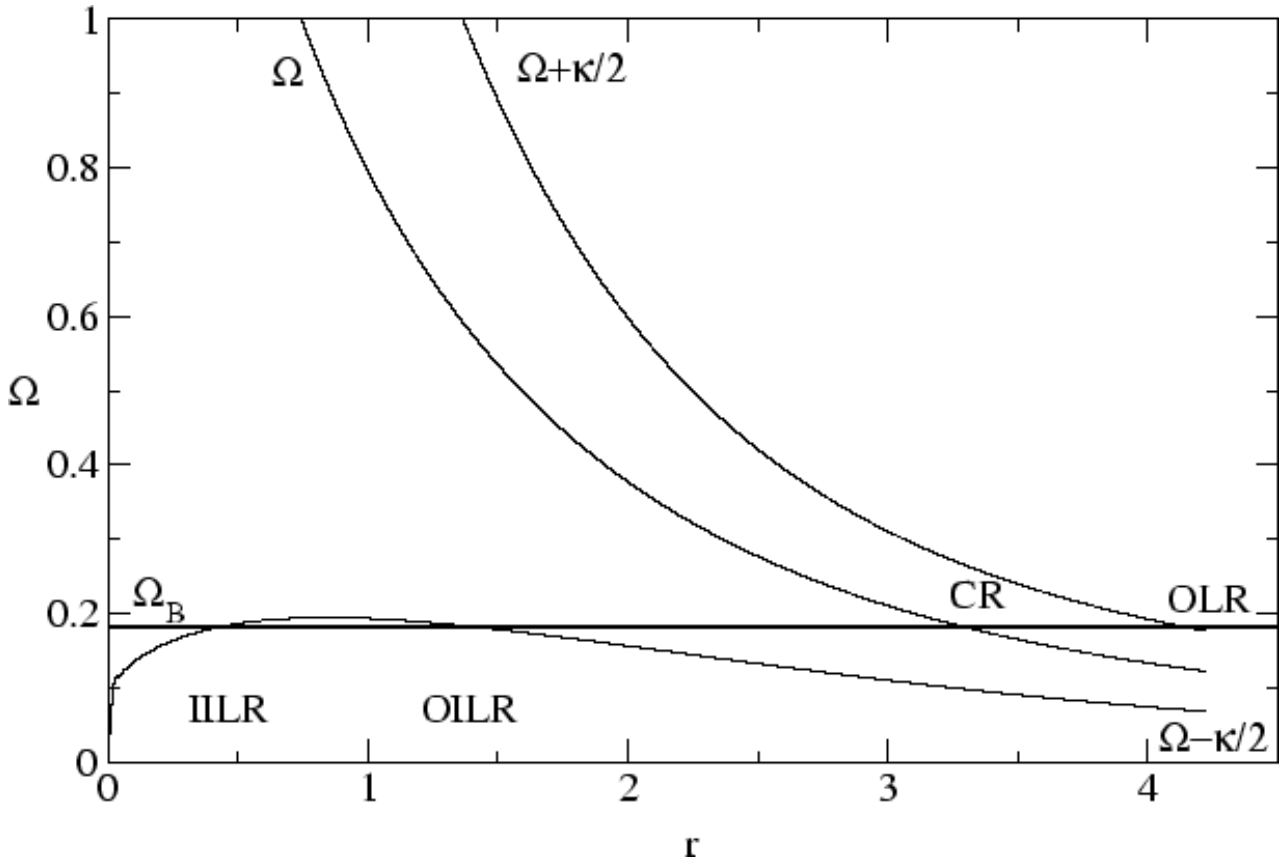

Gonzalez & Gadotti 2016

Bar

When did bars form?

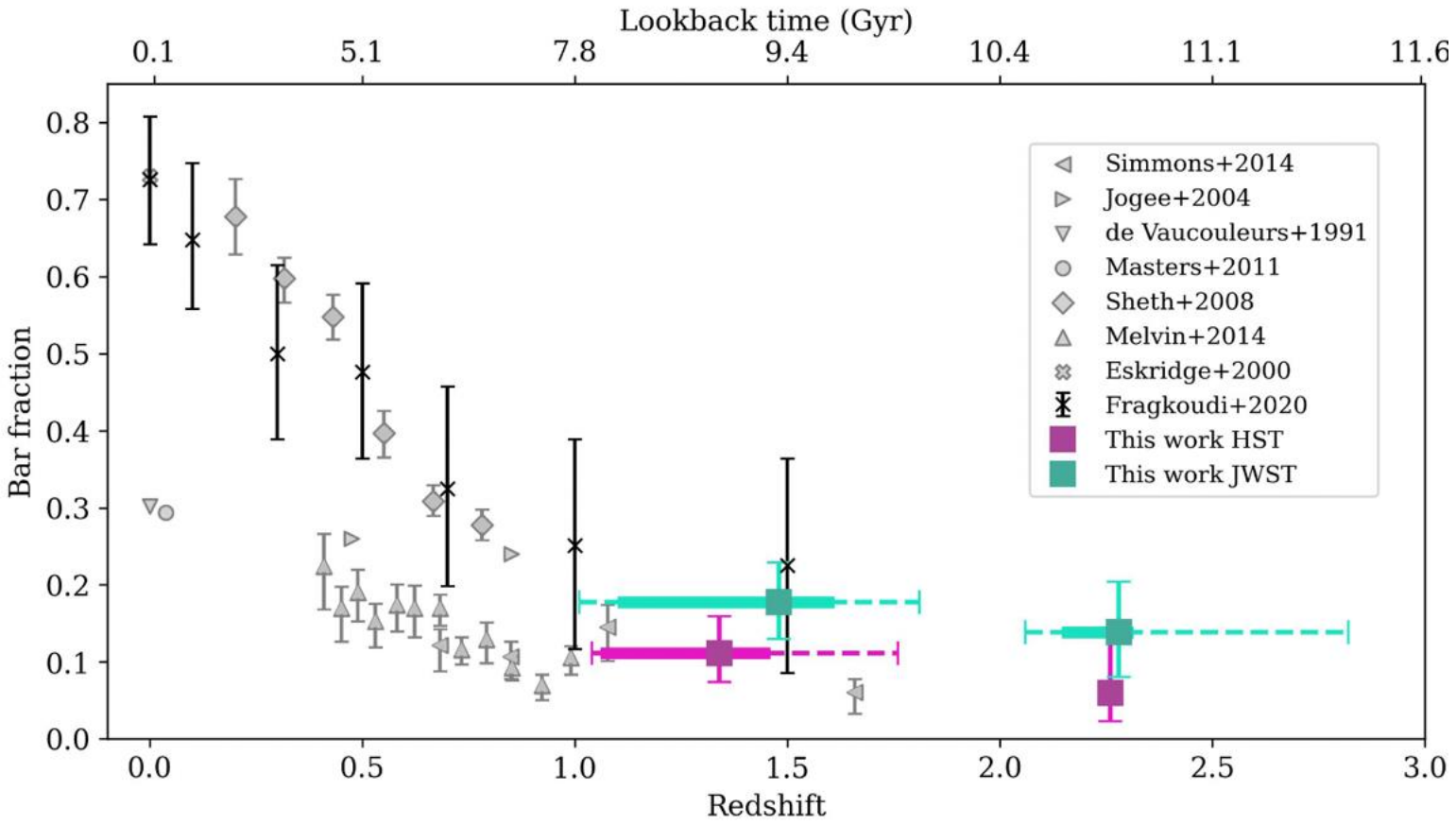

Le Conte+2024

- Bar fraction seems to decrease at high redshifts, although difficulty in seeing bars at those distances may play a major role
- Nonetheless, bar fraction is about 20% between redshifts 1 and 2 and 15% between redshifts 2 and 3 (Le Conte+2024), with some bars seen up to z ~ 4 (see also Guo+2023, Costantin+2023, Tsukui+2023, Smail+2023, Amvrosiadis+2024).

Box/Peanut

- Stick out of the disc plane (not easy to see at low inclinations)
- Show a boxy or peanut-like morphology
- Usually featureless (no sub-structures)
- Usually do not show signs of dust obscuration, young stellar populations or star-forming regions
- Kinematically colder, i.e., dynamically supported by rotation of its stars V_{rot}

- Are simply the inner parts of bars, seen at an edge-on projection

Box/Peanut

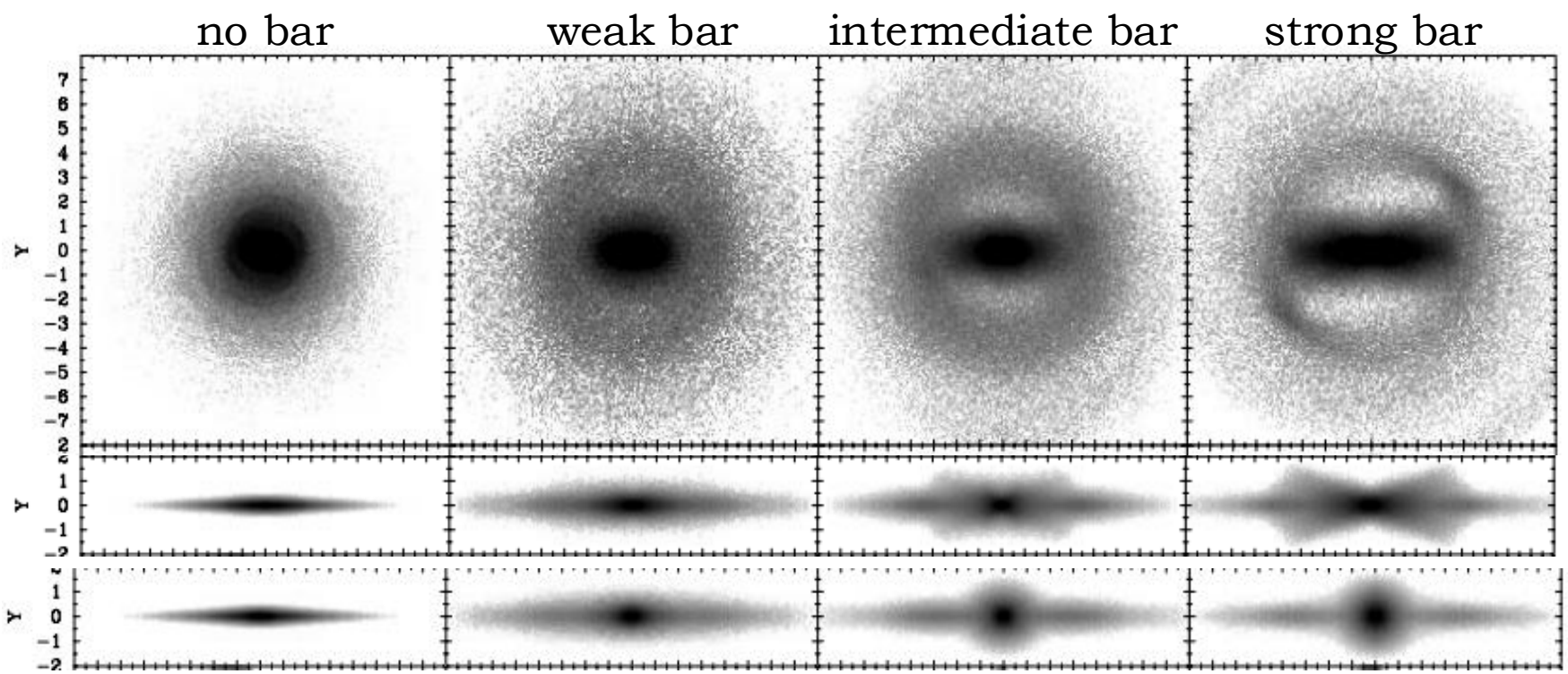

Bureau & Athanassoula (2005)

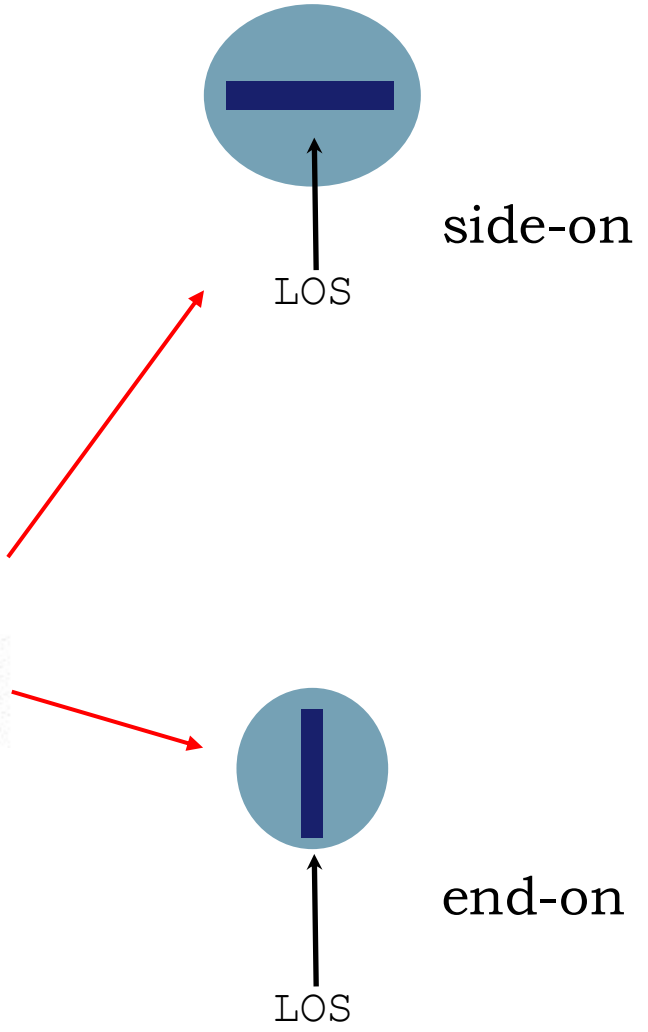

Barlens

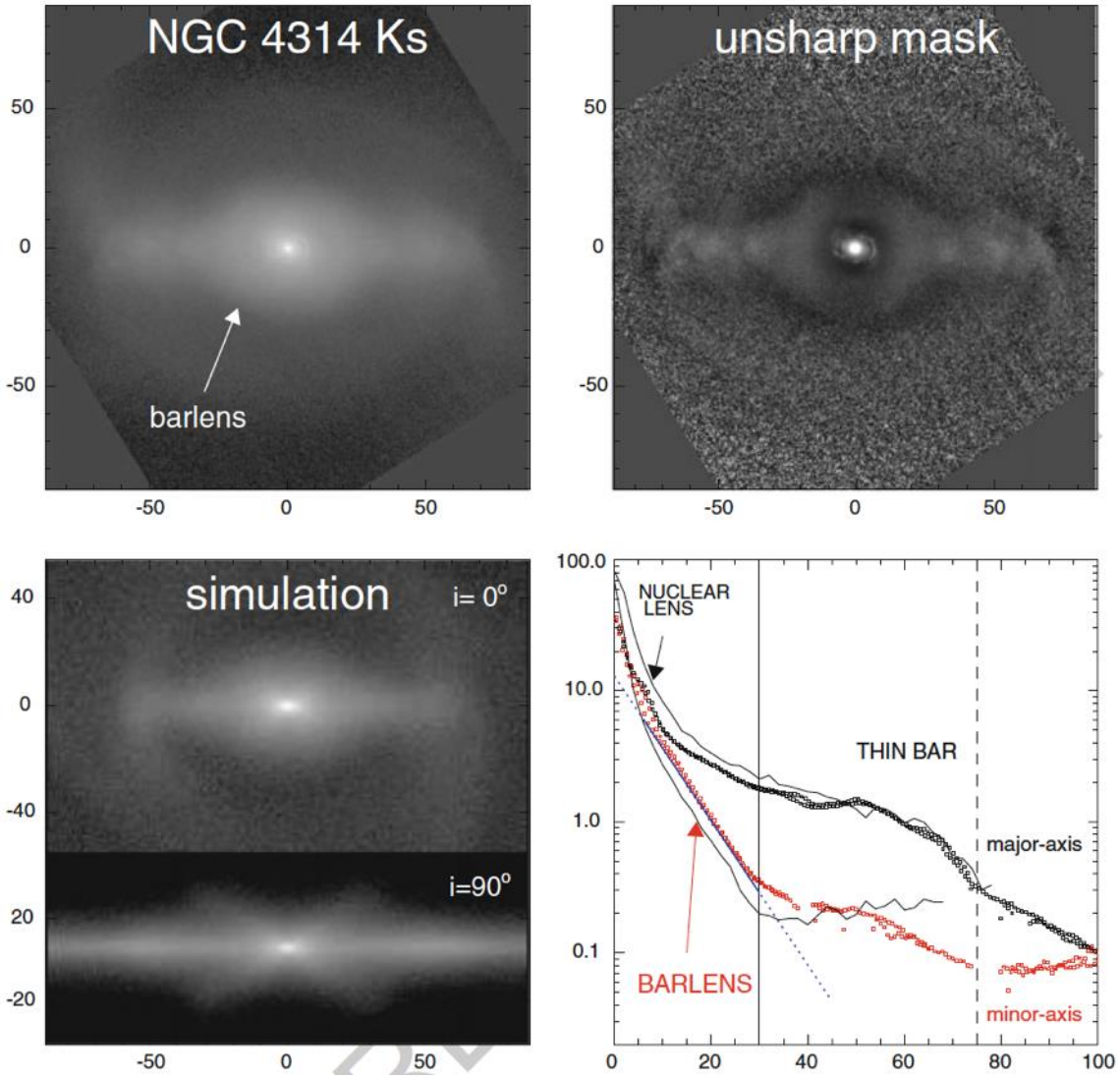

Laurikainen & Salo 2016

- Barlenses are just the box/peanut seen face-on! So they are also just part of the bar.
- So the inner parts of bars are more extended that the outer parts both in the vertical direction and in the plane of the disc.

Gonzalez & Gadotti 2016

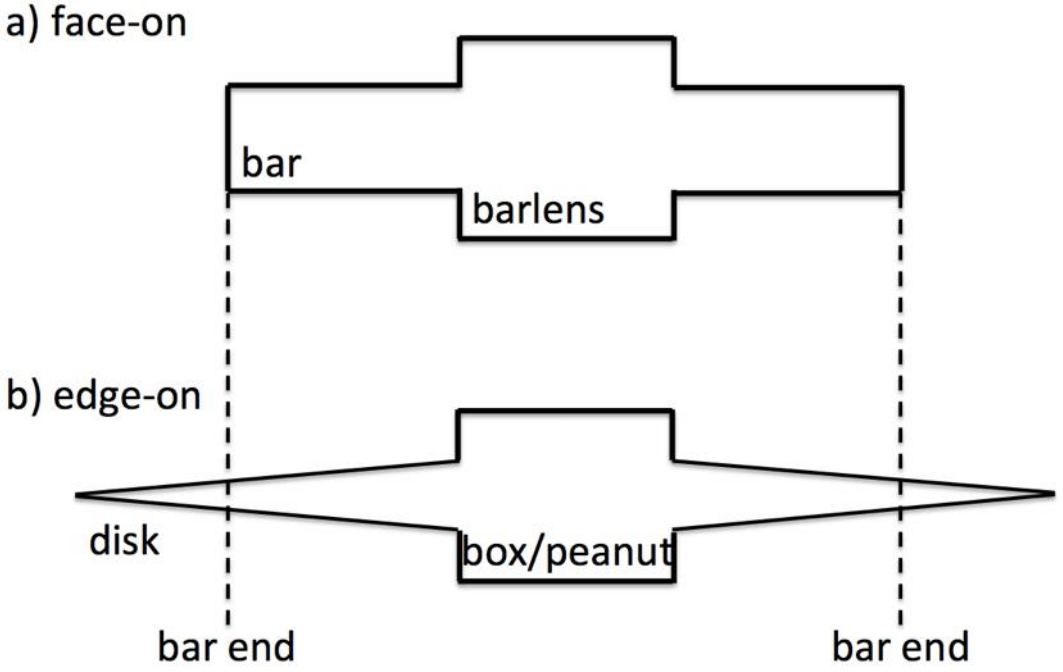

Nuclear Disc

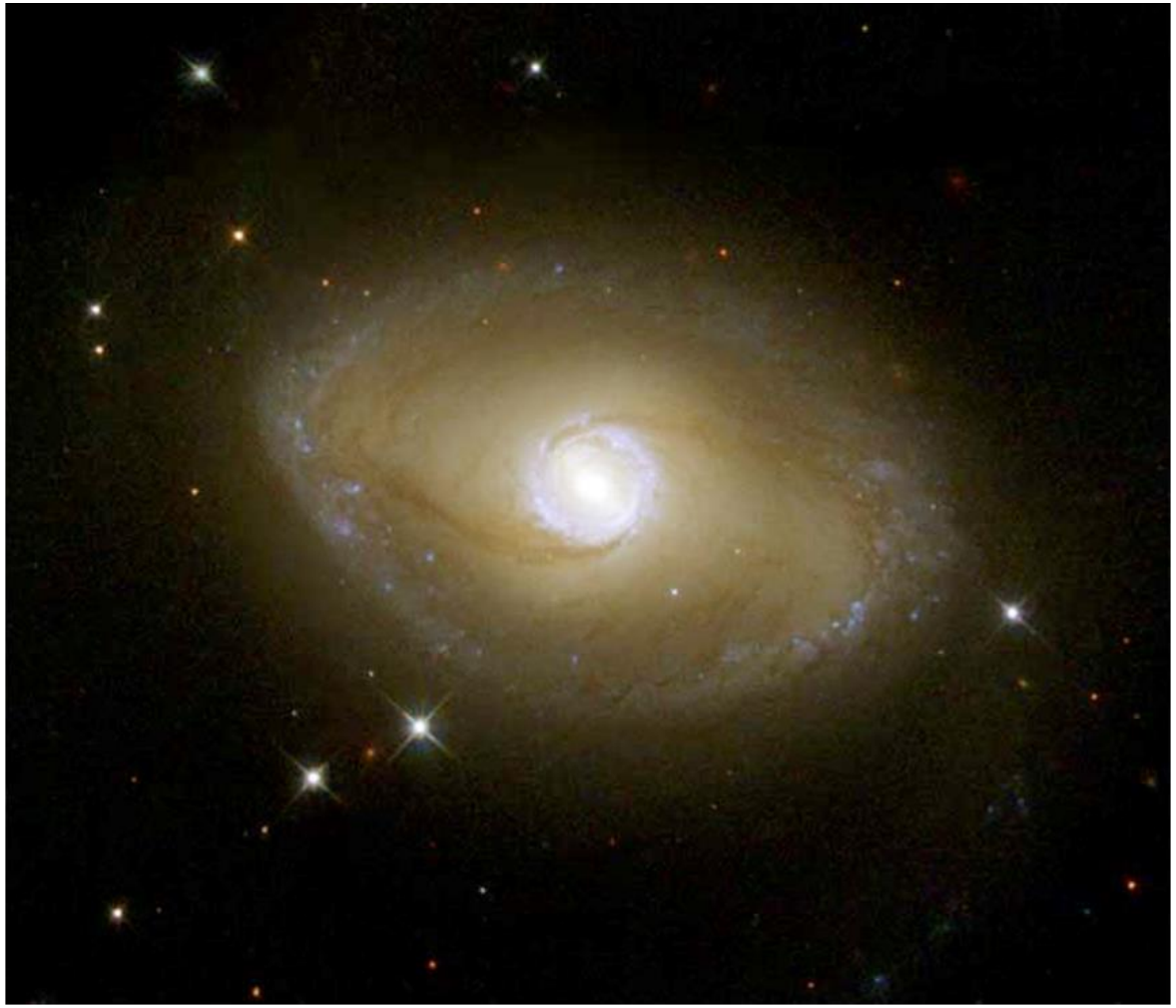

Nuclear Disc

- As flat (or almost as flat) as the disk (not easy to see in very inclined galaxies)
- May contain sub-structures such as nuclear bars, spiral arms, rings…
- May show signs of dust obscuration, young stellar populations or ongoing star formation
- Kinematically colder, i.e., dynamically supported by rotation of its stars V_{rot}

- Built mostly via bar-driven gas inflow

Nuclear Disc

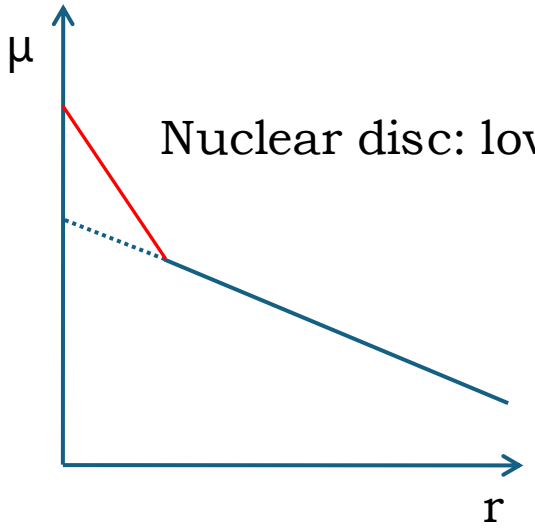

Nuclear disc: low Sérsic index (n<2)

The Sérsic Function

$$\mu_b(r) = \mu_e + c_n[(r/r_e)^{1/n} - 1]$$

NGC 1433

Bars induce tangential forces and shocks, causing gas inflow…

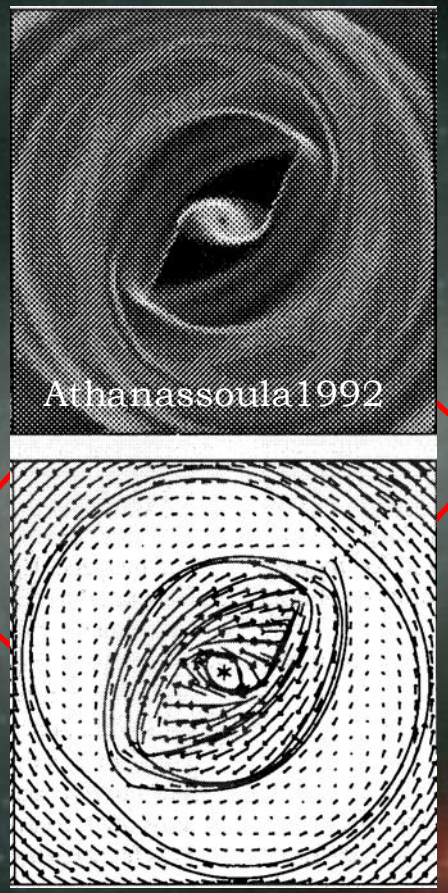

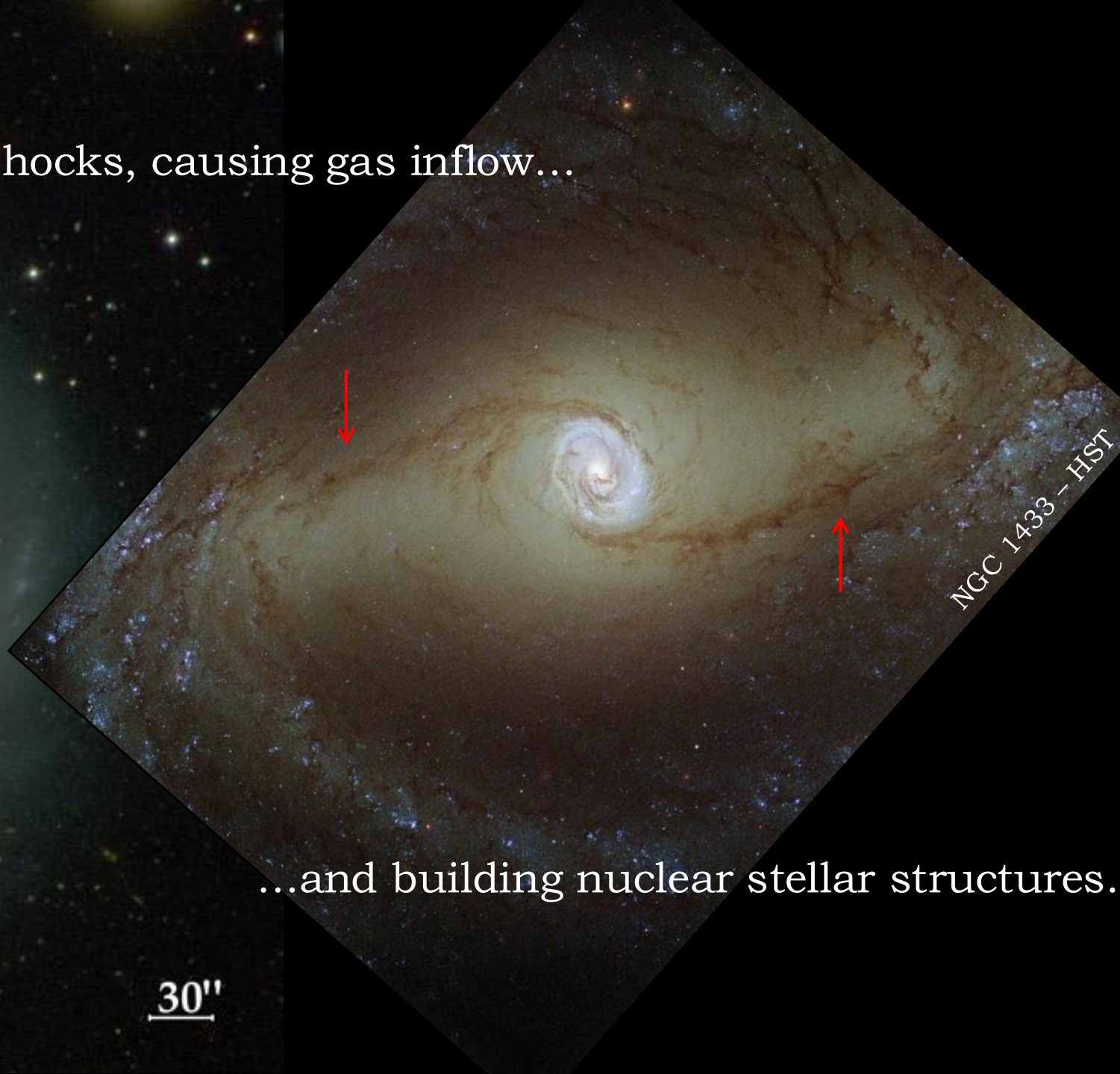

…and building nuclear stellar structures.

30''

CGS: Ho+2011

Nuclear Disc

- Can have its own bar, spiral arms and star-forming rings (e.g., Gadotti+2019)

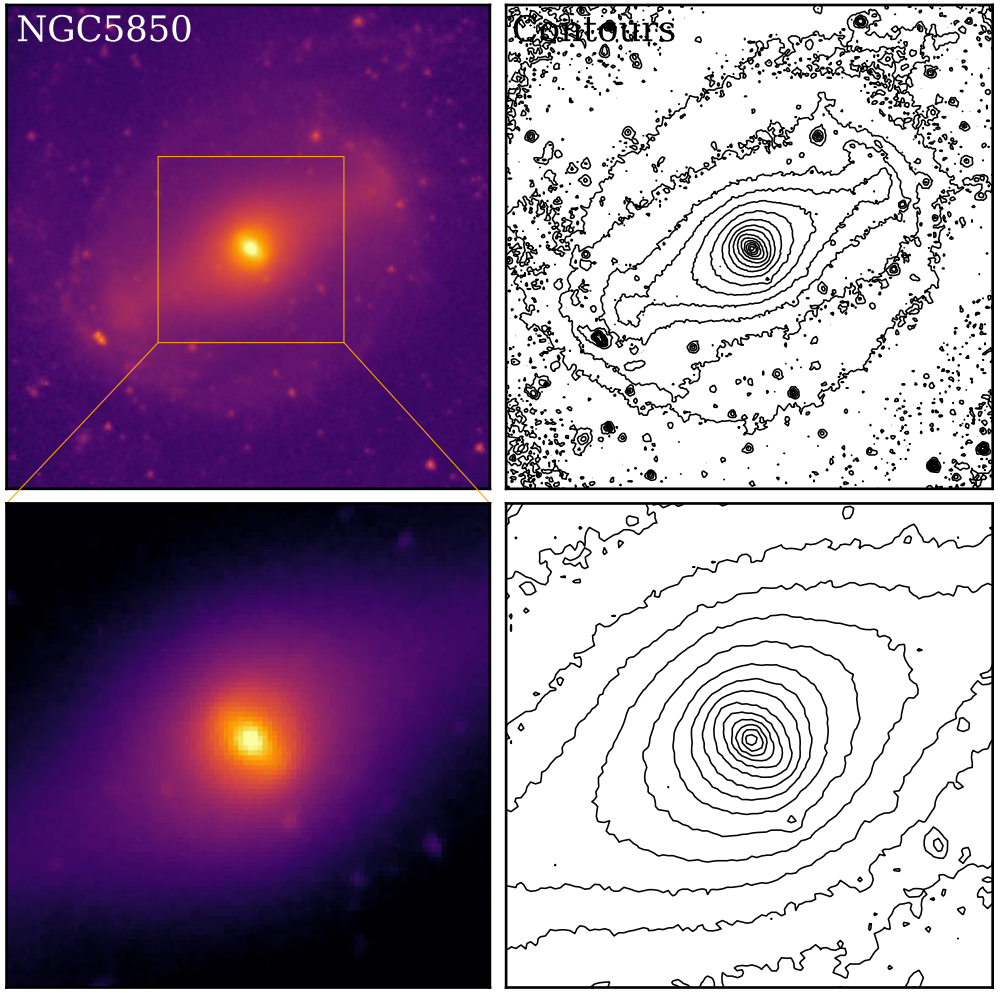

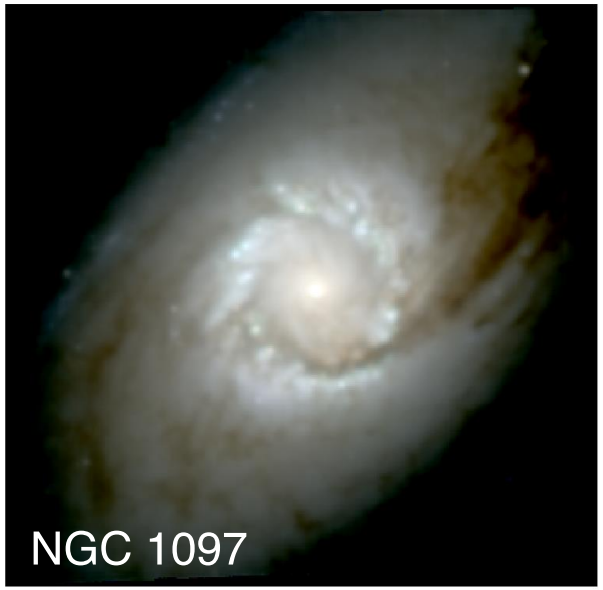

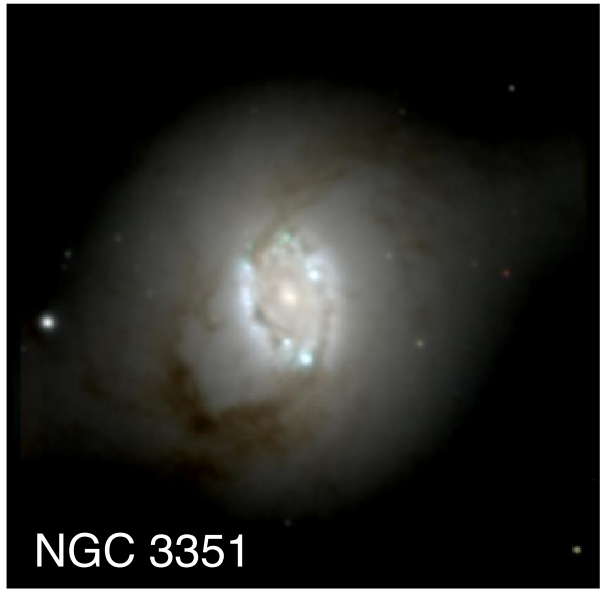

- Milky Way also has its own nuclear disc and nuclear ring (the CMZ; e.g., Sormani+2022)

Composite Bulges

- Galaxies can host several stellar structures in the centre, e.g., a bar and box/peanut plus a nuclear disc:

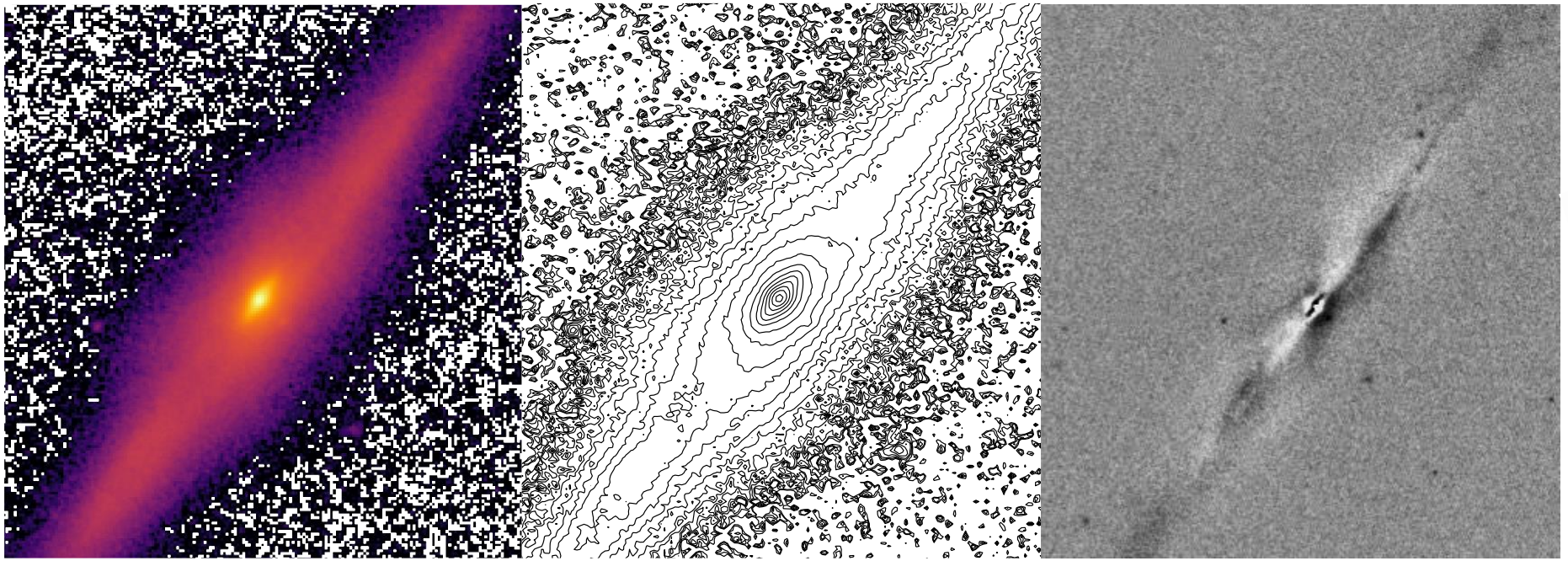

VIRCAM H band

Isophotes

Residuals

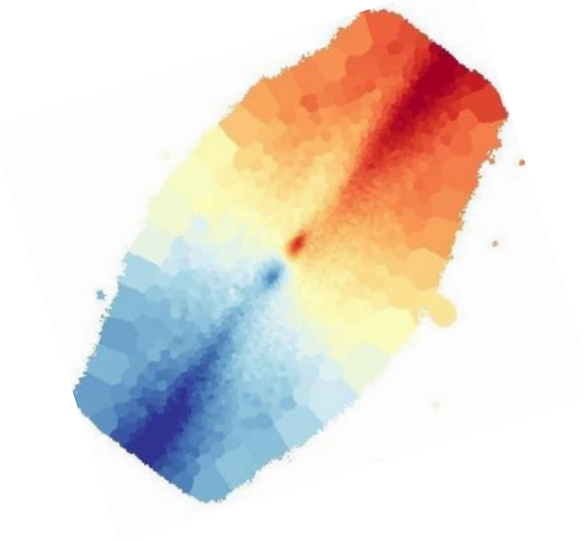

Stellar Kinematics

Fraser-McKelvie+, in prep. – GECKOS

Composite Bulges

- Small classical bulges may also exist at the centre of nuclear discs (e.g., Nowak+2010; Erwin+2015)

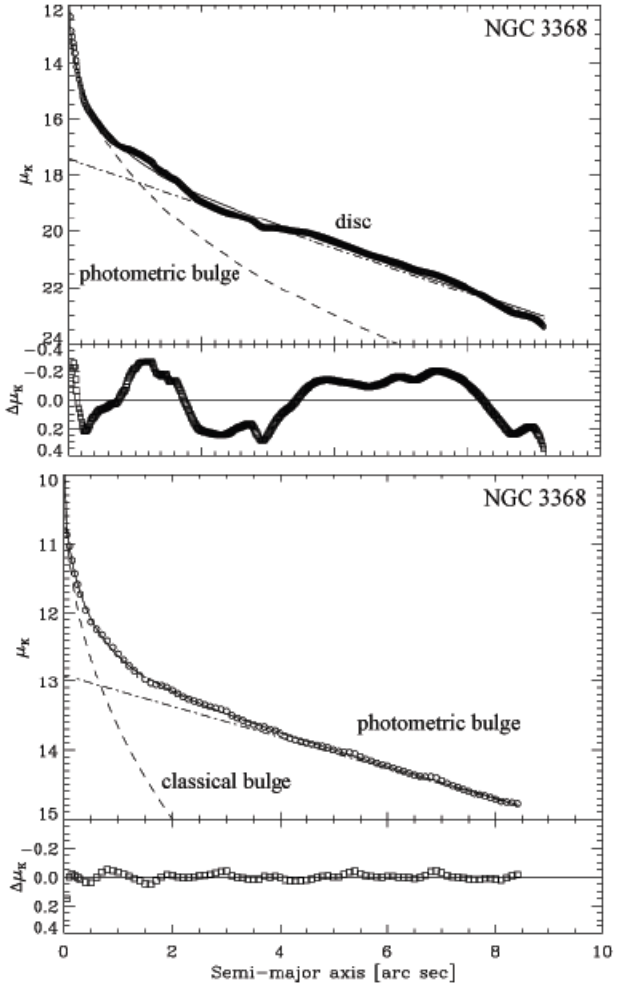

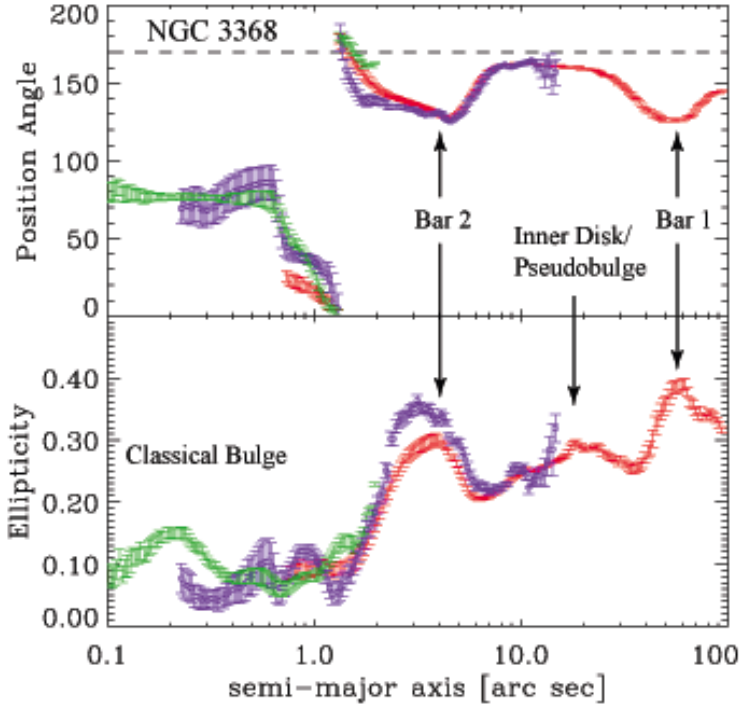

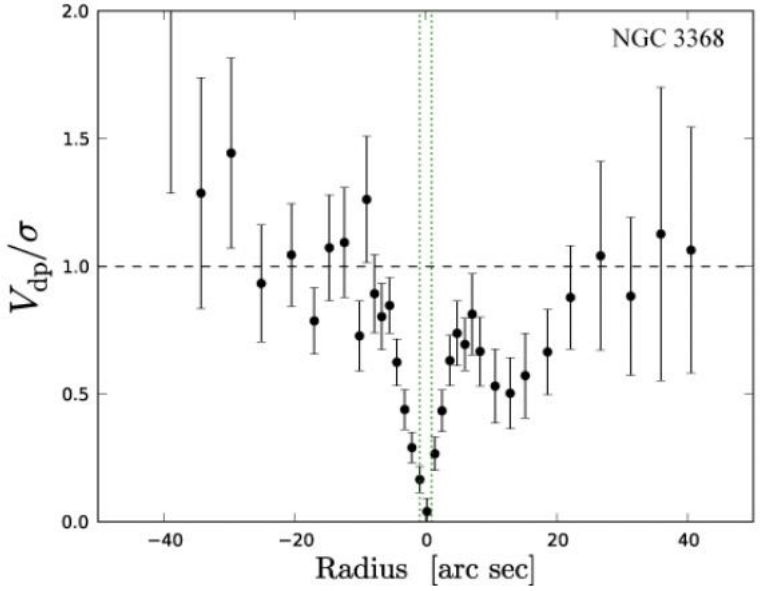

Although they don't bulge from the disc and may be very large nuclear star clusters (?)

Composite Bulges

- The Milky Way has a composite bulge

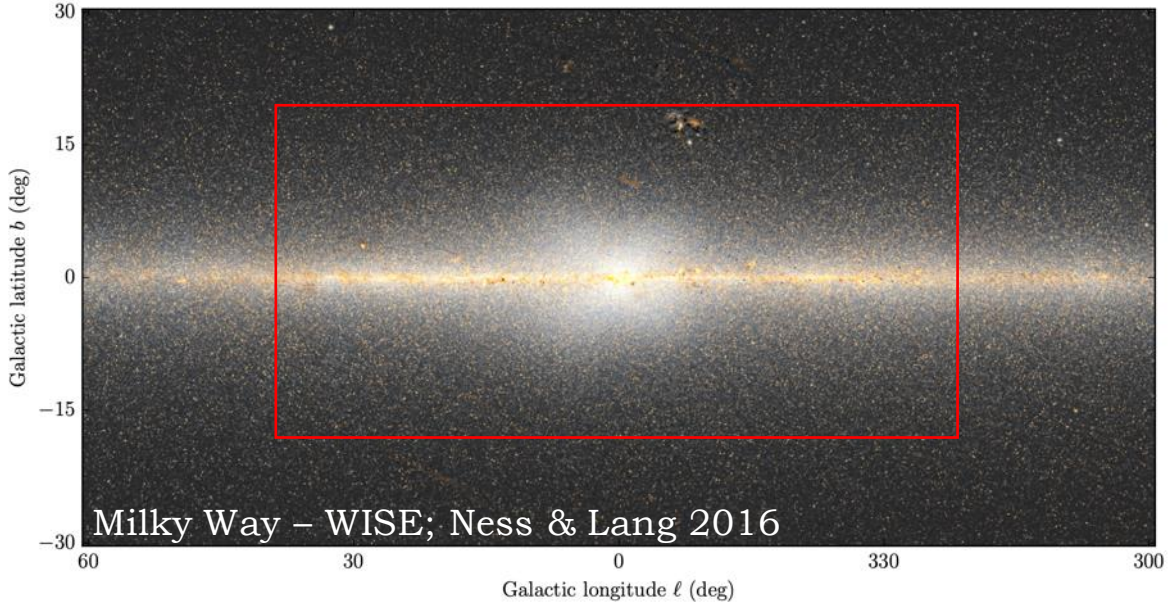

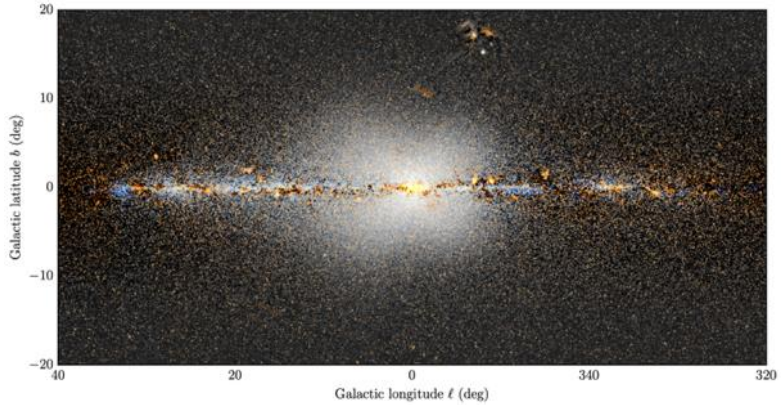

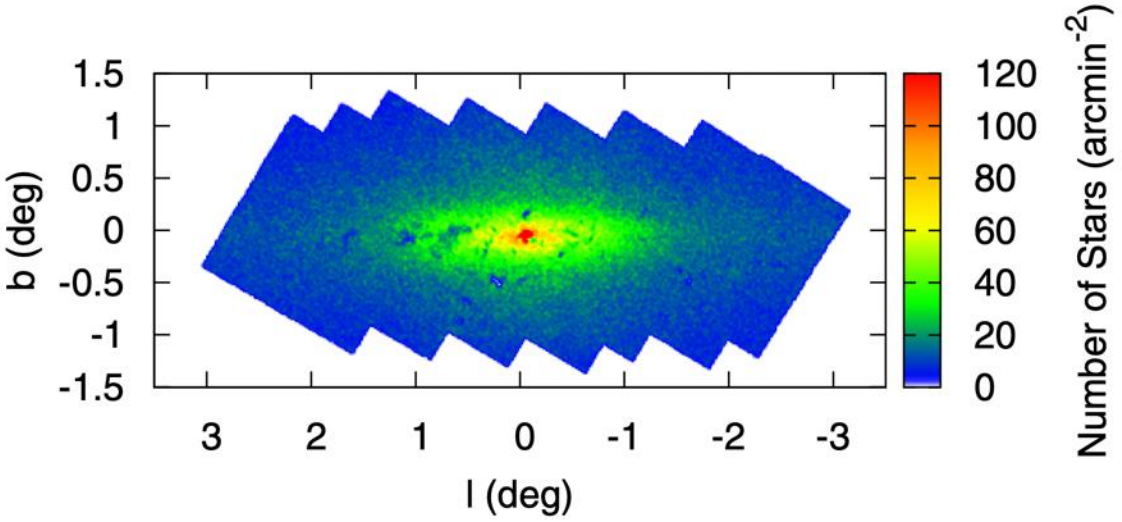

Nishiyama+2013

Spiral Arms, Inner and Outer Rings

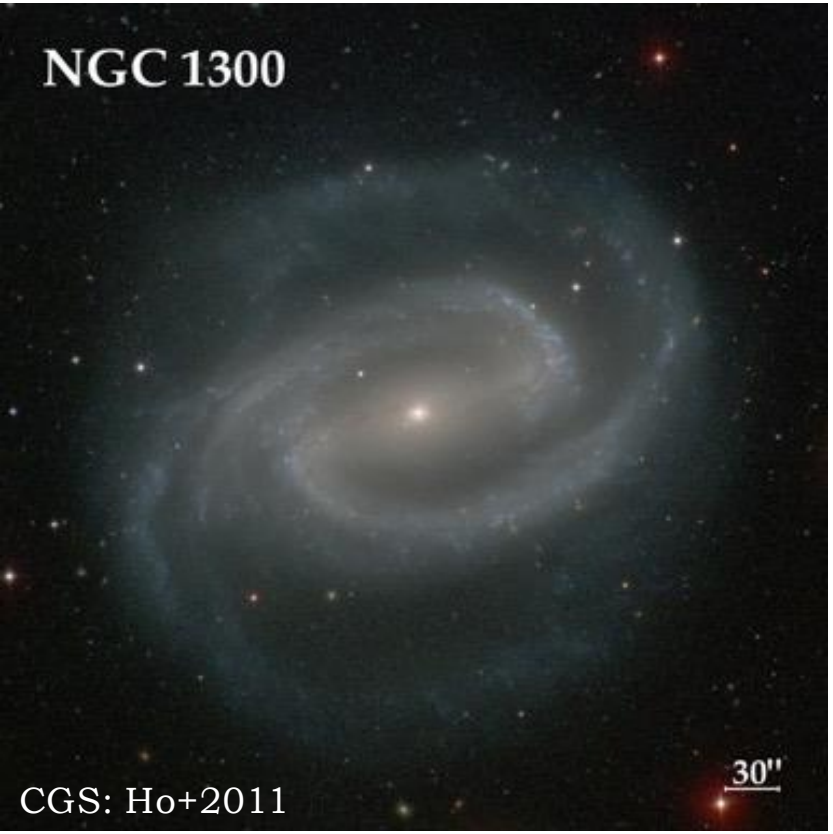

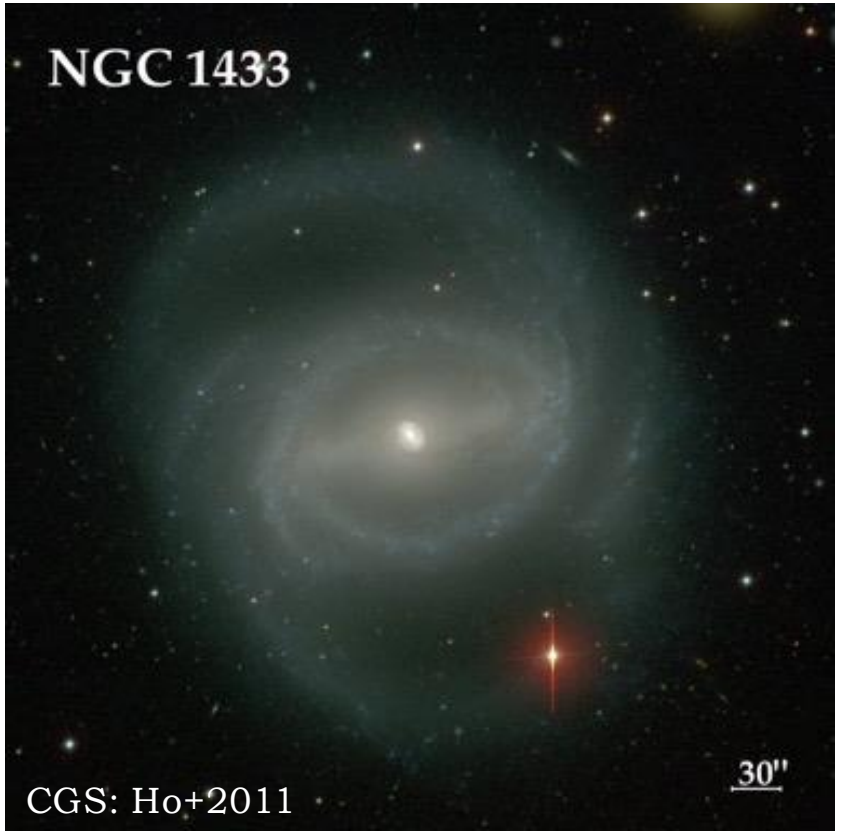

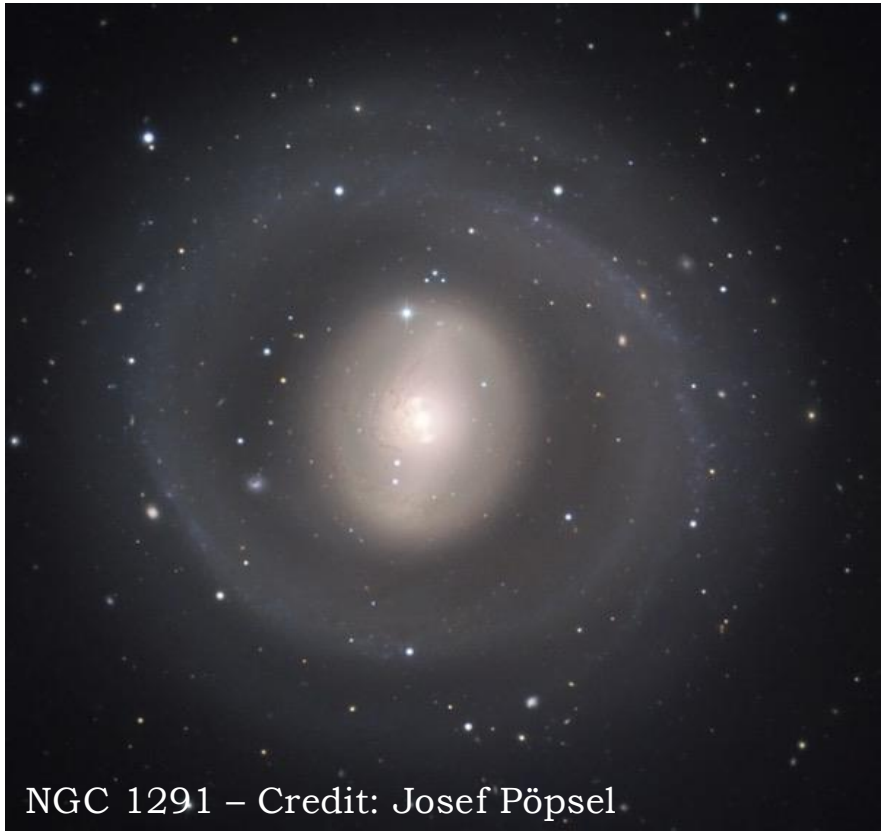

- Bars may induce spiral arms and seem to induce also inner rings and outer rings, which could indicate the positions of dynamical resonances. The inner ring would be near corotation or the 4:1 resonance, whereas outer rings are near the Outer Lindblad Resonance (OLR). Nuclear rings seem to be near one of the Inner Lindblad Resonances (ILR). But all of this is still debated.

Spiral Arms, Inner and Outer Rings

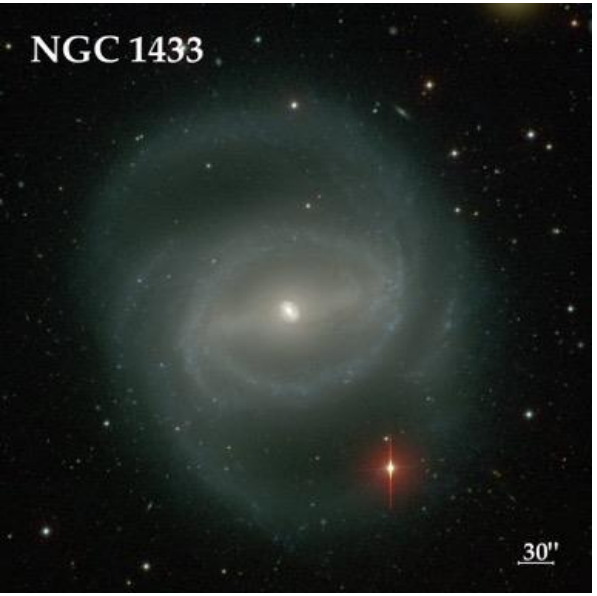

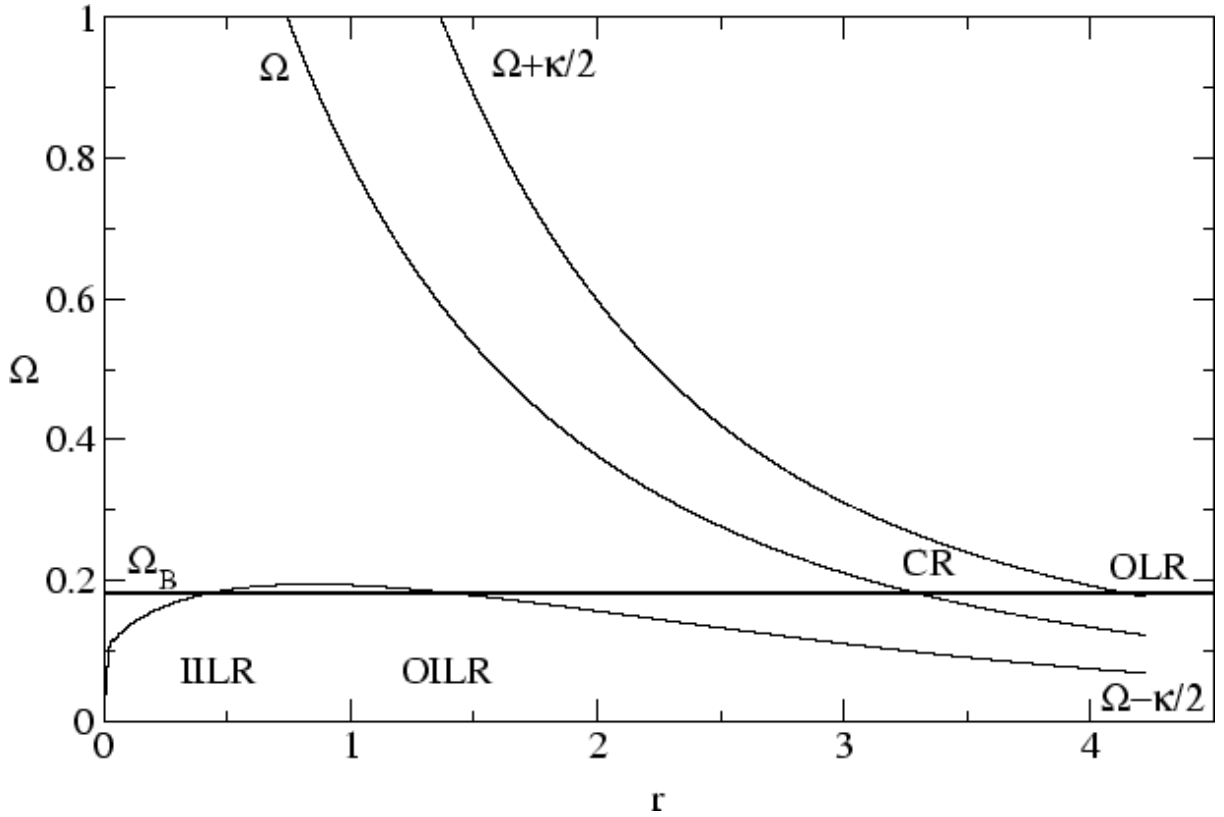

Gonzalez & Gadotti 2016

- Bars may induce spiral arms and seem to induce also inner rings and outer rings, which could indicate the positions of dynamical resonances. The inner ring would be near corotation or the 4:1 resonance, whereas outer rings are near the Outer Lindblad Resonance (OLR). Nuclear rings seem to be near one of the Inner Lindblad Resonances (ILR). But all of this is still debated.

Stellar Halo

- The Milky Way and other disc galaxies have a stellar halo of old, metal-poor stars, presumably formed at the first stages of galaxy formation (the most metal-poor stars of the Galaxy are in the halo).

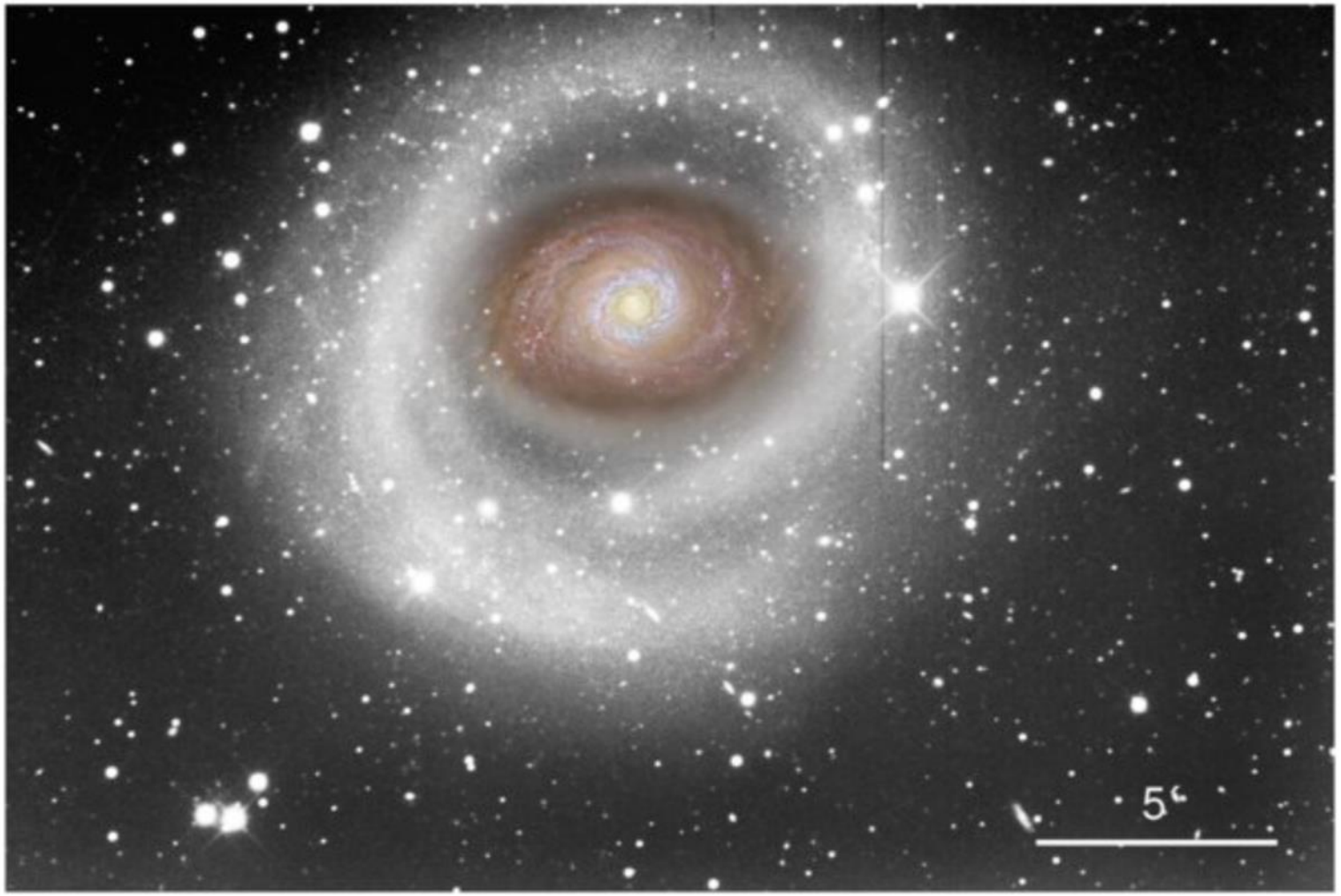

Trujillo+2009

Stellar Halo

- But it also contains sub-structures, due to interactions with companion galaxies, and so many of the stars in the halo may have formed in the companions.

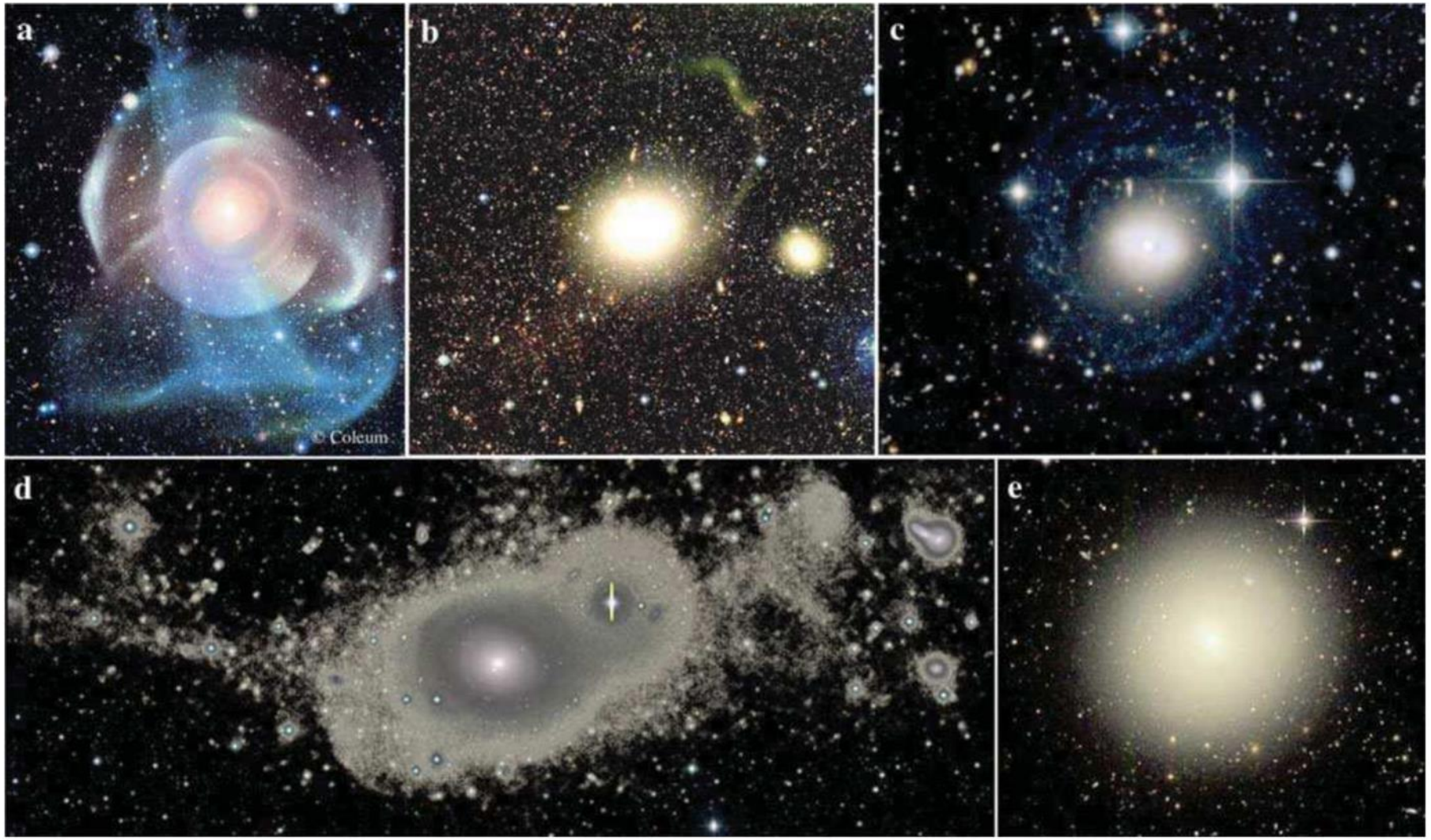

Duc+2013

Stellar Halo

- It is not yet clear how often galaxies host stellar haloes, and what is the fraction of stars in haloes that were formed in companion galaxies.

- It is also not clear what is the predominant shape of the halo.

Gadotti & Sánchez-Janssen (2012)

Some renderings are misleading…

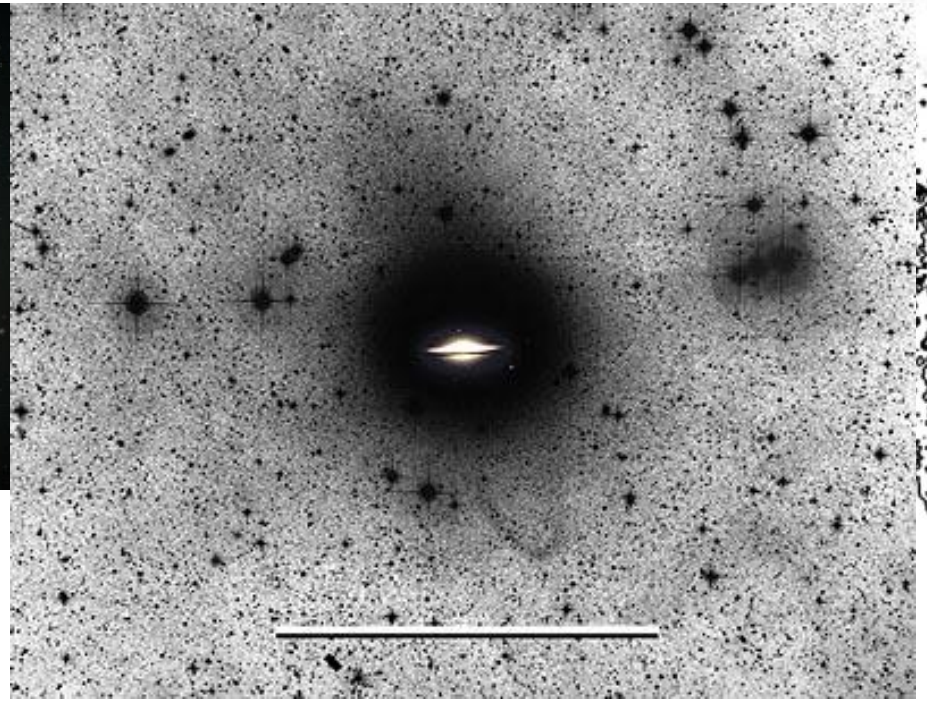

David Malin - AAO

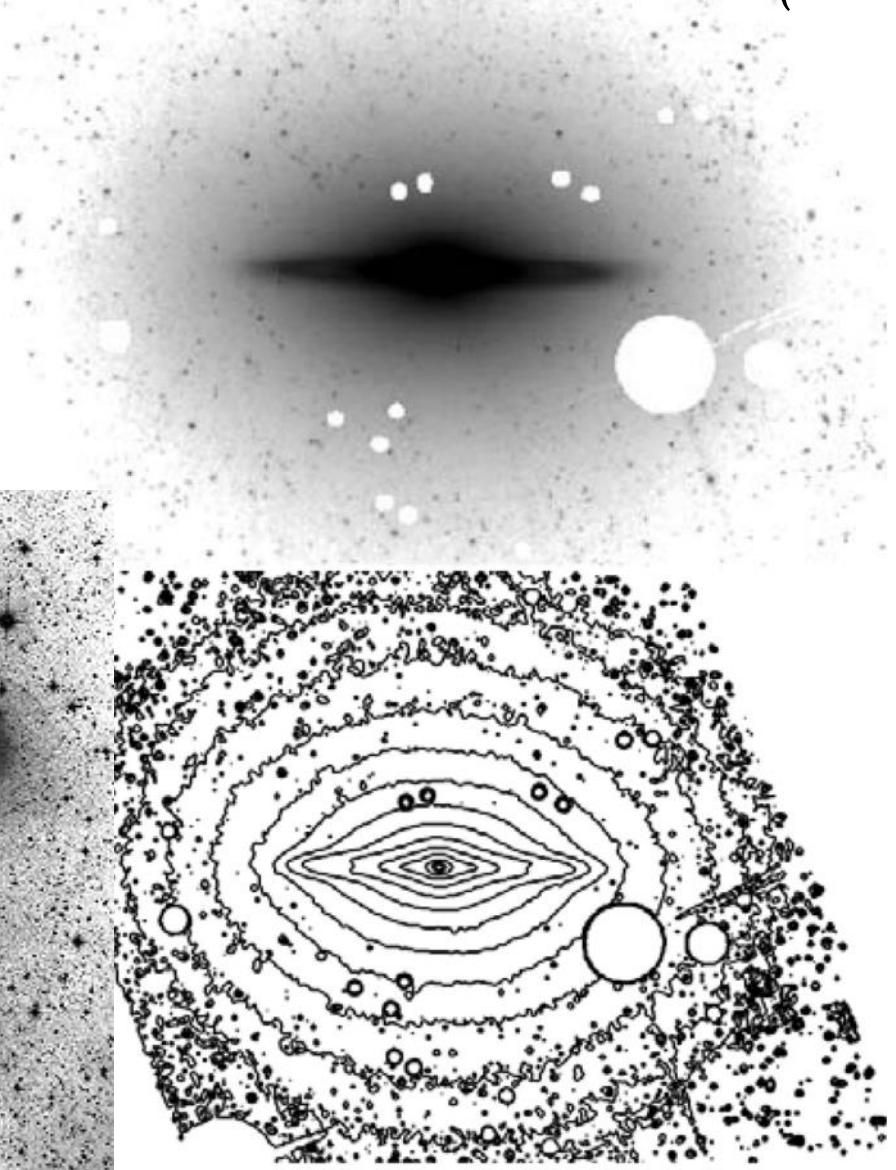

Figure 1. Top: IRAC channel 1 image of the Sombrero galaxy (NGC 4594) at 3.6 μm, used in this study. Bottom: isophotal contours from the same image. Foreground stars are removed. The stellar halo stands out clearly and appears rounder than the central bulge.

Nuclear Star Cluster

- Found often in galaxies of all types, except the most massive (core) ellipticals (e.g., Böker+2002, Côté+2006).

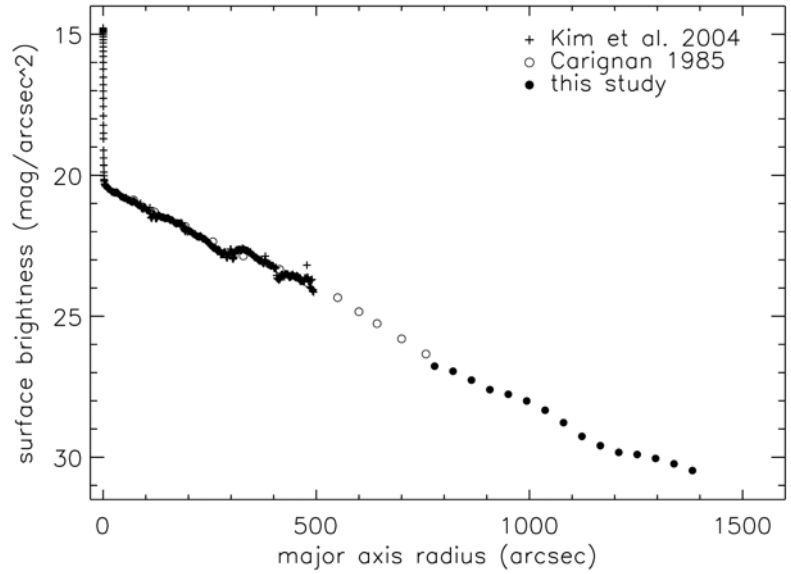

FIG. 8.—Observed r' surface brightness profile of NGC 300 derived *directly* from the star counts. The inner plus signs are taken from Kim et al. (2004): these are *I*-band measurements shifted downward by 0.5 mag. The open circles are taken from the B_J photographic measurements of Carignan (1985) and are shifted upward by 1.1 mag. The GMOS data points are derived from the 3 σ source catalog presented in Fig. 7*b*. After correcting for incompleteness (−0.65 mag) and inclination (+0.33 mag), we obtain the intrinsic surface brightness profile (see § 6); this amounts to shifting all points upward by 0.32 mag.

Bland-Hawthorn+2005

Nuclear Star Cluster

- With masses ~10^6-$10^8 M_\odot$ and sizes ~5pc, these clusters are the densest known stellar systems ($10^5 M_\odot/pc^2$; Walcher+2005).

- Two formation scenarios (e.g., Fahrion+2021):
  - From infall of globular clusters
  - In situ, central star formation

- There is evidence for both, with in situ formation dominating in the most massive systems.

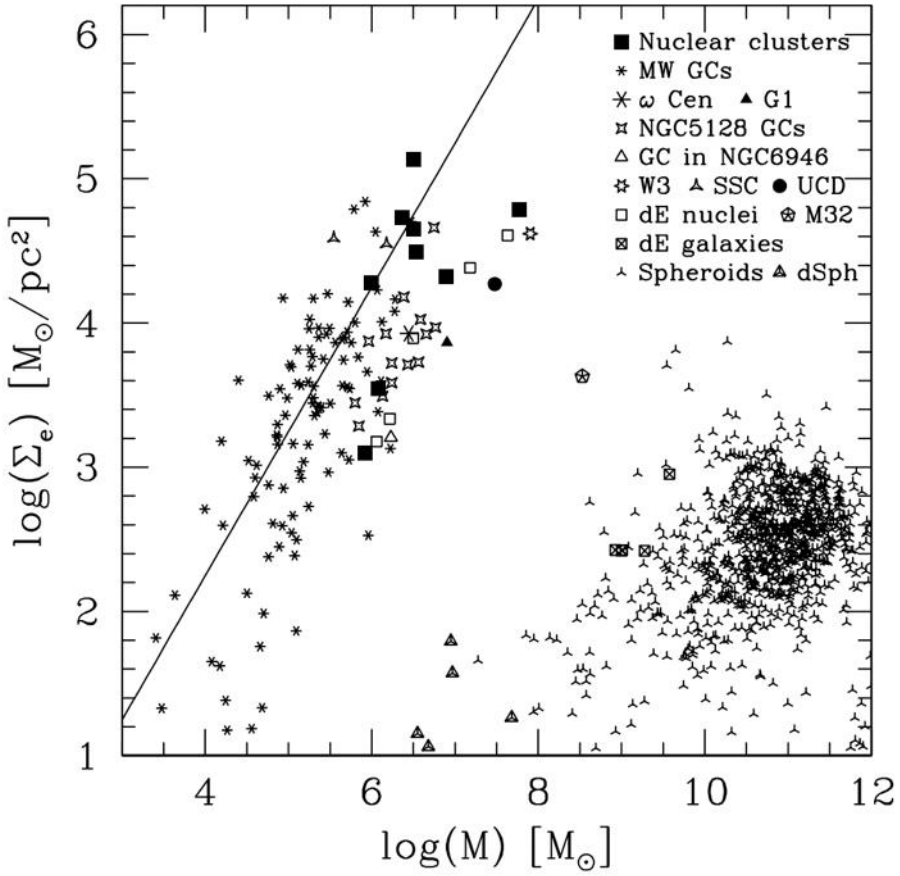

FIG. 3.—Mean projected mass density inside the effective radius against the total mass. This is similar to face-on view of the fundamental plane. Symbols represent different types of dynamically hot stellar systems. NCs occupy a region together with different types of massive stellar clusters and are well separated from any bulge. The solid line represents the locus of clusters with constant radius, α pc.

Nuclear Star Cluster

- While the mass of SMBHs correlate better with the bulge mass, the mass of NSCs correlate better with total galaxy mass, arguing against common formation and growth mechanisms (Erwin & Gadotti 2012).

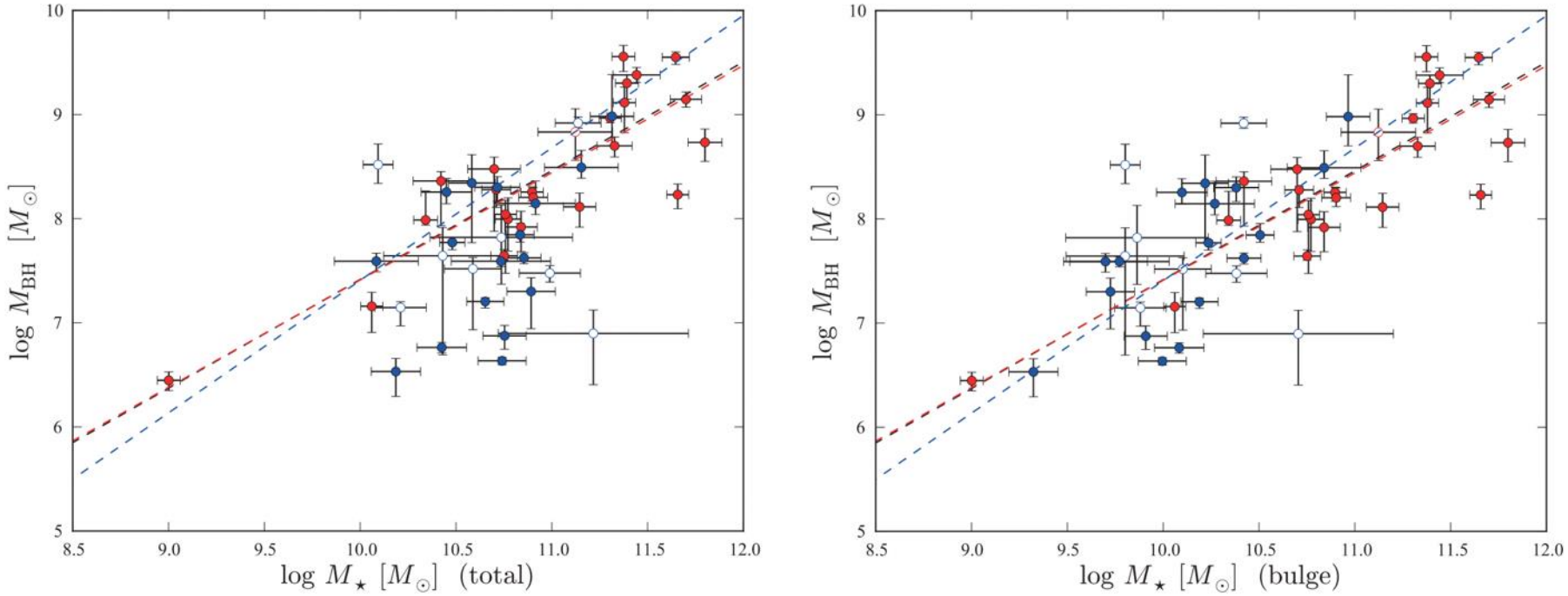

Fig. 2. Left: SMBH mass (red = elliptical galaxies, blue = disk galaxies) versus total galaxy stellar mass. Right: SMBH mass versus bulge stellar mass. (Data and sources in Table A.1.) The diagonal dashed lines are the best fits to the M_{BH}-$M_{\star,bul}$ relation for the whole sample (black), for the elliptical galaxies (red), and for bulges of the disk galaxies (blue). Open symbols are galaxies without precise distances, which are not used in the fits. It is clear that the SMBH masses of S0 and spiral galaxies (blue) correlate better with the *bulge* stellar mass than with total galaxy mass.

Nuclear Star Cluster

- While the mass of SMBHs correlate better with the bulge mass, the mass of NSCs correlate better with total galaxy mass, arguing against common formation and growth mechanisms (Erwin & Gadotti 2012).

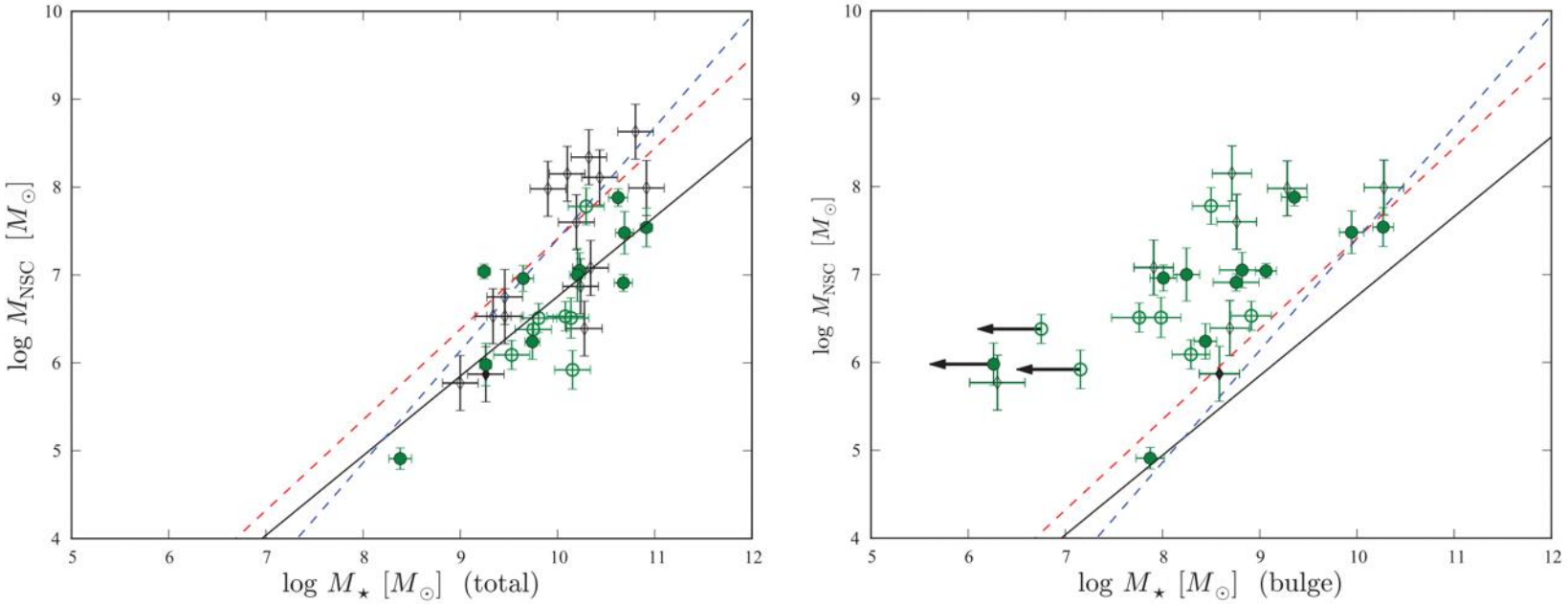

Fig. 3. As for Figure 2, but now plotting NSC mass versus total stellar mass (left) and bulge stellar mass (right). (Data and sources in Table A.2.) Green circles are galaxies with dynamical mass estimates for their NSCs; black diamonds are the spectroscopically estimated masses of Rossa et al. [11] (bulge mass estimates are not complete for these galaxies). Filled symbols indicate galaxies with direct distance measurements (e.g., from Cepheid stars). Arrows show nominal upper limits for three *bulgeless* spirals (assuming $B/T \leq 0.001$). The diagonal black line is a fit of NSC mass to total stellar mass for the dynamical-mass sample (green circles); for comparison, the diagonal dashed red and blue lines are the M_{BH}-$M_{\star,bul}$ fits for ellipticals (red) and disk galaxies (blue) from Figure 2. The situation is now the reverse of that for SMBHs: NSC masses clearly correlate better with *total* galaxy mass than they do with bulge mass.

Deriving Stellar Kinematics

Gadotti & de Souza (2005)

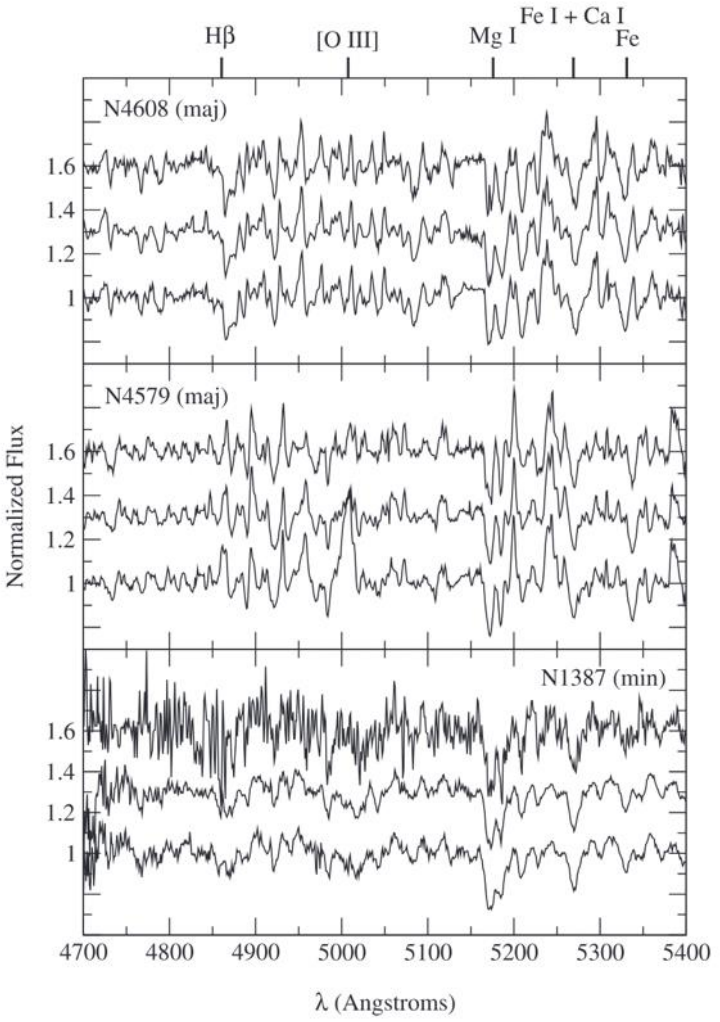

FIG. 2.—Some typical examples of the spectra we obtained. The top two panels refer to spectra obtained along the bar major axis of NGC 4608 and NGC 4579, both from the north sample. The bottom panel shows spectra obtained along the minor axis of the bar in NGC 1387 from the south sample. For each galaxy, as indicated, the bottom spectrum is the central one, while the middle one was extracted at 4.″5 from the center and the top one at 19.″3. The latter were artificially dislocated in this figure to avoid crowding. The emission line at $\lambda \approx 5200$ Å in NGC 4579 is the [N I] doublet.

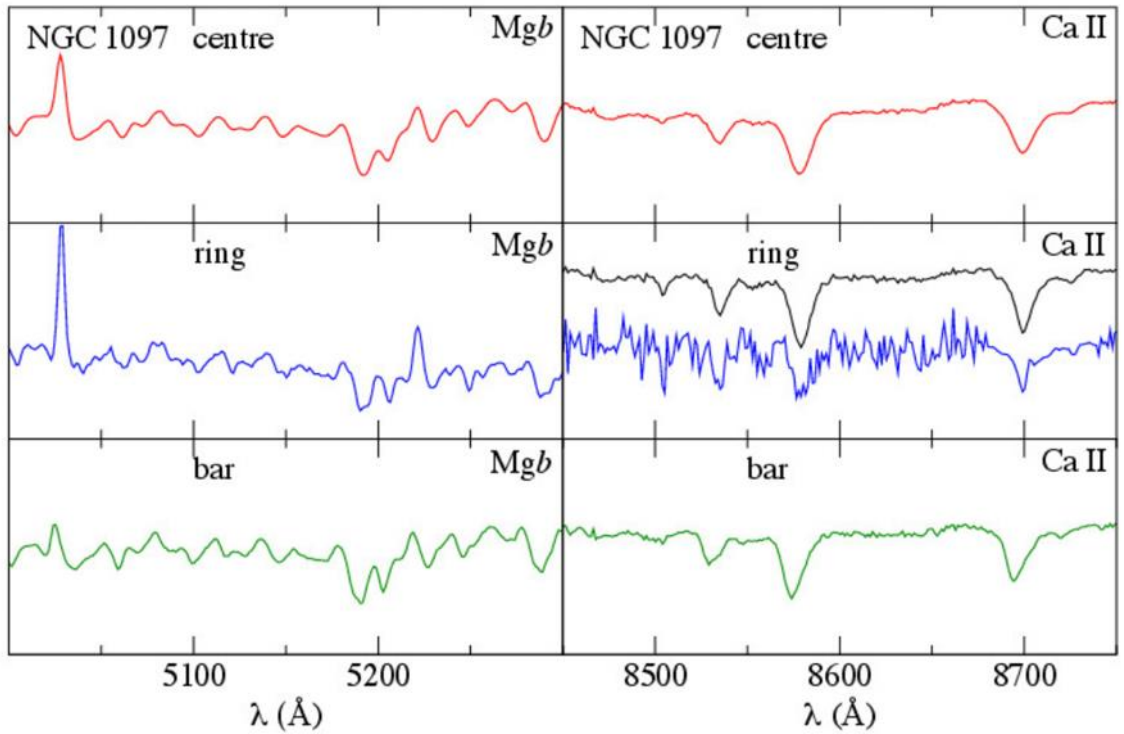

Gadotti+2019

Contamination from Paschen lines (strong star formation)

Broadening of absorption lines is caused by the stellar line of sight velocity distribution (LOSVD), which can be recovered from fitting a combination of template spectra, convolved with a line profile (templates can be from spectra of observed stars or from stellar evolution models, both with pros and cons).

Deriving Stellar Kinematics

- Line profile can be written using a Gauss-Hermite parameterisation:

$$L(v) = \frac{\gamma\alpha(w)}{\sigma}\sum_{j=0}^{4} h_j H_j(w)$$

$$\alpha(w) = \frac{1}{\sqrt{2\pi}} e^{-w^2/2}$$

$$w \equiv \frac{v - v_0}{\sigma}$$

- h_3 is the skewness (asymmetric deviations from a Gaussian), while h_4 is the kurtosis (symmetric deviations)
- While a correlation between v and h_3 indicates elongated orbits, an anti-correlation indicates near circular orbits, simply because the circular speed is the maximum allowed
- Positive values of h_4 indicate overlapping populations with different σ

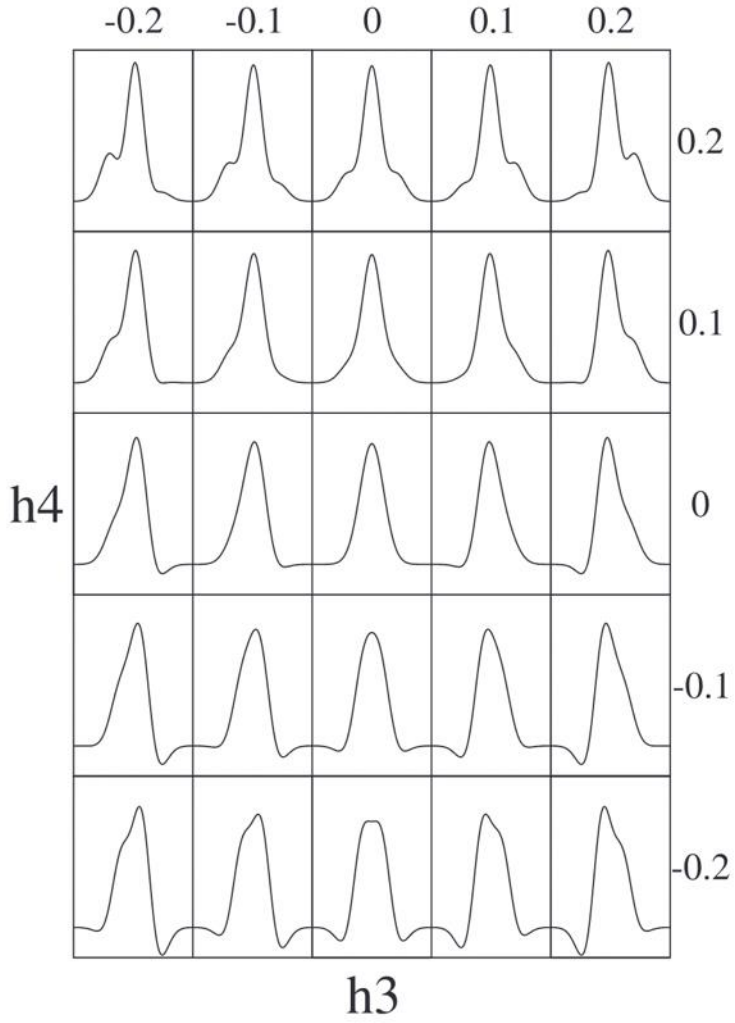

FIG. 3.—A pure Gaussian ($h_3 = h_4 = 0$) may suffer asymmetric deviations when $h_3 \neq 0$ and symmetric deviations when $h_4 \neq 0$.

Deriving Stellar Populations

- Mean stellar ages and metallicities, but also α/Fe and star formation histories.

- Ingredients to build a template library are stellar evolution tracks in the Hertzprung-Russel diagram (for a selection of given masses and chemical composition) and the Initial Mass Function (IMF).

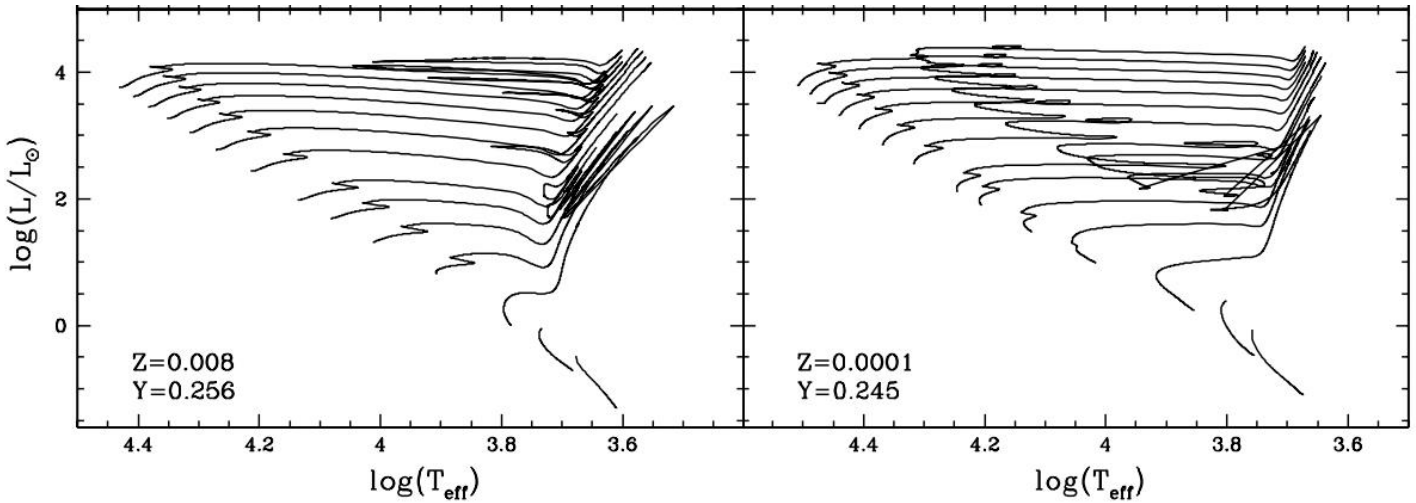

Pietrinferni+2004

FIG. 3.—Selected evolutionary tracks for the 10 metallicities of our model grid. The plotted tracks correspond to models with the following initial masses: $M/M_{\odot} = 0.5, 0.7, 1.0, 1.5, 2.0, 2.5, 3.0, 4.0, 5.0, 6.0, 7.0, 8.0, 9.0,$ and 10.0.

Deriving Stellar Populations

- Mean stellar ages and metallicities, but also α/Fe and star formation histories.

- Ingredients to build a template library are stellar evolution tracks in the Hertzprung-Russel diagram (for a selection of given masses and chemical composition) and the Initial Mass Function (IMF).

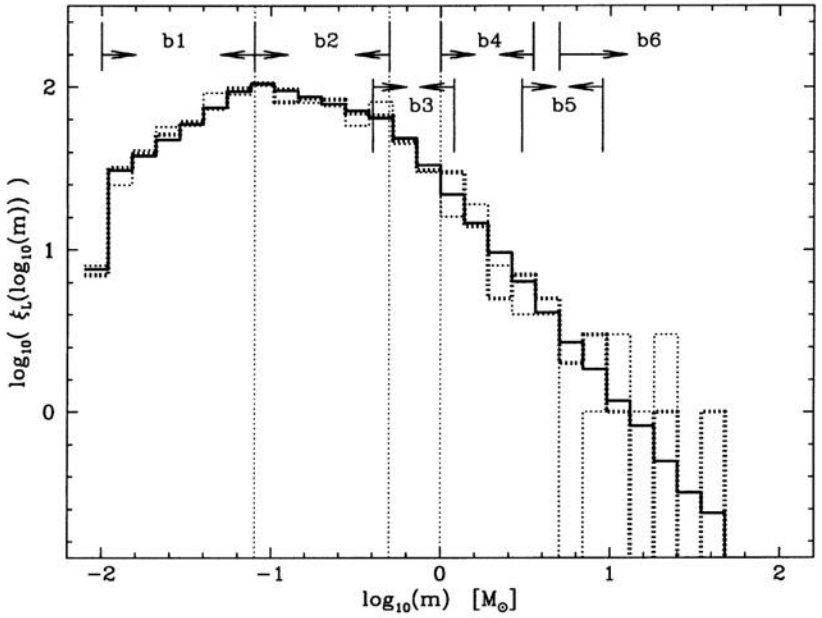

Figure 2. The adopted logarithmic IMF (equations 2 and 3), $\xi_L/10^3$, for 10^6 stars (solid histogram). Two random renditions of this IMF with 10^3 stars are shown as the heavy and thin dotted histograms. The mass ranges over which power-law functions are fitted are indicated by the arrowed six regions (equation 4), while thin vertical dotted lines indicate the masses at which α_i changes.

Kroupa (2001)

Number of stars formed at each mass bin.

Deriving Stellar Populations

Figure courtesy of Russell Smith

- Template spectra will depend on these ingredients
- Spectra are very similar at old ages

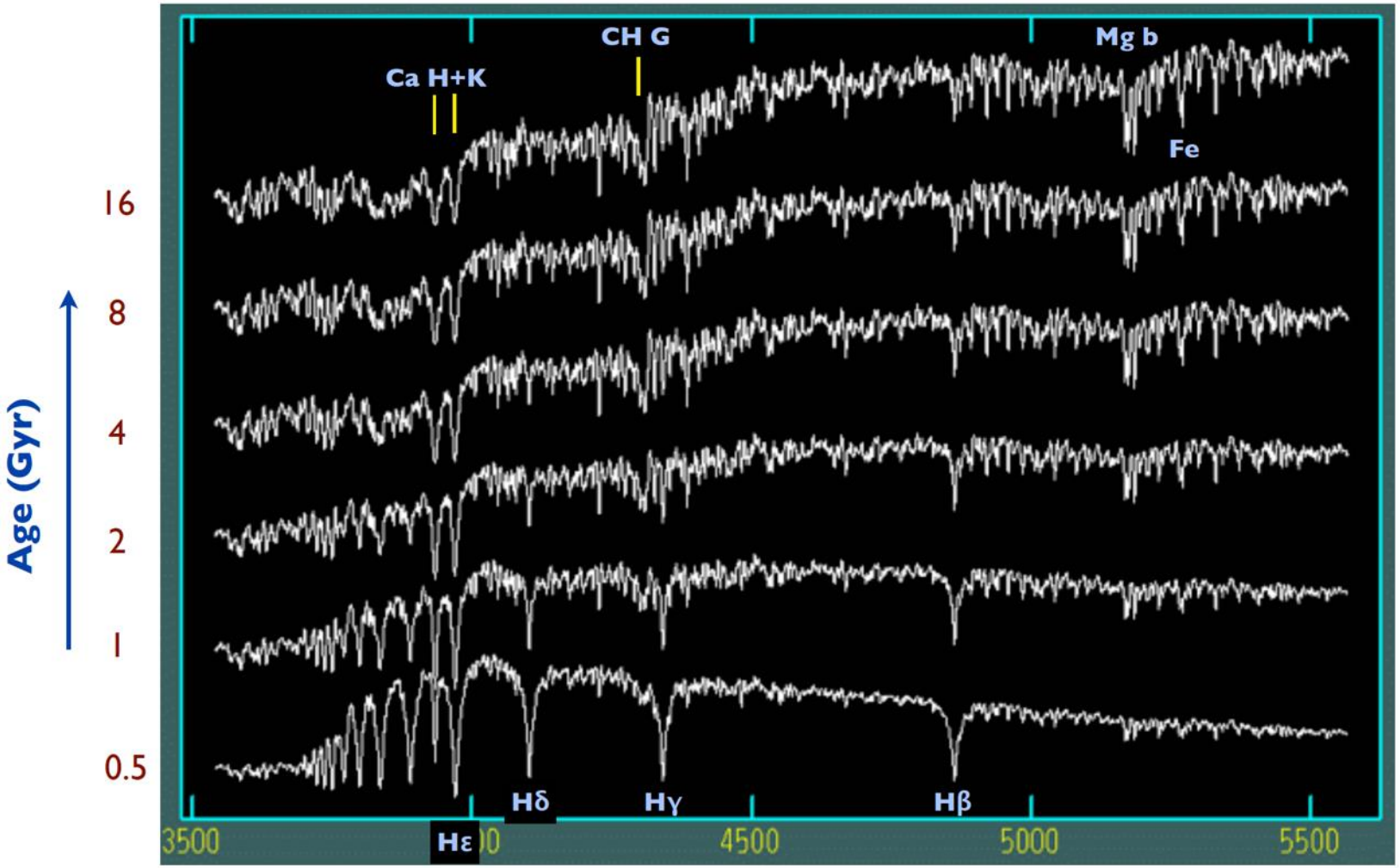

Vazdekis et al. (2010) models at solar Fe/H from MILES library.

Deriving Stellar Populations

Figure courtesy of Russell Smith

- Template spectra will depend on these ingredients
- Spectra are very similar at old ages
- More and deeper lines at high metallicities

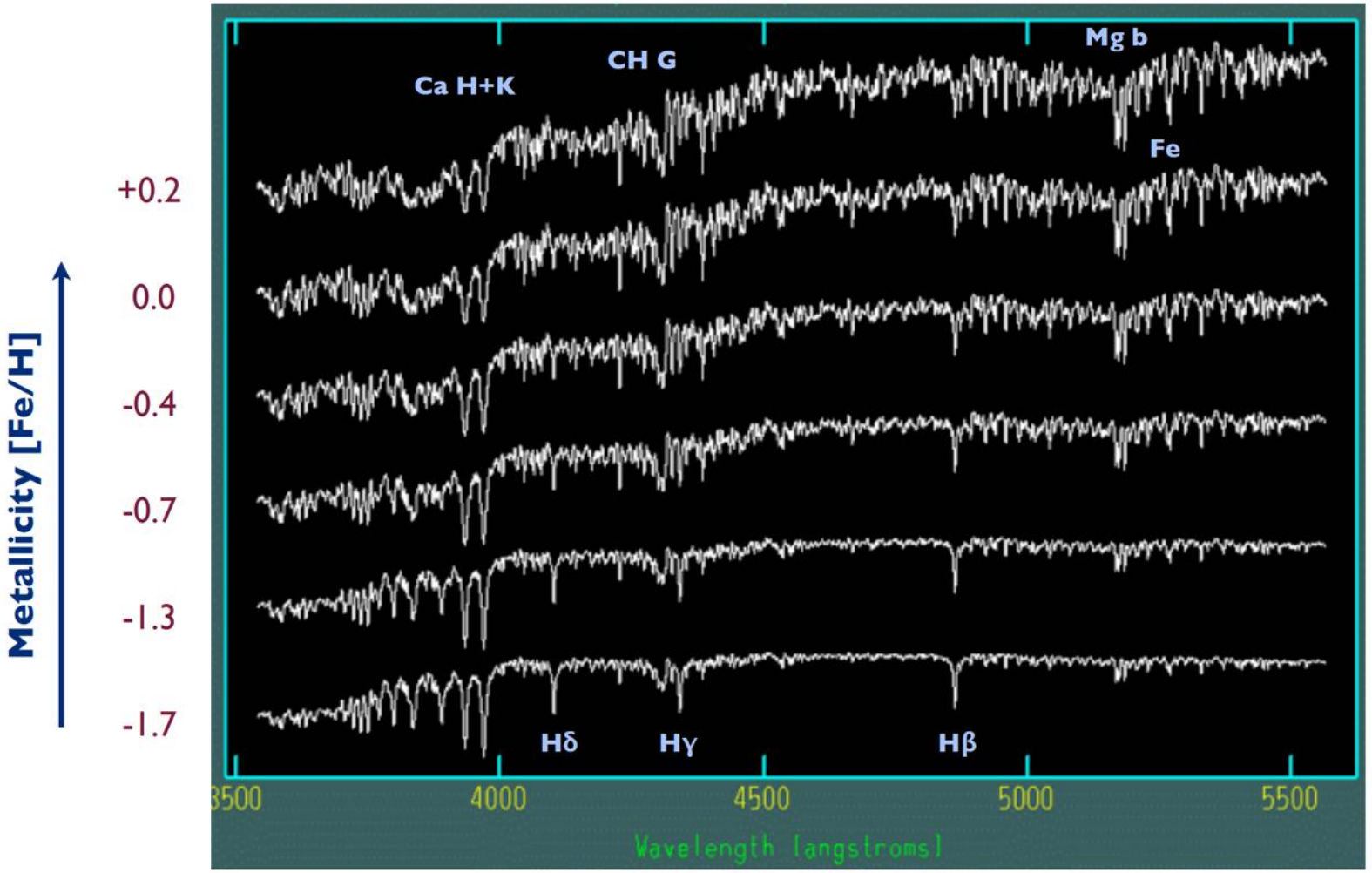

Vazdekis et al. (2007) models at age 10 Gyr from MILES library

Deriving Stellar Populations

Figure courtesy of Russell Smith

- Template spectra will depend on these ingredients
- Spectra are very similar at old ages
- More and deeper lines at high metallicities
- Age-Metallicity degeneracy is clear but can be beaten with information on Balmer lines and below 4000Å

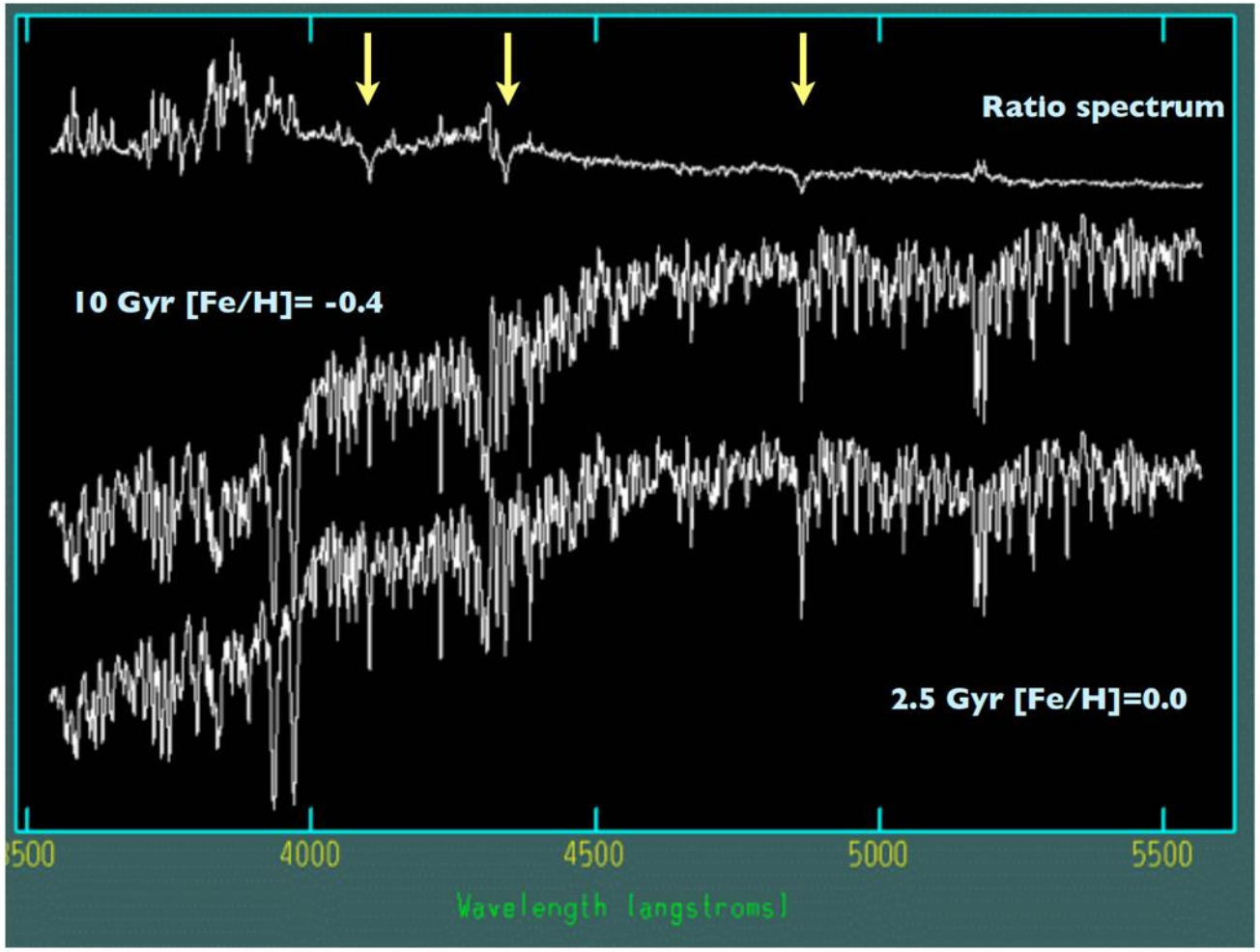

Vazdekis et al. (2007) models from MILES library

Deriving Stellar Populations

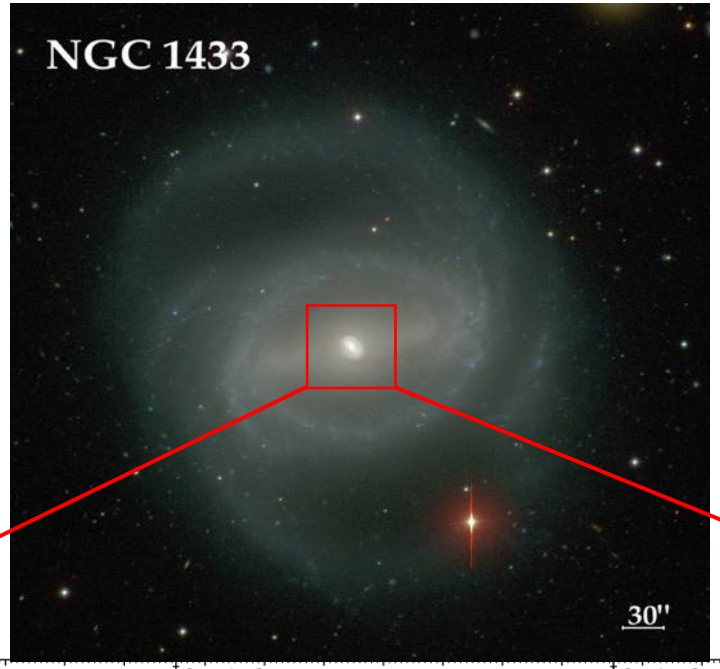

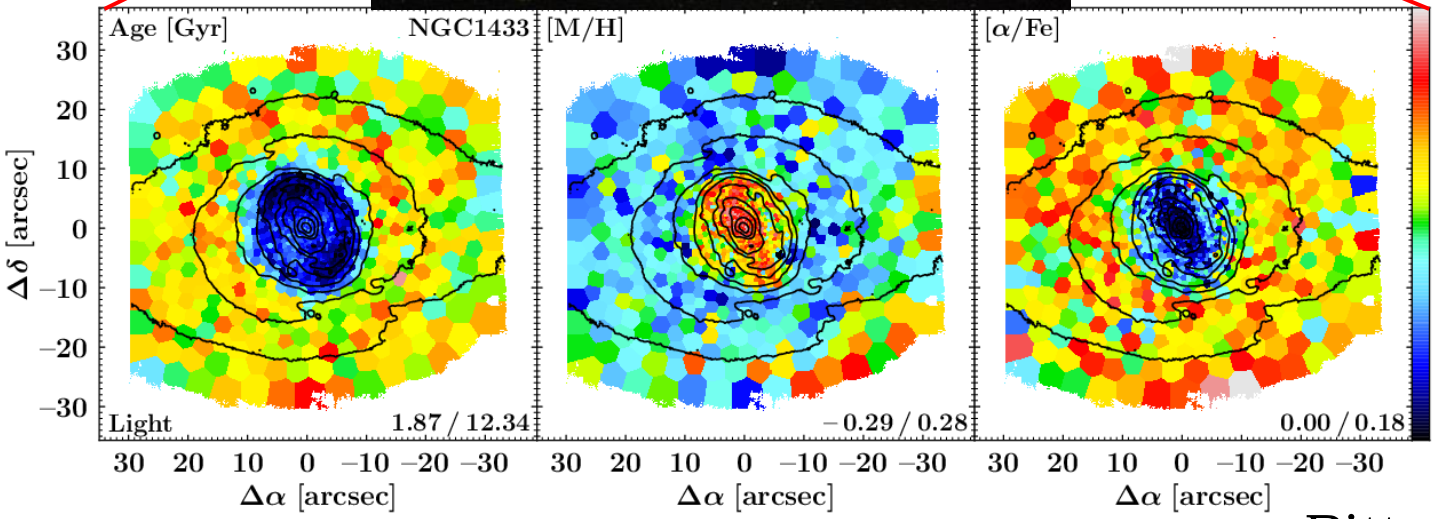

Bittner+2020

And this is how one can build maps of mean stellar age, metallicity and α/Fe, as well as star formation histories.

de Sá-Freitas+2023

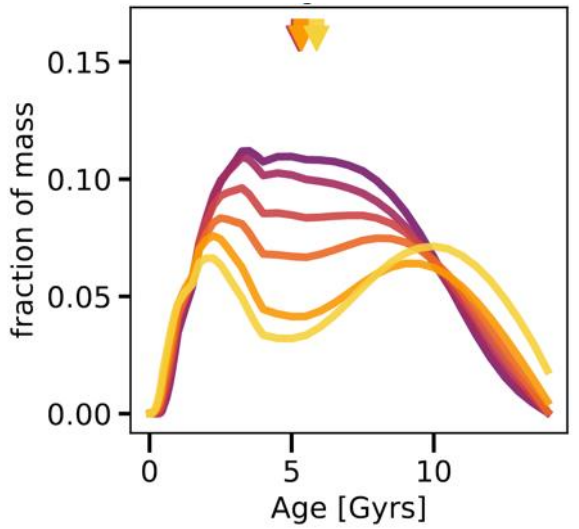

The End

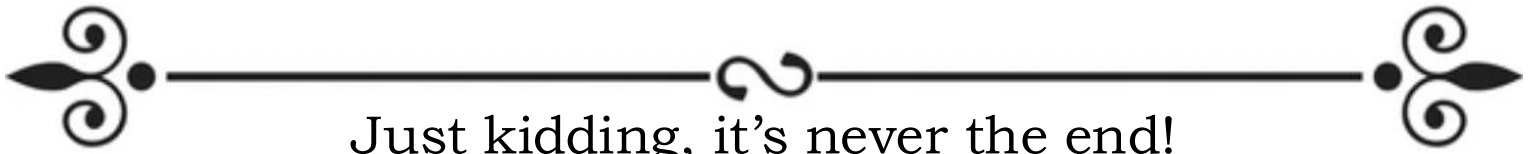

Just kidding, it’s never the end!